



HAL
open science

Thermodynamics and magnetism of antiferromagnetic spinor Bose-Einstein condensates

Camille Frapolli

► **To cite this version:**

Camille Frapolli. Thermodynamics and magnetism of antiferromagnetic spinor Bose-Einstein condensates. Quantum Gases [cond-mat.quant-gas]. École normale supérieure de Paris, 2017. English. NNT: . tel-01515042v1

HAL Id: tel-01515042

<https://theses.hal.science/tel-01515042v1>

Submitted on 26 Apr 2017 (v1), last revised 2 Jun 2017 (v2)

HAL is a multi-disciplinary open access archive for the deposit and dissemination of scientific research documents, whether they are published or not. The documents may come from teaching and research institutions in France or abroad, or from public or private research centers.

L'archive ouverte pluridisciplinaire **HAL**, est destinée au dépôt et à la diffusion de documents scientifiques de niveau recherche, publiés ou non, émanant des établissements d'enseignement et de recherche français ou étrangers, des laboratoires publics ou privés.



Distributed under a Creative Commons Attribution - NonCommercial - NoDerivatives 4.0 International License

THÈSE DE DOCTORAT
de l'Université de recherche
Paris Sciences Lettres – PSL Research University
préparée à l'École normale supérieure

Thermodynamics and magnetism of antiferromagnetic spinor Bose-Einstein condensates

Thermodynamique et magnétisme
dans des condensats de Bose-Einstein de spin 1
avec interactions antiferromagnétiques

par **Camille Frapolli**

dirigée par Fabrice Gerbier
& Jean Dalibard

École doctorale n°564
Spécialité : Physique
Soutenue le 29.03.2017

Composition du Jury :

Mme. Patrizia Vignolo
Université de Nice – Sophia Antipolis
Présidente du jury

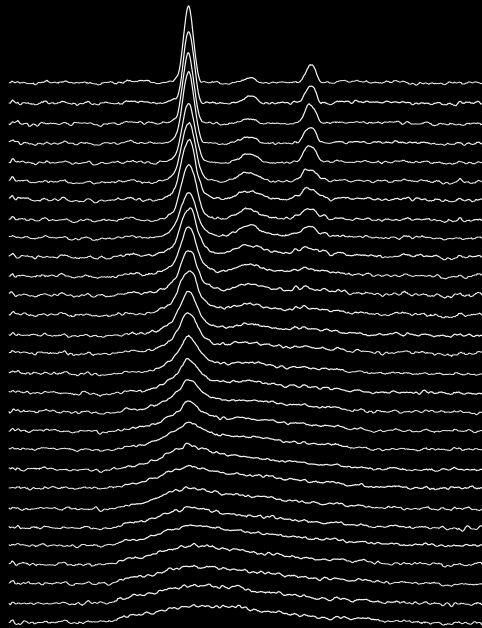
M. Gabriele Ferrari
Università degli Studi di Trento
Rapporteur

M. Bruno Laburthe-Tolra
CNRS, Université Paris 13 – Villetaneuse
Rapporteur

M. Fabrice Gerbier
CNRS
Directeur de thèse



Thermodynamics and magnetism of antiferromagnetic spinor Bose-Einstein condensates



Contents

0	Introduction	9
1	Elements of theory for spinor Bose gases	13
1.1	Single component Bose gas at finite temperature	13
1.1.1	Ideal gas in a harmonic trap	14
1.1.2	Finite size effects	17
1.1.3	Role of interactions	19
1.1.4	Role of realistic trapping potentials	21
1.2	Single component Bose-Einstein condensates at $T=0$	29
1.2.1	Ground state of Bose-Einstein condensates	29
1.2.2	Free expansion of Bose-Einstein condensates	31
1.3	Spin-1 Bose-Einstein condensate at $T=0$	32
1.3.1	Spinor scattering properties	32
1.3.2	Zeeman energy	34
1.3.3	Single mode approximation	36
1.4	Critical temperatures of ideal spin-1 gases	39
1.5	Conclusion	42
2	Production and diagnostics of ultracold gases of sodium atoms	43
2.1	Experimental realization of spinor Bose-Einstein condensates	44
2.1.1	Overview	44
2.1.2	Laser cooling and trapping	45
2.1.3	Optical dipole traps and evaporative cooling	48
2.1.4	Absorption imaging	50
2.1.5	Characterization of the trapping potential	53
2.2	Spin-dependent imaging	57
2.2.1	Stern-Gerlach Imaging	57
2.2.2	Imaging noise reduction	58
2.2.3	Magnification	66
2.2.4	Determination of the scattering cross-sections	68
2.3	Image analysis	71
2.3.1	Fit of images	71
2.3.2	Extraction of temperatures	72
2.4	Manipulation of the atomic spin	73
2.4.1	Rabi oscillations	73
2.4.2	Adiabaticity in magnetic field ramps	76

2.4.3	Diagnostics of the magnetic environment	77
2.4.4	Preparation of the magnetization	80
2.4.5	Adiabatic rapid passage	81
2.5	Conclusion	82
3	Magnetic phases of antiferromagnetic spinor BEC at low temperatures	85
3.1	Mean-Field description of spinor Bose-Einstein condensates	86
3.1.1	Alignment and spin-nematic order	87
3.1.2	Mean-Field description at $T=0$	88
3.1.3	$T=0$ magnetic phase diagram (D. Jacob <i>et al.</i> PRA 86 061601)	89
3.2	Observation of phase locking in spinor BEC	91
3.2.1	Methods	91
3.2.2	Observation of phase locking	93
3.2.3	Effect of a finite kinetic temperature	96
3.2.4	Effect of a finite spin temperature	98
3.3	Spin fluctuations	100
3.3.1	Spin fluctuations for low magnetization	101
3.3.2	Experimental measurement of fluctuations	101
3.3.3	Spin thermometry	103
3.4	Conclusion	106
4	Thermodynamic phase diagram of a spin 1 Bose gas	109
4.1	Experimental methods	111
4.1.1	Overview	112
4.1.2	Boost to the Stern-Gerlach separation	114
4.1.3	Image Analysis	115
4.2	Experimental thermodynamic phase diagram of a spin 1 Bose gas	121
4.2.1	Extraction of the critical temperature	121
4.2.2	Graphical representation of the data	124
4.2.3	Thermodynamic phase diagram	126
4.3	Hartree-Fock model	130
4.3.1	Hartree-Fock description	130
4.3.2	Semi-ideal “four gases” formalism	132
4.3.3	Numerical resolution of the HF model and comparison with data	136
4.4	Conclusion	143
5	Conclusion	145
5.1	Summary	145
5.2	Prospects	147
	Appendices	149
A	Alternative laser source for laser cooling and Raman transitions	151
A.1	Second Harmonic Generation	151
A.2	Intracavity frequency doubling	153
A.3	Iodine spectroscopy	155

B	Light-Atom Interaction in the ground state electronic manifold	157
B.1	Derivation of the lightshift hamiltonian	157
B.2	Lightshift operator in the hyperfine basis	161
C	Raman Schemes	163
C.1	Rabi oscillations with copropagating beams	163
C.2	Spin Orbit coupling: <i>Spielman</i> scheme	166
C.3	Spin orbit coupling: 4 photons transitions	166
D	Spin-mixing oscillations	171
D.1	Spin mixing oscillations after a Rabi Oscillation	171
D.2	Evolution of the populations during a magnetic field ramp	174
E	Perturbative development around the point of simultaneous condensation	177
F	Remerciements	181
	Bibliography	183

O

Introduction

MANY BODY PHYSICS describes the behavior of physical systems with a large number of constituents. Its applications covers many domains such as quantum chemistry, where it describes the behavior of electrons in atoms or molecules, nuclear physics, condensed matter physics where it describes electrons in a crystal or ultracold atoms physics where it describes small gaseous samples (up to a few billions atoms). The N body problems with $N \gg 1$ are not exactly solvable despite their ubiquity in physics. Many approximate solutions were developed to circumvent this issue and obtain effective descriptions of these systems that can be used to predict their properties.

In almost all cases, a statistical approach (see refs. [1, 2]), allowed by the large number of particles, is used to describe the system by a limited set of macroscopic state functions (temperature T , pressure P , density $n...$). The relations between these are derived from specific assumptions on the microscopic system. Perhaps the simplest assumption consists in considering the constituents of the gas to be independent, which leads to the ideal gas model. Ideal gas theory however fails when the interparticle distance becomes small enough such that interactions between atoms or molecules are not negligible. This happens in dense samples (condensed matter, nuclei) and also, perhaps more surprisingly, in dilute atomic gases at ultralow temperatures. In this case, the deviations from ideal theory can be treated perturbatively, for example with a virial expansion. The parameters of such expansion depend on the microscopic properties of the system and are in general challenging to compute for large corrections.

A particularly spectacular failure of this type of theories is observed when interactions lead to a particular ordering at the macroscopic level, *i.e.* to a new state of matter. This new state often form collective states and are usually observed at “low” temperature. The ordering characteristic of the collective state washes out due to thermal fluctuations above a second order phase transition at a temperature that depends on the interaction strength. Examples of such systems are realized with ferromagnetic materials (see ref. [3]), in which a permanent magnetic moment can be observed even in absence of magnetic fields below the Curie temperature, due to the alignment of the spins within the material. Another example of collective behavior results from the observation of superfluid flow in liquid helium at low temperatures (see refs. [4, 5]). This originates from a peculiar effect of the quantum statistics of bosonic particles predicted by Bose for photons (see ref. [6]) and generalized by Einstein (see ref. [7]) in 1924 that leads to a large fraction of the liquid composed of atoms being in the lowest energy single particle state (a plane wave at rest in uniform systems). This phenomenon called Bose-Einstein condensation, is predicted even for an ideal

gas. The large interactions in liquid helium complicates the theoretical description of its exact properties (see ref. [5]).

The advances in laser cooling of atoms (that were awarded by a Nobel prize to S. Chu, C. Cohen-Tannoudji and W. Phillips in 1997, see ref. [8–10]) enabled the production of extremely cold gaseous samples at temperature in the microKelvin range. Further advances in trapping and evaporative cooling led to the production of even lower temperature clouds and to the first gaseous Bose-Einstein condensate, where a macroscopic population appears in the ground state of the trapping potential containing the gas. Their realization was awarded by a Nobel prize to E. Cornell, W. Ketterle and C. Wieman in 2001, see refs [11–13] in 1995. Depending on the details of the trap (size, shape, dimensionality), BECs can display many peculiar properties due to their quantum nature and to interactions between their components, in particular superfluidity (see reviews in refs. [14, 15]). Bose-Einstein condensates provide an advantageous experimental platform for the study of quantum fluids as they are created in a well controlled and isolated environment. Additionally, as compared with liquid helium or electrons in solid state systems, the interactions strength in ultracold gases are well understood and can (for several atomic species) be accurately controlled using Feshbach resonances (see ref.[16, 17])

Following their discovery, the coherent nature of Bose-Einstein condensates have been experimentally demonstrated by interference type experiments (see refs.[18, 19]) and their superfluid nature by the observation of quantized vortices (see refs.[20–22]) and superfluid flow (see ref. [23]). The cooling and trapping techniques developed for Bose gases were extended to fermionic systems, leading to the realization of a degenerate Fermi gas (see refs. [24]). The degree of control in the potentials in which these gases are created led to the study of low-dimensional gases, for example Tonk-Girardeau gases in 1D (see refs. [25, 26]), or superfluid gases below the so-called Berezinsky-Kosterlitz-Thouless (BKT) transition in 2D (refs. [27, 28]). The equilibrium thermodynamics of Bose gases near the Bose-Einstein transition was also studied [14] and measured [29]. Another direction that is still extensively explored results from trapping ultra cold atoms in lattice-like potentials created with interfering laser beams. These geometries opened new possibilities regarding the simulation of complex states of condensed matter. Spectacular results in this field include the observation of the superfluid-Mott insulator transition [30–32], many-body localization in disordered potentials [33] and the detection of inter-site magnetic correlations [34, 35].

In the first Bose-Einstein condensate experiments, only single components gases were studied due to the use of magnetic trapping [11–13]. Few years later, the development of optical trapping (see ref. [36, 37]) allowed the study of multicomponent gases. In all multi-component quantum fluids, the internal degree of freedom plays a significant role in the physical behavior of the system (for example in the superfluidity of ^3He [38, 39]). Ultracold Bose gases with a spin degree of freedom are called “spinor Bose gases” and constitute another example of spinful quantum fluid. They present a wide variety of novel physical phenomenons and constitute a good system for the study of magnetic phases of matter.

The most striking differences between spinor BEC and their single component counterpart results from the interactions between their internal components. These are of two types: spin-exchange contact interaction and dipole-dipole interactions. Contact interactions are present in all spinor gases and give rise to spin dynamics analogous to Josephson oscillation in superconductor junctions (see [40–51]), to spin textures (see refs. [52, 53]), and to magnetic ordering in the ground state (see refs. [47, 54–57]). On the other hand, dipolar interactions are significant mostly for

higher spin atoms (such as chromium, erbium or dysprosium), even though they were shown not to be completely negligible for rubidium atoms as discussed in ref. [58]. Nevertheless, in these higher spin atoms, the relatively high magnitude of the dipole-dipole interactions modifies the physics significantly as compared with low spin species. Examples of such effects are strong dipolar relaxation phenomena (see refs. [59–61]) or anisotropic behavior (see refs [60, 62, 63]).

This manuscript studies some of the properties of spin 1 Bose gases at thermal equilibrium. We will show that the physics of this system is governed by spin exchange contact interactions and Zeeman energy. The ground state of spin 1 Bose gases is predicted to present two magnetic phases for spin 1 [47, 54–57, 64, 65]. One of the phase is called an antiferromagnetic phase, and bears similar properties to the Néel phase of spin 1/2 antiferromagnets. The other magnetic phase is a polar phase [66, 67] and does not exist in spin 1/2 systems. In polar phases, the magnetic order is not set by a magnetization, but rather by spin fluctuations transverse to a preferred axis. Spin nematic order takes its name from the similarity of the order parameter to the one of nematic liquid crystals (see ref. [68]). Spin 1 nematic phases have been widely studied in the context of solid state physics (see refs. [69–71, 71–81]). The unambiguous demonstration of nematic order in condensed matter systems remains challenging (see refs. [70, 72–74, 76, 82]) because the bulk properties that are often measured such as the magnetic susceptibility mostly depend on magnetization which vanishes in polar phases. Ultracold spinor Bose gases (see refs. [47, 51, 54–56, 65, 77–79, 81, 83, 84]) allow for more controlled and thorough measurements, and as such offer a good alternative to study such a magnetic phase. In this thesis, we study experimentally this kind of magnetic ordering using an antiferromagnetic spin 1 Bose-Einstein condensate.

Considering finite temperature properties, the onset of magnetic ordering in spin 1 Bose gas has also been covered theoretically in many references (see refs. [85–92]), and is predicted to offer a rather rich behavior. However, the thermodynamic of spin 1 Bose gases was only scarcely explored experimentally. We present in this manuscript a thorough study of the thermodynamic properties of a spin 1 Bose gas using a sodium gas with antiferromagnetic interactions.

Summary

In the chapter 1, we first recall in section 1 introductory notions about Bose-Einstein condensation in scalar gases merely as an occasion to set notations. We start by introducing the thermodynamics of Bose gases near the critical temperature for Bose-Einstein condensation, and what are the expected deviations to the ideal gas picture due to interaction and finite atom number. We then describe a more sophisticated formalism that we have developed to estimate the deviations from the harmonically trapped gas model due to the anharmonicity and final trap depth of the trapping potential. This modifies the critical temperature for Bose-Einstein condensation and we estimate the resulting shift. In sections 2 and 3, we recall the methods to describe the ground state of scalar and spinor Bose-Einstein condensates. In section 4, we introduce the thermodynamic of the ideal spin 1 Bose gas. This chapter is intended as a detailed introduction to the topic and to give the reader an overview of the theoretical tools that we use in the following chapters.

The experimental techniques that we use to create and observe the spinor Bose gases are introduced in chapter 2. In section 1, we start by giving an overview of the cooling sequence, and of the trapping potentials that we use to create spinor Bose gases. We then discuss in section 2 the detection of spinor Bose gas with spin dependent imaging, and its limits in term of noise. In section 3, we detail the fitting methods that we use to extract thermodynamic quantities from images. In section 4, we discuss a particular set of techniques more specific to spinor Bose gases,

that are used to manipulate the spin degree of freedom of the gas.

In chapter 3, we discuss low-temperature properties of a spin 1 Bose gas with antiferromagnetic interactions, *e.g.* its ground state and magnetic phases. In section 1, we recall the general properties of the antiferromagnetic phase observed for low magnetic fields, and of the broken axisymmetry phase observed for high magnetic field. They mostly differ by the length of their transverse spin that vanishes for the former, and is minimal for the latter. We show that the minimization of the transverse spin in the broken axisymmetry phase results from a phase locking mechanism mediated by spin changing interactions. In section 2, we study this phase locking mechanism using spin rotations, and demonstrate experimentally the minimization of the transverse spin. We discuss modifications of this results that comes from the finite temperature of the gas. In section 3, we mention the measurement of fragmentation near zero magnetic field due to the degeneracy of all three Zeeman components. This leads to large population fluctuations and we discuss that these can originate from a finite spin temperature.

In chapter 4, we measure the thermodynamic properties of spin 1 Bose gas near the Bose-Einstein transition. In section 1, we describe the modifications to the experimental setup that we had to implement to measure “high temperature” gases, and describe the data analysis procedure that we have applied to extract thermodynamic quantities from absorption images. In section 2, we show the measurement of the thermodynamic phase diagram of a spin 1 Bose gas and compare our measurement to the predictions of ideal gas theory for several strengths of the Zeeman energy. We discuss how to interpret a large deviation from ideal gas theory by the effect of interactions, and show that these are enhanced below the first critical temperature by the presence of a condensate. In section 3, we compare the data to the results of a numerical resolution of an Hartree-Fock model and discuss possible additional effects (finite atom number and trap anharmonicities) that affect the measured critical temperature.

Chapter 5 concludes the thesis. We first summarize the content of each chapter and also discuss prospects for future work.

“À raison d’un enfoncement de la ville de trente centimètres par siècle, expliquais-je, donc de trois millimètres par an, donc de zéro virgule zéro zéro quatre-vingt-deux millimètres par jour, donc de zéro virgule zéro zéro zéro zéro zéro un millimètre par seconde, on pouvait raisonnablement, en appuyant bien fort nos pas sur le trottoir, escompter être pour quelque chose dans l’engloutissement de la ville.”

LA SALLE DE BAIN
Jean-Phillipe Toussaint



Elements of theory for spinor Bose gases

THIS CHAPTER will expose some of the basic phenomenons that govern the behavior of dilute spinor Bose gases at very low temperatures. We will recall these notions as a mean to set notations and to introduce more complicated concepts in the rest of the manuscript. In section 1, we will start by discussing the Bose-Einstein transition for an ideal scalar Bose gas, as an introduction to the case of spin 1 gases that we cover later on. We will recall the refinements over ideal gas theory such as the effect of interactions and finite atom numbers. I will take advantage of this chapter to introduce a slightly less common notion, which is the modification of the thermodynamics of Bose gases due to the anharmonicity and finite depth of the trapping potential. In this paragraph, we determine the critical atom number in a realistic trapping potential that corresponds to the one created by two crossed laser beams. We discuss how we define the trap depth from the mechanisms at stake in evaporative cooling, and we will derive the expected shift in critical temperature. In section 2, I will recall how to describe a pure single-component Bose-Einstein condensate at zero temperature and describe its expansion dynamics in free space. In section 3, I will introduce the physics of spinor Bose-Einstein condensates through scattering properties and interactions with magnetic fields. Both these section will set the grounds for the study of low temperature phases of spin 1 Bose-Einstein condensates in chap. 3.

In section 4, I will introduce the thermodynamic of an ideal spin 1 Bose gas near the Bose-Einstein critical temperature. This section is intended to give the reader a taste of the experimental study of the problem in chapter 4. We will see that ideal gas theory predicts a surprisingly rich thermodynamic behavior due to the conservation of the magnetization.

1.1 Single component Bose gas at finite temperature

Bose-Einstein condensation results from the role of the quantum statistics of bosons [6, 7] at low temperature. In the grand canonical ensemble [2], the minimization of entropy given the mean energy \bar{E} and particle number \bar{N} lead to the density operator:

$$\hat{\rho} = \frac{1}{\Xi} e^{-\beta(\hat{H} - \mu\hat{N})}, \quad (1.1)$$

where μ , the chemical potential, and $\beta = 1/k_B T$ are two Lagrange multipliers for the particle number and energy respectively. Ξ is the grand canonical partition function:

$$\Xi = \text{Tr} \left(e^{-\beta(\hat{H} - \mu\hat{N})} \right). \quad (1.2)$$

The Gibbs Free energy is deduced from the grand partition function:

$$G(N, T, V) = -k_B T \ln(\Xi), \quad (1.3)$$

the total atom number is:

$$\bar{N} = \frac{\partial G}{\partial \mu} = -\frac{1}{\beta} \frac{\partial \ln \Xi}{\partial \mu} = \sum_i g_i \bar{N}_i, \quad (1.4)$$

where g_i is the degeneracy of the energy level i and the average occupation number of the state i , \bar{N}_i is expressed as:

$$\bar{N}_i = \beta \frac{\partial \ln \xi_i}{\partial \mu} = \frac{1}{e^{\beta(E_i - \mu)} - 1}, \quad (1.5)$$

In particular, the occupation number of the ground state is:

$$\bar{N}_0 = \frac{1}{e^{\beta(E_0 - \mu)} - 1}. \quad (1.6)$$

We note that expression (1.6) imposes an important bound on the chemical potential:

$$\mu < E_0, \quad (1.7)$$

where E_0 is the the energy of the ground state of the system. If the temperature is high ($\beta(E_k - E_0) \ll 1$), the Bose-Einstein statistics is equivalent to the Maxwell-Boltzmann statistics used to described classical gases:

$$\bar{N}_{MB} \simeq e^{-\beta(E_k - \mu)}. \quad (1.8)$$

An important difference between Bose-Einstein and Maxwell-Boltzmann statistics is that in the former case the occupation number of the ground state diverges as $\mu \rightarrow E_0$. Then, the ground state can become macroscopically populated even if $k_B T \gg (E_1 - E_0)$. The fraction of ground state particles of this type of gas is called a Bose-Einstein condensate (BEC). It is often convenient to treat the BEC separately such that the total number of atom N is written as:

$$N = N_0 + N', \quad (1.9)$$

where N' is the population of the normal component, defined as the atoms that does not belong to the condensate.

1.1.1 Ideal gas in a harmonic trap

Density of states

Ultracold atomic gases are created and cooled in traps, usually well approximated by a 3D harmonic potential:

$$V(x, y, z) = \frac{1}{2} m \omega_x^2 x^2 + \frac{1}{2} m \omega_y^2 y^2 + \frac{1}{2} m \omega_z^2 z^2. \quad (1.10)$$

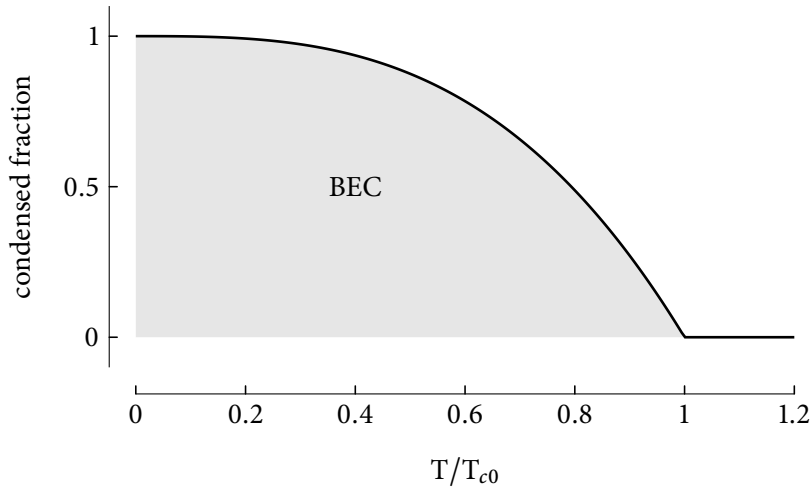


FIGURE 1.1: Condensed fraction of an ideal Bose gas in a harmonic trap.

The characteristic length scales of the ground state wavefunction are the harmonic oscillator lengths:

$$a_{\text{ho},i} = \sqrt{\frac{\hbar}{m\omega_i}}. \quad (1.11)$$

where i stands for x, y, z . The spectrum of such a potential is given by three quantum numbers $n_x, n_y, n_z \in \mathbb{N}^3$ such that we obtain:

$$\varepsilon(n_x, n_y, n_z) = \left(n_x + \frac{1}{2}\right)\hbar\omega_x + \left(n_y + \frac{1}{2}\right)\hbar\omega_y + \left(n_z + \frac{1}{2}\right)\hbar\omega_z, \quad (1.12)$$

With the spectrum, the population of the normal component N' in the trap is calculated explicitly by summing over the occupation numbers of all excited states and we have:

$$N' = \sum_{i=1}^{\infty} \frac{g_i}{\exp \beta(\varepsilon_i - \mu) - 1}, \quad (1.13)$$

We note however that the spectrum, and its degeneracies are not known for anisotropic harmonic traps or for more complicated trap shapes.

For now, we will study the case of an isotropic harmonic potential of trapping frequency $\bar{\omega}$, and instead of considering the full spectrum in Eq. (1.12), we will study the case $k_B T \gg \hbar \bar{\omega}$ and consider a continuous spectrum where the density of states $\rho(E)$ can be expressed as:

$$\rho(E) \simeq \frac{E^2}{2\hbar^3 \bar{\omega}^3}, \quad (1.14)$$

The excited state population is then given by:

$$N' = \int_0^{\infty} \rho(E) g_{\text{BE}}(E) \quad (1.15)$$

where we have defined the Bose distribution function :

$$g_{\text{BE}}(E) = \frac{1}{\exp \beta E - 1}. \quad (1.16)$$

We remark that even for a vanishing chemical potential, the integral in Eq. 1.15 converges, and provides a finite population N_c in the excited states:

$$N_c = \left(\frac{k_B T}{\hbar \bar{\omega}} \right)^3 g_3(1). \quad (1.17)$$

where we have defined the Bose function of order n , see fig.1.2:

$$g_n = \sum_{k=1}^{\infty} \frac{x^k}{k^n}. \quad (1.18)$$

If the total atom number is larger than N_c , the excess population goes to the ground state and constitutes a Bose-Einstein condensate. As such, N_c is called the critical atom number and is associated with a critical temperature T_c (that is defined by $N = N_c$ for $T_c = T$) that we deduce from Eq. (1.17):

$$T_c = \frac{1}{k_B} \hbar \bar{\omega} \left(\frac{N}{g_3(1)} \right)^{1/3}. \quad (1.19)$$

The condensed fraction defined as $f_c = N_0/N$ is plotted on figure 1.1:

$$f_c = 1 - \left(\frac{T}{T_{c0}} \right)^3. \quad (1.20)$$

As we noted earlier, in more complicated potentials, the spectrum $\{\varepsilon_i\}$ and the density of states $\rho(\varepsilon)$ are in general not known, and another approach is needed.

The semiclassical approximation

We turn to a description of the gas using canonical variables \mathbf{r} and \mathbf{p} and rather than considering the spectrum, we compute the phase space distribution by directly evaluating the density of states with expression [14, 93]:

$$\rho(E) = \frac{1}{(2\pi\hbar)^3} \int d^3\mathbf{r} d^3\mathbf{p} \delta(E - H(\mathbf{r}, \mathbf{p}) - \mu), \quad (1.21)$$

where $H = \mathbf{p}^2/2m + V(\mathbf{r})$ is the Hamiltonian of the system. We note that with this method, we make no assumption regarding the nature of the potential, such that potential shapes beyond the harmonic one can be considered, as we shall discuss in a later paragraph. We can define a phase space distribution $f(\mathbf{r}, \mathbf{p})$ using the Bose distribution

$$(2\pi\hbar)^3 f(\mathbf{r}, \mathbf{p}) = g_{\text{BE}} \delta(E - H(\mathbf{r}, \mathbf{p})) = \frac{1}{\exp(\beta(p^2/2m + V(\mathbf{r}) - \mu)) - 1} \quad (1.22)$$

The excited state population is computed by integration of the phase space distribution:

$$N' = \iint f(\mathbf{r}, \mathbf{p}) d^3\mathbf{r} d^3\mathbf{p}, \quad (1.23)$$

We note that using the potential for an isotropic harmonic trap $V_{\text{ho}} = m\bar{\omega}^2|\mathbf{r}|^2/2$ we recover the same critical atom number as in Eq. (1.17)

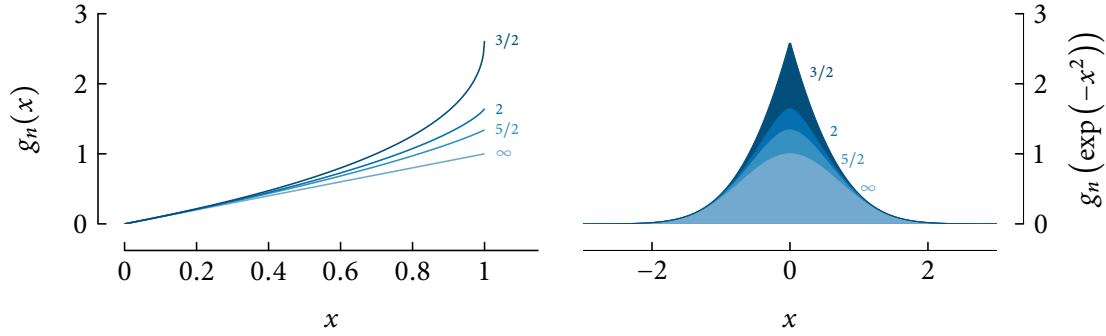


FIGURE 1.2: Bose functions and density profiles of Bose gases. We see that “integrated” density profiles ($g_2, g_3, g_{5/2}$) show a “smoother” behavior near $x = 0$.

Density distributions

The density of the thermal component is obtained through integration of the phase space distribution $f(\mathbf{r}, \mathbf{p})$ over momentum space:

$$n_{3D}(\mathbf{r}) = \frac{1}{(2\pi\hbar)^3} \int \frac{d^3\mathbf{p}}{e^{\beta(p^2/2m+V(\mathbf{r})-\mu)} - 1} = \frac{1}{\lambda_{dB}^3} g_{3/2} \left(e^{\beta(\mu-V(\mathbf{r}))} \right), \quad (1.24)$$

where $\lambda_{dB} = \sqrt{2\pi\hbar^2/mk_B T}$ is the de Broglie wavelength. In experiments, the quantities that are measured are integrated over one or two dimensions of space. This type of profiles obtained from integration of Eq. (1.24) are of the form g_k (gaussian), with $k = 3/2, 2, 5/2$ for respectively 3D, 2D and 1D density profiles, see fig.1.2. The densities differ significantly in the case of a high temperature or a saturated gas. At high temperature, the chemical potential goes to infinity: $\mu \rightarrow \infty$, and the density profiles are 3D Gaussian functions. Indeed, the Bose functions of any order are well approximated by $f(x) = x$ close to the origin as seen in figure 1.2.

Close to the Bose-Einstein transition, as $\mu \rightarrow 0$, both the density and momentum distribution of the thermal gas become more peaked than a Maxwell Boltzmann distribution as seen in figure 1.2. However, the “wings” of both distributions are still well approximated by Gaussian functions. It is also worth noting that the condition for condensation $\mu \rightarrow 0$ (for $V(\mathbf{0}) = 0$) applied to the thermal gas density yields $n_{3D}(\mathbf{0}) = g_{3/2}(1)/\lambda_{dB}^3$. This condition means that a condensate is created at the center of the trap when the central density reaches the critical value for an homogeneous gas.

1.1.2 Finite size effects

The thermodynamic properties of Bose gases are usually defined within the *thermodynamic limit* in which both the particle number N and the volume V goes to infinity while the density of the gas N/V stays constant. In analogy, we define a procedure in which the trapping frequencies ω_i go to zero while the ratio $N\bar{\omega}^3$ is kept constant [93, 94]. In this limit, $k_B T_c \gg \hbar\bar{\omega}$, which is equivalent to say that many levels are populated, and justifies the semiclassical approximation used to obtain the critical temperature before. Besides, this procedure leaves expression (1.19) unchanged, thus allowing the description of Bose-Einstein condensation. We note it also produces a divergence of the peak density of the ideal condensate which scales as $N\omega^{3/2}$. However, this does not affect the critical temperature evaluation as the ground state is always considered separately in the calculations.

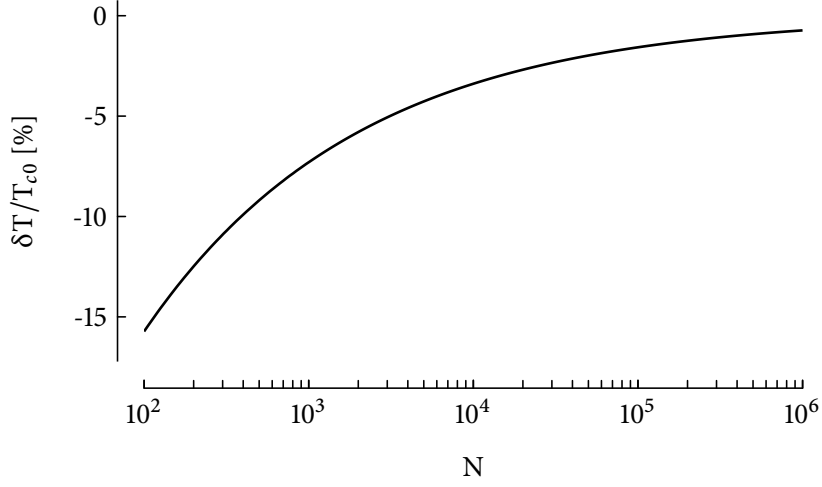


FIGURE 1.3: Finite size shift for a Bose gas in an isotropic harmonic trap.

Finite-size critical temperature shift

Since the number of atoms we can work with is finite, we determine the differences with infinite systems (see refs. [95–99]). We consider an isotropic trap of angular frequency $\bar{\omega}$. The density of states of the system is modified from the semi-classical density of states given in Eq. (1.14):

$$g(\epsilon_k) = \frac{1}{2}(\epsilon_k + 1)(\epsilon_k + 2) \sim \frac{\epsilon_k^2}{2\hbar\omega} + \frac{3\epsilon_k}{2\hbar\omega}, \quad (1.25)$$

with $\epsilon_k = E_k/\hbar\omega$. Above T_{c0} , to first order in $\hbar\bar{\omega}/k_B T$, the total atom number is modified:

$$N' = \left(\frac{\hbar\bar{\omega}}{k_B T}\right)^3 g_3(\tilde{z}) + \frac{3}{2} \left(\frac{\hbar\bar{\omega}}{k_B T}\right)^2 g_2(\tilde{z}) + O\left(\frac{\hbar\bar{\omega}}{k_B T}\right), \quad (1.26)$$

with $\tilde{z} = e^{\beta\mu}$. The correction to critical atom number and temperature to first order $N \rightarrow N_{c0} + \delta N_{FS}$ and $T \rightarrow T_{c0} + \delta T_{FS}$:

$$\delta N_{FS} = \frac{3}{2} \left(\frac{k_B T}{\hbar\omega}\right)^2 g_2(1) \quad (1.27)$$

$$(1.28)$$

We can then use the $N^{1/3}$ scaling in Eq. (1.19) critical temperature to obtain the expression of the shift of the critical temperature δT_{int} with $\delta T_{int}/T_{c0} = -\delta N_c/3N_{c0}$, and compute a practical formula:

$$\frac{\delta T_{FS}}{T_{c0}} = -\frac{g_2(1)}{2g_3^{2/3}(1)} N^{-1/3} \simeq -0.73 N^{-1/3} \quad (1.29)$$

The density of states of a 3D anisotropic harmonic trap cannot be expressed analytically. While it is possible to compute it numerically, it is more convenient to use an alternative, but equivalent approach. Instead of using the modified density of state, we use the semi-classical expression keeping the zero-point energy as a first order correction to the chemical potential (see ref. [100]):

$$N_c = g_3\left(ze^{-\frac{3\tilde{\beta}}{2}}\right) = g_3(z) - \frac{3\tilde{\beta}}{2} g_2(z). \quad (1.30)$$

In the case of an anisotropic trap we have:

$$N_c = g_3 \left(z e^{-\frac{\beta \hbar}{2} (\omega_x + \omega_y + \omega_z)} \right) = \left(\frac{k_B T}{\hbar \bar{\omega}} \right)^3 g_3(z) \prod_{i=\{x,y,z\}} \left(1 - \frac{\beta \hbar \omega_i}{2} g_2(z) \right). \quad (1.31)$$

After simplifications, this gives a very similar result to the isotropic case with a correction factor depending on the geometric average of the trap frequencies:

$$\frac{\delta T_c}{T_{c,\text{ideal}}} = -0.73 \frac{\omega_x + \omega_y + \omega_z}{3\bar{\omega}} N^{-1/3}. \quad (1.32)$$

For our parameters, this is a small correction from Eq. (1.29). We show the finite size correction to the critical temperature for typical experimental parameters in fig.1.3.

1.1.3 Role of interactions

Inter-atomic interaction potential

The gases we study are very dilute. For example, if we consider a Bose gas in a harmonic trap at a typical temperature in our experiment $T \sim 1 \mu\text{K}$, the density will be $n \sim 10^{13} \text{ at/cm}^{-3}$. In this density regime, only binary collisions play a significant role. Three-body collisions take place at a much lower rate. When three atoms are close to each other, two of them may form a molecule in a highly energetic vibrational state. The third atom takes away the energy released by the dimer formation. Since the energy released by the process is usually very high compared to typical trapping energy scales, the third atom is lost with the excited molecule, and three body collisions are treated as a loss process [101].

We now study the scattering between two atoms. We consider the center of mass frame, and consider the asymptotic behavior of the relative motion between the two particles well before and well after the scattering event [102, 103]. We first consider the decomposition of the incident wavepacket into the plane wave basis, and study the behavior of each term of its decomposition. The effect of the collision is given by a scattering amplitude $f(\theta, k)$, where k is the incident wavevector and θ is the relative angle between the incident and diffused wavefunction. With this definition, we write a stationary scattering state: $\psi_k = \exp(ikz) + f(k, \theta) \exp(ikr)/r$. The next step consists in developing this state on the basis of spherical harmonics: $\psi_k = \sum_{l=0}^{\infty} \sum_{m=-l}^l Y_{lm}(\theta, \Phi) u_{kl}(r)/r$ where u_{kl} are the partial wave amplitudes. These obey to a radial equation that includes a centrifugal barrier term $\hbar l(l+1)/(2\mu r^2)$, where μ is the reduced mass. In the case of ultracold gases, atoms have very low relative speed. In particular, partial waves with $l > 0$ never reach the interaction region due to the centrifugal barrier, only the $l = 0$ - s-wave - channel contributes.

The complexity of the short range inter atomic potentials makes the calculation of such scattering amplitude difficult. Instead, we take the low energy limit of the partial wave amplitude solution such that f does not depend on the incident energy. In this limit, the binary interactions can be described by a single parameter: the scattering length a such that $f(k, \theta) = -a$. A positive scattering length indicates repulsive interactions. The scattering properties generally depends on the internal state of the atom. For example, we consider sodium in the $F=1$, $m_F = +1$ hyperfine state, which scattering length is [104]:

$$a = 54.54 a_B = 2.89 \text{ nm}, \quad (1.33)$$

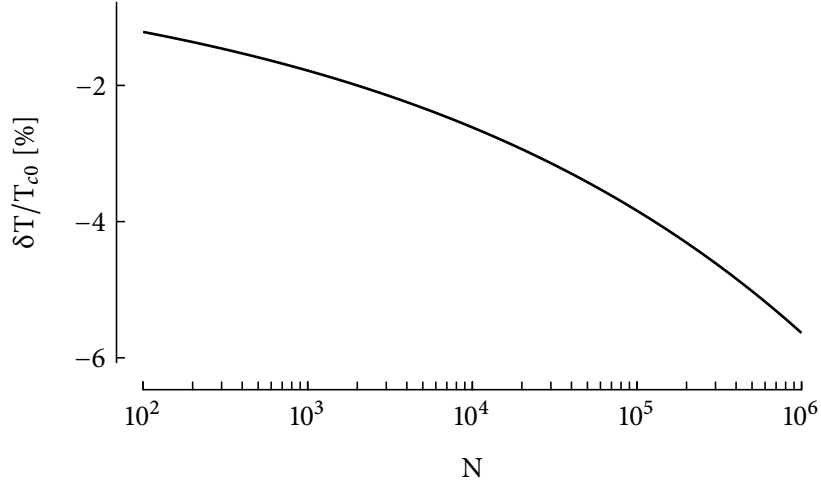


FIGURE 1.4: Interaction shift of the critical temperature for Bose-Einstein condensation of a sodium Bose gas in the $F = 1$, $m_F = +1$ component in a harmonic trap of angular frequency $\omega = 2\pi \cdot 1$ kHz.

where $a_B = 53$ pm is the Bohr radius. The short range potential is generally unknown (or too complicated) and the value of the scattering length is very sensitive on its details. We define a pseudo potential whose properties are simple, but which allows us to retrieve the same scattering length as the actual atomic potential. We choose a contact potential:

$$V(\mathbf{r}, \mathbf{r}') = g\delta(\mathbf{r}, \mathbf{r}'), \quad (1.34)$$

where the interaction coupling constant is chosen to reproduce the correct scattering length:

$$g = \frac{4\pi\hbar^2 a}{m}. \quad (1.35)$$

Scalar gas critical temperature shift due to interactions

In a harmonically trapped Bose gas repulsive interactions tend to “spread” the gas, hence lowering its density at the center. The many body Hamiltonian of the interacting Bose gas in second quantization is [93]:

$$\hat{H} = \int d\mathbf{r} \hat{\Psi}^\dagger(\mathbf{r}) \left(-\frac{\hbar\nabla^2}{2m} + V(\mathbf{r}) \right) \hat{\Psi}(\mathbf{r}) + \frac{g}{2} \int d\mathbf{r} \hat{\Psi}^\dagger(\mathbf{r}) \hat{\Psi}^\dagger(\mathbf{r}) \hat{\Psi}(\mathbf{r}) \hat{\Psi}(\mathbf{r}) \quad (1.36)$$

We adopt an Hartree-Fock (HF) approach (see refs. [93, 105, 106]) in which the gas generates a repulsive potential $2gn(\mathbf{r})$, where n is the atomic density, that is determined self-consistently. The potential then experienced by the gas is:

$$V_{\text{eff}}(\mathbf{r}) = V_{\text{ext}}(\mathbf{r}) + 2gn(\mathbf{r}). \quad (1.37)$$

This in turn modifies the chemical potential of the gas $\mu = \mu^{(0)} + \delta\mu$. Because the condition to fulfill condensation remains $n(\mathbf{0})\lambda_{\text{dB}}^3 = g_{3/2}(1)$, The shift in chemical potential $\delta\mu$ is determined by the interaction energy at the center:

$$\delta\mu = 2gn(\mathbf{0}) \quad (1.38)$$

We apply a perturbative treatment to the ideal gas formula (see refs. [93, 100, 107, 108]) and take $N_c \rightarrow N_{c0} + \delta N_c$. We compute the change in critical atom number δN_c within the local density approximation, and we obtain:

$$\delta N_c = \frac{1}{(2\pi\hbar)^3} \left(\iint \frac{d^3\mathbf{p}d^3\mathbf{r}}{\exp(\beta(p^2/2m + V_{\text{eff}}(\mathbf{r}) - \delta\mu)) - 1} - \iint \frac{d^3\mathbf{p}d^3\mathbf{r}}{\exp(\beta(p^2/2m + V(\mathbf{r}))) - 1} \right), \quad (1.39)$$

The expression (1.39) has been computed by Giorgini *et al.* in ref. [107]:

$$\frac{\delta N_c}{N_{c0}} \simeq 4 \frac{a}{a_{\text{ho}}} N^{1/6}. \quad (1.40)$$

In term of temperature shift, this gives:

$$\frac{\delta T_{\text{int}}}{T_{c,\text{ideal}}} = -1.33 \frac{a}{a_{\text{ho}}} N^{1/6}. \quad (1.41)$$

We plot the interaction shift for typical experimental parameters in fig. 1.4.

1.1.4 Role of realistic trapping potentials

Optical traps used in our experiment are only approximately harmonic near the potential minimum. Deviations from harmonicity can affect the thermodynamics of the system. In this section, we investigate the effect of finite trap depth and anharmonicities on the Bose-Einstein critical temperature.

Optical traps

In the experiment, far detuned optical traps are used to confine ultra cold atoms. Optical dipole traps (ODT) are created with laser beams, and generate an atomic potential $V(\mathbf{r}) \propto -\alpha I(\mathbf{r})$ where α the atomic polarizability described in annex B and ref. [37]. If the laser frequency is lower than the atomic transition frequency – the laser is then red detuned – the polarizability is positive, and atoms are attracted towards high intensity regions. Instead, if the laser frequency is higher than the transition frequency – the laser is then blue detuned – the polarizability is negative and atoms are attracted towards low intensity regions. For alkali atoms, the polarizability is independent on the internal state if the detuning is large enough.

Gaussian trapping potentials

Laser beams are described by Gaussian optics [109], where intensity is a Gaussian function of the distance to the optical axis. In the case the laser is red detuned, there is a potential minimum at the intensity maximum that is located in the focal plane, on the optical axis. We will see in the following that such a trap is not harmonic away from the center, and also, that unlike a harmonic trap, it has a finite depth, related to the peak intensity of the laser beam.

The simplest kind of ODT consists in a single beam from a red detuned laser. The simplest ideal laser beams are in the TEM₀₀ mode whose intensity distribution is (in the case of a laser beam

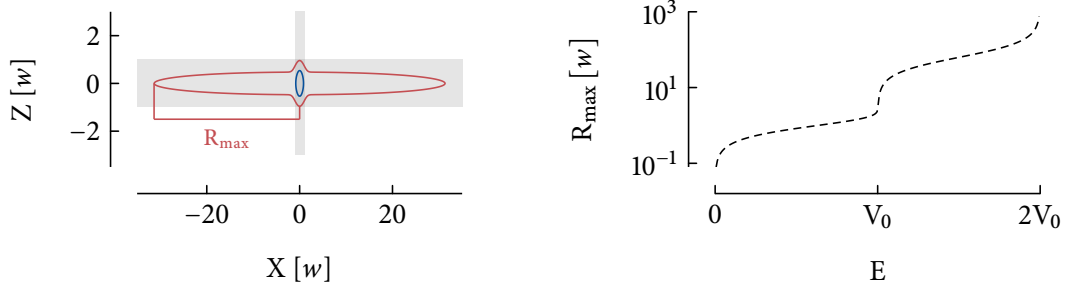


FIGURE 1.5: Maximum radii of classical trajectories in a crossed optical dipole trap, neglecting gravity, expressed in units of beam waists w . On the left we show examples of classical trajectories (blue for an atom of energy $E < V_0$ and red for an atom of energy $V_0 < E < 2V_0$) and the definition of the maximum radius. The shaded area corresponds to one waist on each arm. On the right we show the maximum radius versus the energy of the trajectory. The escape from the crossing region is seen as a sudden increase of the maximum radius at $E = V_0$.

propagating along z):

$$I(r, z) = I_0 \frac{w_0^2}{w^2(z)} \exp\left(\frac{-2r^2}{w^2(z)}\right), \quad (1.42)$$

We defined the beam width $w(z) = w_0(1 + (z/z_R)^2)^{1/2}$, with the *waist* of the laser beam w_0 and the Rayleigh length $z_R = \pi w_0^2/\lambda_L$. The potential created from such a beam can be written, referencing the energy zero at the trap bottom:

$$V_{\text{ODT}}^{(z)}(x, y, z) = V_0 - \frac{V_0}{1 + (z/z_R)^2} \exp\left(-\frac{2(x^2 + y^2)}{w^2(1 + (z/z_R)^2)}\right). \quad (1.43)$$

where V_0 is the single beam potential depth $V_0 = \alpha I_0$. Near the origin, the trap is well approximated by a harmonic trap with trapping frequencies:

$$\omega_{x,y} = \sqrt{\frac{4V_0}{mw^2}}, \quad \omega_z = \sqrt{\frac{2V_0}{mz_R^2}}. \quad (1.44)$$

Given the wavelength $\lambda \sim 1 \mu\text{m}$ and the waist (typically $w_0 \sim 10 \mu\text{m}$) of the laser beam, the aspect ratio of such a trap is rather large (“cigar-shaped” trap). In order to obtain more spherical traps, we cross two beams of comparable waists propagating along z and along x respectively. Such a trap will be referred to as a crossed dipole trap (CDT) and is:

$$V_{\text{CDT}}(\mathbf{r}) = V_{\text{ODT}}^{(z)}(\mathbf{r}) + V_{\text{ODT}}^{(x)}(\mathbf{r}). \quad (1.45)$$

The CDT is harmonic near $\mathbf{r} = \mathbf{0}$ and its trap frequencies can be obtained by $w_i^{(\text{CDT})} = \sqrt{\omega_i^{(x)2} + \omega_i^{(z)2}}$ where i denote the axis x , y or z , and $\omega_i^{(x,z)}$ the trap frequencies of the single beams from Eq. (1.44). The behavior of a classical particle in the potential (1.45) can be understood by considering the iso-energy contours plotted in figure 1.6. These contours correspond to the position of the turning points of classical trajectories of energy E . We observe three regimes depending on the mechanical

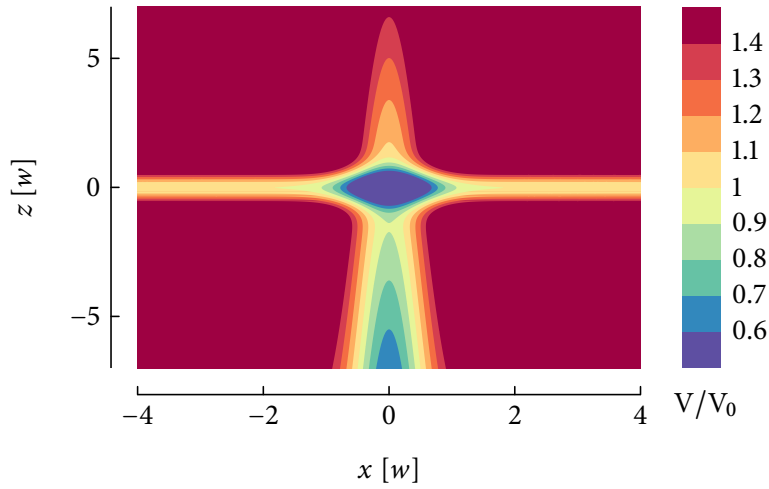


FIGURE 1.6: Contour plot of the potential $V_{\text{CDT}} - mgz$ felt by atoms in the CDT, including gravity. We notice a minimum along x corresponding to the crossing region, and a saddle point along the z direction at $(x, z) \sim (0, -1)$ at energy $V \sim V_0$ that indicates that atoms are not confined in the vertical arm due to gravity.

energy E . A first regime, where $E < V_0$, corresponds to atoms trapped in the crossing region. A second regime, where $V_0 < E < 2V_0$ consists in atoms exploring the arms of the crossed dipole trap, and a third regime where atoms are not trapped for $E > 2V_0$. The two first regimes can be distinguished by the maximum radius of their classical trajectories in figure 1.5. We observe a sharp rise of R_{max} , defined as the largest radius of the iso-energy contour when $E = V_0$. This increase reveals the transition from the first to the second regime.

So far, we have solely considered the trapping potential due to the optical dipole trap. However, trapped atoms are also affected by gravity. This is shown on fig. 1.6 as a saddle point on the z direction near $V = V_0$, indicating that with chosen parameters, the isolated vertical arm cannot hold atoms against gravity, and that the trap depth, defined as the highest energy at which classical trajectories are bound, is reduced to $\sim V_0 - mgw$. We shall discuss this definition of the trap depth later on. Another effect of gravity on the potential, hardly visible with the scale of the figure 1.6, is a displacement – “sag” – of the potential minimum:

$$z_{\text{sag}} \approx -\frac{g}{\omega_z^2}. \quad (1.46)$$

For $\omega_x \sim 2\pi \cdot 1 \text{ kHz}$, the sag is $\sim 250 \text{ nm}$. In the case of a Gaussian optical dipole trap, this result holds as long as the sag remains much smaller than the waist of the laser. In principle, the horizontal arm is not affected by gravity. However, a small tilt of the laser propagation axis would result in an effective reduction of the potential height on this direction, eventually to the point where atoms cannot be held in the horizontal arm. We estimate the tilt should be small compared to $z_R \omega_x^{(x)2}/g \sim 0.07 \sim 4^\circ$ for $\omega_z \sim 2\pi \cdot 5 \text{ Hz}$, $w = 15 \mu\text{m}$.

density of states in the crossed dipole trap

In order to study the thermodynamic of Bose gases in such potentials, we turn to the computation of the density of states as discussed in Sec. 1.1.1. We evaluate it in the potential V_{CDT} using the

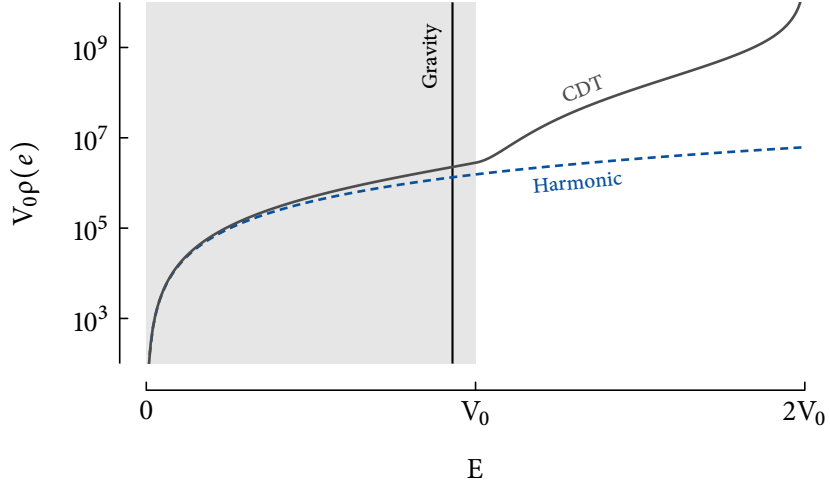


FIGURE 1.7: Comparison of the density of states of the CDT and in a harmonic trap. The shaded area represent the energy range where atoms stay within the crossing region.

semiclassical approximation [14, 93]:

$$\rho(E) = \frac{1}{(2\pi\hbar)^3} \int d^3\mathbf{r} d^3\mathbf{p} \delta(E - H), \quad (1.47)$$

where $H = p^2/2m + V_{\text{CDT}}(\mathbf{r})$ is the Hamiltonian. Integrating over momentum, this becomes:

$$\rho(E) = \left(\frac{2mw_0^2}{\hbar^2}\right)^{3/2} \sqrt{V_0} \int_{V_{\text{CDT}}(\mathbf{r}) \leq E} \sqrt{\frac{E - V_{\text{CDT}}(\mathbf{r})}{V_0}} \frac{d^3\mathbf{r}}{4\pi^2 w_0^3}, \quad (1.48)$$

We compare in figure 1.7 the density of states in the CDT with the one of the harmonic trap with the same curvature, see Eq. (1.14). When the energy is small, the density of states of the CDT is close to the one given by the harmonic approximation. However, at higher energy the density of states of the Gaussian trap is always larger than the one of the harmonic trap. This is due to the fact that the Gaussian trap is “looser” than the harmonic trap away from the center. Furthermore, we observe a rapid rise of the density of states at energy $E = V_0$. This is due to the much larger extent of the classical trajectories at this energy, with atoms exploring the arms. As a conclusion, we see that the effect of anharmonicity of the CDT potential is in general to increase the density of states compared to the case of a harmonic trap. This will lead to an increase in critical atom number (and associated decrease in critical temperature) that we will discuss in the next paragraph.

Critical atom number in the crossed dipole trap

We compute the total number of excited states in the trap with the help of the Bose-Einstein distribution function from Eq. (1.16):

$$N' = \int_0^\infty dE \rho(E) g_{\text{BE}}(E). \quad (1.49)$$

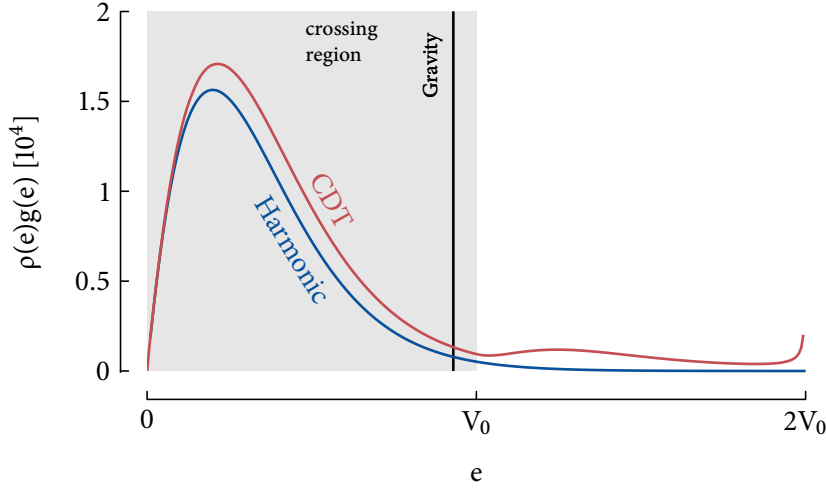


FIGURE 1.8: Density as a function of energy for $\eta = 8$. We see that the cross dipole trap bears a relatively larger populations at high energy compared to the harmonic trap due to its increased density of state at $E > V_0$.

It is convenient to express (1.49) using dimensionless quantities, remarking that the density of states in Eq. (1.48) only depends on E/V_0 :

$$e = \frac{E}{V_0}, \quad \eta = \frac{V_0}{k_B T}, \quad (1.50)$$

$$\rho(e) = V_0 \rho(E), \quad (1.51)$$

such that we can write very simply the excited states population as a function of the evaporation parameter η :

$$N' = \int_0^\infty de \rho(e) g_{BE}(e) = \int_0^\infty \frac{de \rho(e)}{\exp(\eta e) - 1}. \quad (1.52)$$

As we did in the case of a harmonic trap in section 1, we compute the excited population for a given value of η (or T equivalently), which gives a critical atom number for Bose-Einstein condensation. The critical temperature is obtained by finding the temperature at which the gas is saturated, corresponding to $N' = N$.

The situation we discuss is related to the one described by Simon in [110] *et al.* for a single beam ODT. They described the critical atom number for a single beam ODT (1.43). In such a trap, the ‘‘Lorentzian’’ dependence of the trapping potential along the propagation direction leads to a logarithmic divergence of the critical atom number, that prevents the occurrence of BEC. This divergence will probably not survive realistic experimental effects such as optical aberrations, that make the beam diverge more strongly on axis than an ideal Gaussian beam limited only by diffraction.

The situation will be different in a crossed dipole trap, where atoms mostly stay in the crossing region, in which the potential has a Gaussian dependence in all axis. In fig. 1.8, we show the atomic density as a function of energy. It shows the influence of this increased density of states on the energetic atom density. We notice that a small but visible portion of the atoms explore the arms of

the CDT ($E > V_0$), and that there is a divergence of the atomic density near $E = 2V_0$ of the same origin as the one discussed for the single beam ODT. Experimental realities such as gravity, or a tilt of the horizontal arm would however prevent the divergence by introducing an effective energy cutoff for the thermal distribution.

In the following, we will analyze the relevance of the above picture for the evaporation dynamics, and determine the proper energy cutoff for the calculation of thermodynamic quantities such as the critical atom number.

Principle of evaporative cooling

The extreme temperatures required for Bose-Einstein condensation are reached through evaporative cooling, see ref. [111]. This method relies on the elimination of atoms whose energy is above the trap depth V_{td} and thermalization occurs through binary collisions. Thermalization refers to the establishment of thermal equilibrium starting from a perturbed energy distribution. This process requires only a few scattering events per particle to retrieve an equilibrium distribution (see refs [111, 112]). As such, we can define a thermalization rate $\Gamma_{th} \simeq n\sigma\bar{v}$ where n is the average density, $\sigma = 8\pi a^2$ is the collision cross-section and $\bar{v} = (8k_B T/\pi m)^{1/2}$ the average thermal velocity. The evaporation process requires that atoms with an energy above $E > V_{td}$ escape from the trap. In the case the evaporation parameter $\eta = V_{td}/k_B T$ is large $\eta \gg 1$, ref. [111] provides an expression for the evaporation rate $\Gamma_{ev} \simeq n\sigma\bar{v}\eta e^{-\eta}$. We remark that in this description, thermalization is necessarily fast in regard with the evaporation process. This is actually a requirement for evaporation, along with ergodicity, which we will discuss further in a moment.

The reduction of temperature is obtained by a progressive diminution of the trap depth, at a rate – the cooling rate $|\dot{V}_0/V_0|$ – that should be comparable to Γ_{ev} or slower. We note that in experiments, the cooling rate needs to be faster than the rates of collision with the background gas or of three-body recombination¹. A typical lifetime of Bose-Einstein condensates is ~ 40 s in this experiment. Besides, we estimate for example that for a sodium gas at $T = 5 \mu\text{K}$, that $\Gamma_{th} \simeq 1000 \text{ s}^{-1}$ and $\Gamma_{ev} \simeq 7 \text{ s}^{-1}$. We note that the evaporation rate is slightly faster than the typical cooling rate that we use in the experiment $\sim 1 \text{ s}^{-1}$.

At this point, it may be useful to discuss the ergodicity of the dynamics of atoms in phase space in our experimental situation. If we consider a single atom in a three dimensional harmonic trap, a trajectory along a particular trap eigenaxis will never explore the two other degree of freedom due to the separability of harmonic potentials. As such, single particle trajectories in such traps are not ergodic since they explore only a small part of the phase space available for a given energy. Realistic traps however display asymmetries and anharmonicities that restore an ergodic behavior. The degree of ergodicity of trajectories in a trap is measured by the ergodic mixing time, which corresponds to the time scales required for an excitation along a single axis to propagate along other directions in space. This has been measured to be very long in magnetic traps (0.5 s in [113] and 50 s in [114] for example²). We however expect optical trapping potential to deviate more strongly from the harmonic model due their inherent anharmonicity and because

¹Ultracold Bose gases are inherently in a metastable state as their true chemical equilibrium state is solid. The formation of a solid phase (or smaller size clusters) is inhibited by the very low density. Hence, the formation of molecules by 3-body collisions can provide an upper bound for the experimental time scales.

²We remark that even if magnetic traps can be extremely harmonic, this is a design feature rather than an intrinsic property. Ioffe-Pritchard traps can be made extremely harmonic for example. The reference [115] shows a study in a non separable magnetic trap.

of possible optical aberrations. For these reasons, the ergodic mixing time could be shorter than in the magnetic traps of refs. [113, 114].

We illustrate the effect of ergodic mixing on evaporation by considering the case of 1D evaporation due to gravity. We shall consider two situations. In a first case, the atom is alone in the trap, and we consider its energy is $V_0 - mgw < E < V_0$, such that it remains bound on horizontal trajectories but escapes on vertical ones. If the atom starts in an horizontal trajectory, the typical time before it escape will be similar to the ergodic mixing time. In a second case, there are many atoms in the trap and the typical time between collisions is short compared to the ergodic mixing time. If we consider the result of an hypothetical collision between two atoms, such that one of them end up with an energy $V_0 - mgw < E < V_0$. Then, we can discuss whether this atom will end up in a bound or an unbound trajectory from the amount of phase space available in each case. Given unbound trajectories are limited to purely vertical ones, they will be described by a phase space with a lower dimension than the one of bound trajectories that can explore both other directions. Hence, it is much more likely that the atom ends up in a bound trajectory in this case. Given the ergodic mixing time is much longer than the intercollision time, this atom will undergo another collision before it can escape from the trap, will redistribute its energy and will not be lost. This argument is often summarized by stating that one dimensional evaporation processes are inefficient (see ref. [111]), and that the dimensionality of the selection process should be as high as possible.

The first situation that we have considered here would correspond to an almost non interacting gas, where the mean free path is much larger than the typical size of trajectories. The typical situation in the crossing region of the CDT is however the opposite as the mean free path $l = \bar{v}/\Gamma_{\text{th}} \sim \mu\text{m}$ is smaller than the dimension of the classical trajectories. As we will discuss in the next paragraph, the situation is not the same for the fraction that explore the arms of the CDT.

Evaporation in a crossed dipole trap

In this paragraph, we turn to the situation in a crossed dipole trap typically described by fig.1.8. The atomic cloud trapped in the CDT is composed of a dense, interacting component confined in the crossing region, and of a less populated, much more dilute component that resides mostly in the horizontal arm (atoms exploring the vertical arm are expelled by gravity, see Sec. 1.1.4). We will first recall the mechanisms and time scales for evaporation, then discuss the role of gravity, and finally discuss the coupling between the component in the crossing region and the one that explore the arms. In a crossed dipole trap, if $k_B T \ll V_0$, most of the atoms remain in the crossing region as seen in figure 1.8. As such, the density in the arm region, which is both much larger and less populated, is lower than in the center of the CDT by several orders of magnitude $n_{\text{arm}} \ll n_{\text{cross}}$. In this case the mean free path becomes comparable to the trap dimension, and it is reasonable to assume that the only relevant collision process for the gas exploring the arm happens when they pass through the crossing region. In this case, the intercollision time depends mainly on their trajectories and we can estimate the number of collision per passage through the crossing region from their speed $v_{\text{arm}} \sim (2E/m)^{1/2}$, the size of the center $R_{\text{th}} \sim (2k_B T/m\bar{\omega}^2)^{1/2}$, and the time to go through the crossing region $\tau_{\text{ac}} \sim R_{\text{th}}/v_{\text{arm}}$:

$$N_{\text{coll}} \sim n_0 \sigma v_{\text{arm}} \tau_{\text{ac}} \sim n_0 \sigma R_{\text{th}} \sim 0.1 \text{ to } 1 \quad (1.53)$$

The timescales for trajectories in the arms ($\sim 100 \text{ ms}$) being much longer than the time between collisions in the crossing region ($\sim 1 \text{ ms}$), the component in the arms are effectively decoupled

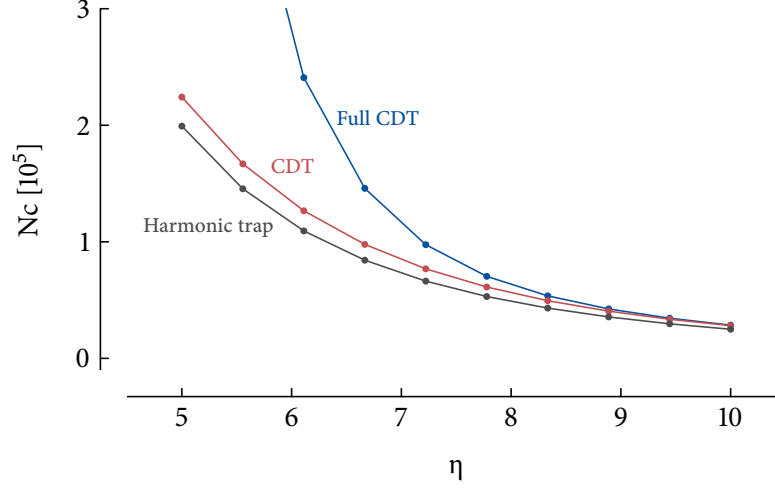


FIGURE 1.9: Critical atom number for several condensation scenarii for a CDT with two crossed Gaussian traps with waists $w = 20 \mu\text{m}$. We consider either atom from the whole trap (Full CDT), atoms in the crossing region (CDT), or the prediction from the harmonic approximation near the trap minimum (Harmonic). We observe that taking into account atoms in the arms, the critical atom number rises quickly with η . However, considering only atoms from the crossing region, the rise is limited by the energy cutoff imposed by the hypothesis on the evaporation dynamics. We note that with an efficient evaporation procedure, the lowest values of η cannot be observed.

from the one in the crossing region. They will be lost eventually as the HDT power is decreased. In the following, we will only consider the thermodynamic of the component located in the trapping region.

Summarizing on energy selection, there are two processes to consider which are atoms escaping to the arms and atoms escaping through the saddle point created by gravity (see fig. 1.6). Even though gravity impose a slightly lower energy threshold compared to atom escaping to the arms, the much lower evaporation efficiency of 1D evaporation processes make us choose the energy threshold for atoms escaping through the arms as the trap depth $V_{\text{td}} = V_0$.

Conclusions about the critical atom number in crossed dipole traps

Now that we have discussed how to define properly the trap depth, we shall explore three particular realistic situations for the sake of completeness. We take a realistic crossed dipole trap composed of two beams of waist $w = 20 \mu\text{m}$ and of trap depth $V_0 = 20 \mu\text{K}$. We consider three evaporation situations:

1. We define the modified critical atom number by integrating over the crossing region only:

$$N_c = \int_0^1 \frac{d\rho(e)}{\exp(\eta e) - 1}. \quad (1.54)$$

2. We define the modified critical atom number by integrating over the whole trap:

$$N_{c,\text{full}} = \int_0^2 \frac{d\rho(e)}{\exp(\eta e) - 1}. \quad (1.55)$$

3. We only consider the harmonic description near the center of the trap and compute the critical atom number “naively” from this potential

$$N_{c,ho} = \int_0^\infty \frac{d\rho_{ho}(e)}{\exp(\eta e) - 1}. \quad (1.56)$$

We plot the critical atom numbers determined for these three situations on in figure 1.9 as a function of the evaporation parameter η . We note that in absence of gravity, this is the only relevant parameter, and the actual trap depth V_0 (or equivalently temperature) does not matter. The critical atom number in the first situation is not very different from the harmonic prediction in the third situation. This demonstrates that the increased density of states due to the anharmonicity of the trapping potential (see fig. 1.8) is mostly compensated by the cut-off of the energy distribution imposed by the trap depth of the crossing region. Nevertheless, there is a small but experimentally measurable shift of a few percents (up to 10% depending on assumptions on the trap sizes and *eta*) as we will discuss in more details in chapter 4.

The shift in critical temperature due to this effect will be limited to a few percents in the first scenario, while it can be rather large in the second scenario. However, gravity should be taken into account within this second scenario, such the predictions will depend on the precise shape of the trap (along the vertical direction) and on the trap depth (gravity will have a larger effect for low trap depths at the end of evaporation). We shall discuss more in detail this shift in the context of the measurement of the critical temperature of spinor Bose gases in chapter 4. We note that we did not simulate our evaporation process such that a quantitative prediction of the shift to the critical temperature is not within reach. Besides, the significance of these estimations is also limited by our knowledge of the exact trapping potential (we suspect the traps are not perfect Gaussian beams due to aberrations for instance).

1.2 Single component Bose-Einstein condensates at T=0

In the first section, we discussed the excited states populations and the associated thermodynamic quantities. We now consider what happens below the critical temperature. As discussed in section 1.1, the lowest energy state needs to be considered independently from the rest of the gas (the normal component). In particular, the large densities achieved by the condensate result in a large effect of interactions, modifying substantially the equilibrium state of the system. For the sake of simplicity, we will focus in this section on the single component case.

1.2.1 Ground state of Bose-Einstein condensates

The condensate wavefunction of an ideal Bose-Einstein condensate is the ground state of the harmonic oscillator:

$$\Psi = \sqrt{N} \prod_{x,y,z} \left(\frac{1}{\pi a_{i,ho}^2} \right)^{1/4} \exp\left(-\frac{x_i^2}{2a_{i,ho}^2} \right), \quad (1.57)$$

where $a_{i,ho}$ are the harmonic oscillator length given by Eq.(1.11). However, most experiments are incompatible with the prediction (1.57), because the BEC wavefunction is strongly affected by interactions. Taking into account interactions, the ground state of the system is then described by

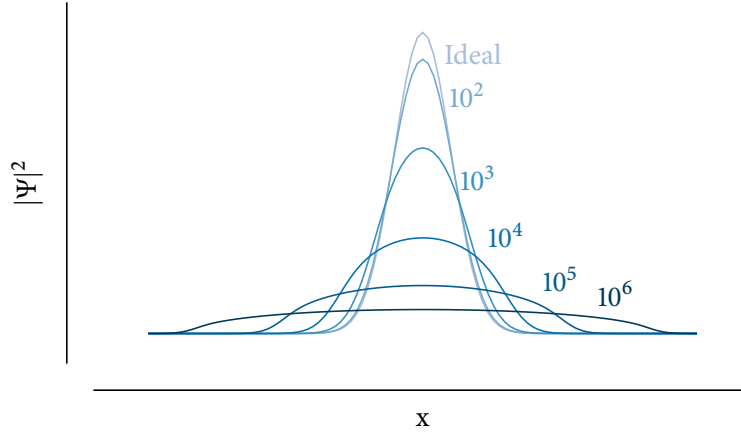


FIGURE 1.10: 3D simulated density profiles of condensates, normalized by their area, of varying atom number in an isotropic harmonic trap of trap frequency $\omega = 2\pi \cdot 500 \text{ s}^{-1}$. The density profile evolve from a Gaussian profile (labeled ideal) for small condensates to an inverted parabola (for profile with one million atoms for example).

the Gross-Pitaevskii equation (GPE, see ref [93]):

$$\left(-\frac{\hbar^2 \nabla^2}{2m} + V(\mathbf{r}) + g |\Psi(\mathbf{r})|^2 \right) \Psi(\mathbf{r}) = \mu \Psi(\mathbf{r}), \quad (1.58)$$

where μ is the chemical potential. We recover the harmonic oscillator as the ground state of the Hamiltonian when the interaction strength g goes to zero. The opposite limit in which interactions are so strong that they make the kinetic energy term negligible is called the Thomas-Fermi limit. For a harmonic potential V , the cloud takes the form of an inverted parabola as shown in figure 1.10:

$$|\Psi(\mathbf{r})|^2 = \max\left(\frac{\mu_{\text{TF}} - V(\mathbf{r})}{g}, 0 \right). \quad (1.59)$$

The chemical potential μ_{TF} is given by the normalization of the wavefunction:

$$\mu_{\text{TF}} = \frac{\hbar \bar{\omega}}{2} \left(15N \frac{a}{a_{\text{ho}}} \right)^{2/5}, \quad (1.60)$$

where $\bar{\omega} = (\omega_x \omega_y \omega_z)^{1/3}$ is the geometric average of the trap angular frequencies. The condensate wavefunction is characterized by the Thomas-Fermi radii, defined as the distances to the center at which the wavefunction vanishes:

$$R_{\text{TF},i} = \sqrt{\frac{2\mu_{\text{TF}}}{m\omega_i^2}}. \quad (1.61)$$

We discuss the validity of the Thomas-Fermi approximation by defining an interaction parameter:

$$\chi = \frac{Na}{a_{\text{ho}}}. \quad (1.62)$$

On the one hand, if $\chi \gg 1$, interactions dominate, and the condensate wavefunction is well described by equation (1.59). On the other hand, if $\chi \ll 1$, then the condensate wavefunction is well

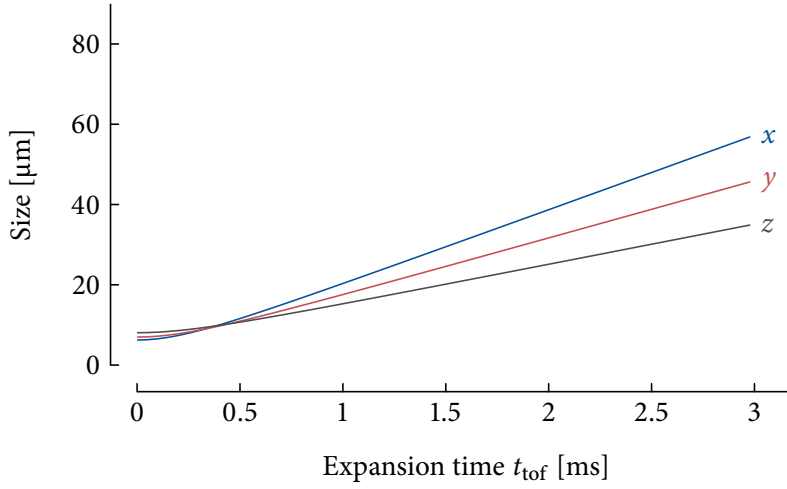


FIGURE 1.11: Thomas-Fermi sizes of a free expanding BEC from a trap of angular frequencies $\omega_{x,y,z} = 2\pi \cdot 300, 400, 500, \text{ s}^{-1}$. We observe that the aspect ratios get inverted after $\sim 1/\bar{\omega} \sim 0.5\text{ms}$.

described by equation (1.57). For $N = 5000$, $\bar{\omega} \sim 2\pi \times 500 \text{ Hz}$, the interaction parameter is $\chi \sim 26$. In this case, the condensate density profile is well described by a Thomas-Fermi profile. However, when the condensed fraction is lower, or when the condensate is made deliberately smaller, the density profile needs to be obtained numerically [116] from the GP equation (1.58) as $\chi \sim 1$.

Finally, it is useful to give the length scale associated with interactions. While this is rather uneasy in harmonically trapped gases, given the interaction strength depends on density, we can instead consider the case of an uniform gas, in which we can define a healing length ξ (see ref. [93]):

$$\xi = \sqrt{\frac{\hbar^2}{2mgn}} \quad (1.63)$$

This length represents the typical length scale on which interactions limit the scale of density changes. Faster spatial variations cost too much kinetic energy and are “smoothed” in the equilibrium state.

1.2.2 Free expansion of Bose-Einstein condensates

Due to their high optical density and small size, Bose-Einstein condensates can be challenging to detect *in situ* with standard imaging techniques. This is often avoided by releasing the cloud from the trap and letting it expand in free space for a time t_{tof} before an image is taken. This step is called *time of flight*. The expansion dynamics of a BEC differs significantly from the one of a thermal Bose gas. For the latter, it is driven (mostly) by the initial kinetic energy of the atoms, and as such is isotropic. In the case of a Bose-Einstein condensate, it is mostly driven by interactions and is in general anisotropic. This is what leads to an inversion of the aspect ratio of clouds released from a harmonic trap during time of flight. This effect has been used as a signature of Bose-Einstein condensation since its first experimental realizations [13, 117]. In this section, we will discuss the approach from Castin and Dum in ref. [118] describing the expansion of a T=0 BEC in the Thomas Fermi regime.

In this regime, they showed that the expansion is self-similar and characterized by scaling factors $\lambda_{x,y,z}$ such that $\lambda_i(t=0) = 1$ and $R_{x,y,z}(t) = \lambda_{x,y,z}(t)R_{x,y,z}(0)$ are scaled Thomas-Fermi radii. The scaling factors obey a set of classical equations including the time-dependent potential energy and interaction energy:

$$\ddot{\lambda}_i = \frac{\omega_i^2(0)}{\lambda_i \lambda_1 \lambda_2 \lambda_3} - \omega_i^2(t) \lambda_i, \quad i = x, y, z. \quad (1.64)$$

A time of flight experiment consists in setting all trap frequencies to 0 simultaneously at $t = 0$. The most confining axis (with largest trap frequencies) expands the fastest as seen in figure 1.11.

In order to address the intermediate case where $\chi \sim 1$, one must use a time dependent Gross-Pitaevskii equation:

$$i\hbar \frac{\partial \Psi(\mathbf{r}, t)}{\partial t} = \left(-\frac{\hbar^2 \nabla^2}{2m} + V_{\text{ext}}(\mathbf{r}, t) + g |\Psi(\mathbf{r}, t)|^2 \right) \Psi(\mathbf{r}, t). \quad (1.65)$$

The equation is solved numerically by finite difference methods, with the initial condition $\Psi(\mathbf{r}, 0)$ previously calculated with imaginary time propagation of the GPE (see ref [116]). A particular issue associated with equation (1.65) lies in the very different length scales at the beginning and at end of the expansion. We deal with this issue by choosing an adaptative grid with a discretization size varying with the Thomas-Fermi scaling factors. This procedure is described in ref. [119].

1.3 Spin-1 Bose-Einstein condensate at T=0

The first atomic Bose-Einstein condensates were created in magnetic traps and in a single internal state (see refs [11–13]). A few years later, optical trapping techniques allowed to confine atoms in several internal states, *e.g.* in several hyperfine or Zeeman states. This resulted in the realization of a BEC in such a trap [36] and opened the way for the study of new systems called *spinor* Bose-Einstein condensates [83, 120]. Magnetism in these systems arise from the interaction between the different internal components. In this section, we will introduce the main effects governing their physics such as atom-atom scattering and interaction with the magnetic field.

1.3.1 Spinor scattering properties

We consider ultra-cold collisions of two sodium atoms in the lowest hyperfine manifold $3S_{1/2}$, $F = 1$ [65, 120] as in section 1.1.3, considering additionally the spin of the atoms. The microscopic interaction Hamiltonian – given by Van der Waals interactions – is rotationally invariant in spin space, which ensures that the total spin of the system remains unchanged during the collision. In the cold collision limit, like for the scalar case only the *s*-wave channel contributes, such that the spatial part of the stationary scattering state is symmetric under exchange. Furthermore, the total wavefunction must also be symmetric under exchange given that we consider a pair of bosons. As such, the spin part of the asymptotic scattering state must be even and the total spin of the pair must be 0 or 2. We decompose the interaction pseudo-potential into two collision channels:

$$\hat{V}(\mathbf{r}, \mathbf{r}') = \delta(\mathbf{r}, \mathbf{r}') \otimes \left(g_0 \mathcal{P}_{F_p=0} + g_2 \mathcal{P}_{F_p=2} \right), \quad (1.66)$$

where $\mathcal{P}_{F_p=f}$ is the projector into the subspace $F_p = f$. This expression can be written in a more convenient way, as a function of the spins of each particles \hat{F}_1 and \hat{F}_2 . For this we use the following

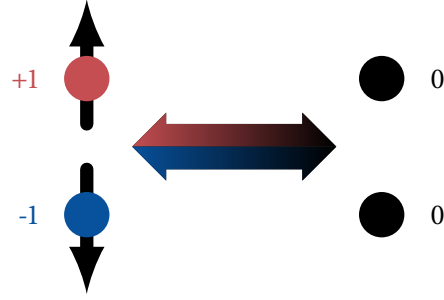


FIGURE 1.12: Illustration of the effect of spin changing collisions on the Zeeman populations. The populations to the left and the right of the arrow represent the state of each atom before and after collision.

relations:

$$\mathcal{I}d = \mathcal{P}_2 + \mathcal{P}_0, \quad (1.67)$$

$$\hat{\mathbf{F}}_1 \cdot \hat{\mathbf{F}}_2 = \mathcal{P}_2 - 2\mathcal{P}_0. \quad (1.68)$$

This yields the more convenient expression of the interaction potential:

$$\hat{V}(\mathbf{r}, \mathbf{r}') = \delta(\mathbf{r}, \mathbf{r}') \otimes (\bar{g}\hat{I}d + g_s\hat{\mathbf{F}}_1 \cdot \hat{\mathbf{F}}_2). \quad (1.69)$$

where the expression of the spin independent and the spin dependent coupling constants are:

$$\bar{g} = \frac{2g_2 + g_0}{3}, \quad (1.70)$$

$$g_s = \frac{g_2 - g_0}{3}. \quad (1.71)$$

These coupling constants can also be parametrized as scattering lengths through the relation $g_i = 4\pi\hbar^2 a_i/m$. For sodium atoms the relevant scattering lengths have been measured in reference [104]:

$$\bar{a} = 52.66a_B = 2.8 \text{ nm}, \quad (1.72)$$

$$a_s = 1.88a_B = 98 \text{ pm}. \quad (1.73)$$

It is worth noticing that $a_s > 0$, which indicates antiferromagnetic interactions as the pseudo potential favors minimization of $\langle \hat{\mathbf{F}}_1 \cdot \hat{\mathbf{F}}_2 \rangle^1$.

We now consider a N-particle system described in the second quantization formalism. The interaction term (1.69) is composed of one spin independent term analogous to the interaction term for scalar gases (1.34) and a weaker spin dependent term. The interaction Hamiltonian associated with Eq. (1.69) reads:

$$\begin{aligned} \hat{H}_{\text{int}} = & \int d\mathbf{r} \frac{\bar{g}}{2} \sum_{i,j} \hat{\Psi}_j^\dagger(\mathbf{r}) \hat{\Psi}_i^\dagger(\mathbf{r}) \hat{\Psi}_j(\mathbf{r}) \hat{\Psi}_i(\mathbf{r}) \\ & + \int d\mathbf{r} \frac{g_s}{2} \sum_{\alpha} \sum_{i,j,k,l} (F_{\alpha})_{ij} (F_{\alpha})_{kl} \hat{\Psi}_l^\dagger(\mathbf{r}) \hat{\Psi}_k^\dagger(\mathbf{r}) \hat{\Psi}_j(\mathbf{r}) \hat{\Psi}_i(\mathbf{r}), \end{aligned} \quad (1.74)$$

¹In $5S_{1/2}$, $F = 1$ rubidium atoms, another widely studied spin system, interactions are ferromagnetic and $a_s < 0$.

where \hat{F}_α are the spin-1 matrices:

$$\hat{F}_x = \frac{1}{\sqrt{2}} \begin{pmatrix} 0 & 1 & 0 \\ 1 & 0 & 1 \\ 0 & 1 & 0 \end{pmatrix}, \hat{F}_y = \frac{1}{\sqrt{2}} \begin{pmatrix} 0 & -i & 0 \\ i & 0 & -i \\ 0 & i & 0 \end{pmatrix}, \hat{F}_z = \begin{pmatrix} 1 & 0 & 0 \\ 0 & 0 & 0 \\ 0 & 0 & -1 \end{pmatrix}. \quad (1.75)$$

The interaction Hamiltonian can be somewhat simplified by rather tedious calculations:

$$\hat{H}_{\text{int}} = \int d\mathbf{r} \sum_{i,j} \frac{\bar{g} + \Delta g_{ij}}{2} \hat{\Psi}_j^\dagger(\mathbf{r}) \hat{\Psi}_i^\dagger(\mathbf{r}) \hat{\Psi}_j(\mathbf{r}) \hat{\Psi}_i(\mathbf{r}) \quad (1.76)$$

$$+ \int d\mathbf{r} g_s (\hat{\Psi}_{+1}^\dagger(\mathbf{r}) \hat{\Psi}_{-1}^\dagger(\mathbf{r}) \hat{\Psi}_0(\mathbf{r}) \hat{\Psi}_0(\mathbf{r}) + h.c.), \quad (1.77)$$

$$\Delta g = \begin{pmatrix} g_s & g_s & -g_s \\ g_s & 0 & g_s \\ -g_s & g_s & g_s \end{pmatrix}. \quad (1.78)$$

This form of the interaction Hamiltonian distinguishes two contributions from the spin-dependent interaction. The first changes the energy without changing the Zeeman populations and is present in any mixture of quantum gases. The second term, specific to spinor gases, changes the Zeeman populations through spin changing collisions as represented in figure 1.12. This give rise to many physical effects both in the dynamics of the system such as for spin-mixing oscillations (see refs. [44, 47, 49, 51]), and for its equilibrium properties (see refs. [54]).

The interaction Hamiltonian commutes with \hat{F} as a consequence of the rotational symmetry of the interaction potential. However, dipole-dipole interactions and applied magnetic fields can break rotational symmetry of the interaction Hamiltonian. Concerning dipole-dipole interactions, the magnetic moment of sodium is $\mu \sim \mu_B/2$. For a sample polarized in $m_F = +1$, we compare the dipolar interaction strength to the spin-dependent interactions (see ref. [103]):

$$\frac{V_{\text{dd}}}{V_{\text{sd}}} \sim \frac{\mu_0 \mu_B^2 m}{16\pi \hbar^2 a_s} \approx 0.075. \quad (1.79)$$

The dominant antiferromagnetic interactions will favor less polarized samples, making the dipole-dipole interactions even smaller and showing the dipolar interactions are indeed negligible in our system. This is not the case for higher spin atoms such as chromium (see refs. [62, 121]), Dysprosium (see ref. [122]) or Erbium (see ref. [123]) leading to a very different physical behavior.

Experiments are always performed in a magnetic field which breaks rotational symmetry. However, the total Hamiltonian, including the Zeeman Hamiltonian still commutes with F_z , the spin along the quantization axis z . This means that the eigenvalue of the longitudinal spin *i.e.* the magnetization $M_z = N_{+1} - N_{-1}$, is a conserved quantity in atomic spinor gases.

1.3.2 Zeeman energy

Another contribution from the spinor Hamiltonian of the $T=0$ system arises from interaction with the magnetic field (see refs. [124, 125]). We work with alkali atoms (sodium) in the electronic ground state, where the spin, orbital, nuclear, fine and hyperfine quantum numbers are $S = 1/2$, $L = 0$, $I = 3/2$, $J = 1/2$, $F = 1$. The interaction with the magnetic field is given by the Zeeman Hamiltonian $H_Z = \frac{\mu_B}{\hbar} (g_S \mathbf{S} + g_L \mathbf{L} + g_I \mathbf{I}) \cdot \mathbf{B}$, where \mathbf{S} is the electronic spin operator, \mathbf{L} the electron angular momentum operator, and \mathbf{I} the nucleus spin operator. If the Zeeman energy remains small

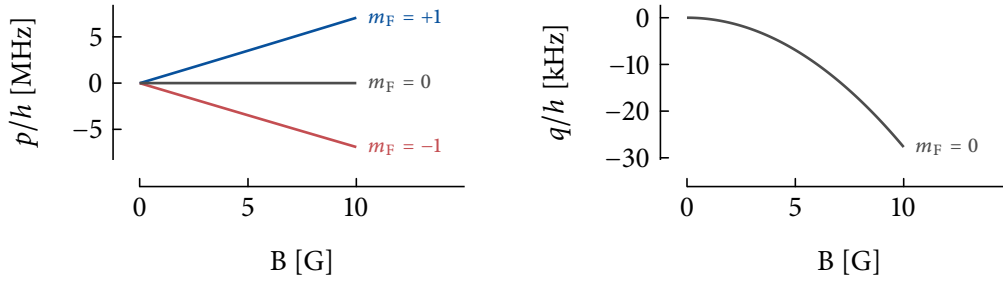


FIGURE 1.13: Zeeman energy. We show the dominant linear contribution on the left, and the relevant quadratic contribution on the right.

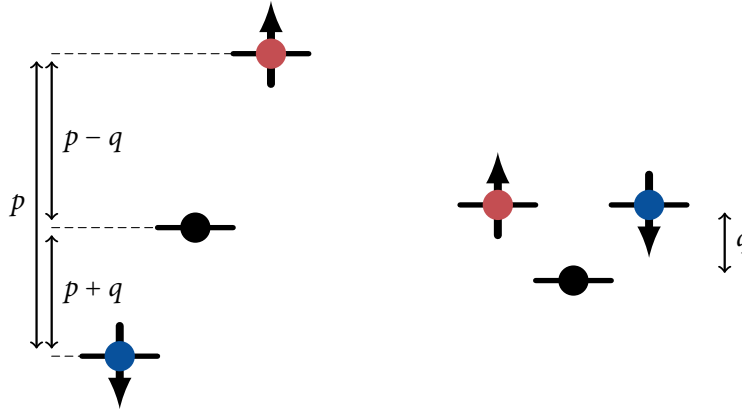


FIGURE 1.14: Schematic of the effect of Zeeman shifts to the energy levels of each Zeeman component. On the right, we remove the constant linear Zeeman shift to keep only the effect of quadratic Zeeman energy, which is the only scale relevant in determining the equilibrium and dynamical properties of the system.

compared to the fine structure splitting, $\mathbf{J} = \mathbf{L} + \mathbf{S}$ is a good quantum number and the Hamiltonian is $H_B \approx \frac{\mu_B}{\hbar} (g_J \mathbf{J} + g_I \mathbf{I}) \cdot \mathbf{B}$. Using the fact the nuclear contribution is much smaller – $g_I \ll g_J$ – we obtain the familiar expression for the linear Zeeman Hamiltonian :

$$E_{LZE} = \mu_B g_J \mathbf{J} \cdot \mathbf{B}, \quad (1.80)$$

At this level, the response of the atom is essentially that of the peripheral electron. Beyond first order, the Breit-Rabi formula [126] includes higher order corrections due to hyperfine coupling between the electron and the nucleus:

$$E_{BR} = -\frac{\delta E_{hfs}}{2I+1} + g_I \mu_B m_F B + m_F \frac{\Delta E_{hfs}}{2} \sqrt{1 + m_F x + x^2}, \quad (1.81)$$

$$x = \frac{(g_J - g_I) \mu_B B}{\Delta E_{hfs}}. \quad (1.82)$$

where the energy of the $m_F = 0$ state is taken as reference. We represent the Zeeman energy of each Zeeman state in fig. 1.13. For weak fields, such that $x \ll 1$, we recover the zero field limit of the Zeeman Hamiltonian eigenvalues (1.80):

$$E_{LZE} = \mu_B g_J m_F B = p m_F, \quad (1.83)$$

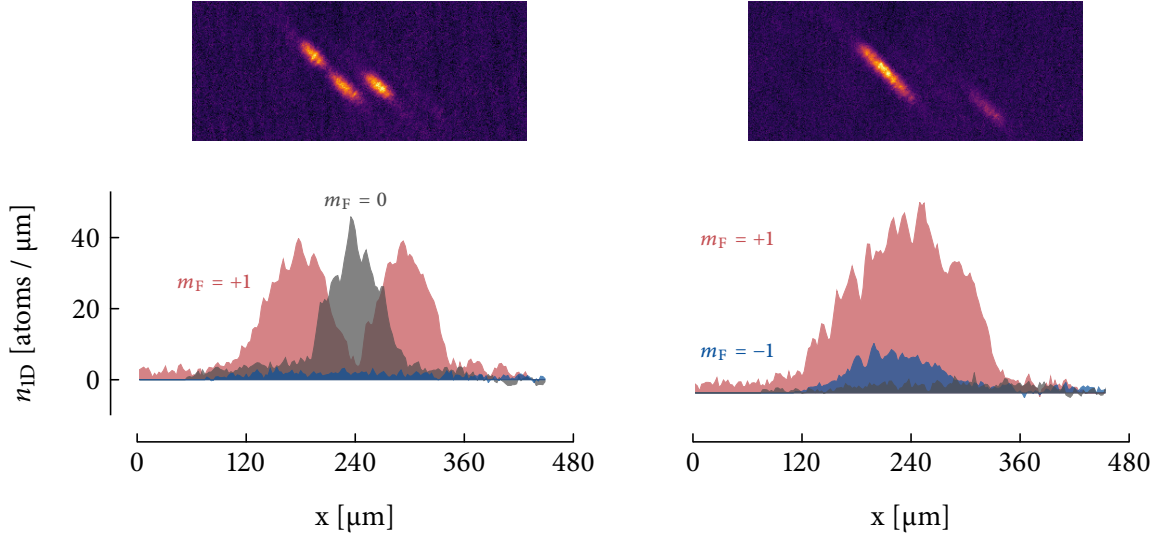


FIGURE 1.15: Experimental 2D densities and integrated density profiles (along the strong axis of a 1D trap) of spinor BECs (the mean to obtain such images and profiles shall be described in more details in chapter 2). On the left, we note that the $m_F = 0$ and $m_F = +1$ components are not miscible while on the right $m_F = \pm 1$ components are.

where μ_B is the Bohr magneton, $m_F = 0, \pm 1$, and g_F is the Landé g-factor $g_F \sim 1/2$. This gives:

$$p/B \approx 700 \text{ kHz} \cdot \text{G}^{-1}. \quad (1.84)$$

The linear Zeeman energy of the cloud is directly proportional to the magnetization and, as such, is conserved during the evolution of the system. Additional corrections to the Zeeman energy arise from the second order expansion of the Breit-Rabi formula:

$$E_Z \simeq pm_F + \frac{(g_I - g_F)^2 \mu_B^2 B^2}{8\Delta E_{hfs}} = pm_F + q(1 - n_0). \quad (1.85)$$

The additional term is proportional to the square of the magnetic field and is called the quadratic Zeeman energy. It increases equally in energy the $m_F = \pm 1$ components as sketched in figure 1.14. The value of q is:

$$q/B^2 \simeq 277 \text{ Hz} \cdot \text{G}^{-2}. \quad (1.86)$$

1.3.3 Single mode approximation

Phase separation of Bose mixtures

At $T = 0$, several Zeeman components of a spin-1 Bose gas can condense. In particular, we will discuss the case of a 2 species mixture, and whether the two components coexist as an homogeneous phase or undergo phase separation as immiscible fluids do (see refs. [127, 128]).

In the case of negligible interactions, each component is independent and their wavefunction can overlap. Phase separation can be triggered (or prevented) by spin-dependent interactions. We

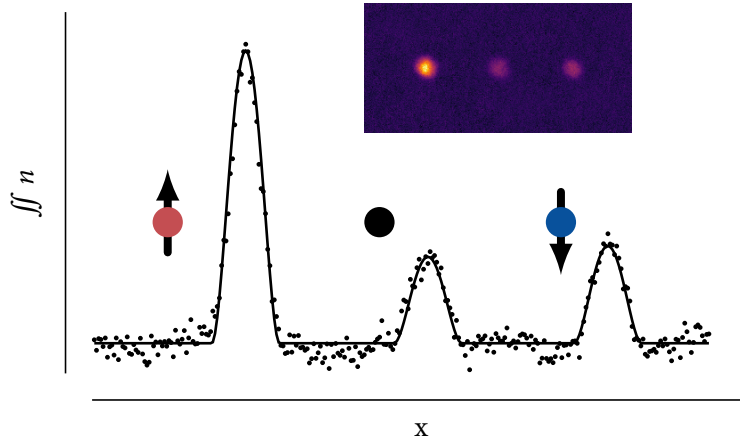


FIGURE 1.16: Density profile of a three component spinor BEC showing identical Thomas-Fermi density profile fitted on the three component.

show in fig. 1.15 an example of demixing. In order to predict qualitatively the behavior of a spinor BEC, we can compare the interaction energy of different configurations. In the simpler case of a condensate in a box of volume \mathcal{V} . Since the density is constant, for a mixture of the components a/b , it is equal to:

$$E_{\text{sep},a/b} = \frac{(\bar{g} + g_{aa})N_a^2}{2\mathcal{V}} + \frac{(\bar{g} + g_{bb})N_b^2}{2\mathcal{V}} + \frac{(\bar{g} + g_{ab})N_a N_b}{\mathcal{V}} \quad (1.87)$$

while the interaction energy of two separate phases (we neglect the contribution of the boundary region) is:

$$E_{\text{sep},a/b} = \frac{(\bar{g} + g_{aa})N_a^2}{2\mathcal{V}(N_a/N)} + \frac{(\bar{g} + g_{bb})N_b^2}{2\mathcal{V}(N_b/N)} \quad (1.88)$$

We examine the difference between these two quantities:

$$\Delta E_{a/b} = E_{\text{mix},a/b} - E_{\text{sep},a/b} = \frac{N_a N_b}{2\mathcal{V}} (2g_{ab} - g_{aa} - g_{bb}), \quad (1.89)$$

In the case of a mixture of the $m_F = \pm 1$ and $m_F = 0$ components, $\Delta E_{\pm} \propto g_s > 0$, and the formation of spin domains is favored as seen in figure 1.15 on the left. The case is different for mixture of the ± 1 components, $\Delta E_{\pm} \propto -4g_s < 0$ and we expect that in the ground state of the system, the components are miscible as observed in figure 1.15. The distribution of the domains can be deduced from energetic arguments. As the interaction parameter for the $m_F = 0$ component is \bar{g} , and the one for the $m_F = +1$ is $\bar{g} + g_s$, the energy is minimized if the $m_F = 0$ component is placed such that it is denser than the $m_F = +1$ one [129]. As such, it is placed at the center of a sufficiently weak harmonic trap. This phenomenon can be observed in figure 1.15, and is also discussed in ref. [55].

Single mode approximation in tight traps

In this section we will discuss the case of tight harmonic traps in which the trapping energy required to form a domain becomes comparable or bigger than the interaction energy. In order to

have a better understanding of the phenomenon, we define in analogy with the healing length defined in Sec. 1.2, a spin healing length:

$$\xi_s = \sqrt{\frac{\hbar^2}{2mg_s n}}. \quad (1.90)$$

This quantity gives the typical thickness of a spin domain boundary in an homogeneous system. As such, intuitively, if the trap size¹ becomes smaller than the typical spin healing length, domain formation is energetically penalized. This is equivalent to say that the trap level spacing becomes larger than the interaction energy. The single mode approximation is valid when the trap is tight enough so the formation of domains is prevented:

$$g_s n(\mathbf{0}) \leq \hbar\omega. \quad (1.91)$$

The Hamiltonian of the system in second quantized formalism is obtained from the expression of the interaction Hamiltonian of Eq. (1.77) is:

$$\begin{aligned} \hat{H} = & \int d\mathbf{r} \overbrace{\left[\frac{\hbar\nabla^2}{2m} + V + \sum_{i,j} \frac{\bar{g} + \Delta g_{ij}}{2} \hat{\Psi}_j^\dagger(\mathbf{r}) \hat{\Psi}_i^\dagger(\mathbf{r}) \hat{\Psi}_j(\mathbf{r}) \hat{\Psi}_i(\mathbf{r}) \right]}^{\text{spatial part : } \hat{H}_0} \\ & + \int d\mathbf{r} \underbrace{g_s (\hat{\Psi}_{+1}^\dagger(\mathbf{r}) \hat{\Psi}_{-1}^\dagger(\mathbf{r}) \hat{\Psi}_0(\mathbf{r}) \hat{\Psi}_0(\mathbf{r}) + h.c.) + p \hat{F}_z + q(1 - \hat{F}_z^2)}_{\text{spin part : } \hat{H}_s}, \end{aligned} \quad (1.92)$$

where $\hat{\Psi}_m$ are the field operators for each Zeeman components. We take advantage of the weakness of the spin changing interactions $g_s \ll \bar{g}$ and follow a perturbative approach (see ref. [46, 127, 130]). The field operator is written:

$$\hat{\Psi}_m(\mathbf{r}) = \Phi_0(\mathbf{r}) \hat{a}_m, \quad (1.93)$$

and where the operator \hat{a}_m create one boson in a mode given by a common ‘‘single mode’’ function $\Phi_0(\mathbf{r})$, and bears the usual bosonic commutation relations $[\hat{a}_m, \hat{a}_n^\dagger] = \delta_{mn}$. The single mode wavefunction is calculated from the spatial part H_0 neglecting terms proportional to g_s such that:

$$\hat{H}_0 \Phi_0(\mathbf{r}) \simeq \left[\frac{\hbar\nabla^2}{2m} + V + \bar{g} N |\Phi_0(\mathbf{r})|^2 \right] \Phi_0(\mathbf{r}) = \mu \Phi_0(\mathbf{r}) \quad (1.94)$$

In a second step, we simplify the spin-dependent part of hamiltonian (1.92) (see ref. [46, 127, 130]) and obtain:

$$\hat{H}_s = \frac{U_s}{2N} \hat{F}^2 - q \hat{N}_0. \quad (1.95)$$

We ignored the linear Zeeman hamiltonian as it commutes with \hat{s} . The spin exchange energy U_s is evaluated from the spin wavefunction as:

$$U_s = g_s N \int d\mathbf{r} |\Phi_0(\mathbf{r})|^4. \quad (1.96)$$

¹The *trap size* is given either by the harmonic oscillator length or the Thomas-Fermi radius depending on the spin-independent interaction parameter ξ .

Within the mean field approximation, the spin wavefunction represent a state with N spins in the mean field state ζ which reads:

$$\zeta = \begin{pmatrix} \sqrt{n_{+1}}e^{i\theta_{+1}} \\ \sqrt{n_0}e^{i\theta_0} \\ \sqrt{n_{-1}}e^{i\theta_{-1}} \end{pmatrix}, \quad (1.97)$$

where n_m are the normalized populations in each Zeeman component and θ_m their phase. The mean field ground state and its properties are discussed in more detail in chapter 3.

1.4 Critical temperatures of ideal spin-1 gases

The spin degree of freedom plays a role at very low temperature, but also for the thermodynamic of the system around the Bose-Einstein condensation threshold. In this case, the conservation of the magnetization imposed by the spin-exchange interactions shapes the phase diagram of the system which can be very different from the one of a single component gas, even when ignoring spin exchange interactions.

Spin-1 ideal gas theory

We calculate the BEC critical temperature of a spin 1 gas with fixed magnetization M_z . The gas is trapped in a harmonic potential of angular velocities ω_i , $i = x, y, z$ (see refs. [64, 131, 132]). The expression of the Gibbs energy is:

$$G = H_{q=0} - qN_0 - \mu N - \lambda M_z, \quad (1.98)$$

$$G = H_{q=0} - (\mu + \lambda)N_{+1} - (\mu + q)N_0 - (\mu - \lambda)N_{-1}. \quad (1.99)$$

Here, N_m is the population of the Zeeman state of quantum number m , N is the total population of the three Zeeman states, M_z is the magnetization defined as $M_z = N_{+1} - N_{-1}$, μ and λ are two Lagrange multipliers ensuring conservation of N and M_z . The effective chemical potentials for the Zeeman components are given by:

$$\mu_{+1} = \mu + \lambda, \quad (1.100)$$

$$\mu_0 = \mu + q, \quad (1.101)$$

$$\mu_{-1} = \mu - \lambda. \quad (1.102)$$

We define two effective fugacities:

$$\alpha = e^{-\beta q}, \quad (1.103)$$

$$\gamma = e^{-\beta \lambda}, \quad (1.104)$$

and a normalized temperature:

$$t = \frac{k_B T}{\hbar \omega}. \quad (1.105)$$

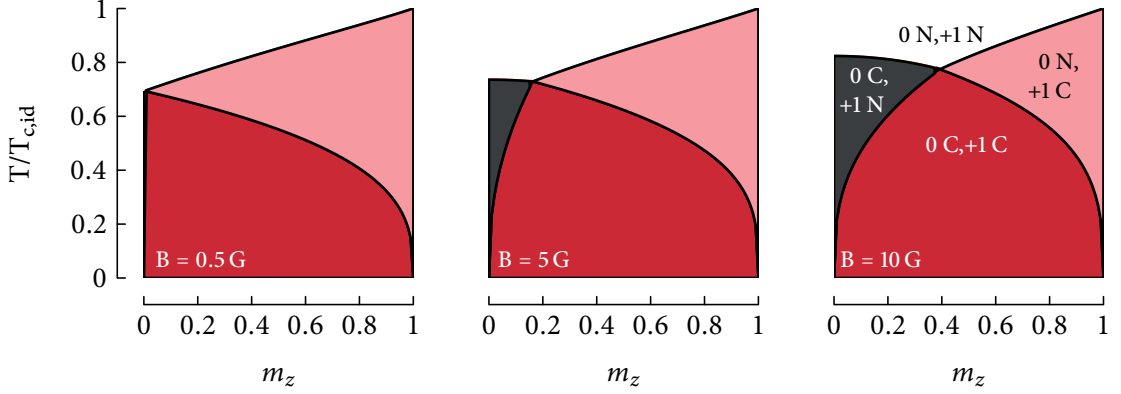


FIGURE 1.17: Critical temperature T_c , renormalized by the scalar gas critical temperature as a function of magnetization computed for a total number of atoms $N = 50000$, trap frequency of $\bar{\omega} = 2\pi \times 1200 \text{ s}^{-1}$. The different phases are described by which component is condensed (C) or thermal (N).

The thermal populations are then written:

$$N'_{+1} = t^3 g_3(z/\gamma), \quad (1.106)$$

$$N'_0 = t^3 g_3(z/\alpha), \quad (1.107)$$

$$N'_{-1} = t^3 g_3(z\gamma). \quad (1.108)$$

The BEC transition takes place when $\mu_m = 0$ (saturated Bose gas), as in the case of spinless bosons and the phase diagram displays two regimes, one where the $m_F = 0$ component condenses first and one where $m_F = +1$ condenses first. We also remark that in presence of quadratic Zeeman shift, the $m_F = -1$ component never condenses in the ideal case. We note that we consider here, and in the following of this study only $M_z \geq 0$. For $M_z \leq 0$, the role of the components $m_F = \pm 1$ is simply inverted as the quadratic Zeeman energy does not distinguish between the two.

$m_F=+1$ condenses first

At the first critical point, $z = \gamma$ ($\mu = -\lambda$):

$$N = t_1^3 (g_3(1) + g_3(\gamma_1/\alpha_1) + g_3(\gamma_1^2)), \quad (1.109)$$

$$M_z = t_1^3 (g_3(1) - g_3(\gamma_1^2)). \quad (1.110)$$

The index 1 corresponds to the values taken at the first critical point. We compute the first critical temperature by solving equations (1.109) and (1.110) numerically.

The second critical temperature takes place for $\gamma = \alpha$ ($\lambda = q$), where the $m_F = 0$ component condenses:

$$N = N_{c,+1} + t_2^3 (2g_3(1) + g_3(\alpha_2^2)), \quad (1.111)$$

$$M_z = N_{c,+1} + t_2^3 (g_3(1) - g_3(\alpha_2^2)). \quad (1.112)$$

Condensation order	+1 → 0	0 → +1
T_{c1}	$\mu = -\lambda$	$\mu = -q$
T_{c2}	$\lambda = q$	$\lambda = q$

TABLE 1.1: Summary of the conditions of condensation in the ideal case

$N_{c,+1}$ is the condensed atom number in the $m_F = +1$ component, and the index 2 indicates quantities taken at the second critical temperature. From equations (1.111) and (1.112), we eliminate $N_{c,+1}$, and obtain

$$N - M_z = t^3(g_3(1) - 2g_3(\alpha^2)). \quad (1.113)$$

The solution of this equation is obtained numerically.

$m_F=0$ condenses first

The situation is very similar except that, at the first critical point $z = \alpha$ ($\mu = -q$) and the equations to solve are:

$$N = t_1^3 (g_3(\alpha_1 \gamma_1) + g_3(\alpha_1/\gamma_1) + g_3(1)), \quad (1.114)$$

$$M_z = t_1^3 (g_3(\alpha_1/\gamma_1) - g_3(\alpha_1 \gamma_1)). \quad (1.115)$$

The equations to solve for the second critical temperature are ($\gamma = \alpha$ ($\lambda = q$)):

$$N = N_{c0} + t_2^3(2g_3(1) + g_3(\alpha_2^2)), \quad (1.116)$$

$$M_z = t_2^3(g_3(1) - g_3(\alpha_2^2)). \quad (1.117)$$

Expression of the point of simultaneous condensation

Regardless of the value of the magnetic field, there exists a point (m_z^*, T_c^*) (equivalently (m_z^*, t_*)) where $m_F = +1$ and $m_F = 0$ condense at the same time:

$$N^* = t_*^3 (2g_3(1) + g_3(\alpha_*^2)), \quad (1.118)$$

$$M_z = t_*^3 (g_3(1) - g_3(\alpha_*^2)). \quad (1.119)$$

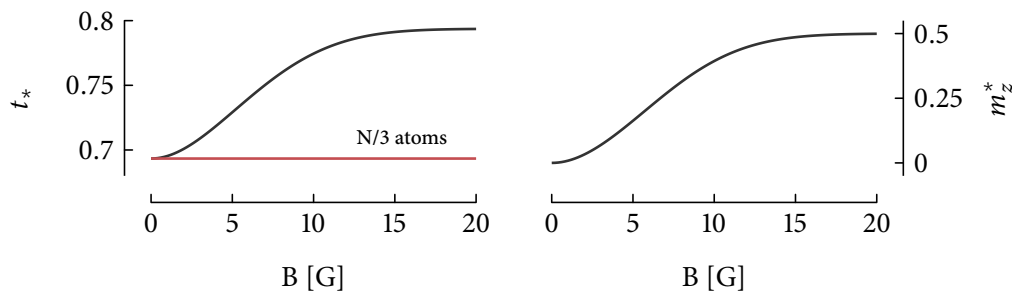


FIGURE 1.18: Magnetization (right) and reduced critical temperature $t_* = T_c^*/T_{c,id}$ (left) at the point of simultaneous condensation of $m_F = +1$ and $m_F = 0$. These figures correspond to $N = 50000$ and $\omega = 2\pi \cdot 1200 \text{ s}^{-1}$. The red horizontal line marks the critical temperature of a single component gas with $N/3$ atoms, $T/T_{c,id} = (1/3)^{1/3}$.

Solving (1.118) and (1.119) for t gives the coordinates of the point of simultaneous condensation. We conclude by showing a summary of the conditions for condensation obtained from the chemical potentials in table 1.1.

1.5 Conclusion

In this chapter, we have introduced some of the theoretical concepts that we shall use and develop in the following chapters. In section 1, we recalled the thermodynamics of Bose gases near the Bose-Einstein transition, then we have discussed the effects of finite atom number and interactions. Additionally, we have discussed more in depth our estimation of the influence of finite trap depth and anharmonicities in the Bose-Einstein critical temperature of a gas trapped in optical dipole traps. We have discussed the evaporation dynamics and the influence of several scenarii on the critical temperature.

In section 2, we have recalled the theoretical treatment used to describe Bose-Einstein condensates and their evolution in time of flight. We then discussed the case of spinor Bose-Einstein condensate within the single mode approximation in section 3. We shall discuss more in detail the ground state of spinor Bose-Einstein condensates in chapter 3, in which we will study their magnetic phases with the quadratic Zeeman energy and the magnetization as control parameters. We will see how to describe each of these magnetic phases, by examining their spin eigenvalues, and demonstrate a measurement method to reveal particular magnetic properties of the system.

In section 4, we have introduced the thermodynamics of ideal spin 1 Bose gases. We have shown that the conservation of magnetization induces several condensation scenarii depending on the magnetization and on the magnetic field. In chapter 4, we will discuss a measurement of the thermodynamics of a spin 1 gas of sodium with antiferromagnetic interactions. We will show that the scenarii predicted by the ideal gas theory are indeed observed, but that a quantitative determination of the critical temperature, and a description of the phase diagram at low magnetic field requires to take interactions into account. In addition to the discussion of the measurement, We shall study in more detail the effect of interactions on the thermodynamics of the system in chapter 4.

L'officier, au voyageur:

“Je veux, en effet, vous décrire d'abord l'appareil et je ne ferai procéder qu'ensuite à l'opération. Vous pourrez ainsi suivre plus facilement.”

LA COLONIE PÉNITENTIAIRE

Franz Kafka

2

Production and diagnostics of ultracold gases of sodium atoms

SPINOR BOSE-EINSTEIN CONDENSATES are created, manipulated and observed with the help of a complex experimental apparatus. It is designed to isolate, trap and cool a gaseous sample so that we can eventually create and observe a Bose-Einstein condensate (BEC). The figure of merit in the characterization of the properties of an ultracold gas is the phase space density (PSD, see refs. [11, 93, 133]) :

$$\mathcal{D} = n(\mathbf{0})\lambda_{\text{dB}}^3, \quad (2.1)$$

where $n(\mathbf{0})$ is the density at the center of the trap and λ_{dB} the de Broglie wavelength defined in Eq. (1.24). The condition for condensation in a non-interacting gas is given by $\mathcal{D} \geq 2.612$.

The realization of a BEC relies on several experimental steps, each designed to increase the PSD. The first is the magneto-optical trap (MOT): it captures and cools atoms from a room temperature vapor. The second step involves loading an optical dipole trap from atoms in the MOT. The third and final cooling stage is evaporative cooling in this optical dipole trap. This is in this step that the Bose-Einstein criterion is reached.

Because the cooling stages were already thoroughly documented in previous theses of our research group refs. [119, 134–136], I will refer to these works rather than go into details and focus on the main developments I have contributed to. In section 1, I will describe the trapping and cooling apparatus and the characterization of the trapping potentials. In section 2, I will detail the detection methods for spinor Bose-Einstein condensates and discuss the influence of noise on absorption images. In section 3, I will discuss how to extract thermodynamic quantities such as atom number and temperature from images by describing several procedures where we fit specific functions to experimentally measured density profiles. In section 4, I will discuss the spin manipulation techniques that allow us to control and prepare the spin of the clouds studied in this manuscript.

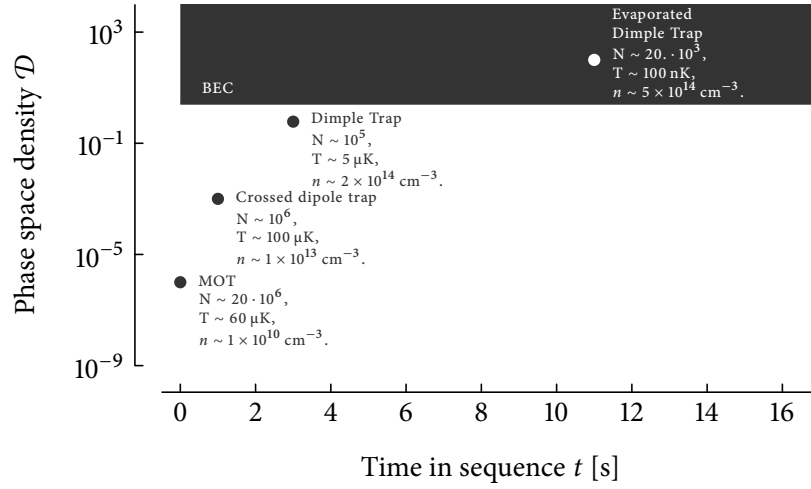


FIGURE 2.1: Summary of some thermodynamic quantities of the gas along a typical experimental sequence. We represent the timing and numbers from the gases studied in chapter 4. We note that $t = 0$ is taken at the end of the step where we load the MOT from the background gas. We observe that loading the dipole trap increases the phase space density, and that two additional evaporation steps in respectively the crossed dipole trap and the dimple trap allows us to cross the BEC transition.

2.1 Experimental realization of spinor Bose-Einstein condensates

2.1.1 Overview

Ultra-cold gases are very fragile systems. They need to be isolated because of their extreme temperature difference with environment. This is achieved by performing experiments in a ultra high vacuum chamber, in which the pressure is on the order of $\sim 10^{-11}$ mbar. This limits collisions between ultra-cold atoms and room temperature molecules from the background gas that lead to losses. It is also worth noting that spinor condensates are very sensitive to magnetic fields, which has been carefully considered in the design of the experiment (see previous theses [134, 135]).

A typical experiment is shown in fig. 2.6 and starts by loading a magneto-optical trap (MOT) from a warm sodium vapor (see refs. [137–140]). While this step increases the PSD strongly, this is not enough to reach Bose-Einstein condensation as the PSD at the end of this step is typically $\mathcal{D} = 10^{-6}$, see fig. 2.1. In order to be able to cross the Bose-Einstein transition, we transfer atoms in an optical trap (see 1.1.4). The final step consists in lowering the optical trap potential height, by reducing the power of the dipole traps in order to achieve a high enough PSD and obtain a BEC.

Before we detail each cooling step, it is important to emphasize the importance of computer control for realizing the experiments presented in this thesis (see ref. [134]). A typical experimental cycle consists in a complex sequence of various events triggered with precise timings – typically μs to ms precision – the combination of which leads to an *experimental run*. We rely on computer control because of the large number of devices to synchronize. We use the software developed by Keshet in Wolfgang Ketterle’s group at MIT, described in ref. [141], to control digital to analog converters (DAC) from National Instrument. The different events are encoded into voltages that are transmitted to the devices in the room. The sequence can be divided in steps, each either preparing – for instance cooling steps – or manipulating – spin rotations – a cold gaseous sample.

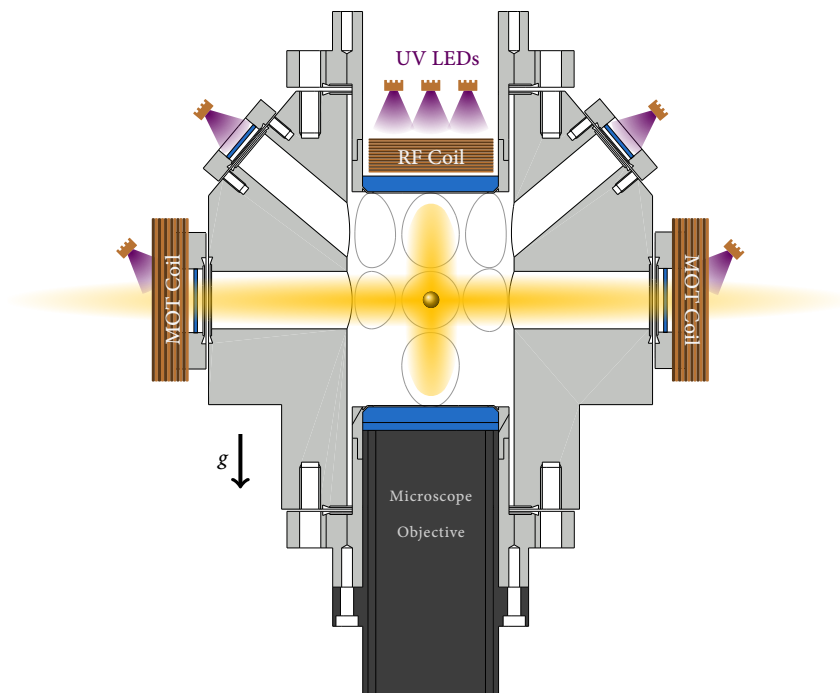


FIGURE 2.2: Schematic of the experimental setup displaying the vacuum chamber, MOT beams, and the location of some of the UV LEDs we use for light induced atomic desorption. It also displays the location of the MOT coils, and of the RF coil used for spin manipulation in later steps. The gravity axis is indicated for reference.

The final step always consists in detecting the sample. These steps may or may not be performed depending on the needs of the experiment. In the following sections we will detail each of these steps.

2.1.2 Laser cooling and trapping

The first cooling step relies on a relatively high vapor pressure of “warm” sodium as a source of atoms to produce a MOT. This “high” pressure is contradictory with the low pressure requirements for the following cooling and manipulation steps of the experiment.

These contradictory requirements are dealt with in most atomic physics experiments by dissociating the very first cooling stages from the final ones, with 2D magneto-optical traps or Zeeman slowers for example (see ref. [137] for example). We choose instead a solution in which the pressure of sodium is modulated in time by a technique called light-induced atomic desorption (LIAD, see ref. [140]). This consists in illuminating surfaces previously coated by sodium atoms with short-wavelength light. The light provokes the desorption of some of the atoms from the surface, hence generating a vapor pressure of sodium. The advantage of this technique is that a sufficiently low background pressure can be reached only a few tens of milliseconds after the light is turned off (see ref. [140]). Experimentally, we use atomic dispensers¹ for coating the chamber and windows

¹These are small metal shells containing, in our case, sodium oxides. These shells can be heated by passing an electric current of a few Ampères. When they reach a certain temperature the oxides dissociate, generating sodium in a

with sodium, and we use ultraviolet (UV) light emitting diodes (LED), at a wavelength $\lambda \approx 375$ nm for the desorption (see ref. [134, 140]). We have observed the efficiency of LIAD for the MOT loading decreases over a few weeks. This is probably due to atoms being slowly pumped off surfaces. Because of this, we turn on the dispensers on a weekly basis to ensure that the LIAD process remains efficient.

Magneto-Optical trap

The vapor pressure of sodium obtained with the LIAD loads a magneto-optical trap in which atoms are trapped and cooled. We typically capture above 20 million atoms within 6 seconds of loading. The MOT confines the atoms with the radiation pressure force of 6 slightly red detuned beams and reduces their temperature via the Doppler cooling mechanism (see refs. [137–139]). We use 6 beams in a geometry that is partially shown on fig. 2.2, and is identical to the one described on previous theses [134, 135]. Each beam contains two optical frequencies (see fig. 2.3). The most intense addresses the cooling transition $3S_{1/2}, F = 2 \rightarrow 3P_{3/2}, F' = 3$ and is detuned by about 2Γ to the red of the transition, where $\Gamma \simeq 2\pi \times 9.8$ MHz is the natural linewidth of the D line for sodium. The second frequency addresses the repumping transition $3S_{1/2}, F = 1 \rightarrow 3P_{3/2}, F' = 2$ and is resonant. This ensures that atoms are recycled in the $3S_{1/2}, F = 2$ manifold, as the cooling transition is not perfectly closed, and atoms can undergo spontaneous emission process and end up in the “dark state” $3S_{1/2}, F = 1$.

The quadrupolar field required for the MOT (see refs [137–139]) is created with a pair of coils in anti-Helmholtz configuration (the MOT coils, see fig 2.2), and 3 pairs of bias coils in Helmholtz configuration (see fig.2.4).

Cooling lasers

The laser light used for cooling is generated with the laser system described in the thesis of Emmanuel Mimoun [134, 143] is based on cavity enhanced sum-frequency generation from two YAG lasers. This solution provides ~ 600 mW of laser light that we use for cooling, trapping and imaging.

The frequency of the laser is locked on a iodine molecular line (see ref. [144]) measured by modulation transfer spectroscopy (see refs. [145–147]). The different frequencies required for cooling, repumping and imaging are generated with the help of acousto-optic modulators (AOM). The AOM used to generate the cooling light is also used to stabilize the MOT intensity by using a feedback loop on the RF amplitude delivered by the AOM driver. It is worth noting that the relatively low hyperfine splitting – $A_{\text{hf}} \simeq 1.77$ GHz – in sodium allows us to produce repump light with a high frequency AOM, and as such, to use a single laser source.

One issue with this laser system is the very small tuning range allowed by the YAG laser sources. Recently, semi-conductor amplifiers have been developed at 1178 nm such that large powers (few W) of infrared light at 2λ can be obtained. I have developed and built a intracavity doubling system similar to the system from [148], that offers large powers of yellow light (typically ~ 700 mW) at the sodium D2 wavelength. It is presented in annex A. Besides being able to replace the current

gaseous form. However, due to poor thermal coupling with the outside (only through the electrical connections), the modulation of the sodium vapor pressure from these devices is quite slow (minutes to hours timescale). This is why LIAD is used on our setup. Note however that a solution to obtain fast modulation of vapor pressure with dispensers has recently been developed in the team of J. Reichel at ENS, see ref. [142].

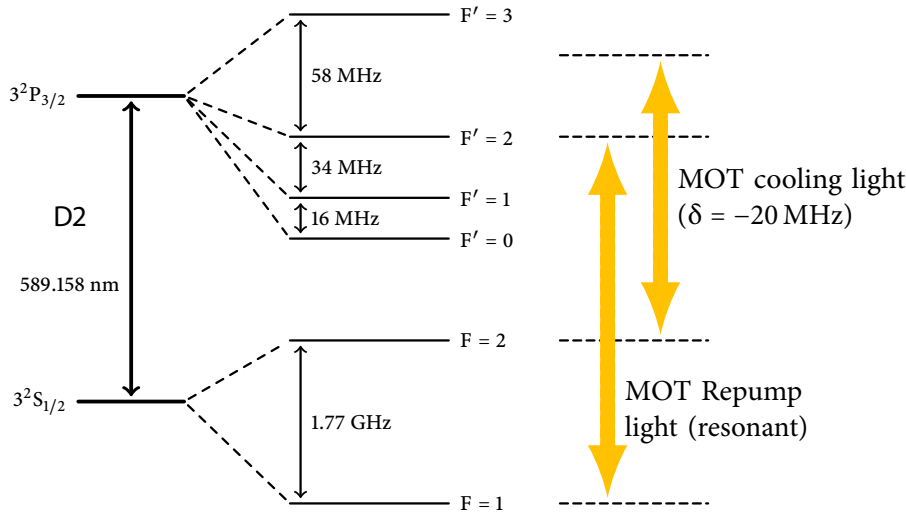


FIGURE 2.3: Level structure of sodium atoms. This figure indicates the cooling and repumping transitions.

cooling system in case of failure, the large tuning range offered by the diode laser technology also allows other applications, such as driving Raman transitions (see annex B,C).

Loading of the dipole trap

The temperature and densities of a MOT are actually limited, such that it is not possible to cool the atoms sufficiently to obtain a Bose-Einstein condensate. The temperature can be decreased a bit further by *sub-Doppler* cooling methods [137, 138]. Typically, the sub-Doppler temperature T_{SD} scales as $T_{SD} \approx \Omega_r^2 / \Delta$ where Ω_r is the coupling strength and Δ the detuning to the cooling transition (see refs. [137, 138]). The limiting temperature for such mechanisms is a few E_r , the *recoil energy*:

$$E_r = \frac{\hbar^2 k_L^2}{2m} \sim k_B \cdot 1 \mu\text{K}. \quad (2.2)$$

This energy corresponds to the kinetic energy transferred upon absorption or spontaneous emission of one photon¹.

The transfer of atoms from the magneto optical trap into a crossed dipole trap (CDT, see ref. [149]) is done with a few extra steps. The CDT has a typical size of $\sim 40 \mu\text{m}$ which is much smaller than the MOT size (typically $\sim 1 \text{ mm}$). We apply a compression phase in order to maximize the density in the center of the MOT and optimize the number of atom transferred into the dipole trap (see refs. [135, 149]). This phase is called “dark MOT” and increases both density and temperature in the MOT by lowering the power of the repumper beam. We then perform a final laser cooling step called “cold MOT” in which the detunings are increased to favor the sub-Doppler

¹These low temperatures can furthermore only be achieved at very low densities such that reabsorption and multiple scattering of photons does not come into play. This is not the situation encountered in a typical MOT where multiple scattering is important. As a result laser cooling is not sufficient to reach Bose-Einstein condensation, and another cooling step is performed in optical dipole traps.

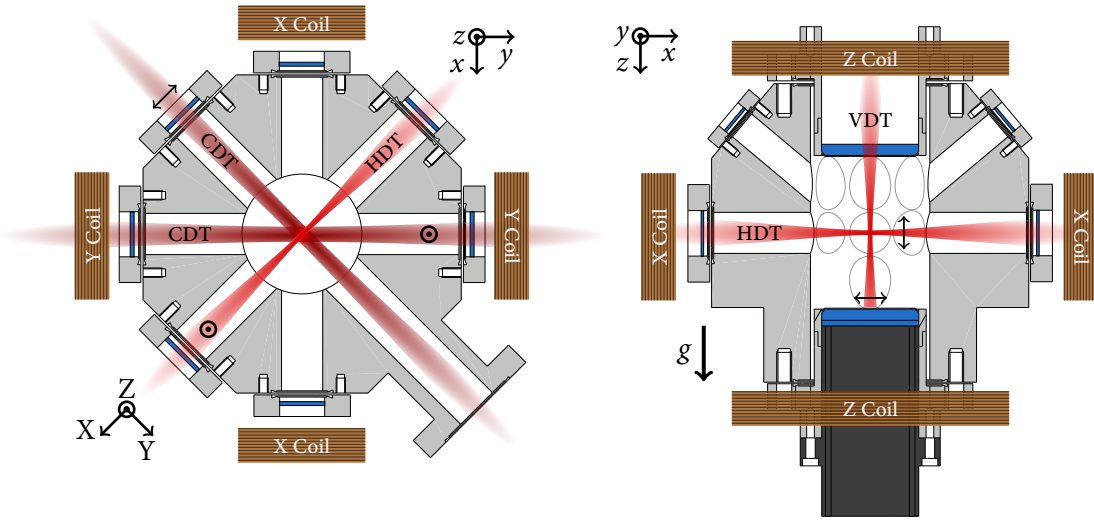


FIGURE 2.4: Schematic of the dipole trapping geometry from two different perspectives. We show the crossed dipole trap (CDT), and the dimple trap geometry (the horizontal arm is labeled HDT, and the vertical one VDT). The polarization of each beam is indicated on the pictures. We also show the bias coils used both for setting the quadrupolar field of the magneto optical trap and the bias fields for evaporation and spin manipulation. Finally, two set of axis coordinates are presented. The capital letters (X, Y, Z) represent the referential set by the dimple trap axes, while the one in lower case letters (x, y, z) corresponds to the one set by the coil axes. The main imaging axis of the experiment is set along z , and an additional imaging axis, mainly used for diagnostics is set along axis y .

cooling mechanism [133, 138]. We end up with typically one million atoms at $T \sim 100 \mu\text{K}$ in the crossed dipole trap (see fig.2.1).

2.1.3 Optical dipole traps and evaporative cooling

Atoms are loaded in a crossed optical dipole trap (CDT) composed of two gaussian beams of waists $w_{\text{CDT}} \sim 40 \mu\text{m}$ (see refs. [134, 135, 149]). We use a crossed geometry, that we show on fig. 2.4 in order to obtain a roughly spherical trap, higher densities, and hence higher collision rates. Interferences between the two arms are avoided by crossing their polarizations.

We control the trap depth using the laser power since $V_0 \propto I_0 \propto 2P/\pi w^2$ (see annex B). The power is stabilized using a servo loop. One way of controlling the power is to adjust the pump diode current of the high power laser. This solution does not allow to access very low intensities as the threshold of the laser may be reached before the target intensity is. The spatial mode of high power lasers also changes as their power is varied which is undesirable for atom trapping. Another way of controlling the power is a motorized $\lambda/2$ waveplate followed by a Glan polarizer. This solution however suffers from relatively low bandwidth (the waveplate rotates at a maximum rate of 10 turns per second) and limited dynamic range. In order to achieve high dynamic range, we use a combination of these control methods (see ref. [150]). The servo loop controls the pump diode current in order to follow a ramp on the dipole trap power (represented in fig. 2.6). The waveplate is rotated simultaneously such that the pump diode current is approximately constant and that the servo loop only compensates for high frequency noise. This solution allows to control

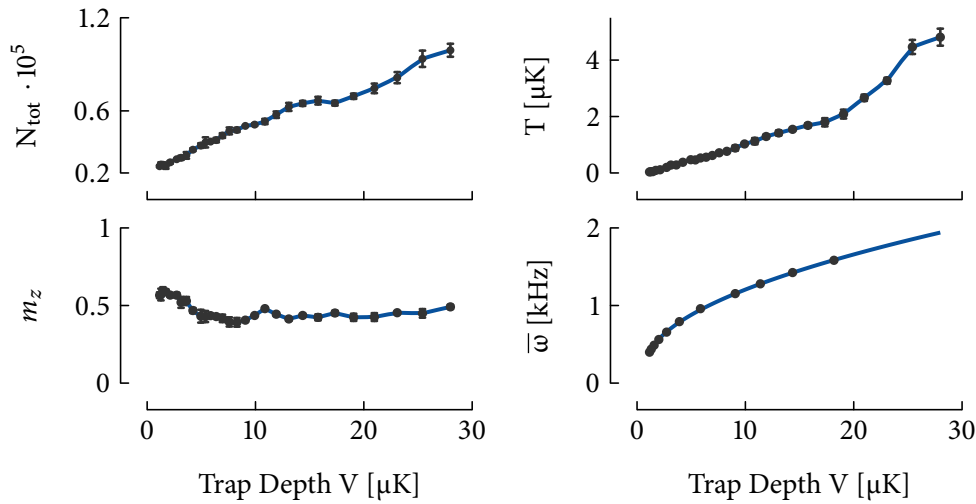


FIGURE 2.5: Evaporation trajectory in the dimple trap, showing the variation of quantities of interest, *i.e.* N , T , m_z , ω for the spinor gas.

the intensity of the optical dipole trap with a dynamic range of 10^4 and a bandwidth above a kHz (limited by the servo loop). We use a maximum power $P_{\text{CDT}} \sim 25$ W corresponding to a trap depth $V_{\text{CDT}} \sim 1$ mK.

We observe that the pump current during this ramp displays a sawtooth-like behavior as a function of time near the end of the evaporation ramp, when the waveplate is rotated very slowly. We believe that this irregular behavior comes either from the finite resolution of the rotary encoder or from slip-stick behavior, that would make the waveplate rotation irregular for slow angular speed.

The collision rate plays a key role in evaporation efficiency as seen in the first chapter and is $\sim n\sigma v_{\text{th}}$ with $v_{\text{th}} = (8k_B T/\pi m)^{1/2}$. In optical dipole traps, the reduction of the trap depth necessary for evaporation comes with a gradual reduction of the trap frequencies $\omega_i \propto (V_0)^{1/2} \propto P^{1/2}$. This translates in a reduction of the density, and a reduction of the collision rate as evaporation goes. Even though the reduction of temperature induces an increase in density, the atom loss and reduction of trap frequencies decrease the density more. This issue is specific for ODT, and has been circumvented with several ingenious technical solutions (see refs. [151–153]) allowing to control trap depth and trap frequency independently.

The dimple method provides another solution (see ref. [154, 155] and later on refs. [149, 156–158]). It consists in superimposing a small volume trap – the “dimple” – to the initial CDT. The evaporation is then divided in two steps (see fig. 2.6). At first, most of the atoms are too energetic to be trapped in the dimple trap (DT). As the first evaporation goes, and as the gas gets colder, atoms “fall” into the dimple trap, which boosts significantly the density hence the collision rate while maintaining a roughly constant temperature. This allows a second evaporation step to be performed, during which we obtain a Bose-Einstein condensate.

In our experiment, the dimple trap is composed of two beams (see fig. 2.4) : the horizontal dipole trap (HDT) and the vertical dipole trap (VDT). We generate HDT and VDT from the same high power infrared (IR) laser at $\lambda = 1064$ nm. As such, we took special care to offset the HDT and the VDT in frequency by ~ 200 MHz with the help of two AOMS, that we use with opposite diffraction order. This also allows us to stabilize the intensity of each dipole trap beam using a

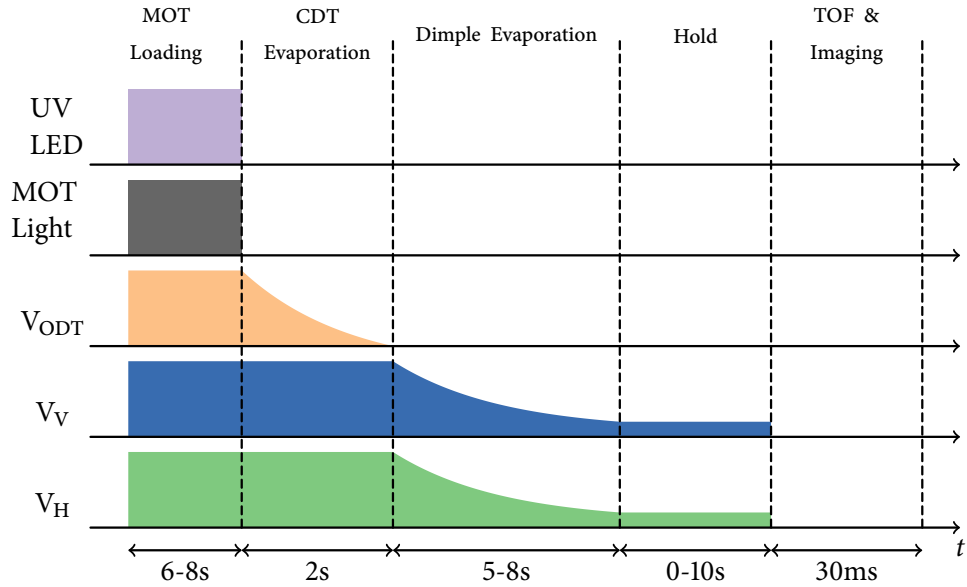


FIGURE 2.6: Typical experimental sequence performed to produce a Bose-Einstein condensate. Spin manipulation typically takes place in a short additional sequence in between hold and imaging.

servo loop on the RF power of each acousto-optic modulator. The waists of the HDT and VDT beams are both set in accordance with the need of the experiment¹. We display the typical PSD, atom number and temperature at the beginning and end of the evaporation ramp in the dimple trap on fig. 2.1.

2.1.4 Absorption imaging

Ultracold atoms are almost always detected through their interaction with light. Most of the techniques used for imaging are based on the direct detection of spontaneously emitted photons (fluorescence imaging), of resonant photons absorbed by the gas – absorption imaging – or on the detection of the phase shift induced by the atoms on slightly detuned light – phase contrast imaging (see refs. [55, 133]).

In absorption and fluorescence imaging, many photons need to be scattered in order to obtain enough signal. The recoil energy E_R transferred to the atom by each scattered photon is typically higher than the energy per atom (see Eq.(2.2)). This means that both absorption and fluorescence imaging are “destructive imaging” as they heat up the gas. Fluorescence imaging enables very low atom counting noise as demonstrated for example in the Oberthaler group in ref. [159]. However, the long integration time requires cooling of the cloud during imaging. This is typically done by turning on an optical molasse, whose scattered photons are collected. This procedure alters substantially the density distribution of the sample, preventing from extracting thermodynamic quantities other than atom numbers.

Absorption imaging is the method we use for the experiments presented in this thesis. It consists in measuring the absorption of resonant light by the atomic cloud. In the experiment the resonant light beam – the *probe* – is sent along the vertical axis, see fig. 2.7. Imaging is performed with a bias

¹For the experiments shown in chapter 3, $w_{\text{HDT}} \approx 9 \mu\text{m}$ and $w_{\text{VDT}} \approx 11 \mu\text{m}$. For the experiments shown in chapter 4, $w_{\text{HDT}} \approx 22 \mu\text{m}$ and $w_{\text{VDT}} \approx 25 \mu\text{m}$.

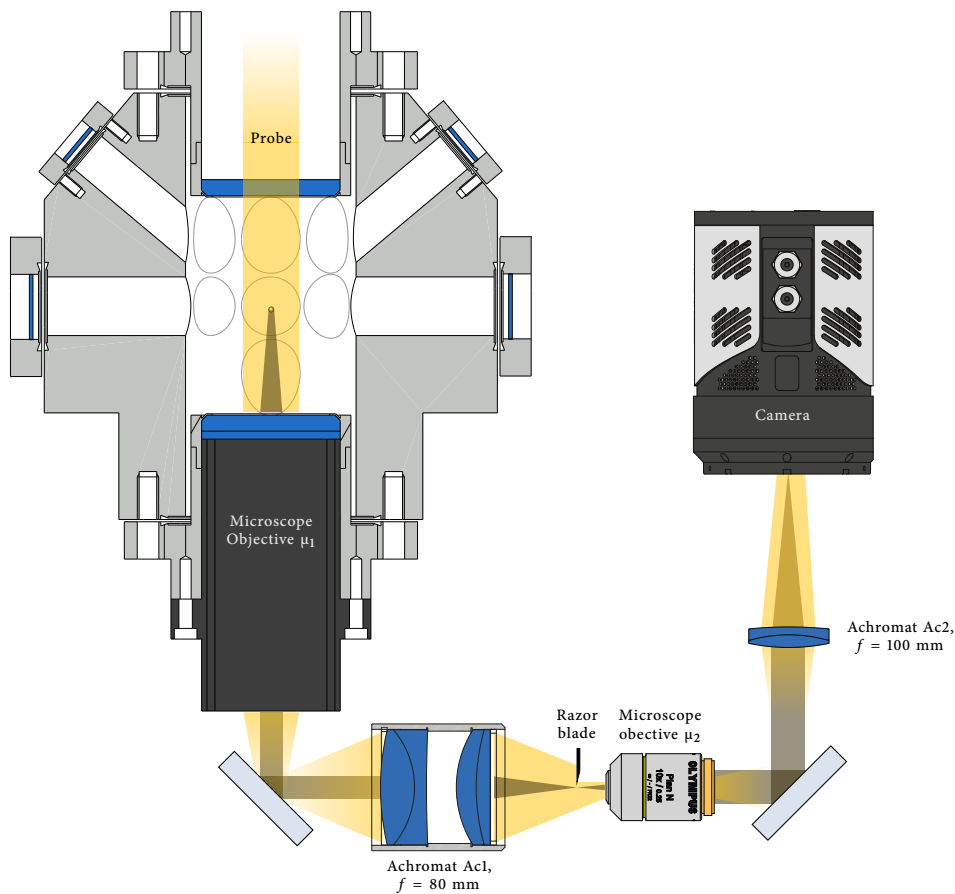


FIGURE 2.7: Schematic of absorption imaging. The probe is sent from above the vacuum chamber and it is roughly collimated. An intermediary image is created by the microscope objective μ_1 and a high NA achromat Ac1. A second microscope objective μ_2 and an achromat Ac2 form the final image on the CCD sensor. The two systems ($\mu_1 + \text{Ac1}$) and ($\mu_2 + \text{Ac2}$) have a calculated magnification of 1.5 and 5 respectively and are designed to work in an afocal configuration. A razor blade is placed at the intermediary image position in order to mask part of the camera sensor for frame transfer.

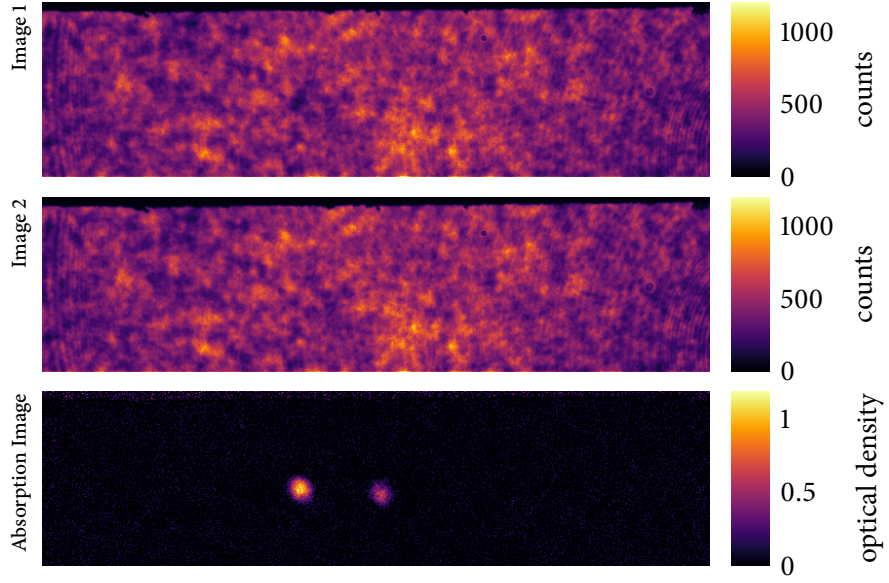


FIGURE 2.8: **Upper** First image, taken in the presence of atoms. The vertical scale is in digital grey levels – “counts” – as returned by the ADC of the CCD camera. **Middle** Second image, taken without atoms. The vertical scale is in CCD counts. **Lower** Optical density computed with equation (2.5).

magnetic field of 1 G along z . The probe is circularly polarized and addresses the cooling transition $3S_{1/2}, F = 2 \rightarrow 3P_{3/2}, F' = 3$. The atoms are previously repumped onto the $F=2$ manifold by a short repumping light pulse sent along the same z axis as the MOT beams (see fig. 2.2).

The imaging system is shown in fig. 2.7. An image of the atoms is created through a first afocal system composed of a microscope objective of effective focal length $f \sim 40$ mm and a high NA achromat Ac1 of focal $f \sim 80$ mm. A second microscope objective μ_2 of effective focal length $f = 18$ mm and an achromat Ac2 of focal $f = 100$ mm form the final image on the CCD sensor. The two systems ($\mu_1 + \text{Ac1}$) and ($\mu_2 + \text{Ac2}$) have a theoretical magnification of 1.5 and 5 respectively and are designed to work in an afocal configuration. Half of the intermediary image is masked by a razor blade image in order to mask part of the camera sensor, which is needed for taking images as we shall discuss in the next paragraph. We have estimated the resolution of this optical system by measuring the *in situ* size of small Bose-Einstein condensates ($N \sim 500$) whose size is predicted to be around one micrometer. We could not detect clouds with a RMS size of less than $2 \mu\text{m}$. We mention here for the sake of completeness the existence of a second imaging axis along axis x , that we mainly use for diagnostics and to calibrate the main imaging setup as we shall discuss in a section 2.

We produce an absorption image by taking two successive images, the first one “ I_1 ” in the presence of atoms and the second one “ I_2 ” in their absence. We use the frame transfer technique where two images can be taken sequentially without waiting for the sensor to be read. The first image is transferred to a masked part of the charge coupled device (CCD) sensor, and a second image can be taken as soon as the shifting is complete. This process is typically much faster than the readout time and allows for a short time between images, which minimizes noise as we will discuss in following sections.

The sensor is read entirely at the end of the imaging step, and we extract pairs of images such as the one shown in fig. 2.8. The probe pulses used for imaging last 10 μs and are separated by ~ 5 ms. Passing through the atomic cloud, the intensity of light obeys the Beer-Lambert law:

$$\frac{\partial I}{\partial z} = -\sigma n I, \quad (2.3)$$

where n is the density and σ is the absorption cross-section. For a two-level atom, the cross-section is given by:

$$\sigma = \frac{\sigma_0}{1 + (I/I_{\text{sat}}) + (2\delta/\Gamma)^2}, \quad (2.4)$$

where $\sigma_0 = 3\lambda^2/2\pi$ is the resonant scattering cross-section, λ the resonant wavelength, δ the detuning, Γ the linewidth of the transition, and I_{sat} the saturation intensity. For most results presented in this manuscript, we have worked at low intensity, $I \ll I_{\text{sat}}$, such that saturation only give rise to a small correction. In the experiment, we measure two images corresponding to the intensity of the probe without any absorption ($I_2 = \lim_{z \rightarrow -\infty} I$) and to $z = +\infty$ corresponding to a region with negligible atomic density ($I_1 = \lim_{z \rightarrow \infty} I$). Using the two level scattering cross-section (2.4), and assuming the probe is resonant ($\delta = 0$)¹, authors of ref. [160] obtained the following formula for the column density n :

$$n(x, y) = \frac{1}{\sigma_0} \left(-\log \left(\frac{I_1}{I_2} \right) + \frac{I_2 - I_1}{I_{\text{sat}}} \right). \quad (2.5)$$

The measurement of the density of ultracold clouds is limited by the dynamic range of the camera. Typically, the *optical density* $\log(I_2/I_1)$ is limited to ~ 5 for a camera with a 16 bits ADC. This prevents from measuring *in situ* distribution in our parameter regime. As such, the density profiles of cold clouds are typically taken after a step of free expansion called *time of flight*, such that $\text{OD} < 2$. This also prevents multiple scattering events (see refs. [161, 162] and methods of ref. [163]), that would complicate the quantitative interpretation of images.

Most of the noise in absorption is produced by the differences between the two images that are not due to the atoms. This is why it is crucial to maintain a short interval between the two images since vibrations and index changes along the imaging path can change strongly the intensity profile due to the high coherence of the imaging light. There might also be artifacts on the edges of absorption images due to diffraction by sharp objects such as the razor blade, or sensor edges. For this reason, we never study signals near the image edges.

The simplest quantity to obtain from Eq. (2.5) is the atom number. We typically obtain it from integration of the optical density over regions of interest where there are atoms. We choose a square region of the sensor \mathcal{S} such that the atom number is obtained from summation of the pixel value over this area: $N = \sum_{\mathcal{S}} n_{x,y}$. More sophisticated analysis rely on fitting model functions and is discussed in Sec. 2.3 and ref. [133].

2.1.5 Characterization of the trapping potential

Many optical elements are used to obtain the optical dipole trap with the precise size and position required for the experiments we perform. Since we have an imprecise knowledge of the

¹If $\delta \neq 0$, one can simply replace $\sigma_0 \rightarrow \sigma_0/(1 + (2\delta/\Gamma)^2)$ and $I_{\text{sat}} \rightarrow I_{\text{sat}}(1 + (2\delta/\Gamma)^2)$ as suggested by Eq. (2.4)

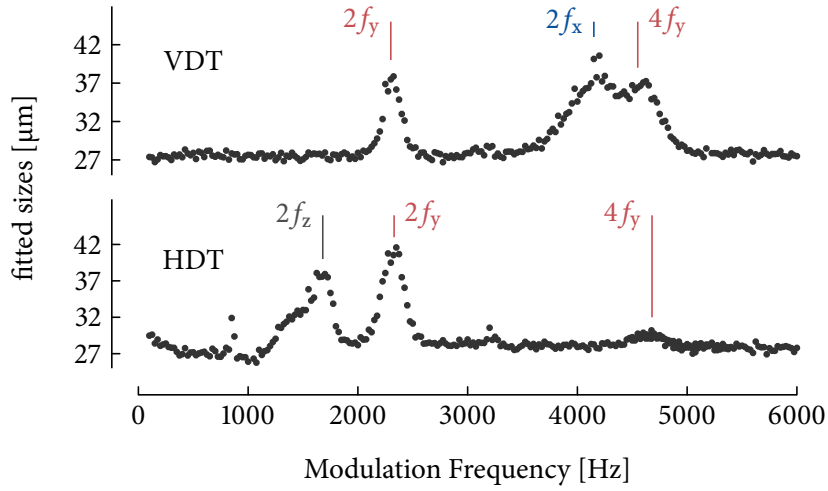


FIGURE 2.9: Parametric heating spectrum with modulation of the power of the vertical dipole trap and of the one of the horizontal dipole trap. Vertical lines indicate peak positions from Lorentzian fits. Red lines are attributed to Y axis and display both ω and 2ω resonances (at $2f$ and $4f$ respectively). Blue lines indicate X axis resonances while black solid lines are attributed to the z axis.

optical characteristics of these elements (that may depend on the wavelength for example), the precise intensity map of the beam cannot be known unless it is directly measured. This is both tedious and imprecise – we cannot for example include the viewports from the experiment in such a measurement – so we adopted another approach. We consider the harmonic approximation is good enough for most atoms in the trap as seen in Sec. 1.1.4 and we measure directly the oscillation frequencies from two kinds of experiments that we will describe in the next paragraphs.

Parametric heating

For thermal clouds in relatively tight traps, we perform parametric heating (see refs [164–167]). It consists in a resonant modulation of the ODT potential to induce heating. We modulate the power – hence both trap frequencies and trap depth – by a sine function. In the case of thermal clouds, which are dilute enough to neglect interactions, the excitation becomes resonant at twice the trap frequency (see ref [164]), and the cloud heats up. This is detected either directly by an increase of the size after time-of-flight as seen in figure 2.9 or equivalently by an atom loss after a hold time as a result of evaporation of the heated cloud. The identification of frequencies in the spectrum (including harmonics) is done by observing their change while tuning the relative power of both arms of the DT.

Unfortunately, this technique becomes more complicated to use for the intensities at which we reach the BEC transition. The parametric heating spectrum becomes difficult to analyze because the resonant frequencies are modified by interactions (see refs. [93, 164]). In the case the Thomas-Fermi approximation is valid, the resonant frequencies in harmonic traps become $\omega_{\text{res},i} = \sqrt{5}\omega_i$ (see [93, 164]). However, in partially condensed clouds, relating the measured parametric resonance spectrum to actual trapping frequencies would require careful modeling of the gas including finite temperature which is a difficult task. In addition, for our experiments, corrections to the Thomas

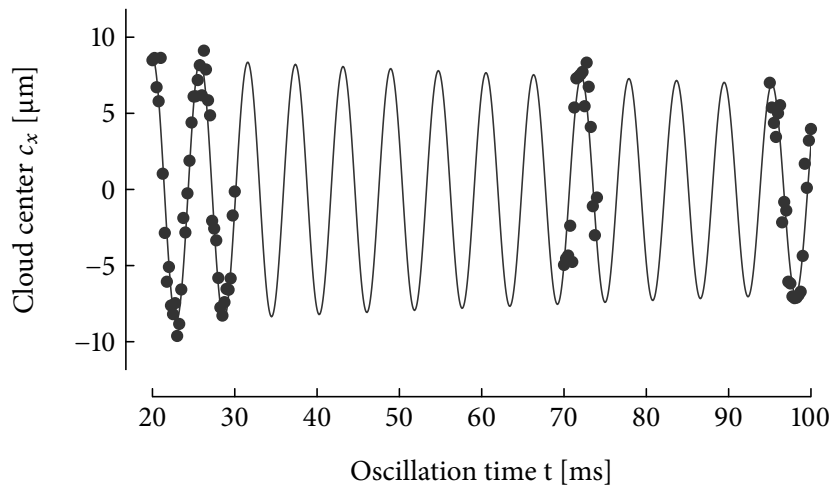


FIGURE 2.10: Center of a BEC during a dipole oscillation along the Y axis. The solid line is a sinusoidal fit of the data.

Fermi approximation can be significant. These corrections lead to potential systematic errors that we avoid with a different technique.

Dipole oscillations

For condensed clouds in relatively loose traps, we measure the frequency of the dipole mode (or equivalently of the center of mass motion). This method consists in inducing center of mass oscillations with the sequence shown in fig. 2.11 in the trap as seen in fig. 2.10. We displace a BEC polarized in $m_F = +1$ with a gradient. The force is oriented towards the $\mathbf{X} + \mathbf{Y} + \mathbf{Z}$ direction. As shown in fig. 2.11, the gradient is then suddenly cut. In this case, the 3 dipole modes are excited, and we observe an oscillation of the cloud center at all three trap frequencies. The different modes can be isolated by projection of their movement on the trap axes X, Y, Z. The displacement is enhanced by time of flight. In a purely harmonic trap, the dipole mode frequency does not depend on the interaction potential (generalized Kohn theorem, see refs. [168, 169]). However, deviations of the actual trapping potential from its harmonic approximation can lead to damping of the dipole mode on relatively long timescales. As such, we extract the oscillation frequencies from fit to the data with a possible exponential damping (see fig. 2.10).

This method shows limitations for high trapping frequencies $f \sim 1$ kHz because the switch-off time of the gradient, that is limited to approximately a millisecond, becomes longer than the typical oscillation period. In this case, the trap is brought back to the equilibrium position “adiabatically”, without inducing dipole oscillations.

Model of the dimple trap for trap depth estimation

Similarly to trap frequencies, it is not possible to obtain the trap depth (see Sec. 1.1.4) from knowledge of the optical set-up, and we need to develop a model of the dimple trap. We consider two crossed Gaussian beams. The potential is then the sum of the two optical potentials given by

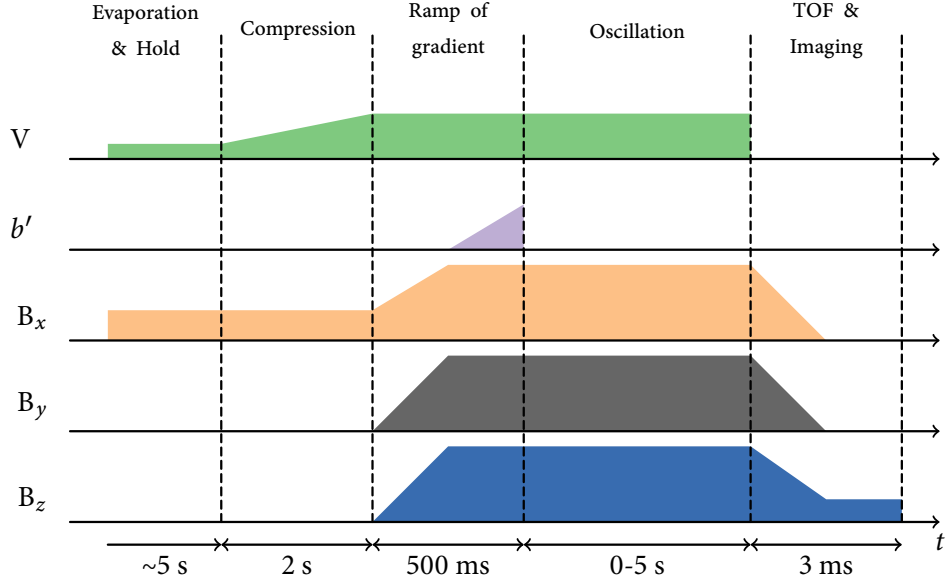


FIGURE 2.11: Experimental sequence for exciting dipole oscillations. We first create a BEC. Then the power of the dipole trap is raised in order to obtain the trap frequencies we want to measure. We ramp a large bias field in the X+Y+Z direction and then ramp a gradient. The strength of the gradient is adjusted depending on the trap frequencies to measure. After the gradient is released the cloud oscillates in the trap during a given time before it is imaged.

[37] (see also annex B and section 1.1.4):

$$V(x, y, z) = V_{\text{HDT}}(y, z) + V_{\text{VDT}}(x, y). \quad (2.6)$$

We have found that we needed to consider the ellipticity of the laser spatial modes to reproduce the data. We found that the VDT could be taken isotropic (with a beam waist w_x) but not the HDT (beam waists w_y, w_z). The trap frequencies are given by a Taylor expansion of the Gaussian potential around the trap minimum:

$$\omega_X = \sqrt{\frac{4V_V}{mw_x^2}}, \quad (2.7)$$

$$\omega_Y = \sqrt{\frac{4V_H}{mw_y^2} + \frac{4V_V}{mw_x^2}}, \quad (2.8)$$

$$\omega_Z = \sqrt{\frac{4V_H}{mw_z^2}}, \quad (2.9)$$

$$V_H = \frac{2\alpha_0 P_H}{\pi w_y w_z}, \quad (2.10)$$

$$V_V = \frac{2\alpha_0 P_V}{\pi w_x^2}. \quad (2.11)$$

where α_0 is the calculated atomic polarisability (see ref. [37] and annex B). P_H and P_V are obtained by direct calibration of the optical power. The sizes of the beams are obtained from fits to the calibrated trap frequencies. The results of such a procedure are summarized on figure 2.12.

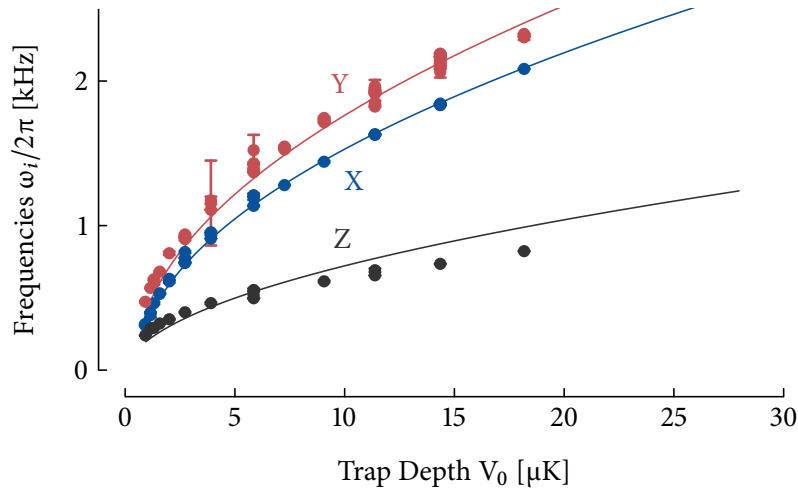


FIGURE 2.12: Trap frequencies along the evaporation ramp. The solid lines are the results of the fit to the interpolation functions from Eq. (2.7), (2.8), (2.9) with waists $w_X, w_Y, w_Z = (21.74 \mu\text{m}, 21.55 \mu\text{m}, 29.79 \mu\text{m})$.

A single measurement of the oscillation frequencies or parametric heating spectrum yields a very precise trap frequency (≤ 1 Hz uncertainty per measurement). However, we observed that when repeating this measurement several times, over a few days for example, we could not reproduce the initial measurement within its uncertainty. The trap frequencies are determined by the optical power and beam mode, which are very stable, but also by the relative alignment of the HDT and VDT which could drift over time. The reproducibility of the trap frequencies has been tracked by repeating the measurements with identical conditions over several days. We found that the trap frequencies were reproducible to within 5 Hz.

2.2 Spin-dependent imaging

The diagnostics of spinor gases require spin-dependent imaging. We perform a Stern-Gerlach (SG) experiment, which consists in applying a spin dependent force, and separate spatially the clouds during the time of flight. As such, different Zeeman components are imaged in different parts of the CCD sensor at the end of the time of flight sequence. Noise in pictures ($\delta\text{OD} \sim 0.02$) provides an upper limit for time of flight thus a limit for the distance between Zeeman components at the time of imaging for a given spin dependent force. Our experimental setup uses relatively high trapping frequencies (hence high temperatures and interaction energies), such that the expansion is practically limited to a few ms in order to keep high enough signal-to-noise. This limit requires special care on the design of a SG sequence as the magnetic fields required to separate the clouds by a large enough distance need to be applied in short time scales.

2.2.1 Stern-Gerlach Imaging

A Stern-Gerlach sequence consists in a spatially dependent magnetic field, that creates a spin-dependent force (see refs. [170–172]). We apply a magnetic gradient by passing current through the MOT coils. In principle, the magnetic field created in the frame (x, y, z) (see fig. 2.4) centered

on the atoms is equal to $\mathbf{B}_q = (b'x, -2b'y, b'z)$. However, small positioning imperfections result in an additional uniform field \mathbf{B}_m at the position of the atoms. We further apply a bias field $\mathbf{B}_0 = (B_{0,x}, B_{0,y}, B_{0,z})$ such that the total field during the Stern-Gerlach experiment is $\mathbf{B}_{SG} = \mathbf{B}_q + \mathbf{B}_m + \mathbf{B}_0$. The potential felt by the atoms is then $V_{SG} = m_F g_F \mu_B |\mathbf{B}_{SG}|$, and the force felt by the atoms, initially at $\mathbf{r} = (0, 0, 0)$ is $\mathbf{F}_{SG} = -\nabla V_{SG}(\mathbf{0})$. The total force is:

$$\mathbf{F}_{SG} = \frac{\mu_B g_F m_F b'}{2|\mathbf{B}_{SG}|} \begin{pmatrix} (B_{0,x} + B_{m,x}) \\ -2(B_{0,y} + B_{m,y}) \\ (B_{0,z} + B_{m,z}) \end{pmatrix}. \quad (2.12)$$

We choose \mathbf{B}_0 mostly along y , and attempt to compensate $B_{m,x,z}$ such that atoms experience a force that is mostly along the y axis. We remark that atoms with $m_F = \pm 1$ will experience an opposite force in this case, while an atom with $m_F = 0$ is not affected. The short time scales (\sim ms) in which we ramp both \mathbf{B}_q and \mathbf{B}_0 lead to eddy currents, and the compensation of $B_{m,x,y}$ cannot be done straightforwardly using calibrated values of the bias field. We instead use a *ad hoc* method in which we apply an additional constant bias field along z and optimize its value so that the trajectories of $m_F = \pm 1$ end up in the same plane as the one of the $m_F = 0$ atoms at the time of imaging.

In order to separate the Zeeman component faster than their expansion, we have to ramp \mathbf{B}_{SG} in a short time. However, the power supply used to control the current generating the magnetic field gradient limits the rise time to a few ms (the voltage being limited to 15 V) resulting in a force too small to separate the cloud enough so they do not overlap. We have developed two types of sequence for the experiments of this thesis. Both are based on gradient pulses, but each with different scopes. The first method is used for experiments with condensed clouds with little thermal fraction. We apply an attenuation sequence (see ref. [135]), where the trap is “opened” before time of flight in order to slow down the expansion while the gradient is simultaneously ramped up. This allows for slightly longer TOF and smaller separations as the atomic clouds are effectively smaller at the time the image is taken [119, 135] than in absence of attenuation sequence.

The attenuation method works well with condensates, but fails with thermal clouds, because the trap depth at the end of the attenuation sequence is too small to hold a cloud at the critical temperature or above. As a result, thermal atoms “spill out” of the trap during the opening (see refs. [135]). We have designed an alternative sequence for these warm clouds that we will detail in chapter 4 that allows to obtain larger separation in absence of an attenuation sequence by applying a short and intense pulse of current through the MOT coils.

2.2.2 Imaging noise reduction

Due to the high spatial coherence of the probe light, the spatial profile of the probe beam displays a contrasted intensity pattern on the CCD camera, see fig. 2.8. If this intensity pattern was static, absorption imaging would not be affected as it would rely on the differences between two similarly patterned images. However, any change of this pattern between the two images translates into noise on absorption pictures. In this section, we will analyze the properties of this pattern and its influence on imaging noise. We will then expose two image analysis methods that allows us to reduce the amount of imaging noise.

Speckle pattern

Speckle typically appears when coherent light (typically laser) is scattered off a rough surface (see refs. [173–175]). It results in an irregular, contrasted intensity pattern. At one point in the

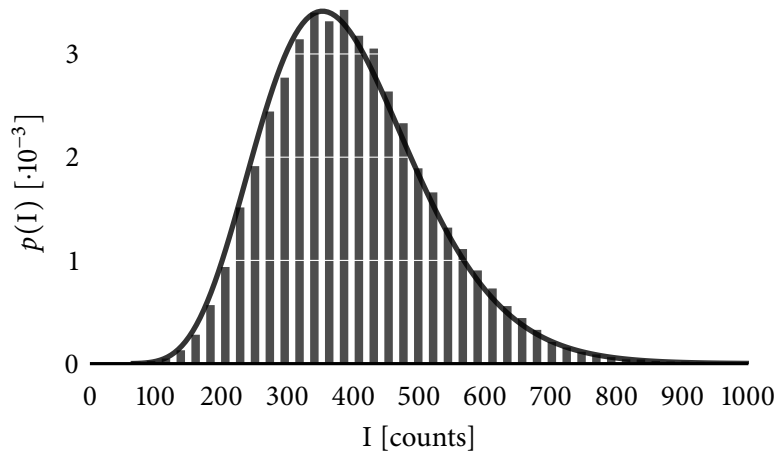


FIGURE 2.13: Distribution of intensity on the probe image (similar to the one shown in fig. 2.8 but with lower average intensity). With our camera settings, the detection efficiency is ~ 0.9 count/photon (in other words, a pixel count is equivalent to approximately 1.1 detected photons).

image plane, the intensity is the sum of contributions from a very large numbers of scatterers and beam paths. As such, the problem can be treated statistically, and the field amplitude is the sum of many random contributions, which leads, using the central limit theorem to an exponential probability distribution function for the density (see refs. [173–176]): $p(I) = (1/\langle I \rangle) \exp(-I/\langle I \rangle)$. At first glance, this is a problem for absorption imaging as the probability to find dark regions, in which we cannot measure absorption, is high. In reality, the integration over a sensor with finite spatial resolution (the CCD camera) somewhat mitigates the issue. The integration over the intensity pattern due to the finite pixel area modifies the detected probability distribution. In particular, the most probable intensity is not necessarily zero if the pixel size is large compared to the speckle typical length scale. The distribution can be expressed as a gamma probability distribution function (see ref. [173, 174, 176]):

$$p(I) = \frac{1}{\Gamma(\mu)} \left(\frac{\mu}{\langle I \rangle} \right)^\mu I^{\mu-1} \exp\left(-\frac{\mu I}{\langle I \rangle}\right), \quad (2.13)$$

where μ is a parameter that depends on the relative size of the speckle grain b and the pixel size a .

We analyzed a sample from a set of “empty” images, taken purposely without atoms. We show the distribution of pixel intensities from this image (see an example of this kind of image in image 2 from fig. 2.13), and find a good agreement Eq.(2.13) where we have found $\mu \sim 10$ by a fitting procedure. This is a good indication that the intensity variations on the spatial profile of the probe originate from speckle and not from straight interference fringes as the one that could result from interference between the main probe beam and a reflection from an imperfect coating. In the case the speckle is small $\mu \gg 1$, an analytic approximation ($4\pi\mu \sim (a/b)^2$ [176]) indicates the speckle size is around $b \sim 1.5 \mu\text{m}$, which is much smaller than the pixel size ($13 \mu\text{m}$). Overall, the main property of interest of the speckle pattern concerning absorption imaging is its large intensity variance $\sigma_I/I \sim 30\%$ (compared to $\sigma_I/I \sim 5\%$ expected from pure shot noise at $I \sim 500$ counts for instance). Despite this large intensity variance, there is no fully dark pixel, which allows us to measure atomic density everywhere in the sensor.

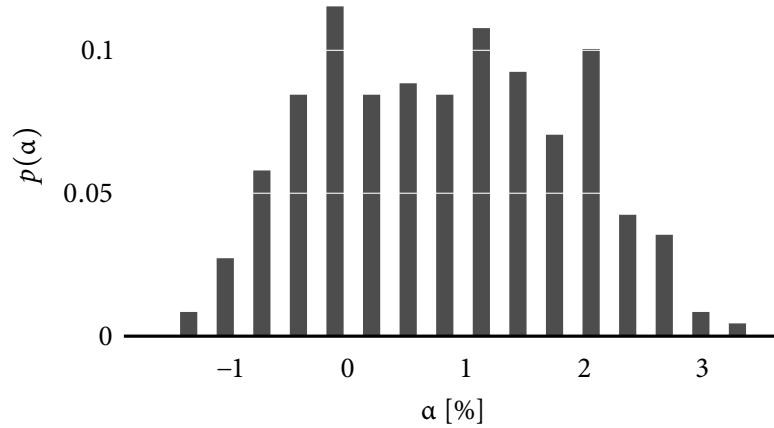


FIGURE 2.14: Distribution of the fluctuations of the differential of averaged intensity I_1 and I_2 (see Eq.(2.14))

Absorption imaging is based on the comparison of two images, one taken as a reference $I_{2,\kappa}(\mathbf{r})$, and one modified by atomic absorption $I_{1,\kappa}(\mathbf{r})$ (see ref. 2.2.1, and 2.1.4). The index κ indicates the experimental run at which the pair of image has been taken. The large intensity variance with \mathbf{r} for each κ does not in principle cause noise on absorption images, unlike the intensity or spatial pattern changes from $I_{1,\kappa}(\mathbf{r})$ to $I_{2,\kappa}(\mathbf{r})$. This can happen due to small displacements of the scattering surface or modifications of the optical path that can arise from vibrations or thermal currents for example. In this experiment absorption images are performed using a time delay between the 2 images as short as possible (see Sec. 2.2.1) in order to minimize these noise sources. In the following, we will quantify the noise due to changes of this intensity pattern and discuss means of reducing it.

Imaging noise from empty absorption pictures

We examine the properties of the speckle pattern by examining a set of ~ 250 “empty” absorption images taken purposely in absence of trapped atoms. First, we remark that there is a scaling of the spatially averaged intensity from the first to the second picture corresponding to a global scaling of the intensity pattern. We quantify this effect by the quantity α_κ :

$$\alpha_\kappa = \frac{\sum_{\mathbf{r}} I_{1,\kappa}}{\sum_{\mathbf{r}} I_{2,\kappa}} - 1, \quad (2.14)$$

We show the binned probability distribution from one set of image on fig. 2.14, and observe typically percent level differences between the two images. It is worth noting that these fluctuations cannot arise from shot noise because of the large number of pixels on which the intensity is averaged and probably arises from technical sources such as polarization fluctuations from the optical fiber output, fluctuations in the coupling efficiency, or on the imaging AOM diffraction efficiency.

Besides the global scaling factor, we examine the change on the properties of the speckle pattern by considering the correlations between two arbitrary images I_a and I_b . We note that for now a and b are generic indexes, and we shall consider in more detail which images to compare later on.

Correlations between images can be measured with the help of a cross correlation function given by $G_{CU}(a, b, \delta\mathbf{r}) = \sum_r I_a(\mathbf{r})I_b(\mathbf{r} - \delta\mathbf{r})$ (see ref. [177]). For two identical images $a = b$, this is the autocorrelation function. We note that it is in principle possible to extract speckle properties from autocorrelation functions, but this is hard to do if the pixel size is large compared to the speckle size (see ref [173]). This is why we will instead analyze cross correlation functions. In order to ease further interpretation, we normalize the value of the cross correlation function by the geometrical mean of the autocorrelation functions such that we obtain:

$$G_C(a, b, \delta\mathbf{r}) = \frac{\sum_r I_a(\mathbf{r})I_b(\mathbf{r} - \delta\mathbf{r})}{\sqrt{(\sum_r I_a(\mathbf{r})I_a(\mathbf{r} - \delta\mathbf{r}))(\sum_r I_b(\mathbf{r})I_b(\mathbf{r} - \delta\mathbf{r}))}}. \quad (2.15)$$

With this definition the autocorrelation function, *i.e.* $a = b$ in (2.15) shows a peak of height 1 near $\delta\mathbf{r} = 0$. Otherwise, the height of the central peak reflects the similarity between the two images. This function also permits to measure whether there is a global translation of the same pattern between two images. This would translate in a displacement of the peak position equal to the relative displacement. We analyzed the position of the maximum of G_C considering different pairs of pictures (nearest neighbor $I_{1,\kappa}$ and $I_{1,\kappa+1}$, each image $I_{1,\kappa}$ compared to their means $\langle I_{1,\kappa} \rangle$, first and second images $I_{1,\kappa}$ and $I_{2,\kappa}$) and could not detect a displacement. The maximum of the cross-correlation function was always found at $\delta\mathbf{r} = \mathbf{0}$ for all considered pairs, and we conclude that the intensity pattern is generally static.

As such, we analyze the similarity between pairs of pictures by considering the maximum value of the cross-correlation function $G_C(a, b, \mathbf{0})$. We plot it on figure 2.15 for three different pairs of images from the set of empty images that we have taken:

1. In a first case we take $I_a = I_{1,\kappa}$ and $I_b = I_{2,\kappa}$, where we recall $I_{1,\kappa}$ and $I_{2,\kappa}$ are respectively the first and second image taken for the image κ from the set.
2. In the second case, we take $I_a = I_{1,\kappa}$ and $I_b = I_{2,\text{brp},\kappa}$, where the second image is obtained with a specific noise reduction algorithm (see refs. [178–180]) that we shall describe in more details later on.
3. In the third case, we take $I_a = I_{1,\kappa}$ and $I_b = \langle I_{1,\kappa} \rangle$. This is a way to discuss the “stability” of the pattern over time.

We plot the cross-correlation function G_C in fig. 2.15 for each of these cases. We note that pairs of images taken with short intervals (as in case 1) are generally more similar than images taken in different experimental run (as in case 3). This tends to confirm that a short time between images helps to obtain a similar pattern between images. We also show on a that image processing (see fig. 2.18 for a more graphic demonstration) can be used to further improve the similarity between images. We will describe the procedures that we use in more details in the next paragraphs.

Modeling of the imaging noise

Given the empirical observations of the previous paragraph, we propose a general model of the intensity pattern:

$$I_{1,2}(\mathbf{r}) = f_{1,2}(\mathbf{r})I_0 + \delta I_{1,2}(\mathbf{r}). \quad (2.16)$$

where $I_0 = \langle \langle I \rangle_r \rangle$ is the doubly averaged intensity, $f_1(\mathbf{r})$ and $f_2(\mathbf{r})$ are random variables describing the variations of the speckle pattern and $\delta I_1(\mathbf{r})$ and $\delta I_2(\mathbf{r})$ describe the shot noise. We write \mathbf{r}

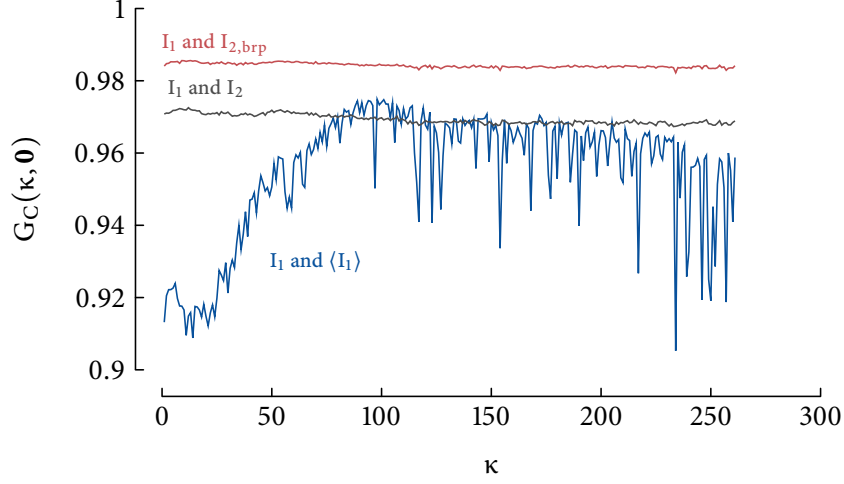


FIGURE 2.15: Normalized cross correlation function between different pairs of images. We remark that the correlation is mostly better between the two images taken with short interval I_1 and I_2 (case 1), than between each image and their mean (case 3). We see that the cross correlation between I_1 and $\langle I_1 \rangle$ shows many incidents that indicate localized changes of experimental conditions (air conditioning, doors...). A third curve displays the cross-correlation between I_1 and I_{brp} , that we obtained by applying a noise reduction algorithm (“best reference picture”). We observe that this algorithm allows us to generate images that are more “similar” to I_1 than I_2 .

the pixel index. Ensemble averages over a set of couples of images $\{(I_{1,\kappa}, I_{2,\kappa})\}$ are written $\langle \cdot \rangle$ and spatial averages over the pixels from the full image will be written $\langle \cdot \rangle_r$. If the intensities are uncorrelated from pixel to pixel, the two operations commute. In Eq. (2.16), the shot noise terms are uncorrelated from pixel to pixel. For each pixel \mathbf{r} it follows a normal distribution of width $(\eta \langle f_{1/2}(\mathbf{r}) \rangle I_0)^{1/2}$ where $\eta \sim 0.9$ counts/pixel is the detectivity of the CCD camera. The general statistical properties of the functions $f(\mathbf{r})$ are far less obvious and can vary with environmental conditions. Nevertheless, by construction of the intensity model, we have $\langle \langle f_{1,2} \rangle_r \rangle = 1$.

In the experiment, the quantity of interest is the column density n , obtained from Eq. (2.5). We derive a formula for sufficiently high imaging intensity such that the shot noise (SN) term is smaller than I_0 ($\delta I_{1,2}(\mathbf{r}) \ll I_0$), and obtain:

$$\begin{aligned} \Delta n(\mathbf{r}) = & \frac{1}{\sigma} \left(-\ln \left(\frac{f_1(\mathbf{r})}{f_2(\mathbf{r})} \right) + (f_2(\mathbf{r}) - f_1(\mathbf{r})) \frac{I_0}{I_{sat}} \right) \\ & + \frac{1}{\sigma} \left(\frac{\delta I_1}{f_1(\mathbf{r}) I_0} \left(1 + \frac{f_1(\mathbf{r}) I_0}{I_{sat}} \right) - \frac{\delta I_2}{f_2(\mathbf{r}) I_0} \left(1 + \frac{f_2(\mathbf{r}) I_0}{I_{sat}} \right) \right). \end{aligned} \quad (2.17)$$

We recall that σ is the absorption cross-section given in Eq. (2.4). Eq. (2.17) does not refer to a real atomic density, but describes how optical noise will affect atom number counting. The first line of formula (2.17) describes the effect of pattern changes, while the second line describes the effect of the shot noise.

Fluctuations of the probe intensity

In this paragraph, we will treat the case of a static speckle pattern with global intensity fluctuations. In this case, we can take $f_1(\mathbf{r}) = f(\mathbf{r})$ and $f_2(\mathbf{r}) = (1 + \alpha)f(\mathbf{r})$ where α is a random variable whose probability distribution is shown on fig. 2.14. For the sake of simplicity, we will consider α follows a Gaussian distribution of mean $\langle \alpha \rangle = 0.007$ and of standard deviation $\sigma_\alpha = 0.01$. Equation (2.17) can be simplified, by keeping only first order noise terms as :

$$\Delta n(\mathbf{r}) = \frac{\alpha}{\sigma} \left(1 + \frac{f(\mathbf{r})I_0}{I_{\text{sat}}} \right) + \frac{\delta I_1 - \delta I_2}{f(\mathbf{r})I_0} \left(1 + \frac{f(\mathbf{r})I_0}{I_{\text{sat}}} \right) \quad (2.18)$$

Instead of the atomic density of a single pixel, we will consider “atom numbers” obtained from integration over square boxes \mathcal{S} of size L pixels. We denote averages over this box as $\langle \cdot \rangle_{\mathcal{S}}$. The atom number extracted from this box is a random variable $N_L = \sum_{\mathcal{S}} \Delta n(\mathbf{r})$. Its mean can be computed for small intensity fluctuations $\alpha \ll 1$ from Eq. (2.18):

$$\langle N_L \rangle = \frac{\langle \alpha \rangle}{\sigma} \left\langle \sum \left(1 + \frac{f(\mathbf{r})I_0}{I_{\text{sat}}} \right) \right\rangle. \quad (2.19)$$

If \mathcal{S} is large enough compared to the characteristic size of the pattern, we will consider $\langle \langle f_{1,2} \rangle_{\mathcal{S}} \rangle = 1$. We have verified that this approximation holds for boxes down to $L=30$ pixels. In this case, above expression simplifies as:

$$\langle N_L \rangle \simeq L^2 \frac{\langle \alpha \rangle}{\sigma} \left(1 + \frac{I_0}{I_{\text{sat}}} \right). \quad (2.20)$$

For $\langle \alpha \rangle \sim 1\%$, this represent ~ 140 “atoms” already for $L=20$ pixels.

In order to compute the variance of N_L we have to consider separately the two terms from Eq. (2.18). The first one, proportional to α , is a random variable that is fully correlated from pixel to pixels, while the second term that represent the shot noise is uncorrelated from pixel to pixel, such that we can swap spatial and ensemble averages. As such, the variance of N_L is:

$$\text{Var}(N_L) = \underbrace{\frac{1}{\sigma^2} \text{Var}(\alpha) \left\langle \sum_{\mathcal{S}} 1 + f(\mathbf{r}) \frac{I_0}{I_{\text{sat}}} \right\rangle^2}_{\text{Global intensity fluctuations}} + \underbrace{\frac{1}{\sigma^2} \sum_{\mathcal{S}} \frac{2}{f(\mathbf{r})I_0} \left\langle 1 + f(\mathbf{r}) \frac{I_0}{I_{\text{sat}}} \right\rangle^2}_{\text{shot noise}}. \quad (2.21)$$

We can simplify further the above expression by considering large enough boxes:

$$\text{Var}(N_L) = \sigma^2 L^4 \text{Var}(\alpha) \left(1 + \frac{I_0}{I_{\text{sat}}} \right)^2 + \sigma^2 L^2 \frac{2}{I_0} \left(1 + \frac{I_0}{I_{\text{sat}}} \right)^2. \quad (2.22)$$

We remark in Eq. (2.21) that the noise due to global intensity fluctuations scale as $(\text{Var}(N))^{1/2} = \Delta N \propto N^2$ while the noise due to shot noise scales as $(\text{Var}(N))_{\text{SN}}^{1/2} = \Delta N_{\text{SN}} \propto N$. Hence we expect the noise due to global intensity fluctuations to be much larger than the one due to shot noise for large boxes.

We plot on fig. 2.16 the measured standard deviation of the atom number from the set of empty picture we have taken. We observe the noise measured from integration of absorption picture scales quadratically with the integration box size indicating that indeed correlated noise dominates. We will detail in the following paragraph a method to circumvent this noise source and reach lower noise levels, comparable to the one allowed by shot noise.

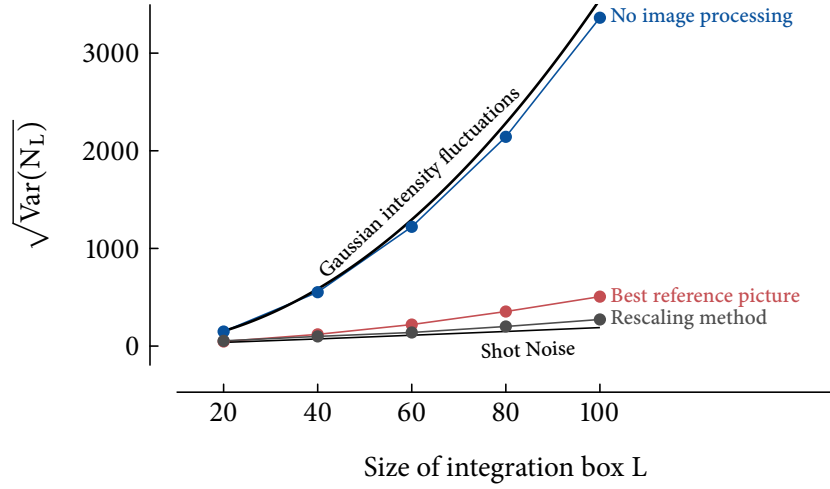


FIGURE 2.16: Atom number noise as a function of integration region size. We remark the quadratic scaling for the uncorrected atom number, indicating correlated noise due to technical intensity fluctuations. On the other hand, atom number from corrected images display a noise level close to shot noise, and the linear scaling indicates uncorrelated noise from pixel to pixel. It is worth noting these data were taken for $I_0/I_{\text{sat}} \sim 0.1$ such that the best reference picture algorithm is not in its best performance regime.

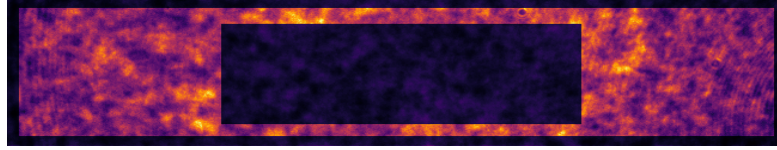


FIGURE 2.17: The lighter area represent a typical region used for the noise reduction algorithms. Darker area are ignored either because they may contain atom or because they are too close to the edges of the image and may contain undesirable features.

Noise reduction by image processing

We present in this paragraph two methods that we use to reduce imaging noise. The first is straightforward and consists in measuring the fluctuating parameter α from a zone without atoms such as the one represented in fig. 2.17. The second image is rescaled in order to cancel the correlated term from Eq. (2.21). We show the effect of this procedure on fig. 2.16, where we compare it to the shot noise obtained from numerical integration of Eq. (2.21). We demonstrate a very strong reduction of the atom number noise, almost down to the shot noise limit.

We have also implemented another method in order to deal with changes of the speckle pattern similar to the one from refs. [178–180]. This algorithm looks for a “best reference picture” $I_{2,\text{brp}}$ from a linear combination $\sum_{\kappa} c_{\kappa} I_{2,\kappa}$ of reference pictures $I_{2,\kappa}$ from all available experimental realizations inside a particular data set. This algorithm finds the most appropriate set of coefficients c_{κ} by minimization of the quantity $\sum_{\text{BG}} (I_1(\mathbf{r}) - \sum_{\kappa} c_{\kappa} I_{2,\kappa}(\mathbf{r}))^2$ where BG designate the zone without atoms from figure 2.17. In the case the background varies in a correlated way from this zone to the region of interest (as it is the case for fringes, or shifts of the speckle pattern), this methods provides minimization of the noise. We observe a large reduction of the noise on figs 2.16, 2.18 and

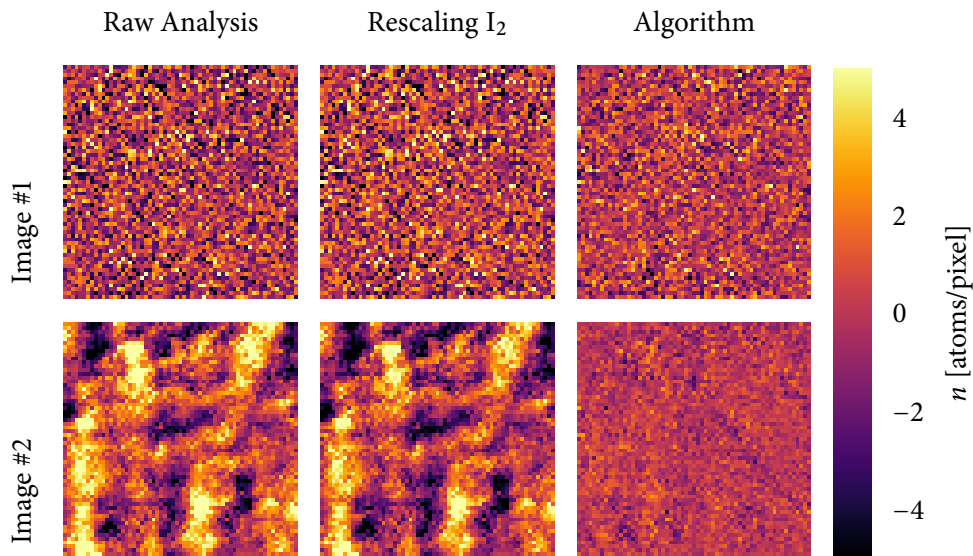


FIGURE 2.18: Example of the noise reduction methods for two different experimental realizations. The first example shows a situation where the best reference picture does not have a sizable effect due to the absence of fringe pattern in the “raw” image. One sees in the other situation the dramatic improvement of the image quality when the fringe reduction algorithm is applied.

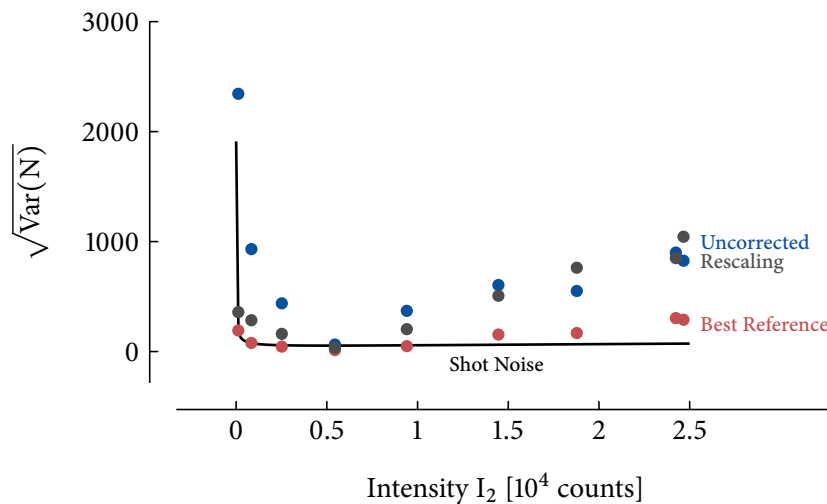


FIGURE 2.19: Imaging noise from boxes of size $L=60$ pixel. We remark the effect of noise reduction method for different intensity, and detect an optimum for the noise around $I \sim I_{\text{sat}}$.

2.19. While this method does not provide a particular advantage for low imaging intensities, when the noise is dominated by shot noise and technical probe fluctuations, it is however extremely efficient for higher imaging intensities. Figure 2.19 shows that the noise varies with intensity and displays a minimum for $I \sim I_{\text{sat}}$. This is predicted by eqs. (2.18) and (2.21), only taking into account shot noise. In general, shot noise dominates for $I \ll I_{\text{sat}}$, while the noise due to pattern changes becomes dominant at high imaging intensities. We observe that the algorithms described in this chapter each has their domain of applicability. The rescaling method works for low imaging intensity where the “log” term in Eq. (2.5) dominates, and fringe noise is negligible (the lower the pattern fluctuations the higher the “crossover” intensity). On the other hand, the best reference picture works better when the difference term in Eq. (2.5) dominates, because it corresponds to the quantity minimized by the algorithm.

If the goal is solely to count populations it is best to work with $I \sim I_{\text{sat}}$ and to use the “best reference picture” algorithm to obtain the minimum noise in population counting. Otherwise, if we rely on fitting to extract populations or temperatures, we will prefer to work at low intensities $I \ll I_{\text{sat}}$. The minimum noise on the population of each component has been measured to be ~ 60 atoms, measured for $I \sim I_{\text{sat}}$ in square boxes of 60 pixels.

2.2.3 Magnification

An important quantity to extract quantitative information from absorption images is the optical magnification of the imaging system. The atoms are imaged on the CCD camera through two afocal systems (see fig. 2.7). In order to avoid systematic errors in the determination of temperatures that could be due to imperfect alignment or poor knowledge of the exact focal lengths of the optical components, we chose to calibrate the magnification using known length scales at the atom position.

A first method to obtain the magnification consists in preparing a BEC, and letting it fall. The magnification is obtained from the gravity acceleration ($g = 9.81 \text{ m s}^{-2}$). We observe the displacement of a polarized sample after a Stern-Gerlach experiment from the horizontal imaging axis (see fig. 2.20). This allows to calibrate the horizontal magnification. We then observe a Stern-Gerlach trajectory on both the horizontal and vertical camera. Since they share one axis, we infer from the calibration of the horizontal imaging setup the calibration of the vertical one. The previous method is indirect, and subject to uncontrolled systematic errors when comparing the two imaging axis, for example from an unknown small angle between the two imaging systems. The recent installation of a retro-reflected lattice beam along the HDT axis, see fig. 2.4, allowed us to use a more direct method. We apply a pulsed lattice to a Bose-Einstein condensate. The cloud get diffracted by the standing-wave (see ref. [181]), and we obtain a momentum pattern composed of clouds that have absorbed $\pm \hbar \lambda_l$, where λ_l is the wavelength of the lattice laser. We reveal the Kapitza-Dirac diffraction by a time of flight, after which we can see several clouds corresponding to the diffraction orders, see fig.2.21. The spacing between the zeroth and first order is known from the laser wavelength λ_l :

$$d_{01} = \frac{\hbar}{m\lambda_l} t_{\text{tof}}. \quad (2.23)$$

We obtain a magnification of 7.75 ± 0.11 with the first method and 7.64 ± 0.07 with the second, which is close to the expected one 7.5 but not completely identical. This could be due to the two systems not being in an afocal configuration for instance.

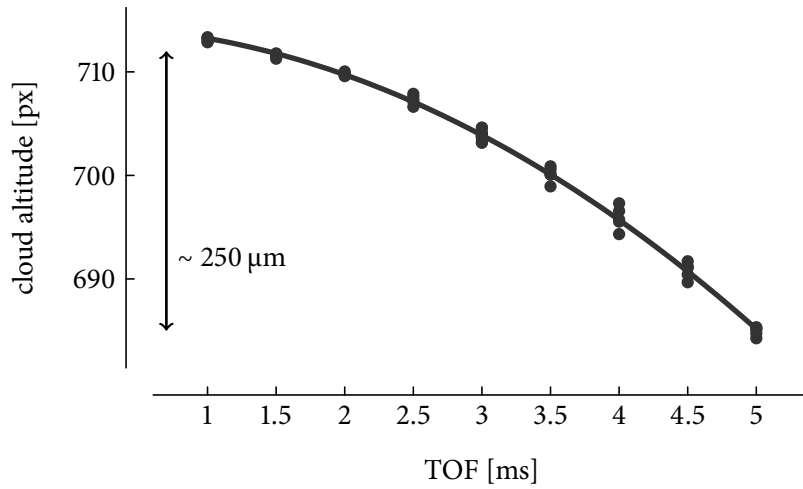


FIGURE 2.20: Center of a BEC in freefall obtained from a fit with a Thomas-Fermi function. The blue line is a parabolic fit of the fall. From this data, we obtain $M = 1.54 \pm 0.01$ (corresponding to $4.2 \mu\text{m}/\text{px}$) for the horizontal axis and $M = 7.75 \pm 0.11$ (corresponding to $1.68 \mu\text{m}/\text{px}$) for the vertical axis.

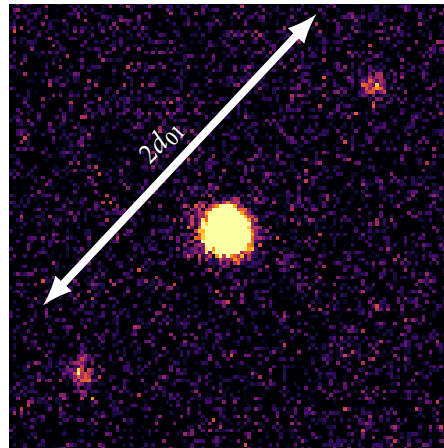


FIGURE 2.21: Kapitza-Dirac diffraction pattern imaged after time of flight. The central cloud is the undiffracted cloud (zeroth order), while the two smaller ones are the +1 and -1 order. The distance between this two clouds is given by twice Eq.(2.23). We extract a magnification $M = 7.64 \pm 0.07$ (corresponding to $1.7 \mu\text{m}/\text{px}$) from this measurement.

2.2.4 Determination of the scattering cross-sections

In our experiments we work with multilevel atoms instead of the idealized two-level atom introduced in Sec. 2.2.1. We see on ref. [182] for example a representation of sodium atom level structure and Clebsch-Gordan coefficients. The two level model is a relatively good representation of the system in the case the atom is in the $F = 2$, $m_F = 2$ state and illuminated by σ_+ polarized light. The transition addressed then is called the *cycling transition* and couples the states $F = 2$, $m_F = 2$ and $F' = 3$, $m_{F'} = 3$.

Given the geometry of the repumping beams, and the initial populations in the $F=1$ state, the repumping step cannot ensure all atoms are transferred to the $F = 2$, $m_F = 2$ state before imaging. Nevertheless, atoms in the $F=2$ manifold illuminated by σ_+ polarized light always end up in the $m_F = 2$ state regardless of their initial Zeeman state by a process referred as optical pumping. This process however requires a few absorption-spontaneous emission cycles. We use $t_{\text{im}} \sim 10 \mu\text{s}$ pulses, and in the worst case scenario, the saturation parameter is $s = (I/I_{\text{sat}})/(1 + I/I_{\text{sat}}) \sim 0.05$, and the number of scattered photon per atom is $Np = \Gamma s t_{\text{im}}/2 \simeq 15$ (see ref. [125] for numbers used). The rather small number of photons scattered during absorption imaging suggests that optical pumping will affect the scattering cross section. The Clebsch-Gordan coefficients of the transitions addressed during optical pumping being smaller than 1 (see ref. [182]), the atoms scatter effectively less photons during the process than when the cycling transition is addressed. Besides, optical pumping will be different for each Zeeman component. In order to account for these effects, we propose a heuristic generalization of the two level formula (2.3):

$$\frac{\partial I}{\partial z} = \sum_m \frac{\sigma_0}{\alpha_m} \frac{n_m}{1 + I/I_{\text{sat},m}} I, \quad (2.24)$$

In Eq. (2.24), we introduce three parameters α_m , $m = 0, \pm 1$ to parametrize three effective absorption cross-sections for each Zeeman component, and three saturation intensities $I_{\text{sat},m}$. As discussed above, atoms scatter less photons if optical pumping occurs rather than if only the cycling transition is addressed, hence $\alpha \geq 1$.

In the case the different Zeeman components do not overlap, as it in the case for condensed clouds (see Sec. 2.2.1), we define three separated analysis zones for each image containing each the contribution of one Zeeman component: I_1^m and I_2^m , $m = +1, 0, -1$. We consider the formula in each of these zones, such that we can extract independently the density of each component n_m from an absorption image (see ref. [160]):

$$n_m = \frac{\alpha_m}{\sigma_0} \left(-\log \left(\frac{I_1^m}{I_2^m} \right) + \frac{I_2^m - I_1^m}{I_{\text{sat},m}} \right). \quad (2.25)$$

The case where the components overlap is more complicated. For this thesis, it is only relevant in chapter 4 and we shall discuss this case in detail there.

We will show in the next paragraphs how to calibrate the scattering cross-sections and saturation intensities in order to extract quantitative information from absorption images. This procedure will contain three steps. First we will calibrate the saturation intensities by examining Bose-Einstein condensates with a varying probe intensity, then we will calibrate two of the relative cross-sections α_{+1}/α_0 and α_{-1}/α_0 by minimizing the observed change in signal while modifying the relative populations by a spin rotation. In a final step, we will calibrate the cross-section of a single component gas (here in the $m_F = 0$ component), by comparing the density profiles of a pure condensate to the one of Gross-Pitaevskii simulations.

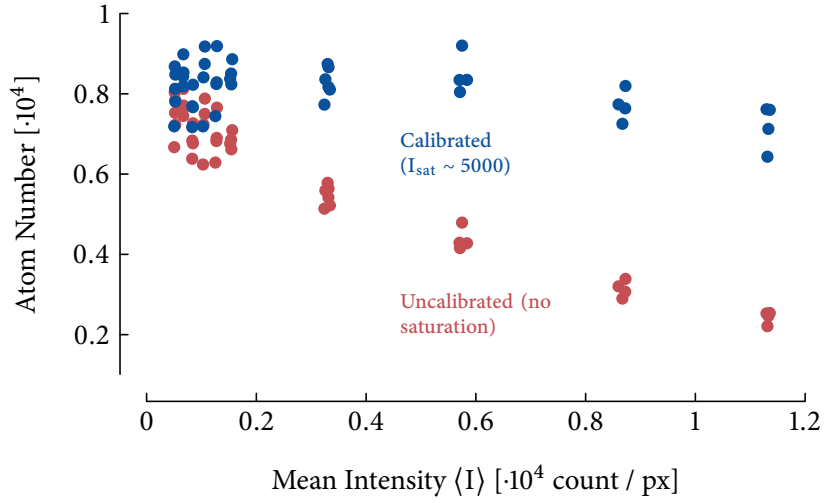


FIGURE 2.22: integrated atom number from $m_F = +1$ cloud (60x60 integration box) imaged with a varying probe intensity. The curve “uncalibrated” shows the prediction of Eq. (2.5) ignoring the term proportional to I_{sat} . This is equivalent to taking the limit $I_{\text{sat}} \rightarrow \infty$, hence no saturation. The corrected atom number uses $I_{\text{sat}} = 5057 \pm 171$, which was determined by a minimization of the slope of $N(I)$.

Saturation Intensity

In a first step, we determine the saturation intensity I_{sat} with the method developed by Reinaudi *et al.* in ref. [160]. The OD is calculated for a given I_{sat} considered as a parameter in equation (2.5). We vary the imaging intensity and calculate the atom number $N[I_{\text{sat}}](I)$ by integrating the density of a condensate. If formula (2.5) describes well the absorption cross-section, then $N[I_{\text{sat}}]$ should not depend on the intensity. We take the saturation intensity to be the value I_{sat} that minimizes the change in OD with I (the slope of $N[I_{\text{sat}}]$). We show the effect of the saturation intensity on fig.2.22 where we compare the case where there is no saturation taken into account ($I_{\text{sat}} \rightarrow \infty$) and the corrected case.

Differential cross-sections

We determine next the difference in scattering between Zeeman components, *e.g.* the two ratios α_0/α_{+1} and α_{-1}/α_{+1} . We vary the relative populations of the Zeeman components at fixed total atom number N by driving Rabi oscillations as explained in Sec. 2.4.1. We adjust the ratios α_0/α_{+1} and α_{-1}/α_{+1} and the Rabi Frequency Ω to fit the evolution of the relative populations ($n_{+1,0,-1}$) predicted by theory (see Sec. 2.4.1). This procedure is in principle equivalent to the one that consists in adjusting both ratio such that the apparent atom number does not vary during the rotation, and in practice provides very similar results. An example of a calibration procedure is shown on fig. 2.23.

Absolute cross-section

In a third step, we determine the last missing coefficient α_0 (we could also measure $\alpha_{\pm 1}$) by comparing Gross-Pitaevskii simulation of pure condensates to actual density profiles. We compare

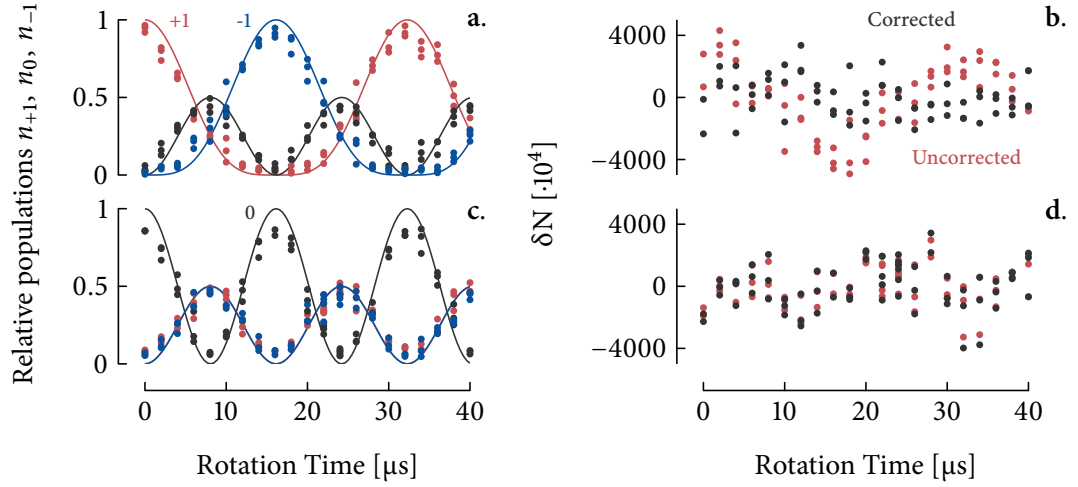


FIGURE 2.23: **a.** : Relative populations during a Rabi oscillation starting from a cloud polarized in $m_F = +1$ (after correction). **b.** difference between the atom number during the oscillation and its mean value. We see that there is a clear oscillation of the population at the Rabi frequency before correction. This is due to the relatively large value of $\alpha_{-1}/\alpha_{+1} = 1.39(5)$, and is eliminated with the calibrated values of the absorption cross-sections. **c.** Relative population in a Rabi oscillation starting from a cloud polarized in $m_F = 0$. **d.** We observe that in this case, the required correction is much smaller because the population of $m_F = \pm 1$ are roughly equal during the oscillation. As such, this is mostly the value of $\alpha_0/\alpha_{+1} = 0.88(4)$, closer to one, that matter. The values of the relative cross sections extracted from this calibration procedure are $\alpha_{+1}/\alpha_0 = 0.88(4)$ and $\alpha_{-1}/\alpha_0 = 1.22(5)$.

the Thomas-Fermi (TF) radii from simulations with the ones obtained from absorption images.

Simulated atomic densities after time of flight (TOF) are obtained from solving the 3D Gross-Pitaevskii equation (GPE) using measured trap frequencies and several atom numbers. We first propagate the GPE in imaginary time to obtain to the ground-state density in the trap. In a second step, we simulate the TOF by propagating the GPE in real time after switching off the trap.

To compare the results of the simulations with data, we fit the simulated column densities as well as the experimental images with the same Thomas-Fermi function $n(x, y) = n_0 \max(1 - (x/R_x)^2 - (y/R_y)^2)$. We then compare the data from the fit and the simulations using an *ad hoc* function for the condensate sizes, where N is the atom number, and a, b, c three adjustable parameters:

$$s = \sqrt{a^2 + b^2(\alpha_{+1}N_{2lv})^c} \quad (2.26)$$

The parameter a have been introduced to account for the quantum pressure of the BEC which is not negligible for small atom numbers (for $N=500$, $\xi \sim 2$) while b, c account for the mean field potential. For a condensate in the TF regime, $a = 0$, $b = 2\mu_{TF}/m\omega^2$, and $c = 2/5$. We obtain the parameters a, b, c from a fit of the simulated data¹, and we finally adjust the parameter α_0 so the ad-hoc function fits the data, see fig. 2.24. Finally, $\alpha \sim 2$, which confirms the two level absorption cross section is not adequate to model the scattering of the light during absorption imaging.

¹Typical values are $a \simeq 12 \mu\text{m}$, $b \simeq 511.5 \mu\text{m}$ and $c = 0.25$.

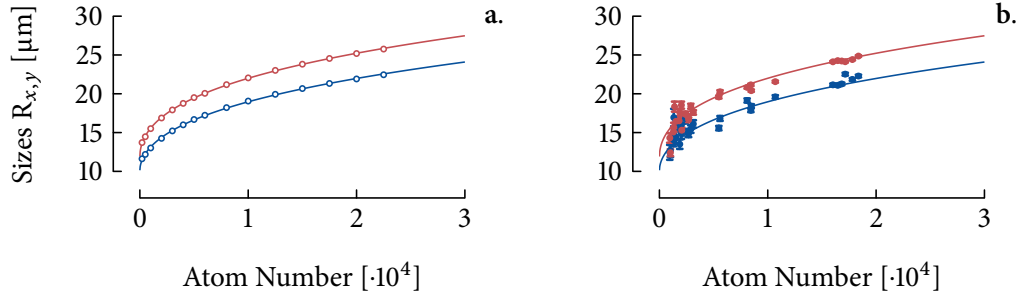


FIGURE 2.24: Determination of α_0 . **a.** and **b.** blue and red symbolize the TF radii in the two trapping directions X and Y. **a.** Empty symbols represent simulated data. The solid lines represent the *ad hoc* fitting functions (2.26) adjusted on the simulated profile sizes. Filled symbols in **b.** represent experimental data for a cloud polarized in $m_F = 0$. We obtain $\alpha_0 = 2.44(22)$ from this data.

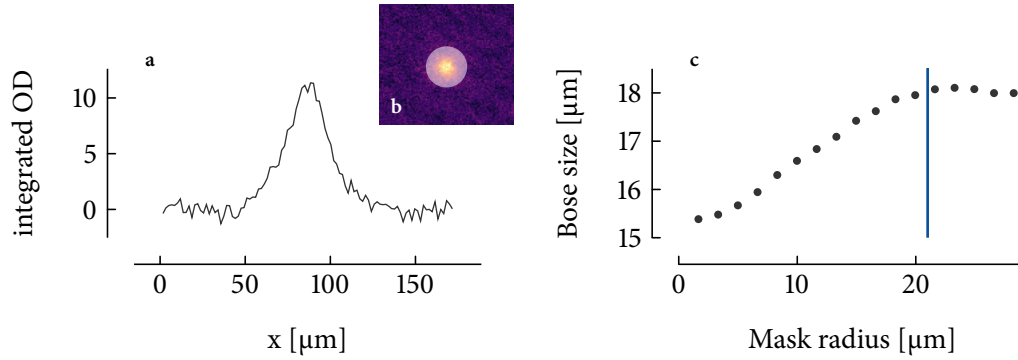


FIGURE 2.25: Representation of the plateau fitting procedure. **a.** single shot absorption image showing masks of radius $40 \mu\text{m}$. **b.** Integrated profile from the same absorption image, showing the overlapping thermal fractions. **c.** Fitted sizes as a function of mask size. The plateau is designated by blue vertical lines.

2.3 Image analysis

In this section we will discuss how to extract quantitative properties of our gases from absorption images that have been obtained as described in sec 2.2.1. We will focus on fitting methods of scalar gases for the sake of simplicity and detail eventual modification for multi component gas in chapter 4.

2.3.1 Fit of images

Thermodynamic quantities can be extracted by fitting appropriate theoretical density profiles to measured atomic densities. The correct modeling depends on the nature of the cloud studied, and can sometimes be non trivial. As it is usual in cold atoms experiments, we fit Bose functions to thermal clouds (see [133]), and inverted parabola – Thomas-Fermi profiles – to pure condensates. For partially condensed clouds, we use a sum of these two functions.

Thermal gases

We consider thermal clouds that are dilute enough so that we can neglect the effect of interactions. In this case, we can deduce the density from Bose statistics as described in Sec. 1.1.1. We use 6 free parameters for the Bose density profiles, 2 centers $c_{x,y}$, 2 “gaussian” sizes $s_{x,y}$, the fugacity $z = \exp(\beta\mu)$, one amplitude A :

$$n(x, y)_{\text{Bose}} = A \cdot g_2 \left(z \exp \left(-\frac{(x - c_x)^2}{s_x^2} - \frac{(y - c_y)^2}{s_y^2} \right) \right), \quad (2.27)$$

We remark that above T_c , A and z are not independent. Furthermore, in the case of high temperature gases, when $z \ll 1$, the function (2.27) is equivalent to a “Gaussian” fit function with amplitude Az . The temperature can be extracted from the size of the Bose distribution (see ref.[133]) through the relation:

$$k_B T = \frac{1}{2} m \left(\frac{\omega_i^2}{1 + \omega_i^2 t_{\text{tof}}^2} s_i^2 \right). \quad (2.28)$$

We also note that at low temperature, the time of flight density (TOF density) of the thermal gas is largely masked by the one of the condensate.

Bose-Einstein condensates

We have shown in chapter 1 that a Thomas-Fermi condensate expands such that the density distribution after time of flight remains an inverted parabola (see refs. [118]). The TF function has 5 free parameters, 2 centers, 2 Thomas-Fermi radii r_x, r_y and an amplitude (that is not independent from the two TF radii because they all depend on the chemical potential):

$$n(x, y)_{\text{Bose}} = A \cdot \max \left(1 - \frac{(x - c_x)^2}{r_x^2} - \frac{(y - c_y)^2}{r_y^2}, 0 \right). \quad (2.29)$$

While Thomas-Fermi profiles are relatively good models for pure condensates in our experiment, they are not always adapted for partially condensed clouds, in which the condensed atom number is not large enough so that the Thomas-Fermi approximation is well verified.

2.3.2 Extraction of temperatures

In the case of partially condensed clouds, the presence of a condensate modifies strongly the momentum distribution for low k . Because of this, it is quite difficult to extract temperatures from the sizes extracted from bimodal fits to the total density. The model of function (2.27) is heuristic as it does not account for interactions, which can substantially modify the expansion speed ($k_B T \ll \mu$ for clouds well below T_c). The high momentum tail – or “wings” – of the momentum distribution are expected to be less affected by interactions, and as such to behave as in Eq.(2.27).

We have developed a method that allows us to determine the size of the normal component without relying on a precise definition of the wings of the distribution that we call the *plateau* procedure. It consists in fitting time of flight distributions in the presence of a mask in the center. When we increase the size of the mask, at some point, we reach high enough momenta so that the distribution is well described by a Bose function (see fig. 2.25). If we observe the fitted thermal sizes as a function of mask size, we observe the condensate modifies the fitted sizes in the case the

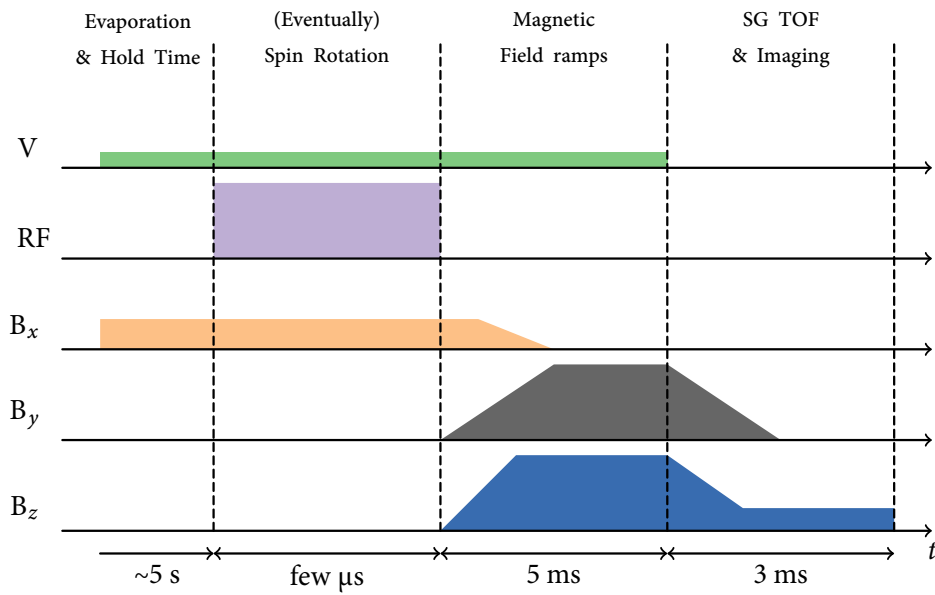


FIGURE 2.26: Experimental sequence for Rabi oscillations used to obtain spin rotations such as the one shown in fig.2.28

mask is small. Above a particular size, that depend on atom number and condensed fraction, the fitted sizes do not change – a plateau is reached – and represent the size of the thermal distribution. Increasing the mask size further and further, the fit eventually fails as the signal to noise ratio (SNR) becomes $\text{SNR} \sim 1$. We found that this methods give much more reliable temperatures than bimodal fitting (see chapter 4 for more details).

2.4 Manipulation of the atomic spin

The rich physics of spinor condensates originates from their internal degree of freedom. The preparation and manipulation of the spin state is a prerequisite of all the experimental data presented in this manuscript. It relies on several spin manipulation techniques first developed by the atomic physics community (see ref. [183, 184]) and further used in nuclear magnetic resonance (NMR, see refs.[185]). It also requires a quiet and well known magnetic environment as these techniques are typically very sensitive on magnetic fields.

2.4.1 Rabi oscillations

Spin rotations are widely used in modern physics, *e.g.* for hydrogen spins (NMR) and alkali atoms spins (atomic clocks). In this paragraph, we will discuss the simple case of couplings obtained with an oscillating magnetic field. We apply a radio frequency (RF) field of amplitude B_{RF} at an angular frequency ω_{RF} along x , orthogonally to the bias field axis z such that the coupling Hamiltonian is written:

$$\hat{H}_{\text{RF}} = \mu_B g_F B_{\text{RF}} \cos(\omega_{\text{RF}} t) \hat{F}_x \quad (2.30)$$

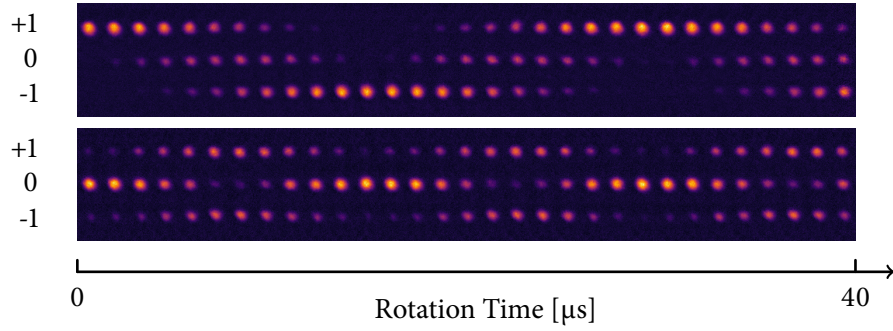


FIGURE 2.27: Graphical representation with stacked images of the Rabi oscillation presented in fig.2.28. On the top panel, we observe an oscillation starting from a state polarized in $m_F = +1$. In the bottom panel, we observe an oscillation starting from a state polarized in $m_F = 0$.

It is convenient to rewrite expression (2.30) in the referential precessing at ω_{RF} with the unitary transformation:

$$\hat{H}'_{\text{RF}} = \hat{U}_{\text{rot}}^\dagger \hat{H}_{\text{RF}} \hat{U}_{\text{rot}} + i\hbar \frac{d\hat{U}_{\text{rot}}^\dagger}{dt} \hat{U}_{\text{rot}}, \quad (2.31)$$

where the rotation is performed by a unitary operator:

$$\hat{U}_{\text{rot}} = \exp(-i\omega_{\text{RF}} t \hat{F}_z). \quad (2.32)$$

A prime will indicate rotated quantities, *e.g.* $F'_+ = F_+ e^{i\omega_{\text{RF}} t}$ and $F'_- = F_- e^{-i\omega_{\text{RF}} t}$. If we also include the Zeeman Hamiltonian to equation (2.31) and perform the rotating wave approximation (RWA), in which we only keep slowly varying terms (see refs. [186, 187]), we obtain a single particle spin Hamiltonian:

$$H' = H'_{\text{RF}} + H_Z = \begin{pmatrix} -\delta & 0 & 0 \\ 0 & -q & 0 \\ 0 & 0 & \delta \end{pmatrix} + \begin{pmatrix} 0 & \Omega/2 & 0 \\ \Omega/2 & 0 & \Omega/2 \\ 0 & \Omega/2 & 0 \end{pmatrix}, \quad (2.33)$$

where $\delta = \omega_{\text{RF}} - p$ is the detuning of the RF field from the resonance frequency and $\Omega = \mu_B B_{\text{RF}}$ is the Rabi frequency. When the excitation is resonant $\delta \simeq 0$, and when the quadratic Zeeman energy is $q = 0$, the evolution of the system is described by a rotation operator:

$$\hat{R}_x^\dagger = \exp(i\Omega t \hat{F}_x) \quad (2.34)$$

In the case of a non-zero detuning δ , the rotation operator is more complicated to write (see [119] for example). When the quadratic Zeeman energy is not zero on the other hand, the RF transitions $m_F = -1 \rightarrow m_F = 0$ and $m_F = 0 \rightarrow m_F = +1$ do not have the same resonant frequency and the evolution cannot be described by a rotation anymore (orientation to alignment transitions are observed for example see ref. [188, 189]).

In the experiment, the coupling field is produced by a coil located in the upper microscope flange, see fig. 2.2. We use RF frequencies from 10 kHz to a few MHz which corresponds to the bandwidth of our high power amplifier. In this frequency regime, the wavelength is very large compared to experiment dimensions¹. As such, the location of this coil is crucial to determine the

¹For a RF field of frequency $f = 1$ MHz, the wavelength is $\lambda_{\text{RF}} = 300$ m.

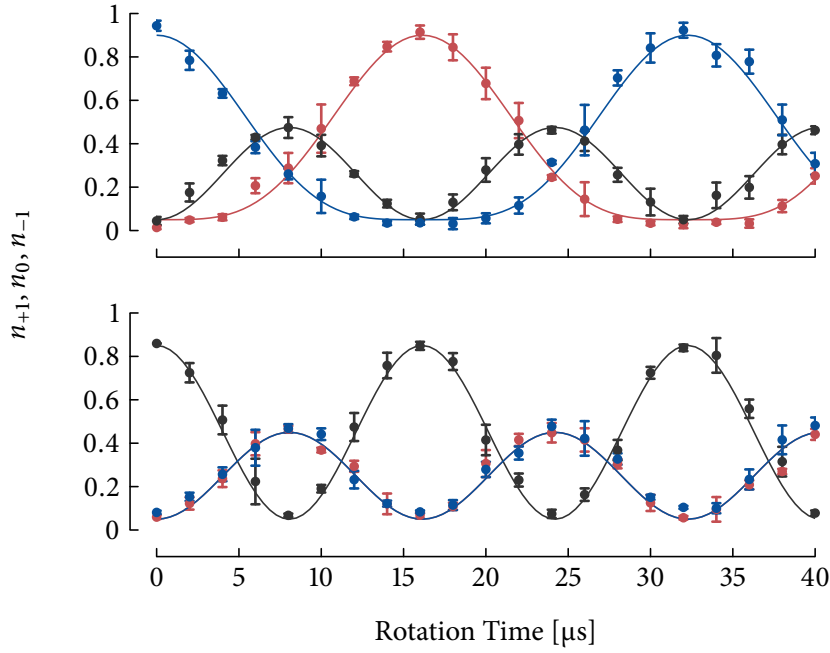


FIGURE 2.28: Rabi oscillations starting from quasi polarized states in **Upper** : $m_F = +1$, and **Lower** : $m_F = 0$. The solid lines are fit of the theory to the data.

coupling strength and we place it the closest possible to the atom, in the largest aperture available which is the upper microscope flange (see fig.2.2). Another limiting factor comes from the very poor impedance matching that we are able to obtain since the dimensions of the coil are much smaller than the wavelength. We can nevertheless obtain coupling strength up to $h \cdot 30$ kHz with this apparatus.

We will present two particular examples to illustrate 3-level Rabi oscillations in a simple manner. Both examples are illustrated with experimental data in fig. 2.28 and 2.27, obtained with the rotation sequence shown in fig. 2.26. The first example is the rotation of a state $\zeta_+ = (1, 0, 0)$, which translates in term of populations as :

$$|\zeta'_+|^2 = \begin{pmatrix} n'_{+1} \\ n'_0 \\ n'_{-1} \end{pmatrix} = \begin{pmatrix} \cos^4(\Omega t) \\ \sin^2(2\Omega t)/2 \\ \sin^4(\Omega t) \end{pmatrix}, \quad (2.35)$$

while the second one consists in the resonant rotation of a state $\zeta_0 = (0, 1, 0)$:

$$|\zeta'_0|^2 = \begin{pmatrix} n'_{+1} \\ n'_0 \\ n'_{-1} \end{pmatrix} = \begin{pmatrix} \sin^2(\Omega t)/2 \\ \cos^2(2\Omega t) \\ \sin^2(\Omega t)/2 \end{pmatrix}, \quad (2.36)$$

The experimental sequence used to obtain such rotations is shown on figure 2.26. Typically, it consists on a pulse of RF, followed by a fast rotation of the B-Field for imaging, which is necessary given the geometry of the setup. The RF coil produces a RF field along z (see fig. 2.2), such that the coupling is a function $\Omega \propto |\sin(\theta)|$, where θ is the azimuthal angle between the z axis and the bias field. As such, a good RF coupling requires a Bias field that is included on the xy plane. On the

other hand, with a vertically propagating probe laser, imaging requires a bias field along z , in order to address the σ_+ cycling transition. In the following paragraph, we will discuss the condition that we need to fulfill to rotate the magnetic field between these two steps without inducing transitions between Zeeman components.

2.4.2 Adiabaticity in magnetic field ramps

We discussed in the previous paragraph how time-varying magnetic fields can trigger transitions between Zeeman sublevels. While this is useful for spin manipulations, this can also be detrimental if the magnetic fields need to be modified without changing the Zeeman populations. In this section, we will derive a criterion for “adiabaticity” for magnetic field ramps such as the one required between a Rabi oscillation and imaging for instance.

In this context, adiabaticity means there is no transition between Zeeman levels. First, we recall the general time varying Zeeman Hamiltonian (see section 1.3.2) with the quantization axis z aligned with the magnetic field axis:

$$\hat{H}_z = A_{\text{hf}} \mathcal{P}_2 + p(t) \hat{F}_z + q(t) (1 - \hat{F}_z^2). \quad (2.37)$$

In this expression, the magnetic field axis rotates over time, and we need to express the actual Hamiltonian in a frame that rotates along with it. In this case, and without loss of generality, we take the y axis as the rotation axis (meaning that \mathbf{B} remains in the xz plane), $\theta(t)$ the rotation angle and express the effective Hamiltonian as:

$$\hat{H}_{\text{eff}} = \hat{H}_z - \hbar \dot{\theta}(t) \hat{F}_y. \quad (2.38)$$

We can determine the angle by the geometric arguments:

$$\theta = \tan^{-1} \left(\frac{B_x}{B_z} \right), \quad (2.39)$$

$$\dot{\theta} = \frac{\dot{B}_x B_z - \dot{B}_z B_x}{B_z^2 + B_x^2}. \quad (2.40)$$

There are two cases of interest in the experiment. Depending on the experimental step, we need either different axes in the magnetic fields (for example for Rabi oscillations, along x , and for imaging along z) or different magnitudes. In any case, the changes of magnetic field are done by linear ramps performed sequentially in the axes concerned. We take as an example a ramp in the axis x while the axis z is kept constant :

$$B_z = B_1, B_x = B_2 t / \tau \quad (2.41)$$

In this case, the change of magnetic field is adiabatic if the coupling is much smaller than the Larmor frequency p/\hbar :

$$\hbar \dot{\theta} \ll p, \text{ or equivalently, } \frac{\dot{B}_x}{B} \ll \frac{\mu_B B}{\hbar}. \quad (2.42)$$

This translates in a condition for the ramp described in Eq. (2.41) :

$$\tau \gg \frac{\hbar}{\mu_B} \frac{B_1 B_2}{[B_1^2 + (B_2 t / \tau)^2]^{3/2}}, \forall t. \quad (2.43)$$

In the case condition (2.43) is not fulfilled, atoms experience “Majorana transitions” (see ref. [133]). They are well known in quadrupolar magnetic traps, in which they happen near the magnetic field zero at the trap center, and result in atoms being lost. In optical traps in which all Zeeman states are trapped, it translates into large fluctuations of the magnetization. This happens mostly when the atom experience a very low magnetic field value. This is referred at as a “zero-crossing”.

The ramp speed is limited by the power supply and is measured around ~ 1 G/ms for the bias coils. Conditions (2.42), (2.43) corresponds to a minimal bias field $B_1 \gg 38$ mG to fulfill the criterion from Eq. (2.43) for a linear ramp. For smoother ramps, *e.g.* quadratic, a similar calculation shows that the criterion is much relaxed.

2.4.3 Diagnostics of the magnetic environment

A precise knowledge of the magnetic field is necessary for experiments with spinor Bose gases, for instance in order to avoid zero crossings during the experimental sequence. This section will expose the methods we developed to characterize the magnetic field environment of the atoms. The atoms are placed in the center of a metallic chamber that forms a Faraday cage. While it does not shield static magnetic field, time-dependent magnetic fields may or may not be attenuated depending on their frequency and the thickness of the vacuum chamber. We find for titanium¹ that the frequency corresponding to a 5 cm skin depth is ~ 150 Hz. Given the chamber does not have uniform thickness, the determination of the cut-off frequency for magnetic shielding may be more difficult. However, this estimation suggests that only relatively low frequency noise will be of interest ($f \leq 100$ Hz). We will then divide the discussion in term of stray quasistatic magnetic fields and of low frequency noise.

Stray magnetic field determination with Zeeman spectroscopy

There are many sources of stray magnetic fields, the most obvious being the earth magnetic field, but it also includes smaller contributions from magnetic objects surrounding the experiment. Even though the experiment was constructed mostly with amagnetic materials such as titanium, aluminum or copper, there are a large number of small steel components close to the chamber². The residual stray field at the position of the atoms is referred as \mathbf{B}_s . We observe that the stray magnetic fields do not vary much over time (mG level or below), such that they can be compensated by fixed – “compensation” – currents in the bias coils $I_{c,i}$, $i = x, y, z$.

The measurement of these compensation currents used to obtain a zero of magnetic fields at the atom position must be done in situ with the atoms as the environment may be different away from the vacuum chamber due to gradients. We measure the local magnitude of the magnetic field by Zeeman spectroscopy. We apply a long, low intensity, RF pulse and detect the rotation of the spin as a function of RF frequency. The sequence is similar to the one of Rabi oscillations, see fig. 2.26. We prepare a Bose-Einstein condensate polarized in $m_F = +1$, such that the resonance is detected by depolarization of the sample. The pulse length is typically 5 ms while the spectrum width is a few kHz. We apply a small transverse field \mathbf{B}_\perp , and detect the resonance frequency ω_{res} as a function of the current in the compensation coil, see fig. 2.29. The curve is fitted by the function:

$$|B|(I_i) = 2\hbar\omega_{\text{res}}/\mu_B = \sqrt{B_{s,\perp}^2 + B_\perp^2 + (B_{s,i} + \alpha_i I_i)}, \quad (2.44)$$

¹We take for AL6V4 titanium, the resistivity $\rho = 1.7 \times 10^{-6}$ Ω m and the relative magnetic permeability $\mu_r = 1$

²Kovar alloy in UV LED glass/cover seals, springs of mirror mounts, steel construction elements in the room, *etc.*

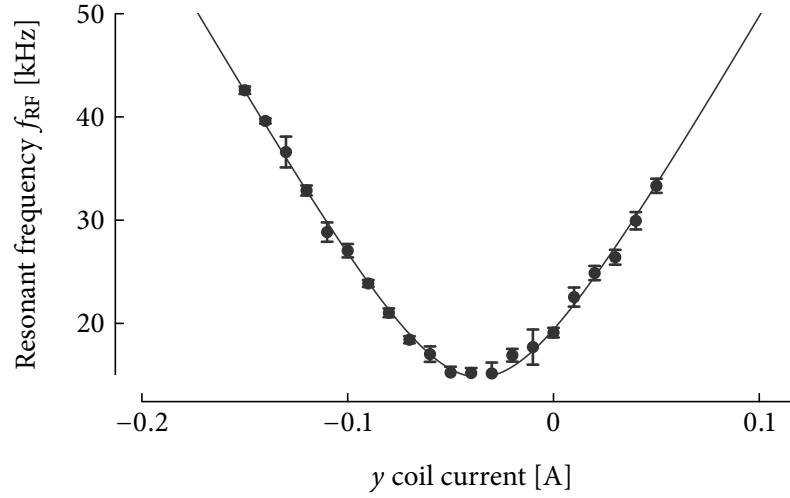


FIGURE 2.29: Resonant frequency, representing the magnetic field magnitude, as the current in varied in the y pair of bias coils. A small field (~ 20 mG) is applied along x to ensure finite resonance frequency at the compensation value. The compensation current is the one that minimizes the resonance frequency.

where α_i is the magnetic field-current characteristics of the pair of coil $i = x, y, z$. The minimum of this function is obtained for $I_{c,i} = B_{s,i}/\alpha_i$ and indicates the compensation current. This procedure assumes each pair of coil creates a field purely along x, y or z , *i.e.* that there is no “cross-talk” between the different axis. We find $B_s = (311(2), 87(2), 352(2))$ mG and $\alpha_x = 0.287(1)$ G/V, $\alpha_y = 0.248(1)$ G/V, $\alpha_z = 0.358(1)$ G/V. The error bars are determined from the fit to Eq. (2.44).

Magnetic field noise

There are many sources of time dependent-magnetic noise. A rather large contribution comes from unshielded mains transformers from various devices located around the experiment. We recognize this noise easily from its characteristic 50 Hz frequency, and this is the dominant source of noise for our experiments. We have also remarked a lower frequency contribution of amplitude ~ 10 mG along axis z . Its amplitude is much reduced between 2:00AM and 5:00AM, which makes us suspect it is related to the subway line, that runs a few hundred meters away from the experiment under boulevard Saint-Germain. Thankfully, we mostly work with bias fields along x or y for spin manipulation sequences, such that this noise does not affect very much the amplitude of the magnetic field¹ and does not perturb these experiments.

One of the main issues associated with magnetic noise is observed during Rabi oscillations where it causes a variation in the detuning. The 50Hz noise translates into a detuning from one experimental cycle to another that reads:

$$\delta = p - \omega_{RF} - \delta\omega_M \cos(2\pi f_M t + \phi), \quad (2.45)$$

where $\delta\omega_M$ is related to the noise amplitude, $f_M = 50$ Hz and ϕ is random from one shot to the next. Given the typical Rabi frequencies we achieve are much higher than 50 Hz, this random

¹A perturbation δB_z affects the modulus of the field $|\mathbf{B}|$ as $\delta|\mathbf{B}| \simeq \delta B_z/2B_\perp$. $B_\perp \gg \delta B_z$ is the modulus of the field applied along x/y . This effect is negligible when $B_\perp > 50$ mG.

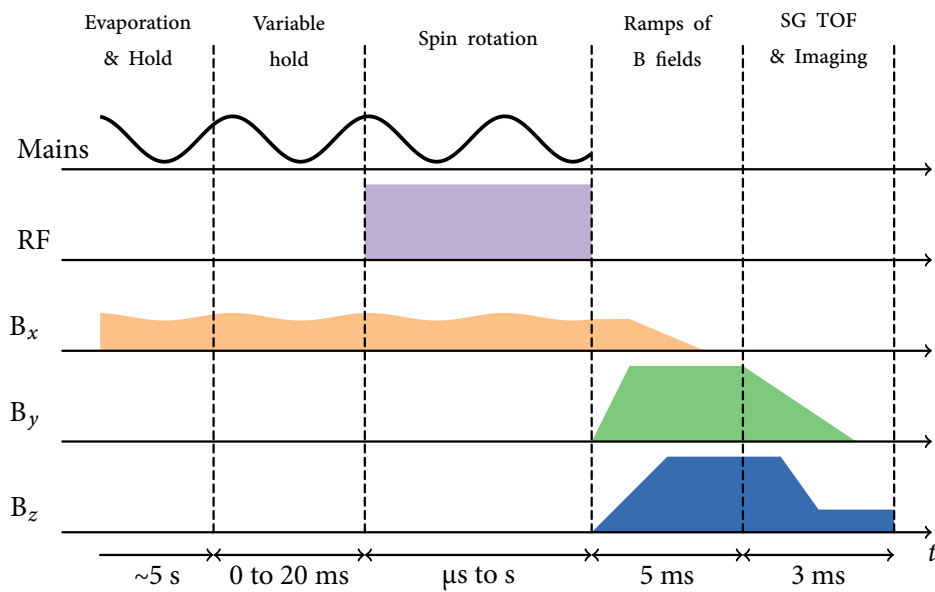


FIGURE 2.30: Typical spin manipulation sequence in which we show the variable hold inserted before the rotation. The phase of the mains is not well defined before the spin rotation sequence, and varies from one experimental run to another. The one during phase rotation is set by the mains trigger.

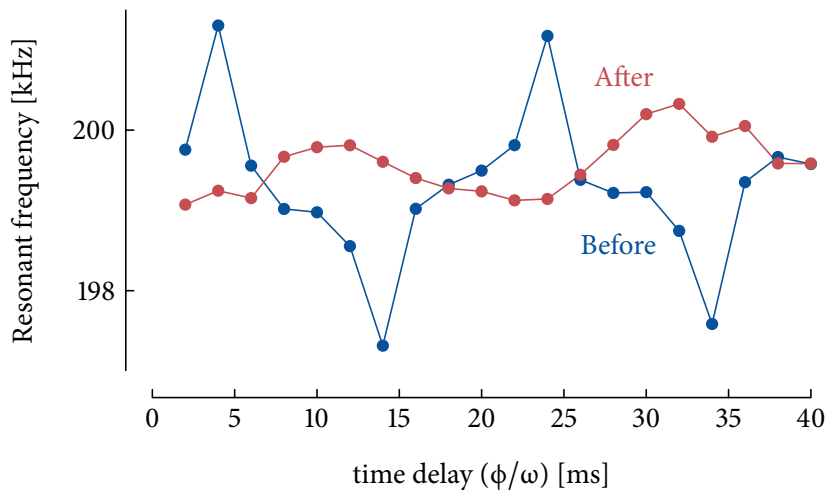


FIGURE 2.31: Magnetic noise measured by time dependent RF spectroscopy. We show two experimental realizations with different positioning of surrounding power supplies. We observe that moving noisy power supplies away reduces the amount of mains noise from 6 mG to 1.5 mG peak to peak in this example.

detuning translates in irreproducibility of the population measurements after a Rabi oscillation. We deal with this issue by triggering the experiment on the mains frequency. We extract a low voltage signal synchronous to the mains with a transformer, and use a Schmitt trigger that provides a rising edge for a given value of the phase ϕ . We insert a small variable hold time step in the sequence. During this step, the DAC “waits” for a rising edge from the Schmitt trigger. As such, the spin rotation starts from a given value of ϕ , fixed from shot to shot. This procedure does not remove the 50 Hz magnetic field noise, however it allows us to perform repeatable spin rotations in time scales much shorter than the mains period.

We measured the magnetic noise by RF spectroscopy using the synchronization of the experiment to the mains. We changed the phase ϕ at which a spectroscopy sequence is performed by adding a time delay before we perform the spectroscopy, and used short pulses time (100 μ s) to resolve the change of resonance frequency with time. We note the resolution of the measurement is reduced by Fourier broadening. We have observed this way a magnetic noise of 5 mG peak to peak (p-p), that we were able to reduce to 1.5 mG p-p by adjusting the position of noisy power supplies as shown in fig 2.31.

2.4.4 Preparation of the magnetization

As exposed in chapter 1, the magnetization is a conserved quantity in our system. In the crossed dipole trap, optical pumping processes during the loading sequence lead to a cloud of magnetization $m_z \sim 0.7$. We adjust this quantity by applying a preparation sequence to the thermal gas, in the CDT, well above the critical temperature. We can choose between two types of sequence depending whether we need higher or lower magnetization (see refs. [54, 119, 135, 136]). The combination of these procedures allows us to control the magnetization of our samples m_z from 0 to 1 continuously.

Depolarization

In order to reduce the magnetization we apply a RF coupling sequence similar to the one of section 2.4.1. We apply this sequence on a thermal gas, in the CDT before evaporation starts, such that the temperature is much above the critical one for Bose-Einstein condensation. We also apply a small magnetic gradient such that there is inhomogeneous broadening, and ensure the addressing of the whole cloud by sweeping the RF frequency.

The combination of spin precession in an inhomogeneous magnetic field and of spin diffusion due to atomic collisions destroys off diagonal coherences created by the RF pulse. The process “randomizes” the populations, and we end up for sufficiently long interaction times with a balanced mixture of the three Zeeman components. The degree of polarization is controlled by the RF power as seen in fig. 2.32 (or equivalently by the pulse length) from the “natural” magnetization $m \sim 0.7$ to a roughly balanced mixture of the three Zeeman components.

Spin distillation

In order to obtain more polarized samples, we use a method called spin distillation. It consist in applying a spin dependent force with a magnetic gradient (see Sec. 2.2.1) during evaporation. The magnetic gradient is created by the MOT coils and a large bias field set the direction of the magnetic force (see Sec. 2.2.1). The magnetic force acts on the $m_F = \pm 1$ ($m_F = 0$ is not affected) and has opposite direction for each component.

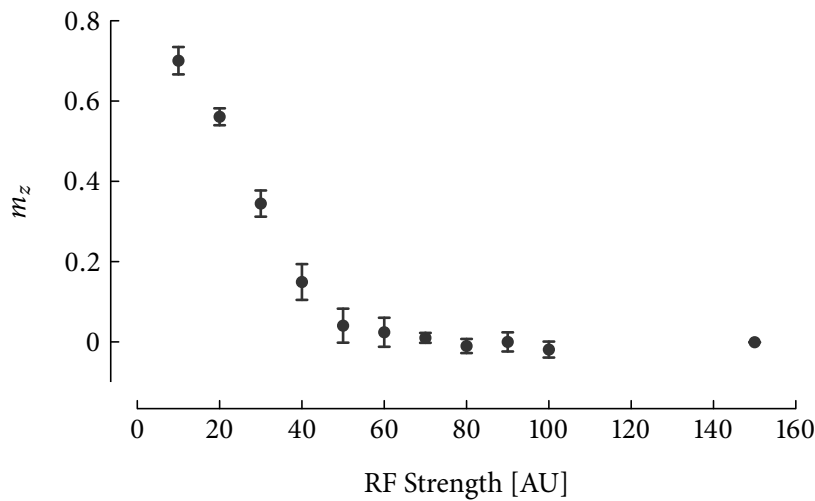


FIGURE 2.32: Effect of the depolarization sequence on the magnetization. We observe that we can tune continuously the magnetization between $m_z = 0$ and $m_z = 0.7$, the pulse length is set to 800 ms and there is a typical resulting noise of 5% RMS on m_z .

The applied force modifies the potential depth seen by the $m_F = \pm 1$ state while $m_F = 0$ is not affected (see chap. 1). We set the bias field along z such that the magnetic force effectively modifies the strength of gravity for species $m_F = \pm 1$. With our geometry, if the coil current is positive, the magnetic force cancels gravity for $m_F = +1$, and strengthens it for $m_F = -1$ that get eliminated preferentially during evaporation (see fig. 2.33). If the coil current is negative, the roles of $m_F = \pm 1$ are reversed. When the bias field is applied in a plane transverse to gravity, the evaporation of both $m_F = \pm 1$ is enhanced, and the cloud produced will be more “polarized” in $m_F = 0$. The effect is further enhanced as the BEC forms.

This technique allows us to produce polarized clouds with magnetization $m_z \sim 1$. The value of the magnetization can be adjusted between $m_z = 0.7$ to $m_z = 1$ by controlling the gradient strength. It is worth noting that the preparation noise for a fully polarized cloud $m_z = 1$ with this technique is on the order of 1% RMS, which is much lower than the one obtained with the depolarization technique (at best 5 % RMS).

2.4.5 Adiabatic rapid passage

Adiabatic rapid passage is a technique well known in the NMR community. It is used to flip spins in the presence of inhomogeneous broadening (see ref. [190]). It consists in applying a RF field at a fixed frequency and varying the magnetic field slowly across the resonance. If this procedure is performed both slow enough compared to the RF transition rate – “adiabatic” – but fast enough compared to the relaxations processes – “rapid” – it leads to an inversion of the spin population regardless on the precise details of the initial and final magnetic fields.

The eigenenergies of the dressed states (see ref. [186]) can be found from diagonalization of the Hamiltonian (2.33). The eigenenergies are shown in fig. 2.35 and are the roots of the equation:

$$e^3 + qe^2 + (\delta^2 + \Omega_0^2/2)e - q\delta^2 = 0 \quad (2.46)$$

We verify that, in the limits of zero coupling or large detunings ($\delta \gg \Omega_0$) we recover the unper-

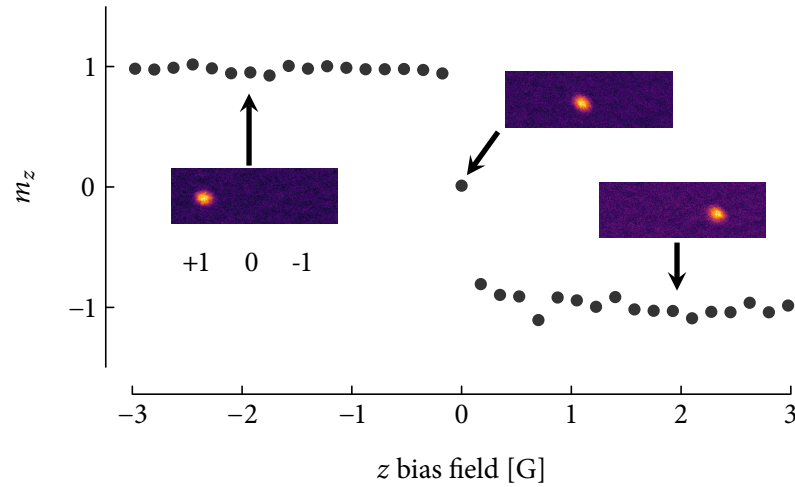


FIGURE 2.33: Effect of a spin distillation sequence on the magnetization of the sample. We observe that depending on the bias field direction, the magnetization of the cloud is either $m_z = +1$ or $m_z = -1$. The higher dispersion observed on the positive side of the z Bias field ($m_z = -1$) originates from a much lower atom number, which results in the presence of a constant imaging noise, in higher dispersion in renormalized quantities such as magnetization. This is due to the positive natural polarization at the beginning of the cooling sequence. Due to an additional bias in x , we can also obtain a state polarized in $m_F = 0$ by setting the z bias field to 0 (“transverse distillation”).

turbed eigenenergies $e = -q, \pm\delta$. The associated eigenvectors are the unperturbed Zeeman states. In the presence of coupling however, the eigenvectors are modified as shown in fig. 2.35. Starting from the $m_F = +1$ state and large detuning, one can “follow adiabatically” one eigenstate in the presence of coupling by varying the detuning δ from $\delta < 0$ to $\delta > 0$, ending up in a different Zeeman state projection.

In this experiment, we keep Ω constant and vary the detuning by a ramp of magnetic field, while applying a RF field (see ref. [191]). The ramp is slow compared to the coupling, such that the state is changed adiabatically. Following the lowest energy branch, starting from a cloud polarized in $m_F = +1$, we can obtain a mixture of $m_F = \pm 1, 0$ or a cloud polarized in $m_F = -1$, see fig. 2.35.

2.5 Conclusion

In this chapter, we have presented the main experimental techniques and diagnostics that we have developed for the experiments that will be shown in chapters 3 and 4.

In section 1, we have presented the main experimental techniques used to cool and trap our sodium Bose gases and obtain Bose-Einstein condensates. We have also shown how to characterize the trapping potential, which will be particularly important for comparing our data with theory in chapter 4.

In section 2, we have presented the detection techniques for Bose gases observed in this experiment. We have discussed how to obtain absorption images, and characterized their level of noise. We have presented the calibrations methods for the magnification and the calibration cross-section. The methods presented in this chapter will be applied directly in chapter 3 for measuring atom numbers (chapter 3, section 2 for example).

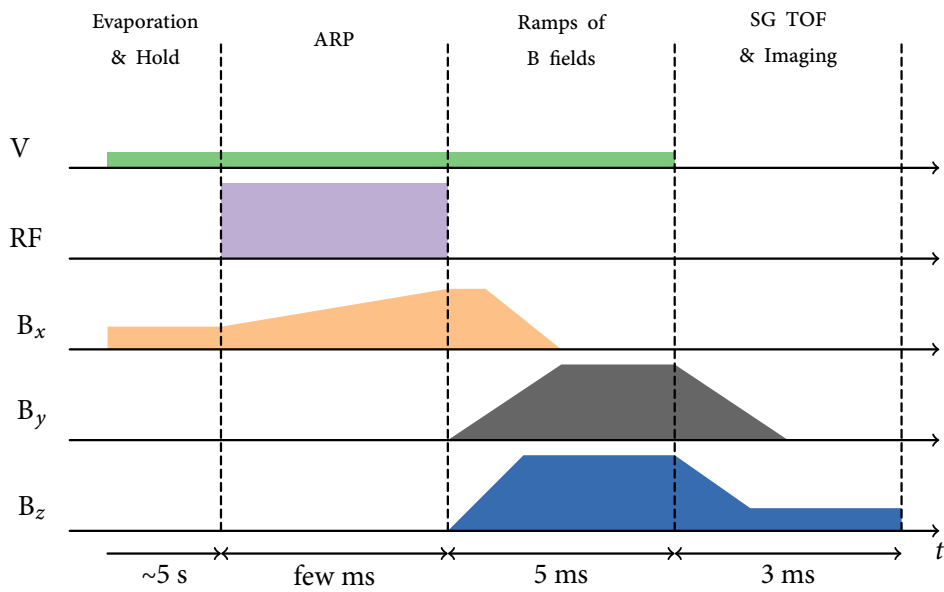


FIGURE 2.34: Typical experimental sequence used for adiabatic rapid passage (ARP). We produce a BEC within a given bias field (along x in this case). We turn on a relatively large RF field, and ramp the magnetic field until the desired value of the detuning is reached. Then we turn off the RF coupling.

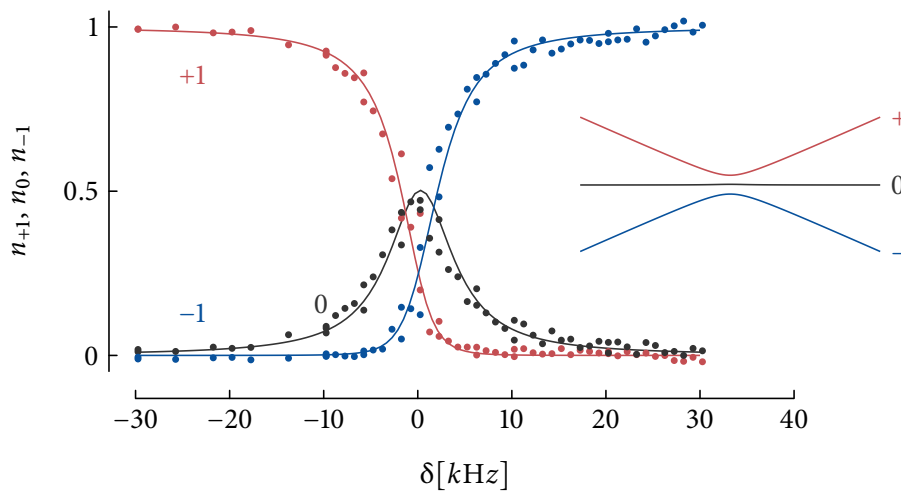


FIGURE 2.35: Population of a cloud, starting from $m_F = +1$, after an adiabatic rapid passage sequence. The x axis give the final value of the ARP magnetic field ramp expressed in term of RF transition detuning. The inset sketches the eigenenergies as a function of detuning.

In section 3, we have described fitting methods to extract thermodynamic quantities from absorption images of scalar Bose gases (methods for multicomponent gases will be detailed in chapter 4). We have also introduced the “plateau” procedure, in which absorption images are fitted with a mask. This method is used to extract temperatures from partially condensed clouds using a big enough mask such that the condensate density is hidden, but not the thermal wings. This method will be used to determine temperatures in chapter 3 (section 3 for example).

In section 4, we have introduced several spin manipulation techniques used in experiments from this manuscript and discussed the diagnostics of the magnetic environment. We introduced Rabi oscillations, that will be used to measure spin nematic order in chapter 3. We discussed the adiabaticity of our magnetic field ramps, and ensured that within the parameters we use, the rate of Majorana transitions is negligible. In the section 2.4.3, we discussed the influence of the ambient magnetic field and shown that we can consider separately two contributions. A stray bias field, that we measure by RF spectroscopy and compensate with static currents in the bias coils and a time varying magnetic noise, mostly at mains frequency, that we circumvent by synchronizing sensitive experiments to the mains. Then we discussed the preparation of the magnetization, which we use to vary the magnetization of our cloud continuously from $m_z = 0$ to $m_z = 1$. Finally we presented adiabatic rapid passage.

“Comme s’il eût voulu montrer qu’il était capable de se redresser. Mais non. Il n’avait rien à prouver. Il avait depuis peu quelque chose en lui qui l’incitait, lui ordonnait de se redresser. Non, ni incitation ni ordre. Cela le dépassait.”

L’INCIDENT

Christian Gailly

3

Magnetic phases of antiferromagnetic spinor BEC at low temperatures

The following chapter is written using material from refs. [192, 193]. Section 3.1.1 is essentially from [192] while other sections have been rewritten. Section 3 uses material from [119].

MAGNETISM IN SPIN 1/2 SYSTEMS is often illustrated by the 1D Ising model, that describes spin ordering on a spin chain with nearest neighbor exchange interactions and an eventual magnetic field. The sign of the exchange interaction J , positive for antiferromagnetic interactions, negative for ferromagnetic interactions, determines the arrangement of the spins at low temperature $k_B T \ll J$. When interactions are ferromagnetic, the total spin of the chain is maximal, and spins are aligned. In presence of a magnetic field, the symmetry between the two orientations is broken. In the case of antiferromagnetic interactions, the spin orientations are staggered, and the spin forms a Néel antiferromagnet.

With a spin $S > 1/2$, the behavior at low temperature is much richer, and many types of magnetic phases, depending on the spin are predicted (see ref. [194]). In the case of spin 1 particles, it is possible to obtain spin nematic phases (see refs [65–67, 69, 70, 80]) in which the average spin is zero $\langle \hat{s} \rangle = 0$ but nevertheless have a preferential axis in space (thus breaking spin rotational symmetry) without having a preferential direction along this axis (thereby preserving time reversal symmetry). Spin nematic phases in spin 1 Bose-Einstein condensates are named after the nematic phase of liquid crystals¹ (see ref. [68]). These systems are composed of rod-shaped molecules that roughly align along their axis (in other words the system exhibit long range directional order) even in liquid phases where there is no long range positional order. In spin nematic phases, the magnetic order translates into spin fluctuations that are preferentially in a plane perpendicular to a certain direction, that is called, in analogy with the liquid crystal terminology, the *director*.

Spin nematic order have been discussed for spin 1 Bose-Einstein condensates with antiferromagnetic interactions in many references (see refs. [47, 51, 54–56, 65, 77–79, 81, 83, 84]). In this chapter, we will demonstrate a new way to reveal and characterize spin nematic order in spin 1 Bose-Einstein condensates, and more generally explore the low temperature magnetic properties of the system.

We have discussed general theoretical considerations about spinor BEC in the first chapter, and how to realize them experimentally in the second chapter. We now focus on very cold clouds, with

¹That themselves takes their name from the greek νήμα, which means thread.

a condensed fraction typically above $f_c \sim 0.9$. In this chapter, we consider that $T = 0$ and that the actual temperature of the system is sufficiently low such that it only affects measurement and theory as small corrections. In this regime, the physics of the system is dominated by a competition between spin changing interactions and the quadratic Zeeman energy. This competition sets the magnetic properties of the system, such that we observe two magnetic phases of which we study the properties in this chapter.

In section 1, we give the theoretical background to understand these phases, then recall the measurement of their equilibrium populations that have been performed during the thesis of David Jacob (see [54, 135]) as it help the understanding of the following sections. We then discuss the measurement of the transverse spin length that we performed by observing the fluctuations of the magnetization after a spin rotation. We show how to relate this measurement to a phase locking mechanism of the relative phase between Zeeman components. We also discuss the influence of a small but finite temperature. Finally, I turn to the measurement of spin fluctuations at low magnetic field and low magnetization. In this regime, the degeneracy between many mean field states leads to large population fluctuations. We measured these populations and extracted a spin temperature that corresponds to the thermal energy of the spin degree of freedom. We then discuss the equilibration of the spin degree of freedom with the kinetic ones.

3.1 Mean-Field description of spinor Bose-Einstein condensates

In this section, we continue the theoretical description of a spin-1 Bose-Einstein condensate that we started in chap. 1, Sec. 1.3. We recall that we work within the single mode approximation (SMA, see ref. [127]) in which the three Zeeman components of the spinor BEC have the same spatial wavefunction (see Sec. 1.3). This approximation is justified by the rather large trap frequencies $\bar{\omega} \sim 2\pi \cdot 500$ Hz compared to typical spin-exchange interaction energies $U_s \sim 40$ Hz. In this section, we will describe several properties of the spin wavefunction, that is solution of the Hamiltonian from Eq. (1.95) that we recall here:

$$\hat{H}_s = \frac{U_s}{2N} \hat{S}^2 - q\hat{N}_0. \quad (3.1)$$

In the following, we will rather work with quantities normalized by the total atom number N , that we will write in lower case. The normalized populations are $n_{0,\pm 1} = N_{0,\pm 1}/N$ and normalized spin operators are $\hat{s} = \hat{S}/N$, $\hat{s}_{x,y,z} = \hat{S}_{x,y,z}/N$. The spin wavefunction can be parametrized as:

$$|\zeta\rangle = \begin{pmatrix} \sqrt{n_{+1}} \exp(i\phi_{+1}) \\ \sqrt{n_0} \exp(i\phi_0) \\ \sqrt{n_{-1}} \exp(i\phi_{-1}) \end{pmatrix}. \quad (3.2)$$

We will discuss in the following the properties of this wavefunction via either its populations or its phases $\phi_{0,\pm 1}$. In the following, we will encounter some specific states that we need to name for the sake of clarity. In the case a single Zeeman component is populated, we will speak of a *polarized* state. The family of states where the spin length is maximal $|\langle \mathbf{s} \rangle| = 1$ is called *oriented*. For example, a state polarized in $m_F = \pm 1$ along z is oriented. Finally, a family of state with $|\langle \mathbf{s} \rangle| = 0$ is called *spin-nematic* state (it is also denoted in the literature as *polar* or *aligned*). For example, the state polarized in $m_F = 0$ is a spin-nematic state. Other states in the oriented or spin-nematic families are deduced from above examples by spin rotations.

3.1.1 Alignment and spin-nematic order

So far, spin 1 states have been described in the standard basis, defined from angular momentum theory as the ones formed from the eigenvectors of \hat{s}_z , $\{|+1\rangle, |0\rangle, |-1\rangle\}$, with eigenvalues $+1, 0, -1$ respectively. It is however sometimes convenient to use instead a Cartesian basis defined as (see refs. [75, 79, 195, 196]):

$$|x\rangle = (|-1\rangle - |+1\rangle)/\sqrt{2}, \quad (3.3)$$

$$|y\rangle = i(|-1\rangle + |+1\rangle)/\sqrt{2}, \quad (3.4)$$

$$|z\rangle = |0\rangle. \quad (3.5)$$

These states obey the relation $S_a |b\rangle = i\epsilon_{abc} |c\rangle$ (ϵ_{abc} is the fully antisymmetric tensor). The states $|a\rangle$ are the eigenvectors of \hat{S}_a with eigenvalue 0. We note with this definition the analogy with the polarization of a photon. In this case the eigenstate in the normal basis correspond to circular polarizations “ σ_{\pm} ” for $|\pm 1\rangle$ and to linear polarization “ π ” for $|0\rangle$. This Cartesian representation can be related to the geometrical representation¹ of a pure spin 1 states in the normal basis by:

$$|\Psi\rangle = \begin{pmatrix} (\Psi_{-1} - \Psi_{+1})/\sqrt{2} \\ i(\Psi_{-1} + \Psi_{+1})/\sqrt{2} \\ \Psi_0 \end{pmatrix} = (\mathbf{u} + i\mathbf{v}) \cdot |\mathbf{r}\rangle, \quad (3.6)$$

where \mathbf{u} and \mathbf{v} are two real vectors that fulfill the normalization relation $\mathbf{u}^2 + \mathbf{v}^2 = 1$. In contrast with the spin 1/2 representation, where each state is represented by one unique vector, there can be multiple definitions of vectors \mathbf{u} and \mathbf{v} because of the gauge freedom in the total phase of the wavefunction². As such, the transformation $\Psi \rightarrow \Psi \exp(i\phi)$ modifies the vectors such that $\mathbf{u} \rightarrow \cos(\phi)\mathbf{u} - \sin(\phi)\mathbf{v}$ and $\mathbf{v} \rightarrow \cos(\phi)\mathbf{v} + \sin(\phi)\mathbf{u}$. We can always choose a value of the phase ϕ such that $\mathbf{u} \cdot \mathbf{v} = 0$ and $\|\mathbf{u}\| \geq \|\mathbf{v}\|$.

The spin corresponding to such state is characterized by a mean spin vector:

$$\langle \hat{\mathbf{s}} \rangle = \frac{\langle \hat{\mathbf{S}} \rangle}{N} = 2\mathbf{u} \times \mathbf{v}, \quad (3.7)$$

and by a spin quadrupole tensor $Q_{ij} = \langle \hat{s}_i \hat{s}_j + \hat{s}_j \hat{s}_i \rangle / 2$ that characterizes the spin fluctuations. There are several possible definitions (see ref. [79]) and we choose:

$$Q_{ij} = \delta_{ij} - (u_i u_j + v_i v_j). \quad (3.8)$$

In order to understand better the link between the tensor \overline{Q} and magnetic ordering in the system, we study two limiting cases.

The first one is the case of an oriented state, where all the atoms are in the Zeeman component $m_F = +1$. In this case, the average spin $\|\langle \hat{\mathbf{s}} \rangle\| = 1$ is maximal, and we deduce from eqs. (3.3), (3.4): $\mathbf{u} = -\mathbf{x}/\sqrt{2}$, $\mathbf{v} = \mathbf{y}/\sqrt{2}$. The tensor \overline{Q} is then diagonal in the x, y, z basis with eigenvalues $1/2, 1/2, 1$.

¹This definition is set in analogy with pure spin 1/2 states that are characterized by two angle θ , and ϕ usually represented on a Bloch sphere. These angles define a unit vector \mathbf{u} such that $|\Psi\rangle = \mathbf{u} \cdot |\mathbf{r}\rangle$, where $|x\rangle = (1, 1)/\sqrt{2}$, $|y\rangle = (1, i)/\sqrt{2}$ and $|z\rangle = (1, 0)$

²There are 6 degrees of freedom allowed by \mathbf{u} and \mathbf{v} . If we remove two due to the normalization of $|\Psi\rangle$ and the global phase, we end up with only four relevant parameters.

The second limiting case consists in a spin-nematic where the spin wavefunction is the eigenvector of $\hat{\mathbf{s}} \cdot \mathbf{n}$ with eigenvalue 0, where \mathbf{n} is a real vector of length 1 that denotes a particular direction in space. In this case, we obtain $|\Psi\rangle = \mathbf{u} \cdot |\mathbf{r}\rangle$ with $\mathbf{u} = \mathbf{n}$. In such state, the average spin vanishes $\|\langle \hat{\mathbf{s}} \rangle\| = 0$ and the spin quadrupole tensor takes the simple form $\overline{\overline{\mathcal{Q}}} = \mathcal{I}d - \mathbf{u} \otimes \mathbf{u}^*$ with eigenvalues $\{0, 0, 1\}$. In such state, the vector \mathbf{u} is the director and the tensor $\overline{\overline{\mathcal{Q}}}$ (or equivalently \mathbf{u}) plays the role of the order parameter of the spin nematic phase.

In the following we propose to quantify the proximity to either of these two limiting cases by defining a quantity called the alignment \mathcal{A} . We can define it by remarking the eigenaxis of $\overline{\overline{\mathcal{Q}}}$ are along \mathbf{u}, \mathbf{v} and $\langle \hat{\mathbf{s}} \rangle$ and by rewriting $\overline{\overline{\mathcal{Q}}}$ as:

$$\overline{\overline{\mathcal{Q}}} = \frac{1 - \mathcal{A}}{2} \underline{\mathbf{u}} \otimes \underline{\mathbf{u}}^* + \frac{1 + \mathcal{A}}{2} \underline{\mathbf{v}} \otimes \underline{\mathbf{v}}^* + \underline{\mathbf{w}} \otimes \underline{\mathbf{w}}^*, \quad (3.9)$$

where we have defined $\underline{\mathbf{u}} = \mathbf{u}/\|\mathbf{u}\|$, $\underline{\mathbf{v}} = \mathbf{v}/\|\mathbf{v}\|$ and $\underline{\mathbf{w}} = \langle \hat{\mathbf{s}} \rangle / \|\langle \hat{\mathbf{s}} \rangle\|$ from normalization of the three eigenaxis from normalization of \mathbf{u}, \mathbf{v} and $\langle \hat{\mathbf{s}} \rangle$. The alignment¹ \mathcal{A} quantifies the proximity to the limiting cases mentioned above. An alignment $\mathcal{A} = 1$ denotes a fully aligned state while $\mathcal{A} = 0$ denotes a fully oriented state.

It is convenient to express the alignment as a function of the spin length which is a more easily measurable observable in the system (as we shall discuss in Sec. 3.2), hence we have:

$$\mathcal{A}^2 + \langle \hat{\mathbf{s}} \rangle^2 = 1, \quad (3.10)$$

So far, we have discussed the state of a single spin. In the following paragraph, we will turn to a N particle system that we will discuss within a mean field approximation. We will discuss how to relate the equilibrium state of the system at zero temperature to the alignment, and more generally how the ground state wavefunction parameters vary with experimental conditions.

3.1.2 Mean-Field description at T=0

We consider the wavefunction from Eq. (3.2) that we rewrite in a more convenient way using n_0, m_z and the relative phases $\alpha = \phi_{+1} - \phi_{-1}$ and $\Theta = \phi_{+1} + \phi_{-1} - 2\phi_0$:

$$|\zeta^N\rangle = e^{i\phi_0} \begin{pmatrix} \sqrt{\frac{1-n_0+m_z}{2}} \exp\left(i\frac{\Theta+\alpha}{2}\right) \\ \sqrt{n_0} \\ \sqrt{\frac{1-n_0-m_z}{2}} \exp\left(i\frac{\Theta-\alpha}{2}\right) \end{pmatrix}. \quad (3.11)$$

The state $|\zeta^N\rangle$ corresponds to a mean spin vector $\langle \hat{\mathbf{s}} \rangle = m_z \mathbf{e}_z + \langle \mathbf{s}_\perp \rangle$, where $m_z = n_{+1} - n_{-1}$ is the magnetization and $\langle \mathbf{s}_\perp \rangle = \langle s_x \rangle \mathbf{e}_x + \langle s_y \rangle \mathbf{e}_y$ is the transverse spin. We recall that the magnetization is a conserved quantity due to the rotational symmetry of Van der Waals interactions (see Sec. 1.3). The phase α determines the azimuthal angle of $\langle \mathbf{s}_\perp \rangle$ while Θ sets its length:

$$\langle \hat{\mathbf{s}}_\perp \rangle^2 = 2n_0 \left(1 - n_0 + \sqrt{(1 - n_0)^2 - m_z^2} \cos(\Theta) \right). \quad (3.12)$$

The ground state of Hamiltonian (3.1) is determined by minimization of the spin energy per particle E_s/N (which is the expectation value of hamiltonian (3.1) for the mean field state in Eq. (3.11)):

$$\frac{E_s}{N} = \langle \zeta^N | \hat{H}_s | \zeta^N \rangle = \frac{U_s}{2} m_z^2 + \frac{U_s}{2} \langle \hat{\mathbf{s}}_\perp \rangle^2 - qn_0, \quad (3.13)$$

¹We note a similar quantity was defined in ref. [79].

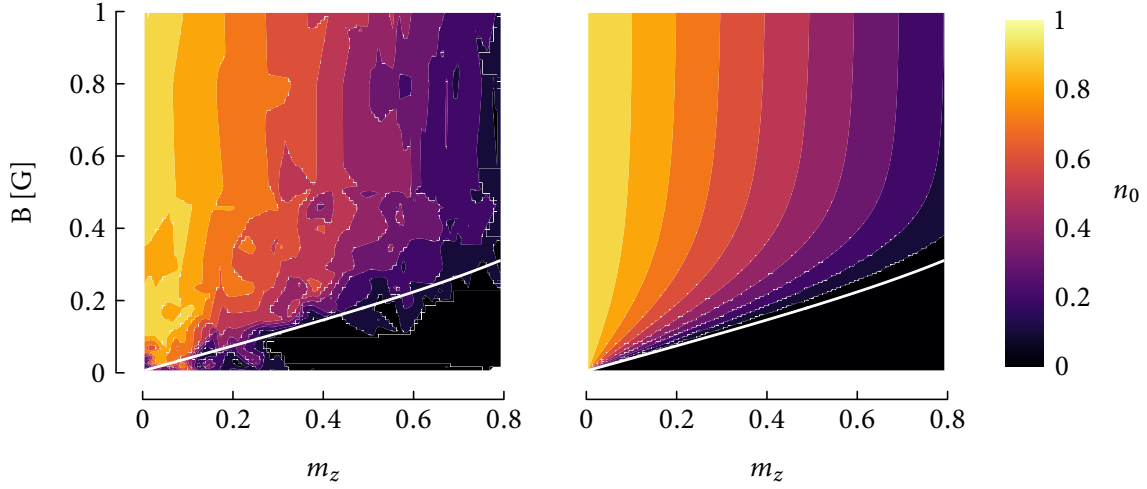


FIGURE 3.1: Magnetic phase diagram of an antiferromagnetic spinor Bose-Einstein at $T=0$. **Left:** Experimental measurement from ref [54], **Right:** Theoretically predicted population in the $m_F = 0$ component by minimizing Eq. (3.13), with $\Theta = \pi$. We plot on both curve the critical line predicted by Eq. (3.16) with $U_s = h \cdot 65.6$ Hz.

where there are two control parameters: the magnetization m_z (that enter in Eq. (3.12)) and the quadratic Zeeman energy q (that is set by the magnetic field with $q \simeq B^2 \cdot 277$ Hz/G²). The population of the $m_F = 0$ component (hence the transverse spin length, hence the alignment) is set by an energy competition between the spin exchange energy $U_s \langle \hat{s}_\perp \rangle^2 / 2$ and the quadratic Zeeman energy q . We remark that the phase α does not appear in expression (3.12) expressing the residual rotational symmetry along the z axis when a magnetic field is present. Besides, for $U_s > 0$ the value of the phase Θ that minimizes the spin energy E_s is $\Theta = \pi$ because of the term proportional to $\cos(\Theta)$ that is set to -1 to minimize the spin length in Eq. (3.12), which in turn minimizes the spin exchange energy for a fixed value of m_z . In the next section, we will discuss the value of the equilibrium populations.

3.1.3 $T=0$ magnetic phase diagram (D. Jacob *et al.* PRA 86 061601)

In this section, we will recall the results of refs [47, 54] concerning the equilibrium phase diagram at zero temperature of a spin 1 antiferromagnetic Bose gas (see also refs.[55, 56]). The spin Hamiltonian (3.13) illustrates the competition between the quadratic Zeeman energy and the spin-exchange energy, such that the equilibrium populations of the gas at a given value of the magnetization m_z will depend on the magnetic field strength. We distinguish two regimes depending on which energy scale dominates. If the magnetic field is small, the quadratic Zeeman energy can be neglected in Eq. (3.13), and the population of the $m_F = 0$ spin vanishes in order to minimize the transverse spin. This forms a first phase where only $m_F = \pm 1$ are present, that can be called antiferromagnetic in analogy with Néel phases in spin 1/2 antiferromagnets (see ref. [64, 84]). As the magnetic field increases, the population in the $m_F = 0$ grows to accommodate for the larger quadratic Zeeman energy, such that in the limit of very high magnetic field, the population of the $m_F = -1$ vanishes. This phase can be called broken-axisymmetry phase (see refs.[84, 197]), in reference to the fact the total spin tilts against the magnetic field axis. The direction of $\langle \hat{s}_\perp \rangle$ is given

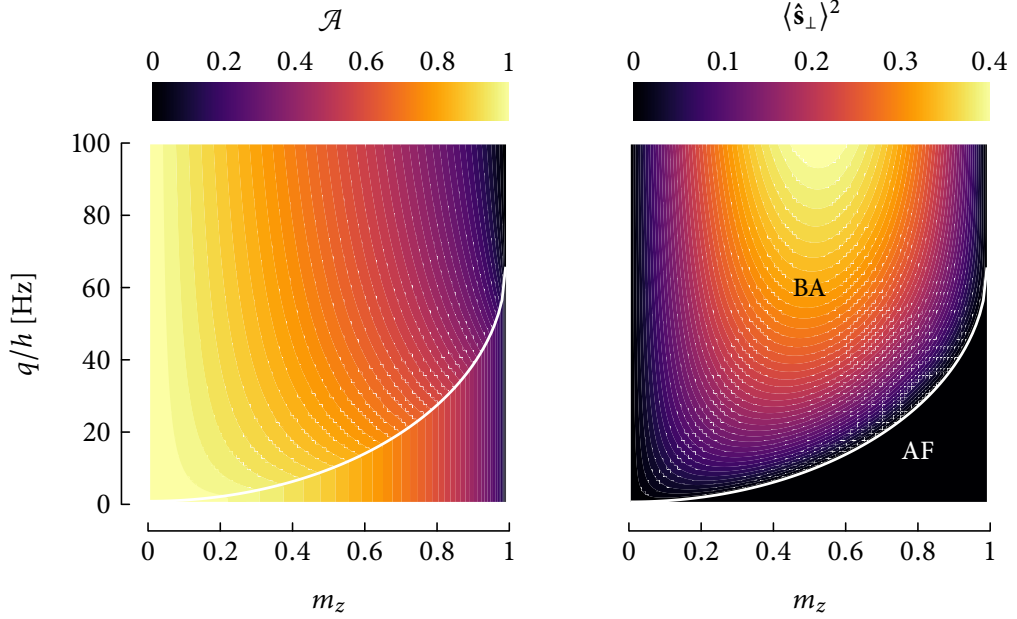


FIGURE 3.2: alignment \mathcal{A} (left) and transverse spin length $\langle \hat{s}_\perp \rangle^2$ (right) calculated for the parameters of ref. [54]. We plot in white the critical line described in Eq. (3.16). We note that $\langle \hat{s}_\perp \rangle^2 = 0$ in the antiferromagnetic phase (AF), while it takes a finite values in the broken-axisymmetry phase (BA). Besides, $\langle \hat{s}_\perp \rangle^2 = 0$ both in the limits $m_z = +1$ and $m_z = 0$ which correspond to oriented and nematic states respectively as can be seen from the alignment that tends to $\mathcal{A} = 0$ and $\mathcal{A} = 1$ respectively.

by the phase α . The hamiltonian (3.12) and Eq. (3.13) indicate that all values of α are degenerate. As such, we consider that α is random from one experimental realization to another. Equivalently, this means the orientation of the transverse spin vector is random from one experimental realization to the other. Even though this does not have any effect on the equilibrium populations that we discuss in this paragraph, we will see this impacts spin measurements after a rotation in a later section.

For a given longitudinal spin length $\langle s_z \rangle = m_z$, the phase boundary between the antiferromagnetic phase and the broken-axisymmetry phase can be calculated by minimizing the energy (3.13). This leads to $\Theta = \pi$ and:

$$n_0 = 0, \quad q \leq q_c \quad (3.14)$$

$$n_0 \neq 0, \quad q > q_c \quad (3.15)$$

where the critical field is:

$$q_c = U_s \left(1 + \sqrt{1 - m_z^2} \right), \quad (3.16)$$

We display on fig. 3.1, the phase diagram measured on refs.[54, 135], which shows the population in the $m_F = 0$ state n_0 as a function of the two control parameters: the magnetic field B and the magnetization m_z . We observe at low magnetic field that the $m_F = 0$ component vanishes as it is predicted by theory. The critical line displayed on fig. 3.1 with the spin exchange energy

$U_s = h \cdot 65.6$ Hz obtained by solving numerically the Gross-Pitaevskii equation (see ref. [54]). We note that this quantity can also be obtained by measuring the period of spin mixing oscillations (see annex D) as done for the results of ref. [192]. In fig. 3.2, we plot the alignment and corresponding transverse spin in a range of parameter similar to the phase diagram. We see that the transverse spin vanishes in the antiferromagnetic phase, and that the corresponding alignment is maximized, given the constraint of magnetization ($\max(\mathcal{A}) = 1 - m_z$). Instead, on the broken-axisymmetry phase, a small transverse spin is required to minimize the total energy (because of the quadratic Zeeman energy), but the alignment is nevertheless maximized when considering the appropriate equilibrium populations (equivalently $\Theta = \pi$). We observe on fig. 3.2 that the antiferromagnetic phase corresponds to a purely longitudinal spin with $\langle \mathbf{s}_\perp \rangle^2 = 0$. Instead, the transverse spin in the broken axisymmetry phase can vary between 0 for clouds polarized in $m_F = +1$ and $m_F = 0$ and 0.5 for $m_z \sim 0.5$, and is set by the maximization of the population of the $m_F = 0$. In the case of $m_z = 1$, the spin is purely longitudinal, and atoms are in an oriented state. In the case $m_z = 0$, the average spin length vanishes $\langle \mathbf{s} \rangle = 0$ and we have a spin nematic state.

3.2 Observation of phase locking in spinor BEC

In the previous section, we discussed several aspects of the mean field theory of spin 1 Bose-Einstein condensates and showed the population dependence on the experimental control parameters. We have observed two magnetic phases that result from a competition between the quadratic Zeeman effect and the spin exchange energy. We have seen that these two phases can be distinguished from the length of their transverse spin, which is finite in the broken axisymmetry phase and zero in the antiferromagnetic phase. Coming back to Eq. (3.12), we note that the transverse spin length is not only set by the value of the populations at equilibrium (here m_z, n_0), but also by the relative phase $\Theta = \phi_{+1} + \phi_{-1} - 2\phi_0$. Its equilibrium value, in case of antiferromagnetic interactions is $\Theta = \pi$, such that the spin length is minimized (see eq. (3.13)). In contrast, the relative phase α cannot be deduced from energetic arguments. The minimization of the transverse spin in equilibrium (to minimize E_s , see Eq. (3.13)) implies the existence of a phase locking mechanism. In this section we demonstrate a method to measure this relative phase by examining spin noise after a rotation. We will first present the experimental methods used for this measurement and discuss whether or not a phase locking mechanism could be detected.

3.2.1 Methods

In experiments, we measure populations from integration of absorption pictures as described in Sec. 2.2.1 such that the phase is not directly accessible. In this section, we propose a measurement of the transverse spin length of the system, that gives us the value of the phase Θ . This is made possible by the measurement of the longitudinal spin expectation value $m_z = n_{+1} - n_{-1}$ from the normalized populations in the $m_F = +1$ and $m_F = -1$ components. As such we propose to map the transverse spin on the longitudinal spin by performing a spin rotation, and to extract the transverse spin length from the value of the magnetization after a rotation. We note similar techniques were used to characterize spin squeezing in refs. [198–200].

Unlike Θ that is locked to a well defined value by spin changing interactions, α is expected to be random from one shot to the next given that it does not enter in the mean field energy Eq. (3.13).

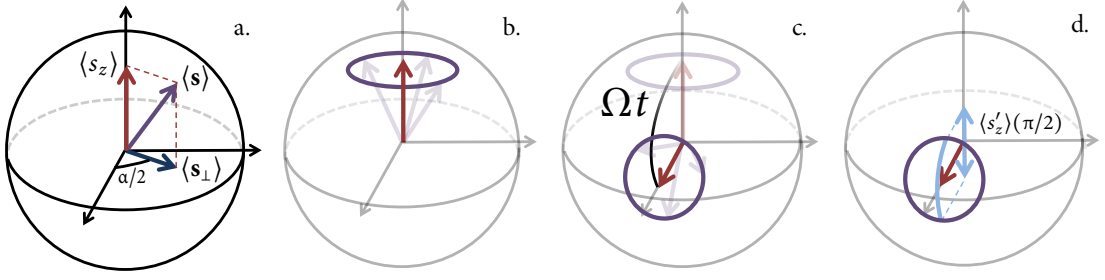


FIGURE 3.3: Schematic showing the principle of the measurement of the transverse spin length. a. We show the representation of the average spin $\langle \mathbf{s} \rangle$ in the Cartesian frame. The magnetization $\langle \hat{s}_z \rangle$ is set in the thermal gas, well above the critical temperature, and the transverse spin $\langle \hat{s}_\perp \rangle$ is given by the minimization of the mean field spin energy from Eq. (3.13). The phase α determines the orientation of the transverse spin $\langle \mathbf{s}_\perp \rangle$. All values of α are energetically degenerate. b. For this reason, the phase α varies randomly from one experimental realization to another, and the density matrix $\hat{\rho}$ is a statistical mixture of all possible values of α that we represent as a circle of radius $\langle \hat{s}_\perp \rangle$, perpendicular to the axis z . c. We perform a Rabi oscillation, that can also be seen as a spin rotation along axis y . Before rotation, the circle does not have a projection on the z axis such that the variations of α do not affect the value of the magnetization. However, after a rotation, this projection becomes non zero, and the fluctuations of α result in fluctuations of the magnetization $\langle s_z \rangle$. After a rotation of angle $\pi/2$, the projection along the z axis is maximal and the transverse spin length is directly proportional to the magnetization variance.

To represent this, we consider the many body state to be a statistical mixture:

$$\hat{\rho} = \int_0^{4\pi} \frac{d\alpha}{4\pi} |\zeta^N\rangle \langle \zeta^N|, \quad (3.17)$$

where $|\zeta^N\rangle$ is a pure state of N bosons in state $|\zeta\rangle$ with given values of Θ , n_0 , m_z and varying α . The randomness of the phase α translates as a random precession around the magnetic field axis when considering many experimental realizations:

$$\hat{\rho} = \int_0^{4\pi} \frac{d\alpha}{4\pi} \hat{R}_z^\dagger(\alpha/2) |\zeta_{\alpha=0}^N\rangle \langle \zeta_{\alpha=0}^N| \hat{R}_z(\alpha/2), \quad (3.18)$$

where the rotation operator (see Eq. (2.31)) is $\hat{R}_z(\theta) = \exp i\theta \hat{S}_z$. We represent this random ‘‘precession’’ as an horizontal circle on fig. 3.3b. We now consider the effect of a spin rotation around y (see Sec. 2.4.1, we recall ω is the Rabi frequency and t the rotation time such that ωt is the rotation angle) on state 3.17. It is described by the rotation operator \hat{R}_y such that :

$$\hat{S}'_z = \hat{R}_y^\dagger(\omega t) \hat{S}_z \hat{R}_y(\omega t) = \cos(\omega t) \hat{S}_z - \sin(\omega t) \hat{S}_x, \quad (3.19)$$

A mapping $S_x \rightarrow S'_z$ is realized for a $\pi/2$ pulse, that corresponds to a 90° rotation¹. We represent the rotation of the state (3.17) in fig.3.3c. The randomness of the phase α then translates into variations of the longitudinal spin $\langle \hat{s}'_z \rangle = \langle \hat{S}'_z \rangle / N$. We consider averages over many measurements such that the value of an observable \hat{O} measured after rotation is:

$$\langle \hat{O}' \rangle_\alpha = \frac{1}{4\pi} \int_0^{4\pi} d\alpha \langle \hat{R}^\dagger \hat{O} \hat{R} \rangle. \quad (3.20)$$

¹A $\pi/2$ pulse corresponds to a Rabi oscillation of angle $\Omega t = \pi/2$ with Ω the Rabi frequency and t the oscillation time.

where $\hat{R} = \hat{R}_y(\omega t) \exp(-i\alpha\hat{S}_z/2)$. $\langle \cdot \rangle_\alpha$ denotes a double average. First we compute the expectation value in the quantum state $|\zeta^N\rangle$ for a given value of α . The second average is realized by the integral in Eq. (3.20), and corresponds to an average over (sufficiently) many realizations of the experiment¹. For example, we can compute the average value of the magnetization after rotation:

$$\langle m'_z \rangle_\alpha = \langle \hat{s}'_z \rangle_\alpha = \cos(\omega t) m_z. \quad (3.21)$$

We remark that the mean value of the magnetization after rotation does not depend on the transverse spin, which is expected from the symmetries on figure 3.3 given that α varies randomly. However, the variance of m'_z depends on α as:

$$\Delta m_z'^2 = \frac{1}{2} \sin^2(\omega t) \langle \hat{s}_\perp^2 \rangle. \quad (3.22)$$

Eq. (3.23) shows that it is possible to measure the transverse spin length from the variance of the longitudinal spin after a Rabi oscillation, as the length of the transverse spin is directly mapped to the longitudinal spin length fluctuations (see fig. 3.3d). We note that when the atom number is large, we have $\langle \hat{s}_\perp^2 \rangle \simeq \langle \hat{s}_\perp \rangle^2 + O(1/N)$. Additionally, there are additional fluctuations Δm_z of the magnetization in the initial state due for example to imperfections of the preparation sequence Eq. (3.22) is modified such that:

$$\Delta m_z'^2 = \cos^2(\omega t) \Delta m_z^2 + \frac{1}{2} \sin^2(\omega t) \langle \hat{s}_\perp^2 \rangle. \quad (3.23)$$

It results in an additional “offset” to the signal after a π pulse for example. In the following paragraph, we will verify whether the population variances extracted from experiment agree with this prediction.

3.2.2 Observation of phase locking

Figure. 3.2 suggests which experimental parameters one should use to measure the transverse spin in the broken axisymmetry phase. The first phase we study (denoted by point a in fig. 3.5) is the broken-axisymmetry phase, but with a magnetic field small enough such that the three Zeeman states are populated. The experiment starts by the preparation of a Bose-Einstein condensate of ~ 7500 atoms in the dimple trap (see chap. 2) that for this particular experiment has trap frequencies of $\omega_{x,y,z} = 2\pi \cdot (460, 540, 270)$ Hz and a trap depth $V_0/k_B \simeq 400$ nK. The magnetization is set to $m_z \simeq 0.33$ (see Sec. 2.4.4) and the quadratic Zeeman energy to $q \simeq 6$ Hz (corresponding to a bias field $B \simeq 150$ mG along x). We estimate from the absence of detectable thermal wings on single component Bose-Einstein condensates, that the condensed fraction is above 80%. We perform a spin rotation as described in Sec. 2.4.1, and measure populations by atom counting from absorption images obtained with the Stern-Gerlach sequence (see Sec. 2.2.1).

We present the results of this experiment on fig. 3.4. We observe a sinusoidal variation of the average magnetization as expected from Eq. 3.21. We also observe the error bars, corresponding to $\Delta m'_z$ increase around $\omega t = \pi/2, 3\pi/2, 5\pi/2$. This corresponds to the fluctuations of the transverse spin that have been mapped on the z axis as predicted in the previous paragraph. We observe the effect on fig. 3.5, in which we plot the expectation values of $\Delta m_z'^2$ using the initial value n_0 measured at $t = 0$ according to eq. (3.23). We plot the theoretical curves corresponding to three

¹We note that when considering experimental imperfections (e.g. fluctuations of the magnetization due to imperfections in the preparation step), a third average over them is also required.

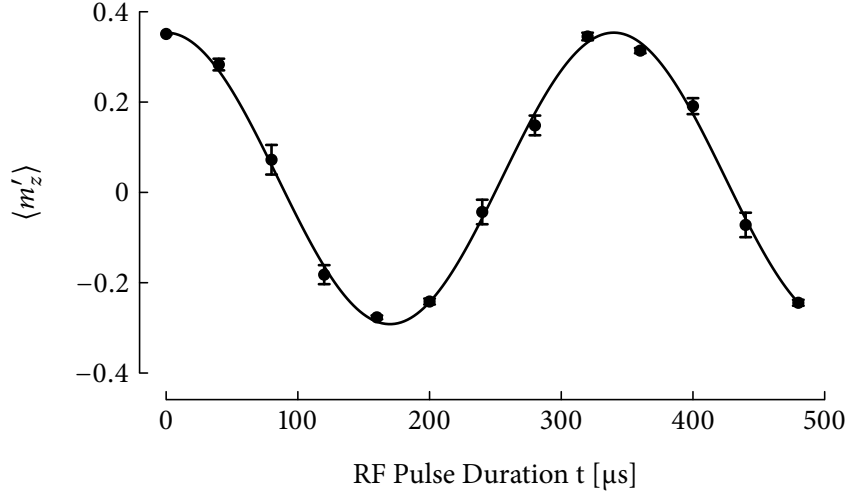


FIGURE 3.4: Mean magnetization during a Rabi Oscillation starting from a BEC created with parameters denoted with a in fig. 3.5. We fit the data to a sine function accordingly with Eq. (3.21). We note the increasing error bars near $t = 75 \mu\text{s}$, $250 \mu\text{s}$, $450 \mu\text{s}$ that corresponds to $\omega t = \pi/2$, $3\pi/2$ and $5\pi/2$.

cases, the first is $\Theta = \pi$ and corresponds to antiferromagnetic phase locking. The second is $\Theta = 0$ and would correspond to ferromagnetic phase locking. A third curve is calculated assuming there is no particular phase relation between the Zeeman components. The phase Θ is then random and the contribution proportional to $\cos(\Theta)$ in Eq. (3.12) averages out.

We observe that the experimental data on fig. 3.5 is indeed incompatible with the prediction that assume ferromagnetism or no phase locking mechanism. However, we remark that the experimental points are always below the theory curves, which indicates the transverse spin is smaller than expected by the $T=0$ mean field theory. We verified that this is not due to a detuning of the radiofrequency used for the Rabi oscillation by fitting the evolution of the magnetization in fig. 3.4 by the expected evolution including a detuning. We have found that the detuning was much smaller than the Rabi frequency. We have applied the same method for two additional sets of parameters b and c and obtained the curves shown in fig. 3.5. Even though they address a different magnitude of the transverse spin, both display the same general behavior as the curve in fig. 3.5, indicating the phase locking mechanism indeed happens regardless of the magnetic phase considered.

Two important questions remained to be addressed in order to obtain a more complete understanding of this mechanism. First, the overestimation of the transverse spin length by mean field theory seems puzzling at first sight. Second, according to fig. 3.2, the value of the transverse spin vanishes at point c, which is in disagreement with the observation plotted in fig. 3.5. We will discuss in the next paragraph that it is possible to explain both effects by taking either the finite kinetic temperature (hence a finite thermal fraction) into account, and also by considering a finite “spin” temperature for the spin ensemble.

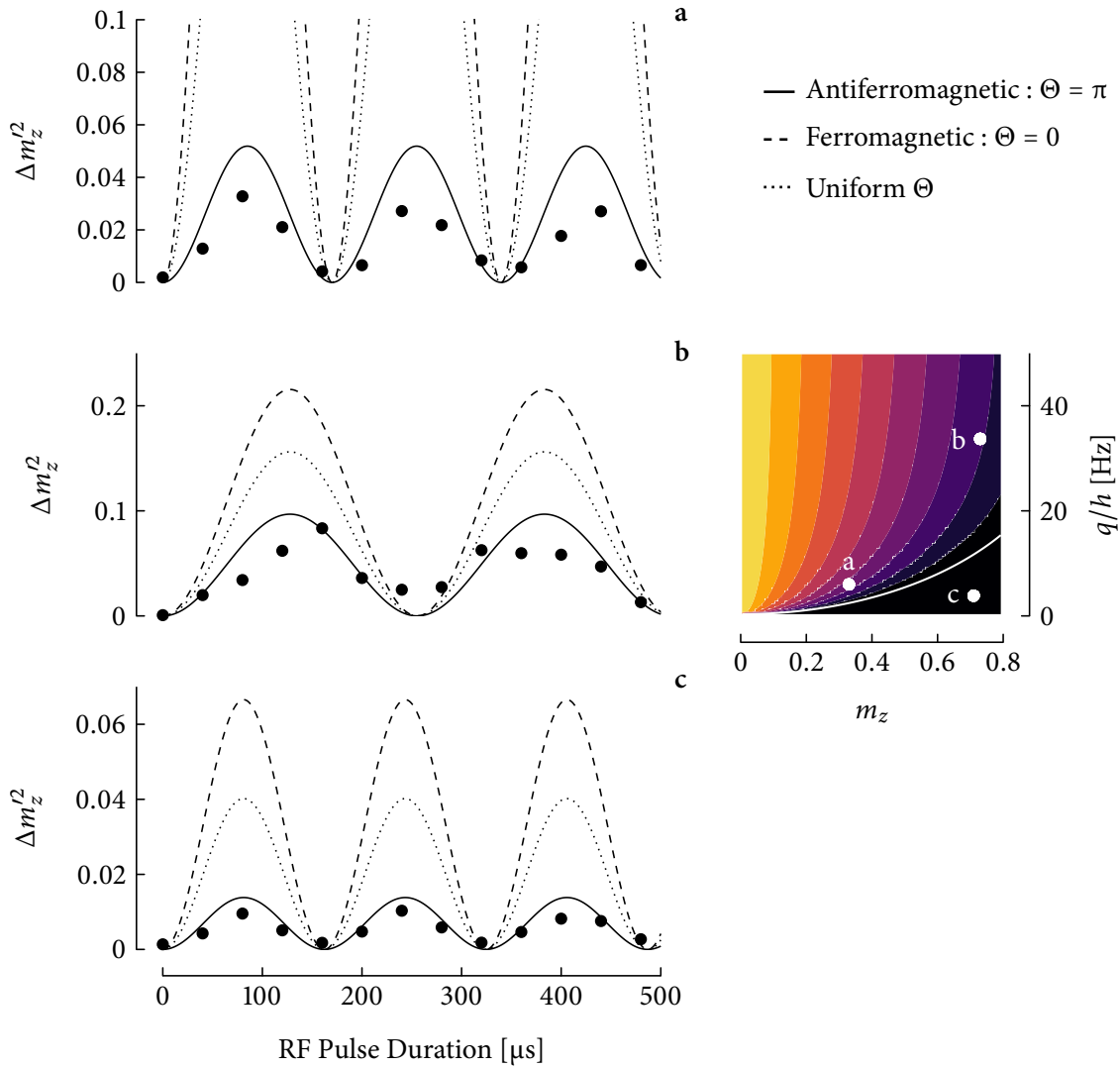


FIGURE 3.5: Magnetization variance during a Rabi oscillation. The initial parameters for figs. a,b,c are shown on the phase diagram above the figure. The solid curves indicate the expectation from eqs. (3.23) with a transverse spin length calculated from initial parameters with Eq. (3.12) and $\Theta = \pi$, which corresponds to antiferromagnetic phase locking. The dashed line indicate the expectation for $\Theta = 0$, which would correspond to ferromagnetic (F) phase locking. The dotted line indicate the expectation value for Θ random from shot to shot, that we would expect in absence of a phase locking mechanism (uniform Θ). We see that our data are only compatible with the theory obtained in presence of antiferromagnetic (AF) phase locking, $\Theta = \pi$ regardless of the initial parameters used before the oscillation. We note that in the panel c, the T=0 theory does not predict the existence of a transverse spin for this parameter regime (see fig. 3.2). This is resolved by considering thermal spin fluctuations that effectively generate a small, but measurable transverse spin for $m_z < 1$.

3.2.3 Effect of a finite kinetic temperature

Eq. (3.17) describe a statistical mixture of pure states and only applies for $T=0$. We can however modify this description, first by considering the thermal depletion of each Zeeman component and then by including thermal fluctuations of the spin state (see ref.[193]). In the next paragraphs we will see that the finite kinetic temperature effectively decreases the transverse spin in the broken axisymmetry phase by depleting the population of the $m_F = 0$ state. We will also see that a finite spin temperature can generate a small transverse spin in the antiferromagnetic phase.

Effect of thermal depletion on the transverse spin

The spin of the normal fraction of a condensed Bose gas is predicted to differ significantly from the one of the condensate. The authors of ref. [91] considered this for uniform gases and show that the spin of the normal fraction tends to oppose the one of the condensate at very low temperatures. In our temperature regime, which fulfills $k_B T \gg q, U_s$, the spin of the thermal component is always of much smaller magnitude than the one of the condensed part.

We performed Hartree-Fock calculations that we have adapted from ref. [91] to include a trapping potential. Details about this can be found in ref. [192] and in the thesis of Vincent Corre [119]. We compute the density matrix of the gas, that we write as the sum of condensates wavefunction ϕ_m and of the density matrix of the thermal gas ρ' :

$$\rho_{mn}(\mathbf{r}) = \phi_m^*(\mathbf{r})\phi_n(\mathbf{r}) + \rho'_{mn}(\mathbf{r}). \quad (3.24)$$

As described in chapter 1 (see. 1.3), we consider the spinor condensate in the single mode approximation such that $\phi_m = \sqrt{N}\bar{\phi}\zeta_m$, where ζ_m is the spin mean-field wavefunction and $\bar{\phi}$ is the single-mode wavefunction obtained by numerical resolution of the Gross-Pitaevskii equation (see ref. [119]). The mean field spin wavefunction is found from minimization of the mean field spin energy as described in Sec. 3.1.2. The thermal density matrix is computed within a semi ideal model (see ref. [201]), where we neglect the influence of the thermal atoms on the condensate. We expect this approximation to be valid for high condensed fractions, at temperatures well below the critical temperatures. We determine explicitly the modes and eigenenergies of atoms in the effective potential obtained from the sum of the external potential and the mean field contribution of the condensate:

$$\left(-\frac{\hbar^2}{2m}\Delta + V_{\text{ext}}(\mathbf{r}) + \bar{\bar{A}}(\mathbf{r}) \right) \mathbf{u}_{(v)} = E_v \mathbf{u}_{(v)}, \quad (3.25)$$

where $\bar{\bar{A}}$ is a matrix that contains the mean field potential of the condensate and Lagrange multipliers to enforce the atom number and magnetization of the thermal gas (the matrix $\bar{\bar{A}}$ is given explicitly in ref. [91]). We note that the mean field potential is in general a non diagonal matrix due to the spin exchange interaction term, and as such $\bar{\bar{A}}$ is not diagonal either. The expression of the matrix $\bar{\bar{A}}$ is given explicitly in ref. [91]. We determine the thermal density matrix ρ' and the condensate wavefunction in a self consistent way. Each step consists in solving a spinor Gross-Pitaevskii equation and computing the density of the thermal gas with the mean field potential determined by the results of the previous step. The process is repeated varying the value of the Lagrange multipliers until the target magnetization and atom number are reached. We use an isotropic potential as it reduces significantly the numerical complexity and should provide accurate result given our trap geometry is nearly spherical (the trap frequencies are in the ratio $\omega = 2\pi(1.17 : 1 : 0.59) \cdot 344\text{Hz}$).

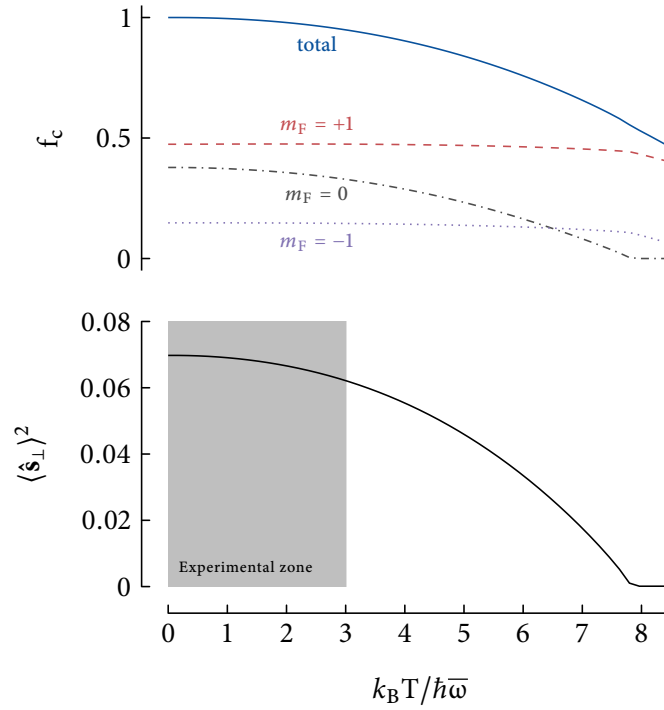


FIGURE 3.6: Condensed fraction f_c and transverse spin length $\langle \hat{s}_\perp \rangle^2$ as a function of temperature obtained by solving Hartree-Fock equations adapted from ref. [91] to include a trapping potential. We observe a sequential condensation of the $m_F = \pm 1$ and the $m_F = 0$ (see chap. 4 for more details). Given $U_s \simeq 0.08\hbar\omega$, the condition $k_B T \gg U_s$ is always fulfilled such that the thermal fraction of the gas can be considered to have $m_z \sim 0$. Until the temperature reaches the BEC critical temperature for the $m_F = 0$ component, the transverse spin remains equal to 0. The dependence of the transverse spin on the total condensed fraction is rather steep, as the condensed fraction of the $m_F = 0$ component decreases faster than the overall thermal fraction around $T=0$. As such, a thermal fraction of 10% reduces the transverse spin by as much as 30%.

We plot the result of this Hartree-Fock calculation in fig. 3.6, in which we show the condensed fraction of each component as a function of the temperature, along with the transverse spin length. We observe that the condensation of the components is not simultaneous (as studied in greater details in chapter 4), and that the transverse spin rises as the $m_F = 0$ component condenses. This happens at relatively low temperatures, and a diminution of 20% of the total condensed fraction reduces the condensed population of the $m_F = 0$ by a factor of almost 60%. The diminution of the population of $m_F = 0$ translates directly in a diminution of the transverse spin. This effect can be taken into account in Eq. (3.23) by only considering only condensed atom such that $n_0 \rightarrow n_{0c} < n_0$ in 3.12 which effectively reduces the magnitude of the transverse spin. We show the effect of such treatment on fig. 3.7, in which we plot an additional dashed line compared to fig. 3.5, representing the predictions of HF theory for a condensed fraction $f_c = 0.9$. The shaded area represent $0.8 < f_c < 1$ corresponding to the experimental zone in fig. 3.6.

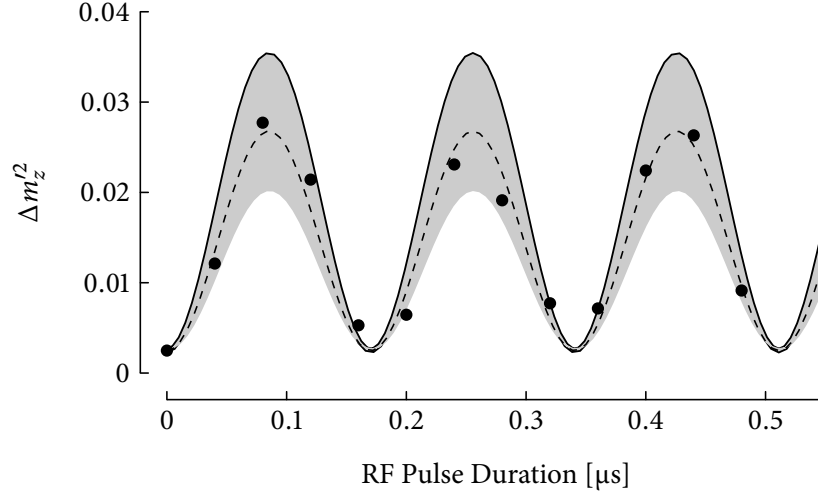


FIGURE 3.7: We reproduce the magnetization variance along a Rabi oscillation of dataset a presented in fig. 3.5. We compare the data, with the $T=0$ theory (plain line) and with the theory for $f_c = 0.9$ (dashed line). We indicate by a shaded area the magnetization variances expected for $0.8 < f_c < 1$.

3.2.4 Effect of a finite spin temperature

In section 3.2 we discussed the measurement of phase locking in the antiferromagnetic phase by the measurement of a small transverse spin length (dataset c from fig. 3.5). We have shown that this small but finite transverse spin is compatible with the minimization of the spin energy given a finite value of the population n_0 that we observe without a spin rotation. This however is incompatible with the mean field prediction in the antiferromagnetic phase, where the transverse spin length should vanish (see fig. 3.12). This small, but observable deviation to mean field theory can be accounted for by taking into account the finite temperature of the spin degrees of freedom in the determination of the equilibrium state of Eq. (3.13).

We have developed a theory to describe the changes in the observables due to finite spin temperatures (see refs. [119, 193]). We used a statistical ensemble, obtained from modifying the grand canonical ensemble. We account for a given magnetization probability distribution by adding two additional Lagrange multipliers $\lambda_{1,2}$ to the free energy \mathcal{F} of the system to enforce a particular average value and standard deviation of the distribution of magnetization (more details are found in ref. [193]). In the $N \gg 1$ limit, average values of observables can be determined by considering the family of states $|\zeta^N\rangle$ and by weighting their contributions by a modified Boltzmann factor $\exp(-\beta\mathcal{F})$ (see ref. [119, 193]). The average value of an observable describe by operator \hat{O} is:

$$\langle \hat{O} \rangle = \frac{1}{Z} \int dn_0 dm_z d\alpha d\Theta \langle \zeta^N | \hat{O} | \zeta^N \rangle \exp(-\beta\mathcal{F}(n_0, m_z, \alpha, \Theta)), \quad (3.26)$$

where Z is a normalization factor. We can express the free energy $\mathcal{F} = \langle \zeta^N | \hat{H}_S - \lambda_1 \hat{s}_z - \lambda_2 \hat{s}_z^2 | \zeta^N \rangle$ as:

$$\beta\mathcal{F} = \frac{\beta'_z}{2} (m_z - m_z^*)^2 - \eta n_0 + \beta' \underbrace{\left(n_0(1 - n_0 + \sqrt{(1 - n_0)^2 - m_z^2} \cos(\Theta)) \right)}_{\langle s_\perp \rangle^2}, \quad (3.27)$$

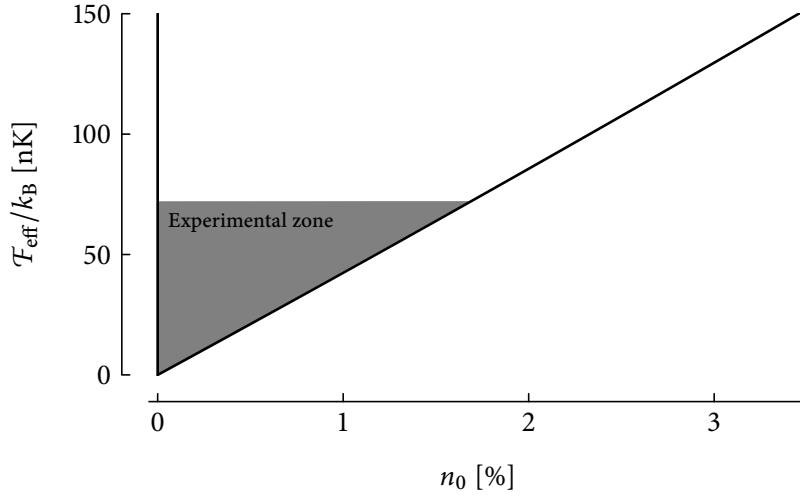


FIGURE 3.8: Sketch of the Free energy as a function of the population in n_0 . We note that within our experimental temperature range (indicated as experimental zone), the average population in the $m_F = 0$ can be almost 1% such that the data for point c can be explained by the transverse spin from Eq. (3.31) resulting from finite spin temperature.

where we introduced two external parameters:

$$\eta = N\beta q, \quad (3.28)$$

$$\beta' = N\beta U_s. \quad (3.29)$$

We reexpressed the two Lagrange multipliers $\lambda_{1,2}$ in a more convenient way : $\beta'_z = \beta' + 2N^2\lambda_2$ and $m_z^* = -N\lambda_1/\beta'_z$. With these definitions, the inverse temperature β' characterizes the fluctuations of the transverse spin while β'_z characterize the fluctuations due to the prior distribution of m_z (technical preparation noise for example). A purely thermal prior distribution would be characterized by $\beta'_z = \beta'$. In our experiments we find that $\beta'_z \gg \beta'$ in general, which corresponds to a “narrow” prior distribution.

In order to understand better the effect of the finite spin temperature, we consider an antiferromagnetic state such that the mean field state predicts $n_0 = 0$ (such as in the case of point c in fig. 3.5 for example), we will study the case of finite magnetization and small magnetic field. In this case, we develop Eq. (3.27) around $n_0 = 0$, $\Theta = \pi$ and obtain:

$$\mathcal{F}_{\text{eff}} = Nq_c \left[\sqrt{1 - \overline{m_z}^2} n_0^2 - \left(\frac{q}{q_c} - 1 \right) n_0 \right] + O(n_0^3, n_0\Theta^2), \quad (3.30)$$

where q_c is the critical quadratic Zeeman energy defined in Eq. (3.16) and $\overline{m_z}$ is the average magnetization. We represent the free energy on fig. 3.8 for the parameter of our point c . We also represent the typical temperature range in our experiments ($k_B T \leq 3\hbar\overline{\omega}$) by a shaded area, that we estimate by considering that the absence of visible thermal wings on absorption picture indicates a condensed fraction above 80%. As we can see, for finite β' , a detectable population can build in the $m_F = 0$ component due to spin fluctuations. For small average population \overline{n}_0 and small fluctuations of Θ , when Eq. (3.30) holds, we apply eq. (3.26) and we have:

$$\langle \mathbf{s}_\perp \rangle_{\text{th}} = \frac{2\overline{n}_0 q_c}{U_s} + O(n_0^2, n_0\Theta^2). \quad (3.31)$$

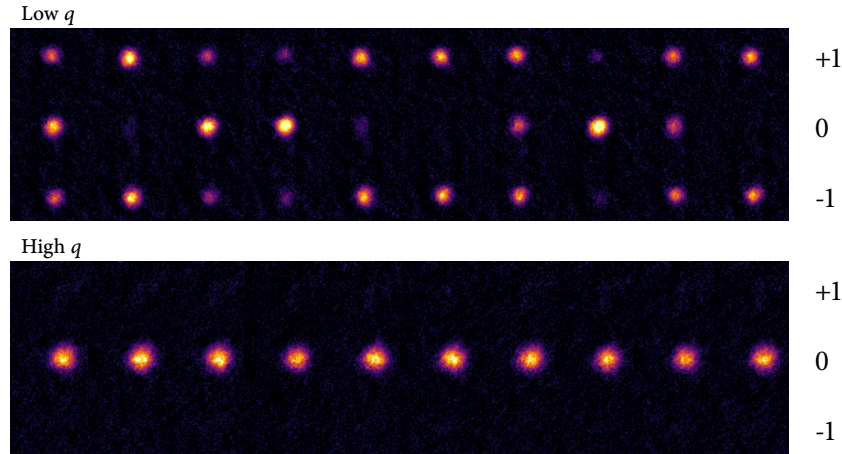


FIGURE 3.9: Comparison of 10 experimental realizations at low ($q \sim h \cdot 0$ Hz) and high magnetic field ($q \sim h \cdot 200$ Hz). We see that in the case of the quadratic Zeeman energy is low, there are large fluctuations of the populations in the $m_F = 0$ component. At high quadratic Zeeman energy, the fluctuations disappear, and all the atoms are in the $m_F = 0$ component, as expected from the mean field picture.

With our experimental parameters estimate that $n_0 \leq 0.02$. This would result in $\langle s_{\perp} \rangle_{\text{th}}^2 \leq 0.012$ which is compatible with the observations from fig.3.5.

So far, we focused on situations where $m_z > 0$. In the next section, we will examine the case $m_z \simeq 0$ and explore regions of low magnetic field, where the three Zeeman states are nearly degenerate. In this case, the population of the three Zeeman states can become comparable, but more interestingly, large population fluctuations arise from the finite spin temperature.

3.3 Spin fluctuations

This section gives an overview of the work performed in our team during the beginning of my PhD thesis. The methods and results are detailed in the thesis of Vincent Corre (ref. [119]).

For $q=0$, the three Zeeman sublevels of a spin 1 Bose-Einstein condensate are degenerate. In the theoretical frame that we have developed so far, there are multiple possible mean field states, the whole spin-nematic state family, as all possible orientations of spin-nematic states are degenerate. In an experiment where we would prepare a condensate at $q = 0$, this would result in large observed population fluctuations. However, the slightest magnetic field would lift the degeneracy and favor the particular spin nematic state with its director along the field axis, resulting in state polarized in $m_F = 0$. In the experiment, setting the quadratic energy to a low value, we observe large fluctuations of the relative population in the $m_F = 0$ state as shown in fig. 3.9 even for finite magnetic fields ($q \sim 1$ Hz) which indicates that the mean field picture may not be sufficient. In the following, we will show how to account for these fluctuations with a finite spin temperature similarly to what we have discussed in section 3.2.4.

3.3.1 Spin fluctuations for low magnetization

We apply the description introduced in section 3.2.4 to compute the distribution of the population in the $m_F = 0$ component in the regime of low magnetizations and low magnetic fields. We consider $m_z \simeq 0$ and $\Theta \simeq \pi$, and we develop the expression of the free energy \mathcal{F} from Eq. (3.27) and obtain:

$$\beta\mathcal{F} \simeq \frac{m_z^2}{2\sigma^2} + \beta'n_0(1-n_0)\frac{(\Theta-\pi)^2}{2} - \eta n_0, \quad (3.32)$$

$$\sigma^2 = \frac{1-n_0}{\beta'n_0} \beta'_z(1-n_0). \quad (3.33)$$

We note that the overall energy minimum is found for the mean field ground state described in Sec. 3.1.2 *e.g.* $n_0 = 1$, $\Theta = \pi$ and $m_z = 0$. With this expression, we see that if

$$\eta = N\beta q \simeq 1, \quad (3.34)$$

the finite thermal spin energy will translate in large fluctuations of the population in the $m_F = 0$ component. We note that within our experimental parameters $N = 5000$ and $T \simeq 100$ nK, the crossover to the mean field regime happens for $q \sim 0.5$ Hz (corresponding to $B \sim 40$ mG). As such, the use of relatively small clouds here allows to observe large fluctuations in a regime of parameters where ambient field fluctuations are not relevant (we estimate the magnetic field fluctuations along the bias field axis to 1.5 mG peak to peak, see chapter 2).

We use the property 3.26 to compute the probability distribution of the $m_F = 0$ component population (considering narrow distributions of m_z and θ):

$$p(n_0) \propto \iint d\Theta dm_z e^{-\beta\mathcal{F}}, \quad (3.35)$$

Given the Gaussian form of the integrand in m_z and Θ (see eq. (3.32)), the integration can be done analytically and we obtain:

$$p(n_0) \propto \frac{e^{\eta n_0}}{\sqrt{n_0(\beta'n_0 + \beta'_z(1-n_0))}}. \quad (3.36)$$

We calculate the moments of this distribution numerically, and represent them in fig. 3.10. We observe that for high magnetic fields, we retrieve the mean field behavior, *e.g.* the cloud is polarized in $m_F = 0$ and the fluctuations of the population n_0 are small. For $\eta \leq 1$, the fluctuations of populations become very large the mean population tends to $n_0 = 1/3$. We note that when $\eta \leq 1$, we have $\sigma_{n_0} \sim 0.3$ and $\sigma N_0 \propto N$. This corresponds to super-Poissonian spin fluctuations.

3.3.2 Experimental measurement of fluctuations

In this section, we turn to the experimental investigation of spin fluctuations. We will prepare samples with $m_z \simeq 0$ with the help of the demagnetization sequence described in Sec. 2.4.4. We perform evaporative cooling such that we obtain an almost pure BEC. We note that a hold time of 6 seconds at the final trap depth was added to ensure the gas is at equilibrium. We apply a uniform magnetic field during the evaporation, that is taken as a control parameter in a similar way to experiments discussed in secs. 3.1.3 and 3.2. We obtain the atom number from integration on square boxes, from absorption images obtained with the defringing algorithm described in

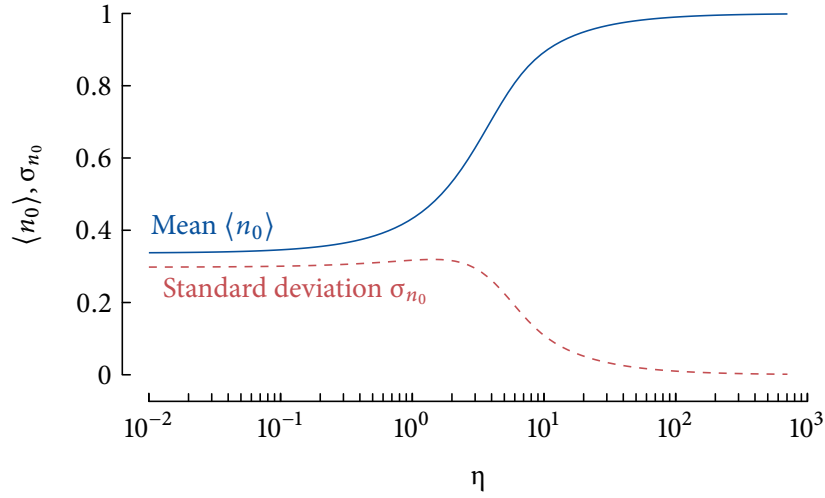


FIGURE 3.10: Moments of the distribution of n_0 . We used $\beta'_z = \beta'$ corresponding to an unconstrained distribution of m_z . We note that considering a temperature of $T \sim 50$ nK, $N = 8000$, $\eta = 1$ corresponds to $q = 0.13$ Hz or a magnetic field of $B = 22$ mG.

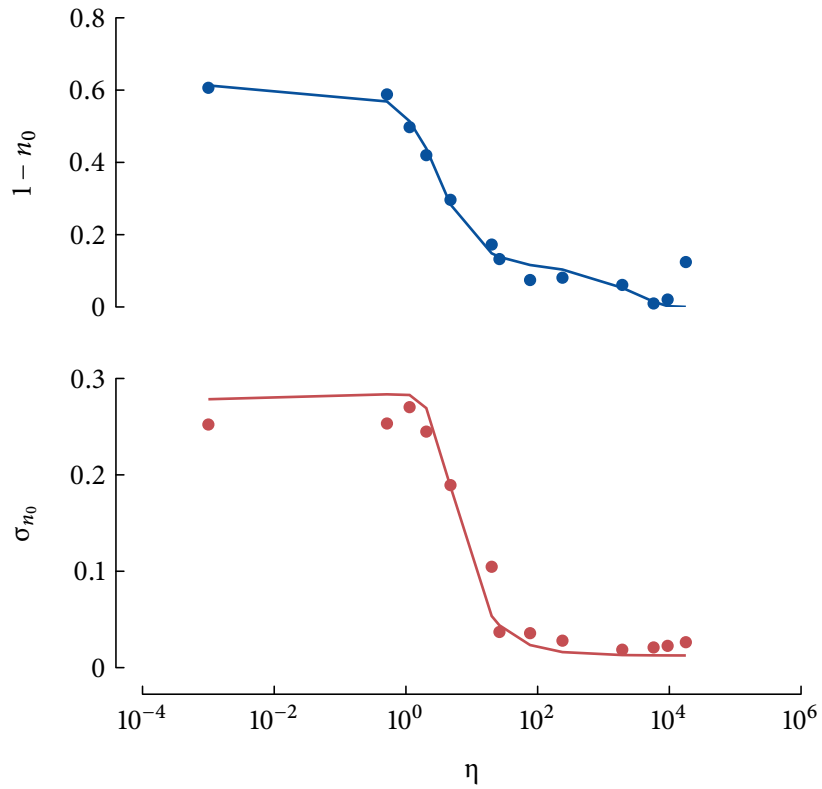


FIGURE 3.11: Mean and standard deviation of the population in the $m_F = 0$ component as a function of magnetic field. The solid line shows a fit to the data by the moments from eq. (3.36), taking into account the prior distribution of m_z and a finite temperature ($f_c < 1$). The fitting method is described in ref. [119]. We see that the regime of large fluctuation is reached to $\eta \sim 1$ corresponding to $B \sim 20$ mG in this case.

Sec. 2.2.2. We repeat the experiment about 150 times per parameter sets and obtain experimental distributions of n_0 such as the ones shown in fig. 3.12. We observe a broadening of the distribution of n_0 as the magnetic field is lowered, that corresponds to spin fragmentation.

We extract a spin temperature from measurements such as the ones shown in figure 3.11. We extract a “critical” quadratic Zeeman energy at which the fluctuations of the population become important. Since we know the theoretical moments, that we compute from eq. (3.36), we can relate this critical magnetic field to a particular value of $\eta = N\beta q \sim 1$, and extract from the knowledge of atom number and critical Zeeman energy, a value for the spin temperature $T_s = 1/k_B\beta$. The extraction of the critical Zeeman energy is done by directly fitting moments computed with eq. (3.36) with the spin temperature as a parameter. We note an alternative approach consists in fitting directly distributions (this is shown on fig. 3.12 by solid lines). This procedure is detailed in ref. [119].

3.3.3 Spin thermometry

In the following paragraph, we investigate the effect of another control parameter which is the final evaporation trap depth. We vary it by stopping at different point of our evaporation ramp, such that the rate of cooling is the same from one experiment to another. However, stopping at higher trap depth allows us to obtain higher temperature clouds (as seen in fig. 3.13) and a smaller condensed fraction. The experiment consists in varying the magnetic field, and measure several realizations of the experiment. The mean and standard deviation of the population of the $m_F = 0$ component are measured, and we can extract the critical value of η at which fluctuations appear. We note that for high temperature clouds, the picture described in section 3.3.1 is modified, as the condensed fraction is predicted to have roughly equal population in all Zeeman states (since $k_B T \gg U_s$). This modifies the distributions shown in figs. 3.10 and 3.11 in several ways. First, in the $\eta \rightarrow \infty$ limit, the mean $\langle n_0 \rangle$ is reduced to a value $1 - 2f_c/3$. Second, in the limit $\eta \rightarrow 0$, as the populations of the thermal fraction do not fluctuate, the value of σ_{n_0} is reduced, and the mean value is also modified (however, this modification depends on the prior distribution of m_z).

We extract the spin temperature from fits to the distributions showed in fig. 3.11 when we vary the final evaporation trap depth. We compare the spin temperatures with the kinetic temperatures we have obtained from direct fits of the thermal component (using the mask method described in Sec. 2.3 on images taken without a Stern-Gerlach sequence). We show on fig. 3.13 the measured kinetic temperatures as a function of trap depth. The fitting procedure fails for low trap depths $V_0 < 4 \mu\text{K}$ due to the absence of visible thermal wings, hence we extrapolate the data by a linear fit to lower trap depth. The spin temperatures are also displayed on fig. 3.13. The value of the spin temperature could not be measured for the highest trap depth because there are too few fluctuations on the population of the $m_F = 0$ component due to the low condensed fraction. We observe that for the lowest values of q the spin temperature is much lower than the kinetic temperature and its value $T_s \simeq 50 \text{ nK}$ does not depend on the trap depth. We note however that for a higher quadratic Zeeman energy, the spin temperature is compatible within error bars to the kinetic temperature.

In order to explain this behavior we shall recall what distinguishes the two temperatures T_s and T_k discussed above. The spin temperature describes the excitation of the spin ensemble described by the hamiltonian H_s , while the kinetic temperature describes thermal excitation from the kinetic hamiltonian. The energy scales in both spectra are very different. Excitation of the spin degree of freedom will have a typical energy $\sim U_s/N \simeq 1 \text{ pK}$ while the excitation in the BEC, will take the

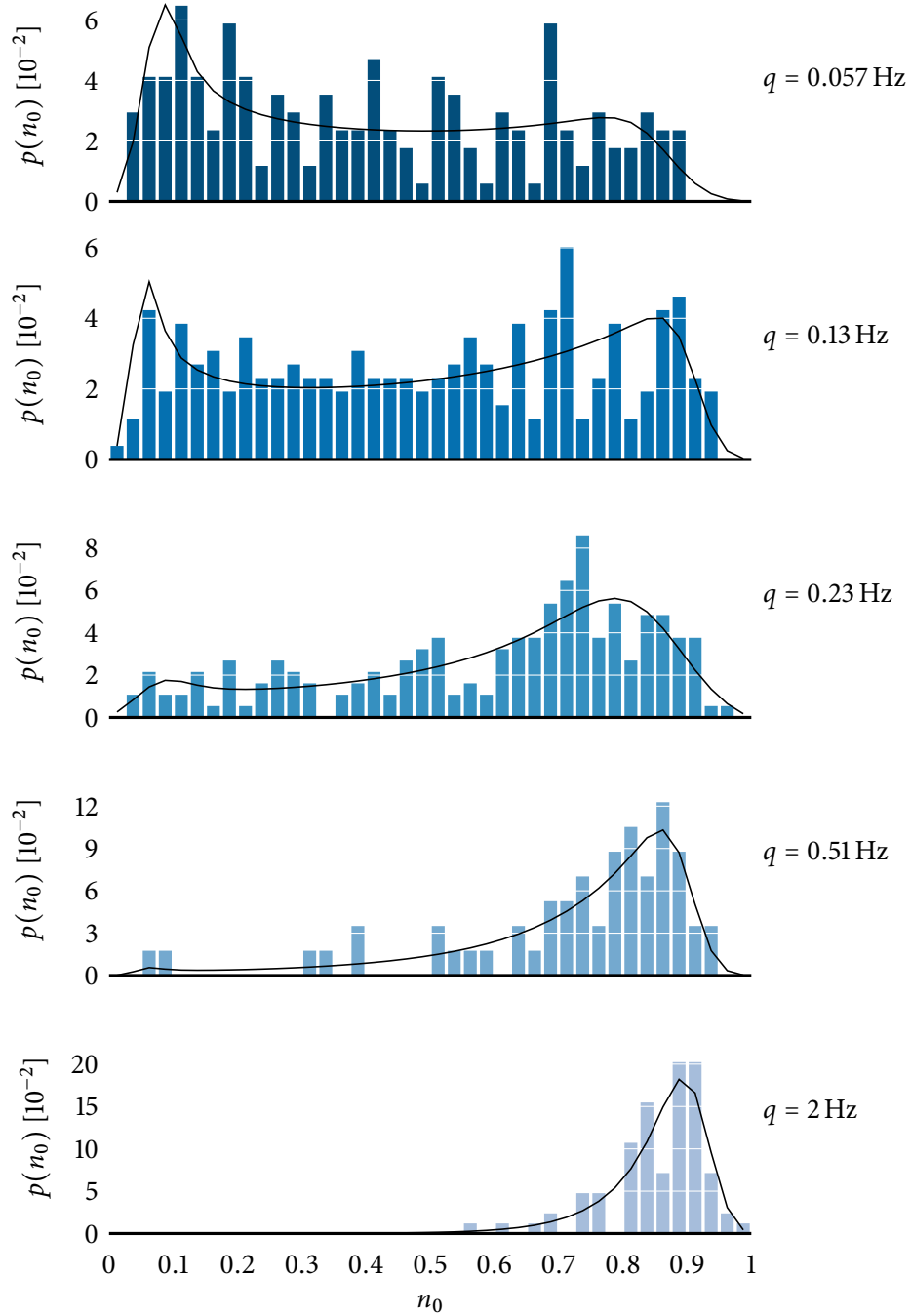


FIGURE 3.12: Experimental probability distribution of n_0 with varying magnetic field. We observe the distribution gets narrower, and more peaked around $n_0 = 0$ as the magnetic field is increased as expected from the SU(3) description presented in this section. We show fits to the function (3.36), where the distribution of m_z and a finite (and fluctuating) condensed fraction is taken into account.

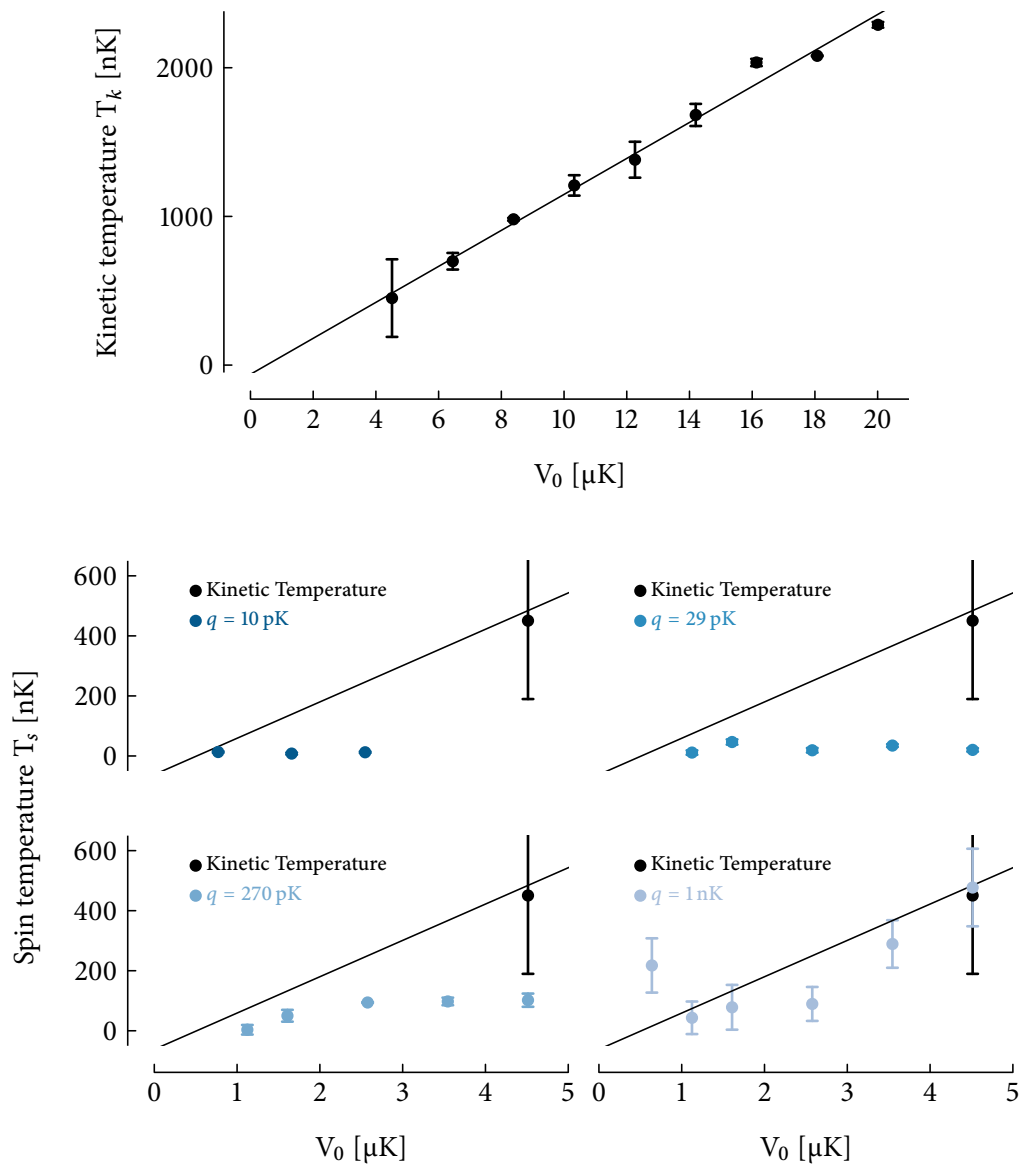


FIGURE 3.13: Summary of the temperature measurement. The kinetic temperature is obtained from fits to the wings of the time of flight distribution of the gas. The absence of points below $V_0 < 4 \mu$ K is due to the absence of visible thermal wings. The spin temperature is obtained from fits to the distribution of n_0 . We note that for the lowest values of q , the spin temperature does not vary with the trap depth V_0 and takes a much lower value than the kinetic temperature. For the highest value of q however, we see the spin temperature is comparable to the kinetic temperature for trap depths above $V_0 = 3 \mu$ K.

form of a spin wave that will have a typical energy scale of $\sim \sqrt{g_2/\bar{g}}\hbar\omega \simeq 6$ nK (see ref. [64]).

This large energy difference can be assimilated to a large detuning when considering energy exchange processes between the two degree of freedom. As such, we believe both degree of freedom, spin and kinetic, equilibrate independently within experimental time scales. For higher values of q , the spectrum of H_s changes. In the ground state, all condensed atoms are in the $m_F = 0$ components and an excitation consists in creating two atoms in the $m_F = \pm 1$ components. As for finite q these components do not condense, this process involves collisions between atoms from the condensate and the thermal fraction, which effectively couples the kinetic and spin degree of freedom, and leads to thermal equilibrium between the two. We observe the transition between these two regimes effectively happens when $q \sim \sqrt{g_2/\bar{g}}\hbar\omega$.

3.4 Conclusion

In this section we have discussed the low temperature magnetic properties of spin-1 Bose-Einstein condensates with antiferromagnetic interactions. We have recalled how the presence of spin exchange interactions define the ground state populations of the system. By varying the magnetic field (hence the quadratic Zeeman energy q) and the magnetization, the authors of ref. [54] were able to detect two magnetic phases. One is called the antiferromagnetic phase, where there is no population in the $m_F = 0$ component such that the spin length is minimized. A second phase is called the broken axisymmetry phase, where the $m_F = 0$ component gets populated because its energy is reduced by the quadratic Zeeman energy. Eventually, they observed that for large quadratic Zeeman energy the population in the $m_F = -1$ component vanishes.

In this chapter, we have shown that these two phases could be distinguished by their spin length $\langle \mathbf{s} \rangle^2$, or equivalently by a related quantity called the alignment \mathcal{A} . In the antiferromagnetic phase, the spin is purely longitudinal, while in the broken axisymmetry phase, a transverse spin appears due to the influence of the quadratic Zeeman energy. As the longitudinal spin length $\langle s_z \rangle = m_z$ is conserved by the spin exchange interactions, it is the transverse spin length $\langle \mathbf{s}_\perp \rangle^2$ that defines magnetic ordering in our system.

We proposed and demonstrated a method to measure the transverse spin length by measuring spin noise after a spin rotation. We have shown that the minimization of the spin length is realized by locking the relative phase $\Theta = \Phi_{+1} + \Phi_{-1} - 2\Phi_0$ between the different Zeeman components. This phase locking mechanism originates from the spin exchange interactions and enforce the magnetic order in the system. We have shown that given the azimuthal angle $\alpha = \Phi_{+1} - \Phi_{-1}$ of the total spin varies from shot to shot, the transverse spin length could be retrieved after a $\pi/2$ rotation along a transverse axis from the magnitude of the magnetization fluctuations (see fig. 3.3). We have performed the measurement with three sets of parameters, two in the broken axisymmetry phase and one in the antiferromagnetic phase, and in each case observed the phase locking of the phase Θ to π . We have shown that a full understanding of our data could only be obtained by taking into account the finite kinetic and spin temperatures of our cloud.

In the following we have considered the particular case of $q \simeq 0$, $m_z = 0$ where the three Zeeman components are degenerate. In this case, the observation of large fluctuations of the relative populations n_0 and $n_{\pm 1}$ contradicts mean field theory that predicts a condensate polarized in $m_F = 0$ even for small values of the quadratic Zeeman energy. We have shown that a refined theory taking into account a finite spin temperature allowed to retrieve large fluctuations $\Delta N \propto N$ for finite quadratic Zeeman energies q . We have extracted the spin temperature from experimental n_0 distributions. We noted a very different behavior for high and low values of the quadratic

Zeeman energy q . For high q , the spin temperature follows the kinetic temperature, while for low q , the spin temperature does not depend on the trap depth and is much lower than the kinetic temperature. We believe this originates from a different mechanism, in which the thermalization between the spin and kinetic degree of freedom is inhibited by the large difference in energy scales at low quadratic Zeeman energies.

Both studies presented in this chapter were performed for quite high condensed fractions $f_c > 0.7$, such that the thermal fraction enters only as a correction to the $T = 0$ model. The study of higher temperature clouds would allow the study the onset of phase locking with condensation. For example, we have seen that the amount of transverse spin was reduced as the kinetic temperature was increased due to the $m_F = 0$ component vanishing. We could measure the transverse spin as a function of temperature and see whether the phase locking mechanism exist regardless of the condensed population in the $m_F = 0$ component, or whether it washes out near the critical point.

Another study could consist in studying the dynamics of thermalization in both system. We could quench through the second critical temperature for Bose-Einstein condensation (we call the second critical temperature, the temperature at which the minority component condenses, see chapter 4 for more details) and observe the spin of the system, either by measuring their transverse spin, or by measuring the fluctuations of n_0 for $m_z \sim 0$ and $q \sim 0$. It would be interesting to study whether the condensate appears already with the correct phase relation, or if the phase goes from random to π within a few spin changing collisions (a time scale $\sim 1/U_s$).

“L’air était frais au fond du puits. Mon état d’excitation devait être telle à mon arrivée en bas, que je n’avais pas du tout pensé à la température. Mais maintenant, je sentais nettement le froid sur ma peau. [...] J’avais complètement oublié que la température au fond d’un puits n’était pas la même qu’à la surface de la terre.”

CHRONIQUES DE L’OISEAU À RESSORT
Haruki Murakami

4

Thermodynamic phase diagram of a spin 1 Bose gas

SPIN-DEPENDENT INTERACTIONS are responsible for many properties of spin 1 Bose-Einstein condensates, such as the existence of several magnetic phases, or of a phase locking mechanism between Zeeman components as discussed in chapter 3. They also conserve the magnetization. As we discussed in chapter 1, section 4, the conservation of the magnetization in the system give rise to several thermodynamic phases where either one or two spin components are condensed depending on the temperature. In this chapter, we study experimentally these thermodynamic phases. We vary the temperature, magnetization and magnetic field and deduce from observation of a spin 1 Bose gas which Zeeman components are condensed and which are not.

In the temperature range that we can explore in this experiment, the thermal energy is much higher than the spin exchange energy $k_B T \gg U_s$. If we considered a naive analogy to magnetism in solid state systems, we would no expect to observe magnetic order in our system. Nevertheless, we have seen in the previous chapter that the large spin degeneracy in the condensed component makes the small spin exchange energy relevant even when small compared to temperature of the gas and the chemical potential of the condensate. One consequence of the relation $k_B T \gg U_s$ can be observed in thermal Bose gases. Above the critical temperature for Bose-Einstein condensation, we observe (see the left part of fig. 4.1 for example) that all Zeeman states are populated although not equally, as the thermal gas has a finite magnetization. At low quadratic Zeeman energies, we typically observe that $N_0 \sim N_{-1}$ and that $N_{+1} \sim N_{-1} + M_z$. Near $T = 0$ on the other hand, where we observe quasi pure condensates, we have seen in the previous chapter that a competition between the spin exchange interactions and the quadratic Zeeman energy sets the magnetic order in the system. In this chapter, we investigate the transition between these two temperature regimes, *e.g.* whether magnetic ordering appears simultaneously to Bose-Einstein condensation or whether they appear in a particular sequence.

The transition from a thermal gas to a magnetically ordered spinor BEC has been extensively studied theoretically both for the ferromagnetic case and antiferromagnetic case (see refs. [64, 85–92]). We recall in particular that ideal gas theory, including a conserved magnetization, predicts five condensation scenarii depending on the magnetization and quadratic Zeeman energy (see chapter 1, sec. 4):

1. $q = 0, m_z > 0$: The $m_F = +1$ component condenses first and the $m_F = 0, -1$ components

condense simultaneously at lower temperature.

2. $q = 0, m_z = 0$: The $m_F = 0, \pm 1$ components condense simultaneously.
3. $q > 0, m_z = 0$: Only the $m_F = 0$ component condenses.
4. $q > 0, m_z < m_z^*$: The $m_F = 0$ component condenses first and the $m_F = +1$ component condenses at lower temperature. The $m_F = -1$ component never condenses. We have seen in chapter 1 (see Sec. 1.4), that m_z^* is defined as the magnetization for which the $m_F = 0$ and $m_F = +1$ components condense simultaneously.
5. $q > 0, m_z > m_z^*$: The $m_F = +1$ component condenses first and the $m_F = 0$ component condenses at lower temperature. The $m_F = -1$ component never condenses. We note that if $0 < q < k_B T_{c,id}$ where $T_{c,id}$ is the critical temperature of the scalar gas, m_z^* is small, and this scenario is the most commonly observed.

In contrast with numerous theoretical investigations (see refs. [85–92]), the thermodynamics of spinor Bose gases was scarcely studied. First, the LPL group in Paris measured the thermodynamic phase diagram of chromium atoms, for which there is no conservation of m_z (see ref. [202]). The physics of this system is strongly affected by dipolar interactions. They lead to a process called dipolar relaxation (see refs. [59, 203]) which prevents the study of multi-component condensed phases at equilibrium (see ref. [41, 203] for out of equilibrium investigations). Because of this, only the first transition, of the majority component was observed in ref. [202]. Second, in the Berkeley group (see refs. [204, 205]), a gas of spin impurities is created from a gas of rubidium atoms polarized in $m_F = -1$ with a radio frequency pulse. This gas of $m_F = 0$ atoms (called magnons) is observed to condense at low temperature. This study highlights that spin-independent interactions affects the condensation of the spin impurity due to the presence of a large condensate in the majority component. We note that the study was limited to nearly polarized samples $m_z > 0.9$ and negligible quadratic Zeeman energy.

In this chapter, we present a comprehensive study of the thermodynamic phase diagram of an antiferromagnetic spinor condensate of sodium for a wide range of magnetizations from 0 to 1. We will demonstrate experimentally the existence of a double condensation scenario, and highlight the effect of interactions (both spin-independent and spin exchange interactions) on the thermodynamic phase diagram of the system. As an introduction, fig. 4.1 presents an overview of the various phases that we observed. We present pictures from the experiment, stacked from left to right with decreasing temperature, for four different parameter sets. Regardless our control parameters (the magnetic field B and the magnetization m_z), we observe all Zeeman components are populated at high temperature. As the temperature decreases we observe the general behavior starts to differ from one parameter set to the other. We observe a phase in which only one component is condensed, below a *first critical temperature* T_{c1} . This phase is common to several values of the experimental control parameters B and m_z . Below a *second critical temperature* T_{c2} , we observe a different behavior for all 4 set of parameters shown in fig. 4.1. We also observe that well below T_{c2} , we recover the magnetic phases observed in ref. [54] for $T=0$.

In section 1, I will present the experimental methods that we developed for the needs of this experiment. Indeed, the measurement of high temperature gases in a way that allows us to distinguish each spin component requires different imaging and fitting methods than the ones described in chapter 2. In section 2, I will present and discuss the exploration of the thermodynamic phase diagram. We have measured numerous samples by varying both magnetization and temperature,

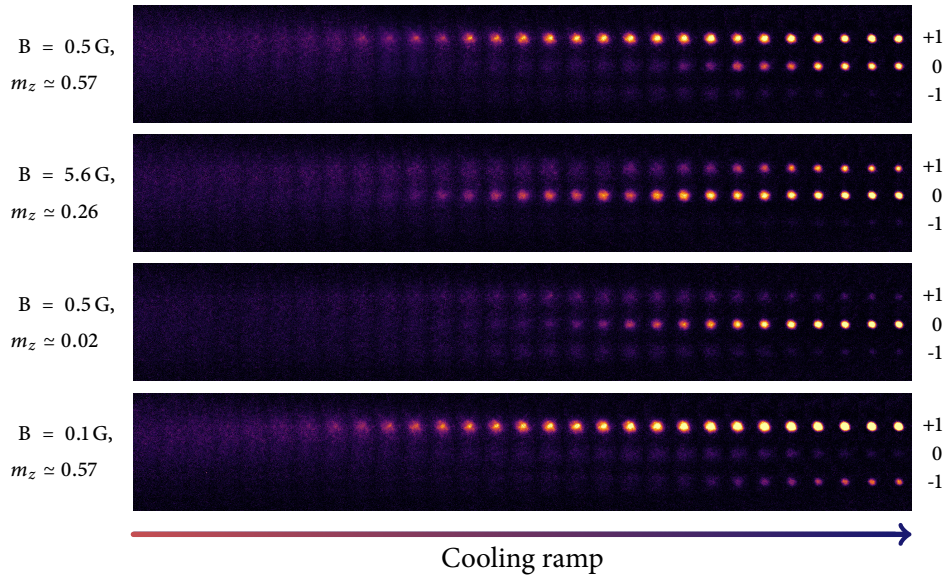


FIGURE 4.1: Stacked pictures of spinor Bose gases with decreasing temperature toward the right. We show the different Bose-Einstein condensation scenarios observed while cooling of an anti-ferromagnetic spin 1 Bose gas. On the first line, $B = 0.5$ G and $m_z = 0.57$, and we observe the sequential condensation scenario 5. The majority component $m_F = +1$ condenses first, followed by the $m_F = 0$ component, while the $m_F = -1$ remains thermal. On the second line, $B = 5.6$ G and $m_z = 0.26$, we observe scenario 4, the $m_F = 0$ condenses first. This is due to the large quadratic Zeeman energy $q \sim k_B T$, which favors the $m_F = 0$ component and increases its density near the critical temperature for low magnetizations m_z . In a third line, $B = 0.5$ G and $m_z = 0.05$, we observe scenario 3, the $m_F = 0$ condenses alone. In the fourth line, $B = 0.1$ G and $m_z = 0.57$, and we observe a scenario that we shall discuss in more details later in the chapter and that is not predicted by ideal gas theory. It suggests that the magnetic ordering demonstrated in chapter 3 for very low temperatures is also observed close to the Bose-Einstein transition and manifests as a different condensation scenario. In this case, the $m_F = +1$ condenses first, but it is followed by the $m_F = -1$, and the $m_F = 0$ component does not condense.

and considered three values of the quadratic Zeeman energy for which the thermodynamic phase diagrams differ. We will present methods to extract critical quantities from these measurements and discuss the results in terms of critical temperatures of each Zeeman component. In section 3, we will discuss how to relate our observations to a realistic theoretical description of the experiment using the Hartree-Fock theory. This is required because, to our knowledge, none of the previous theoretical studies found in refs. [64, 85–92] include all the elements required for a complete description of our gases *e.g.* a trap, the quadratic Zeeman energy and interactions.

4.1 Experimental methods

In chapter 2, we have described the experimental methods used, for example, in chapter 3, to characterize Bose-Einstein condensates and single component thermal gases. In this section we will describe how to modify and extend these techniques in order to measure the thermodynamic

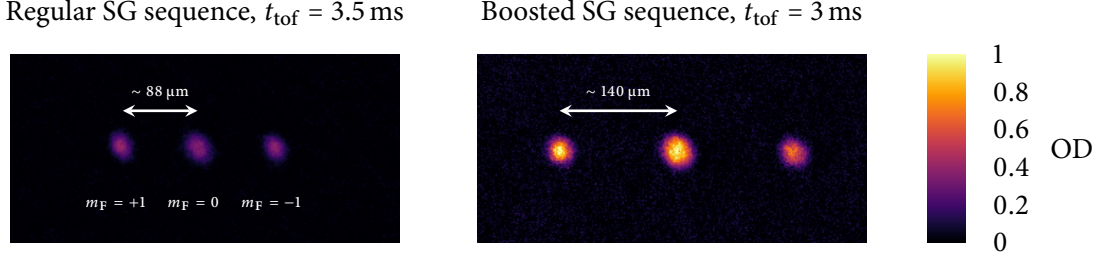


FIGURE 4.2: Pictures of three component condensates after a regular, and a boosted Stern-Gerlach sequence. We observe that the boosted Stern-Gerlach sequence achieves a significantly larger separation in a (slightly) shorter time of flight and without the need of an attenuation sequence.

phase diagram of spin 1 Bose gases. In Sec. 2.2.1, we have seen that we perform spin-dependent detection by separating spatially the Zeeman components, in a Stern-Gerlach experiment, such that we image them in different locations of the CCD sensor at the end of the time of flight. For the highest temperature thermal gases, we observe a fast expansion such that a larger separation between the cloud is needed to distinguish each component than for the case of condensates. Furthermore, we have discussed in chap. 2 that the Stern-Gerlach sequence that we used to observe BECs involves an attenuation sequence during which the gradient is ramped. For warm clouds (around T_{c1} or above) this attenuation sequence leads to thermal atoms “leaking” to the arms of the dimple trap (DT), and as such cannot be used to extract temperatures or total atom number from time of flight distributions near the critical point.

In this section, after having discussed the experimental sequence, we will describe how we achieved this higher separation with a “boosted” Stern-Gerlach sequence. We show an example of image obtained with this boosted SG sequence in fig. 4.2. We observe (see the first line of fig. 4.5 for instance) that for the highest temperatures measured, the expansion is nonetheless faster than the separation axis, such that we needed to develop new fitting methods to extract thermodynamic quantities from absorption images showing overlapping thermal clouds. In a second paragraph, we will present how we fit simultaneously the three components and how we obtain quantities of interest such as atom numbers and temperature.

4.1.1 Overview

We performed this experiment in a dimple trap (DT, see Sec. 2.1.3 and fig. 2.4), of which we adjusted the optical power (hence the trap depth V_0) in order to observe clouds at various temperatures. The experimental sequence is shown on fig. 4.3 and consists in stopping the evaporation ramp at the desired trap depth, and holding the atoms in the DT during 4 seconds to ensure equilibration. Then we apply a modified SG imaging sequence, and obtain an image of the cloud. We measured the trap frequencies as a function of dipole trap optical power by the methods described in Sec. 2.1.5. The sizes of the DT beams were deduced from a fit. We could not obtain a good agreement with a fit function using two isotropic beams because $(\omega_Y^2 - \omega_X^2)^{1/2} \neq \omega_z$ in our measurement. Instead, we considered an anisotropic horizontal beam, such that the three trap frequencies can be set independently. We note that this anisotropy could be an effective way of accounting for optical aberrations on the horizontal arm of the dimple trap. We obtain that the isotropic vertical arm has a waist of $w_V = 21.3 \mu\text{m}$ and that the anisotropic horizontal arm has

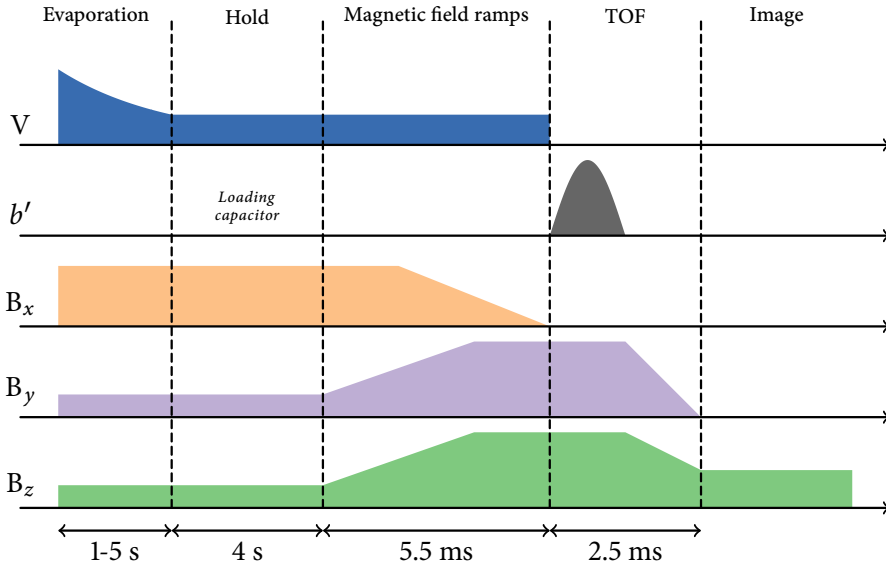


FIGURE 4.3: Experimental sequence for the measurement of the thermodynamic phase diagram of a sodium Bose gas. After a step of evaporation in the dimple trap, the cloud is held during four seconds to ensure equilibration. The hold time is also used for loading the capacitor used for the boosted Stern-Gerlach imaging.

waists of $w_{H,Y} = 21.7 \mu\text{m}$ and $w_{H,Z} = 29.8 \mu\text{m}$ (the data are the one represented in fig. 2.12)¹

We deduce the values of the trap depth V_0 from the dipole trap size, and calibrated dipole trap powers P_V, P_H with the help of Eq. (2.10):

$$V_0 = 2\alpha_0 \min\left(\frac{P_H}{\pi w_{H,Y} w_{H,Z}}, \frac{P_V}{\pi w_V}\right). \quad (4.1)$$

The magnetization of the cloud is prepared (Sec. 2.4.4) by either applying a RF field in presence of inhomogeneous broadening (which decreases m_z) or by applying a magnetic gradient (which increases m_z). We apply this preparation sequence before any of the experimental steps presented in this section, in a thermal cloud above at least twice the critical temperature T_{c1} . It is worth noting that each Zeeman component may undergo a different evaporation dynamics, such that the magnetization is not conserved during the evaporation ramp. However, as discussed in chapter 1 (see Sec. 1.1.4), the dynamics of evaporative cooling is much slower than the thermalization dynamics. As such, we consider the equilibrium state of the gas is determined by a Hamiltonian that conserves magnetization, and which follows the slowly changing magnetization of the ramp remaining in equilibrium at all time.

We find that the magnetization indeed varies, and changes by 10% as V_0 is varied from the highest to the lowest value we use. We illustrate this in fig. 2.5 from chapter 2. In order to account for this effect, we will measure the magnetization in each realization of the experiment, and determine the “critical” magnetization $m_{z,c}$ at the critical point.

¹This model will only be used to determine the trap depth. For the measurement of the thermodynamic phase diagram, we extracted the geometric average of the trap frequencies $\bar{\omega}$ from an exponential interpolation of the data shown in fig. 2.12.

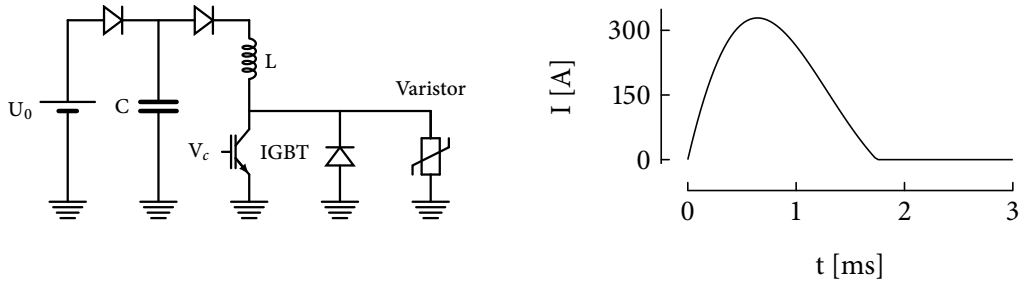


FIGURE 4.4: Representation of the high voltage current pulse generator used for the boosted Stern-Gerlach imaging sequence. **Left:** electrical circuit. Typical values for components are $C \sim 2.2 \text{ mF}$, $L \simeq 140 \text{ } \mu\text{H}$ and $R \sim 112 \text{ m}\Omega$. **Right:** current pulse calculated with a loading voltage of $U_0 = 150 \text{ V}$.

4.1.2 Boost to the Stern-Gerlach separation

The measurement of the thermodynamic phase diagram of a spin 1 gas requires to measure “warm” clouds, above the critical temperature for BEC, while keeping spin-dependent imaging. These clouds have a high thermal energy such that the expansion speed is higher at the release than the one of condensates that we have considered until this chapter. This causes the clouds to overlap on absorption images taken with the Stern-Gerlach sequence described in Sec. 2.2.1.

In order to minimize the overlap, we need to increase the separation between Zeeman components, while keeping high enough signal to noise ratio. This is done by increasing the spin-dependent force used to separate the clouds for a fixed expansion time. According to Eq. (2.12), this can be achieved by a stronger quadrupolar field. The main challenge in obtaining higher gradient lies in the timescales with which the current needs to be settled in the MOT coils (see fig. 2.2), and by the current strength required. The large current pulse is by no means straightforward to obtain as the instantaneous electrical power required for such a process can be quite high. For example, the energy necessary to settle a current of $I = 300 \text{ A}$ in a coil with inductance $L = 150 \text{ } \mu\text{H}$ is $E = 6 \text{ J}$ in absence of any dissipation. If the process is performed in a half a millisecond the average required power is around 12 kW . This value is increased in presence of dissipation (finite resistance of the circuit), and is nevertheless beyond the capabilities of our power supplies.

As a solution, we developed a current pulse generator based on a large capacitance, high voltage capacitors, that can store this large energy and deliver it to the coils in a short time. The modified Stern-Gerlach sequence (see fig. 4.3) starts by loading the capacitor with a low current, high voltage (150 V) power supply during the hold. Then, we ramp an appropriate magnetic bias field such that the separation axis is set along the y axis (see fig. 2.4 and Eq. (2.12)). Finally, we trigger a current pulse when atoms are released from the trap by applying a voltage on the gate of an insulated gate bipolar transistor (IGBT). This triggers half an oscillation of the LC circuit formed by the MOT coil and the capacitor. The peak current can reach up to 1000 A depending on the initial charge in the capacitor. We damp the negative alternation in a large power diode and in varistors placed in parallel to the IGBT (see fig. 4.4). We note that the loading of such capacitor, can require up to a few seconds with a regular high voltage DC lab power supply (power 100 W in our case).

As shown in Eq. (2.12), the strength and direction of the magnetic force is not only determined

by the gradient strength b' but also by the presence of a large bias field:

$$\mathbf{F}_{\text{SG}} = \frac{\mu_{\text{B}} g_{\text{F}} m_{\text{F}} b'}{2|\mathbf{B}_{\text{SG}}|} \begin{pmatrix} -(\mathbf{B}_{0,x} + \mathbf{B}_{m,x}) \\ 2(\mathbf{B}_{0,y} + \mathbf{B}_{m,y}) \\ -(\mathbf{B}_{0,z} + \mathbf{B}_{m,z}) \end{pmatrix}. \quad (4.2)$$

During the current pulse, we observed that a large uniform field was generated along the vertical direction together with the intended quadrupolar field, which we believe can be due to a relative tilt of the MOT coils with each other or to eddy currents. Because of the limited current we could apply to the bias coils (in particular to the vertical pair), it was not possible to compensate for this vertical field and obtain a strong enough bias field along y . As such, we generate an additional, strong, bias field by adding a coil on one side of the setup (at the position of one of the coil from the pair Y bias in fig 2.4) that we connect in series with the MOT coil in the circuit from figure 4.4. In this way, the uniform field during the Stern-Gerlach sequence is mostly along y at all times. We observed the trajectory of the atoms during time of flight were only affected by the current pulse ~ 1 ms after the start of their release. We suspect this delay on the magnetic pulse as compared with the current pulse is due to eddy currents from the vacuum chamber and copper vacuum gaskets. With this setup we can achieve a separation roughly twice as big after 2.5 ms time of flight than with the method from sec 2.2.1 without the need of the attenuation sequence.

The main inconvenient of this method is that the current pulse is so strong that it actually generates vibrations in the setup, which is detrimental for the absorption image quality. Furthermore, due to the vertical component of the uniform field, we observe a tilt of the separation axis along the vertical direction (see Eq. (4.2)). This leads to a vertical separation of the Zeeman components at the time of imaging of roughly $80 \mu\text{m}$. It results in a slight difference in imaging resolution when considering different Zeeman components. For experiments discussed in this chapter, this is not relevant because we only measure objects of size much larger than the imaging resolution.

4.1.3 Image Analysis

Absorption signal

The measurement of the populations of Bose-Einstein condensates, and the extraction of temperatures from single component gases have been discussed in Secs. 2.2.1 and 2.2.4. In this chapter, different methods are required because the Zeeman components can overlap after time of flight. We recall that we measure atomic densities through the absorption of a probe laser of intensity $I(\mathbf{r})$ propagating along z . This intensity is measured twice in the experiment in presence of atoms (I_1) and without atoms (I_2). If we neglect the influence of the changes of probe profile intensity between the two images (which has been considered in Sec. 2.2.2), we have $I_1 = \lim_{z \rightarrow -\infty} I(z)$ and $I_2 = \lim_{z \rightarrow \infty} I(z)$. The expression of $I(z)$ can be obtained by considering the Beer-Lambert law:

$$\frac{\partial I}{\partial z} = - \sum_m \sigma_m \tilde{n}_m I. \quad (4.3)$$

where \tilde{n}_m are the column density of each Zeeman component. We recall that the absorption cross-sections are given by the ad hoc formula:

$$\sigma_m = \frac{\zeta_m \sigma_0}{1 + (I/I_{\text{sat},m}) + (2\delta_m/\Gamma)^2}, \quad (4.4)$$

where ζ_m is a coefficient that describes the deviation of the scattering cross-section to the two-level model due to optical pumping for example.

At this point we shall recall that in experiments with Bose-Einstein condensates, each component sits in a region of the sensor where the density of the two other components is negligible (see chapters 2 and 3). As such, in chapter 2, Sec. 2.2.1, we defined three region of interest each containing one component. In each of them, the right hand side of Eq. (4.4) reduces to one term, and we can use Eq. (2.5) to compute the column densities \tilde{n}_m from images I_1 and I_2 in each zone independently. In this chapter, where components overlap for high temperature clouds, we notice that the extraction of the three column densities \tilde{n}_m from the second image (by solving the equation (4.3) for \tilde{n}_m) is not possible without assumptions on the spatial variations of \tilde{n}_m . In fact, it is not even possible to compute the total column density $\tilde{n} = \sum_m \tilde{n}_m$ from the second image if the cross-sections σ_m take a different form *e.g.* different values of the detunings δ_m , the parameter ζ_m or the saturation intensity $I_{\text{sat},m}$.

From there on, the fitting procedure of such overlapping cloud could be done by converting theoretical column densities into intensities with eq. (4.3). Besides being tedious, this procedure does not allow straightforward averaging given the probe intensity profiles varies from one experimental realization to another (see chapter 2, Sec. 2.2.2). Instead, we take advantage that experiments in this chapter were performed at low intensities $I \ll I_{\text{sat}}$. In this case the right hand side of Eq. (4.3) becomes:

$$\frac{\partial I}{\partial z} \simeq - \sum_m \frac{\sigma_0}{\alpha_m} \tilde{n}_m I \left(1 - \frac{I}{I_{\text{sat}}} + \frac{I \delta I_{\text{sat},m}}{I_{\text{sat}}^2} \right), \quad (4.5)$$

Where we have considered that all Zeeman components have a similar value for their saturation intensities $\zeta_m \alpha_m I_{\text{sat},m} = I_{\text{sat}} + \delta I_{\text{sat},m}$, with $\delta I_{\text{sat},m} \ll I_{\text{sat}}$. The coefficient α_m is expressed as $\alpha_m = (1 + (2\delta_m/\Gamma)^2)/\zeta_m$. We neglect the third term in Eq. (4.5) since $I \delta I_{\text{sat},m}/I_{\text{sat}}^2 \sim 1\% \ll I/I_{\text{sat}} \sim 0.1 \ll 1^1$. For our experimental parameters $I \sim I_{\text{sat}}/10$. This allows us to obtain the following equation:

$$\frac{dI}{I(I/I_{\text{sat}} - 1)} \simeq - \frac{dI}{I} + \frac{dI}{I_{\text{sat}}} \simeq \sum_n \frac{\sigma_0 \tilde{n}_m}{\alpha_m} \quad (4.6)$$

We note that if the column density $\tilde{n} = \sum_n \tilde{n}_m$ is still not directly accessible with Eq. (4.6). We can however extract an absorption signal, that we define as:

$$S_{\text{abs}} = - \frac{1}{\sigma_0} \left[\ln \left(\frac{I_1}{I_2} \right) + \frac{I_2 - I_1}{I_{\text{sat}}} \right] \simeq \sum_m \frac{\tilde{n}_m}{\alpha_m}, \quad (4.7)$$

with an error of about 1% due to saturation effects. We note that if $\alpha_{+1} = \alpha_0 = \alpha_{-1}$, the absorption signal is directly proportional to the total column density.

The absorption signal is in this model composed of the weighted sum of atomic column densities. The atom number N_m in each component m can be recovered from the fits by simple integration of the fits. We calibrate the parameters α_m and I_{sat} using nearly pure BECs that do not overlap at the time the image is taken (see Sec. 2.2.4). In the following we will rather speak of the ‘‘optical density’’ $\text{OD} = \sigma_0 S_{\text{abs}}$.

As discussed in Sec. 2.2.2, an additional benefit of using low imaging intensities comes from the reduction of fringes in absorption images without requiring the defringing algorithm as

¹We estimated the differences in saturation intensity $\delta I_{\text{sat},m} \sim 500 \sim 0.1 I_{\text{sat}}$ by calibrating independently the saturation intensities with non overlapping clouds.

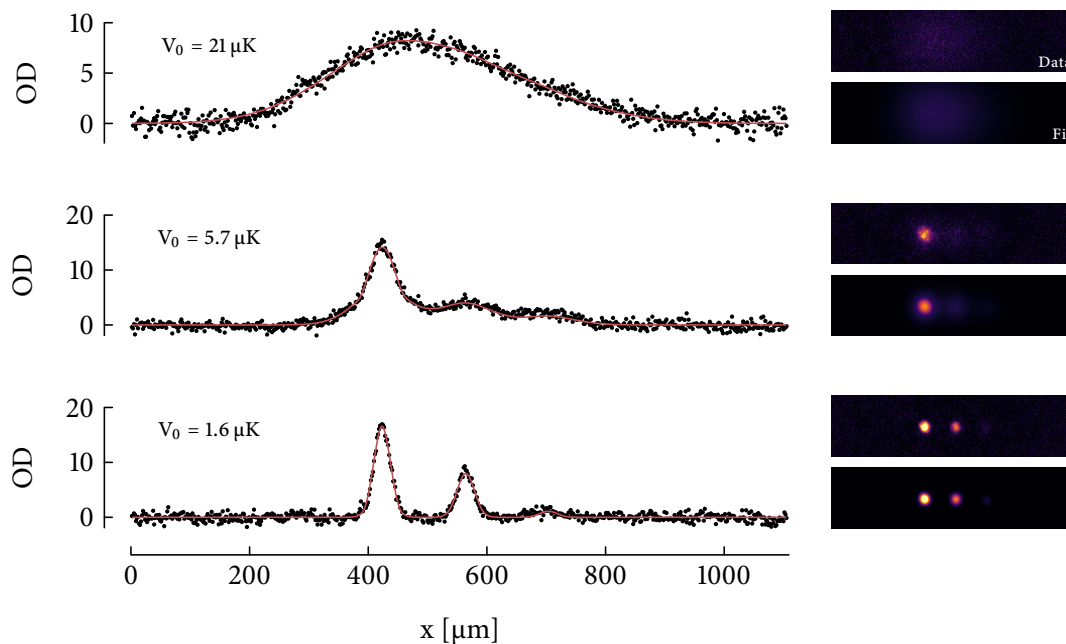


FIGURE 4.5: Example of three bimodal fits on averaged images. On the left we show integrated density profiles (dots represent integrated data, solid lines integrated fits). On the right we show the corresponding pictures for both data and fit. In the first line, we represent a pure thermal cloud, in which we observe that each of the three components are populated, and that they overlap after the Stern-Gerlach imaging sequence. In the second line, we show a lower temperature cloud, in which the $m_F = 1$ component has condensed. We observe the characteristic “double structure” on the $m_F = +1$ component. On the third line, we show an even lower temperature cloud in which both the $m_F = +1$ and $m_F = 0$ component have condensed. We observe a small thermal population in $m_F = -1$.

described in Sec. 2.2.2. Indeed, structured noise that typically appear for high imaging intensity leads to artifacts on the output of the fitting procedure, which is not the case for uncorrelated noise provoked by photonic shot noise. In addition, the defringing algorithm from ref. [179] (see Sec. 2.2.2) requires to be efficient to use a large number of pixels, close to the region of interest for fitting, which is difficult in this experiment due to the large size of the highest temperature thermal clouds. As discussed in Sec. 2.2.2, probe intensity fluctuation are accounted for by including an offset to the fitting functions we use, which eliminates the shift of the optical density caused by the intensity difference between the two images.

Simultaneous fit of the three components

We show examples of absorption images obtained by Eq. (4.7) (averaged on four experimental realizations), and corresponding integrated profiles, obtained after the boosted Stern-Gerlach sequence on fig. 4.5. We extract populations (hence the magnetization) and temperatures from a fit to such images. We extend the fitting methods exposed in Sec. 2.3 and fit our images with the

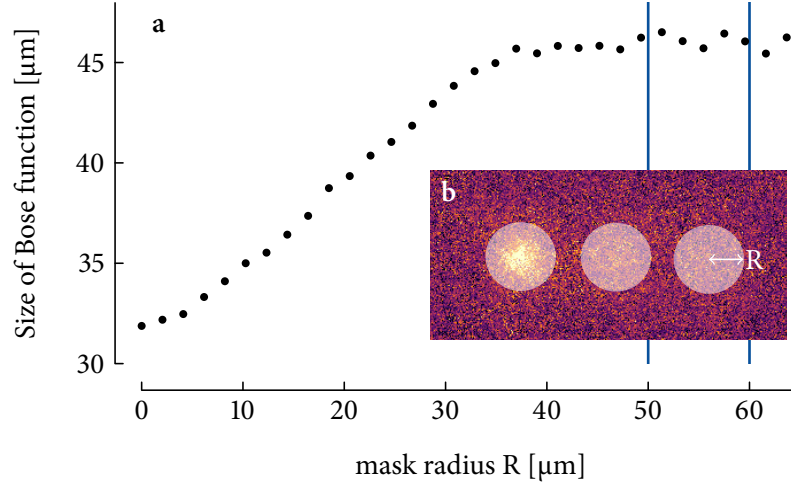


FIGURE 4.6: Extraction of temperature by fitting three Bose functions to masked images. **b** Representation of a masked image for a mask size of radius $R = 50 \mu\text{m}$. **a** Size of a Bose function extracted from fits with varying mask radius. We observe that the size of the Bose distribution is underestimated for small mask radii where the BEC distribution is not completely masked. For mask radii larger than $35 \mu\text{m}$, the fitted size does not depend on the mask, and this value is taken as the size for the thermal distribution.

sum of three Bose functions (2.27) and Thomas Fermi-functions (2.29) (see ref. [133]):

$$S_{\text{abs}}(x, y) = \sum_{m=+1,0,-1} \tilde{n}_{m,\text{Bose}}(x, y) + \tilde{n}_{m,\text{TF}}(x, y). \quad (4.8)$$

We recall for the sake of clarity the expression of the Bose and Thomas-Fermi models for the column densities:

$$\tilde{n}_{m,\text{Bose}}(x, y) = \mathcal{A}g_2 \left(z \exp \left(-\frac{(x - c_x)^2}{s_x^2} - \frac{(y - c_y)^2}{s_y^2} \right) \right), \quad (4.9)$$

$$\tilde{n}_{m,\text{TF}}(x, y) = \mathcal{A} \max \left(1 - \frac{(x - c_x)^2}{r_x^2} - \frac{(y - c_y)^2}{r_y^2}, 0 \right). \quad (4.10)$$

We note that we fit simultaneously the three Zeeman components, which is required because of the overlap of the thermal fractions for highest temperatures (see upper panel of fig. 4.5). We have found that using Eq. (4.8) with its large number of parameters (12 sizes, and 6 amplitudes, in addition to centers and offsets) was difficult. As such, we decided to fix a few parameters in order to make the parameter estimation procedure more reliable. We fixed the position of the clouds, as we did not detect significant variations (less than 1 pixel) of the center of Bose-Einstein condensates. Furthermore, we have set identical sizes for all components, which is justified for thermal clouds if the Zeeman components are in thermal equilibrium with each others, and for the condensates by the single mode approximation, valid in our parameter range $\hbar\omega \gg U_s$ (regardless of the trap depth considered). Finally, we have taken $z = 1$ in the thermal gas (model (4.9)). This does not bias the temperature extraction at the critical point, but may lead to an underestimation for clouds above the critical temperature, which does not play a large role in the following measurement.

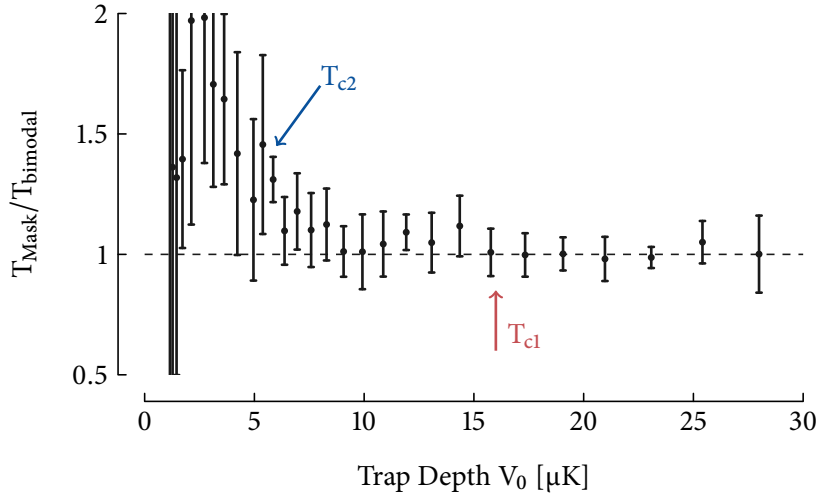


FIGURE 4.7: Comparison of the two temperature extraction methods, from three bimodal fits – T_{bimodal} – and from fit to masked images – T_{Mask} . We see both methods agree within error bars above T_{c1} . However, they disagree slightly below T_{c1} and strongly around T_{c2} .

We show an example of the results of the bimodal fitting procedure in different temperature regimes in fig. 4.5. We observe that the thermal fractions are indeed overlapping such that it is hard to distinguish the different Zeeman components in the upper panel, showing a thermal gas above T_{c1} . The thermal components still overlap below the first critical temperature shown in the central panel, but can be distinguished more easily. We observe on this panel, the familiar “bimodal” distribution composed of a narrow peak on top of a larger Gaussian-like cloud, that is often shown as a signature for Bose-Einstein condensation (see ref. [11]). In the third panel, the condensed fraction is high, and it is hard to distinguish thermal wings on condensed components.

The fitting functions considered in this section are chosen by default in the absence of a more accurate model for the TOF distribution. They are expected to represent faithfully the time of flight distributions in two limiting cases only, a pure BEC (with large atom number) and a warm cloud above T_{c1} . In the case of the condensate, the BEC should be populated enough such that it is in the Thomas-Fermi regime (see chapter 1). We expect this approximation to fail near the critical point (see ref. [107]), and the fitting procedure could miss small condensates. Regarding the thermal component, we expect the Bose function representation of the momentum distribution to hold as long as interactions can be neglected in the determination of the expansion dynamics. In the case a condensate is present, the low momentum part of the momentum distribution will be affected, and the density distribution after time of flight is likely to be affected near the center. As a conclusion, we suspect this procedure is in fact subject to uncontrolled systematic errors in the determination of sizes below the critical point and of condensed fractions near the critical point. We expect however that the determination of atom numbers, by integrating fitted absorption signals, will be faithful because the least square minimization ensures a minimal difference in the integrated densities.

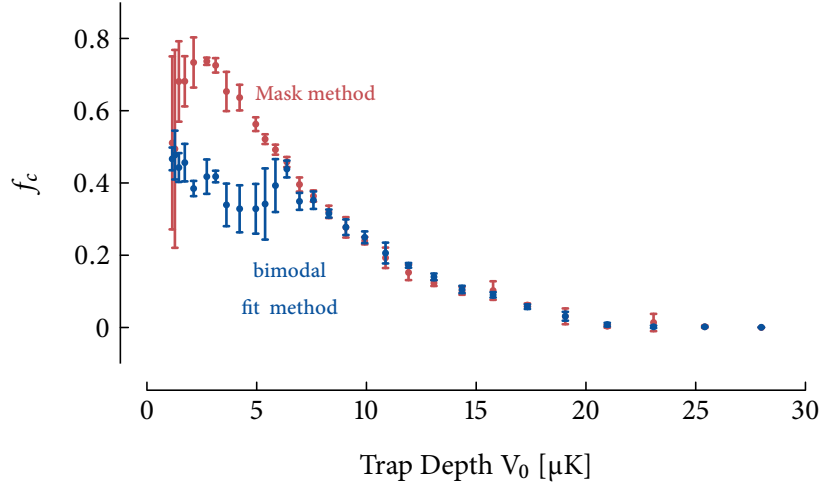


FIGURE 4.8: Comparison of the extraction of the condensed fraction in a gas with $m_z \sim 0.9$ either from fitting Thomas-Fermi profiles to the residuals of the masked fits, or by direct fit bimodal density distributions to the absorption signal. We observe that the determination of the condensed atom number seems to differ around $V_0 \simeq 7 \mu\text{K}$, which corresponds to the points where the two fitting methods disagree on their fitted temperature.

Extraction of the temperature from fits with a mask

As discussed in the previous paragraph, the bimodal fitting procedure uses heuristic fitting functions for the condensed and thermal components which possibly leads to systematic errors of uncontrolled amplitude on the extraction of the temperature or the condensed fraction. However, as we have discussed in chap. 2, Sec. 2.3 the behavior of the thermal wings is expected to match that of an ideal gas distribution at large momenta irrespective of the trap potential or interactions, $n_{\text{th}} \propto_{p \rightarrow \infty} g_2(\exp \beta(\mu - p^2/2m))$. As such, in order to avoid systematic errors in temperature determination when a condensate is present, we generalize the “plateau” (or “mask”) method presented in Sec. 1.11 to three component clouds. We use the sum of three Bose functions that we fit to a masked image such as the one shown in fig. 4.6b. We repeat this procedure with many masks of varying size, and represent the sizes of the Bose distribution as a function of the mask radius as in fig. 4.6a. When the mask is smaller than the condensate size, the fit procedure underestimates the size of the Bose distribution due to the presence of the much narrower condensate distribution. However, as the mask covers fully the condensate, the fitted size does not depend anymore on the mask size (we call it a “plateau”, see ref. [135]). We extract the temperature by averaging the sizes found by fits with mask values between $50 \mu\text{m}$ and $60 \mu\text{m}$, which is always larger than the condensate size, and ensures good signal to noise down to T_{c2} .

For the sake of completeness, we have compared the temperature determination methods either from three bimodal fits or from the mask method in fig. 4.7. We observe that the methods agree with each other within error bars above T_{c1} . However, they disagree around and below T_{c2} . The bimodal fit method systematically returns a lower temperature for the coldest clouds. This could be due to the presence of a large condensate in this temperature regime that would either modify the expansion dynamics of the thermal fraction or result in artifact of the fitting procedure.

Beside the extraction of temperature, the analysis of the residuals of the fits obtained with the mask method allows us to obtain an estimation of the condensed population. We display the

number of condensed atom obtained by integration of these residuals on fig. 4.8. We observe that the integrated residuals suggest a much higher condensed fraction than the bimodal fitting at low temperatures. We believe that in this range of parameter, the time of flight density profile of the thermal cloud is modified near the condensate such that the bimodal fitting procedure finds a larger (and narrower) thermal cloud than the mask procedure, resulting in an underestimation of the condensed fraction.

4.2 Experimental thermodynamic phase diagram of a spin 1 Bose gas

In the previous section, we have described how obtain the optical density and how to extract thermodynamic quantities from absorption images. In this section, we will focus on the determination of the critical points where Bose-Einstein condensates appear, present the measurement of the thermodynamic phase diagram and discuss the thermodynamic phases that we observe. As discussed in the previous section, the condensed fractions are quite difficult to extract from the fits near the critical point, and we discuss in this section an alternative method to determine at which trap depth Bose-Einstein condensation effectively takes place. Once we have exposed the method to obtain the critical points, and associated thermodynamic quantities, we will present our measurement of the thermodynamic phase diagram of a spin 1 Bose gas.

4.2.1 Extraction of the critical temperature

The most natural way to obtain the critical point for Bose-Einstein condensation would consist in plotting the condensed atom number N_c as a function of temperature $N_c = f(T)$ and to search for the lowest temperature at which no condensed fraction is detected $T[N_c = 0]$. However, we have discussed in the previous section, that we could not trust the results of the bimodal method near the critical point. We discussed that the mask method allowed to extract high condensed fractions in a more reliable way than the bimodal fit method. However the detection of a small condensate on top of a large thermal cloud present different constraints. In particular, the adequacy of the fitting function near small momenta is very important if one needs to determine a very small difference in density near the center from a fit to the wings. However, we have discussed that the central region of time of flight distributions, that corresponds to small momenta, is the part of the time of flight distribution that is most sensitive to the effect of interactions on the expansion dynamics. Because near the critical temperature, interactions in the thermal cloud can have a significant effect (see Sec. 1.1.1), we believe the determination of the condensed atom number near T_c with the “plateau” method is also subject to uncontrolled systematic errors near the critical point.

As such, we have decided to determine the critical point by directly analyzing images, using the peak density of the cloud as a proxy for condensed fraction. This procedure avoids systematic errors that any prior fitting procedure could induce in the determination of the critical point and simplifies the extraction of error bars on fit parameters. We measure the peak density from integration of a square zone of 3 by 3 pixels near the center of the time of flight distribution of each component. It is well known that Bose-Einstein condensation manifests by a sharp increase in peak optical density (see ref. [13] for example). As such, the critical point for each Zeeman component is determined by an abrupt change of optical density at a particular trap depth near the center of the time of flight distribution.

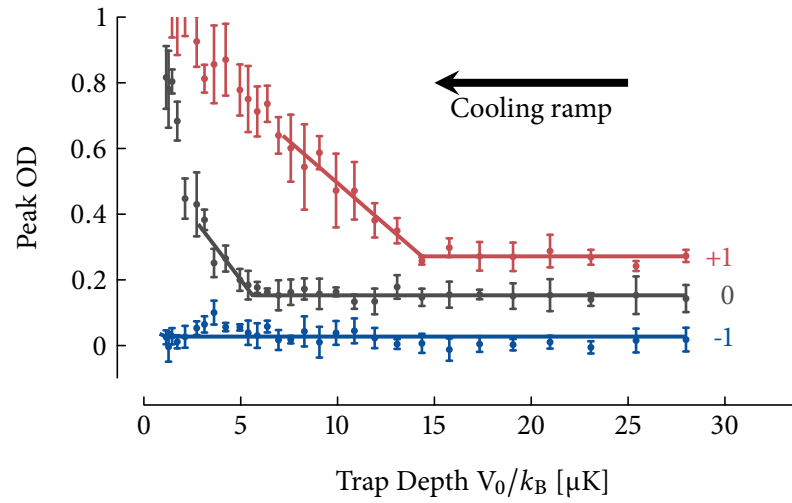


FIGURE 4.9: Determination of the critical trap depths $V_{0,c}$ by fitting two straight lines to the peak OD. We observe a sequential condensation scenario where the $m_F = +1$ component condenses first followed by the $m_F = 0$ component. The error bars represented are statistical, calculated from the peak OD of four images. We have added an offset to the peak OD of 0.1 for the $m_F = 0$ component and 0.2 for the $m_F = +1$ component in order to improve the figure legibility.

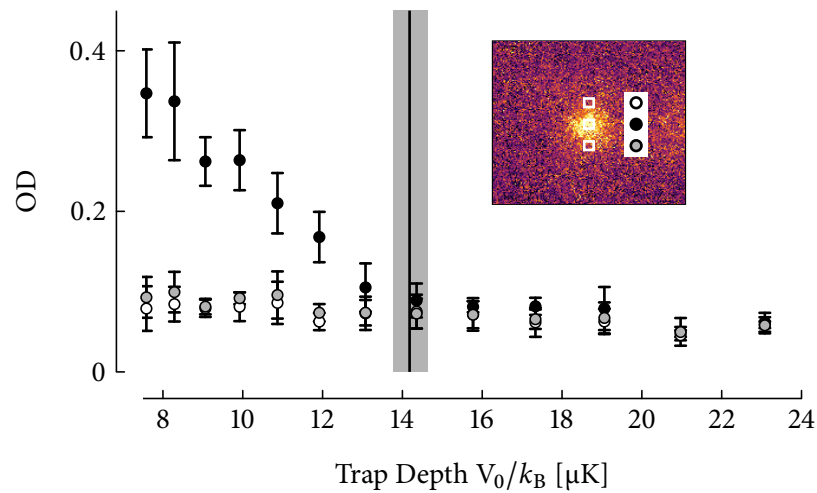


FIGURE 4.10: Peak optical density compared to the OD below and above the center region. This figure shows that the sharp increase in OD is only measured in the center of the momentum distribution. The inset shows the correspondence between the symbols and integration regions. The black line corresponds to the critical point extracted from a fit to the data, while the gray area represent the 1σ confidence interval of the fit.

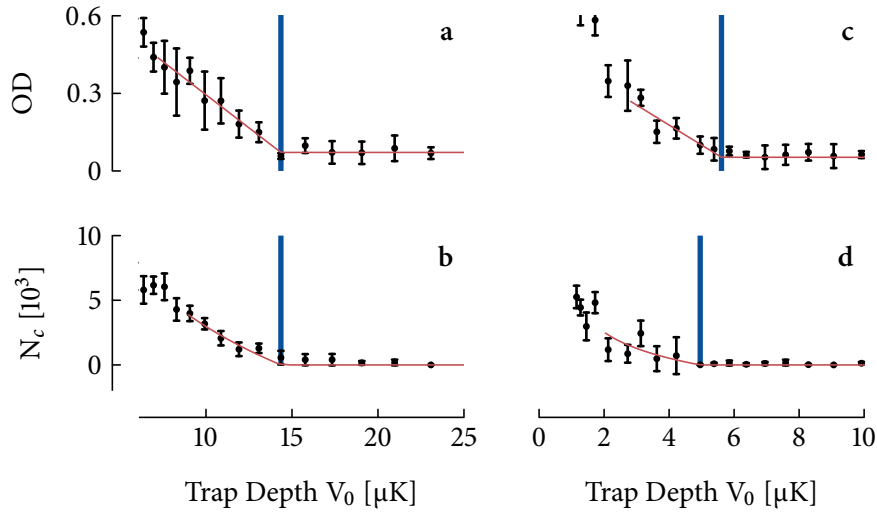


FIGURE 4.11: Comparison of the determination of the critical point either from critical atom number extracted from the increase of optical density (a,c) or from bimodal fits (b,d). We observe that in this particular case, the determination from the critical atom number extracted from fits underestimates the second critical temperature.

We represent the peak optical density as a function of trap depth V_0 fig. 4.9. Note that we added a 0.1 shift to the peak OD of the $m_F = 0$ component and a 0.2 shift to the peak OD of the $m_F = +1$ component for clarity. We observe a sequential condensation scenario where the $m_F = +1$ component condenses first, followed by the $m_F = 0$ component. For this particular parameter set, $m_z \simeq 0.4$ and $B = 0.5$ G, the $m_F = -1$ component never condenses (we observe no steep increase of the peak OD). We obtain the critical trap depth V_c for each component by fitting piece-wise linear functions to the peak OD near the critical point:

$$\text{od}_m = a_m + b_m \cdot \max(0, V_0 - V_{c,m}). \quad (4.11)$$

We display an example of the fitting procedure in fig. 4.9. We extract error bars on the critical trap depth $V_{c,m}$ by considering the sum of the squared residual χ^2 ¹ calculating the contour of value $\min(\chi^2) + 1$ (which is a 3 dimensional surface in $(a_m, b_m, V_{c,m})$ space), and extract a confidence interval on the critical trap depth from the maximum extent of this surface over the dimension $V_{c,m}$.

In order to ensure the validity of this analysis, we verified that the increase of the optical density is limited to the center of the density distribution. For this, we have compared the peak OD to the result of integration on a similar box, translated by 20 pixels upwards or downwards. We display the comparison on fig. 4.10, where we also display the measured critical point and its error bars, and confirm that the sudden increase of optical density we consider for the critical point is indeed limited to the center of the time of flight distribution.

Finally, for the sake of completeness, we compared the method used to determine the critical points from the peak OD as mentioned above to another one that uses the results from the three-component fitting procedure. For this, we consider the critical number of atoms $N_{c,m}$, obtained

¹We recall that, in the case of least square fitting, the χ^2 function is the sum of the squared residuals, and is a good estimator of the proximity between data and fit functions if each datapoint is described by a random variable that follow a normal law, see ref. [206].

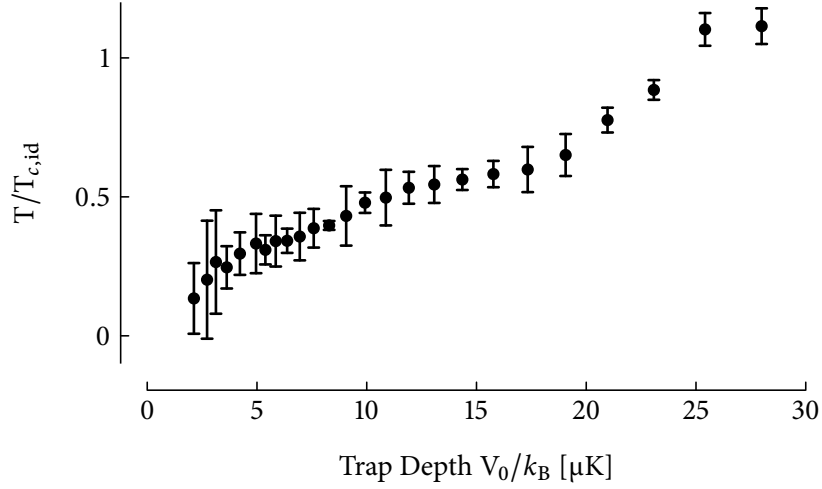


FIGURE 4.12: Renormalized temperature as a function of the trap depth. We show statistical error bars (each data point represent 4 images). The large statistical error bars for the lowest points can be explained by our inability to fit the lowest temperatures due to a poor signal to noise ratio when the thermal fraction vanishes.

from integration of the condensed density $n_{c,m}$ from Eq. (4.8). The critical point is found from a piece-wise linear fit as for the peak OD. The results of this procedure, compared with the one described above is presented on fig. 4.11. We observe both methods are in good agreement for the first critical temperature, but not for T_{c2} where the determination from the critical atom number tends to underestimate V_c as seen in the left panel.

4.2.2 Graphical representation of the data

In the previous paragraph, we have discussed how to determine critical points from the peak density. In this paragraph, before we turn to the actual representation of the critical points, we will first discuss a global representation of the peak OD that is shown in fig. 4.13, which allows a discussion on the general behavior regardless of the fitting method. When the experiment is performed, the precise value of the atom number and temperature varies slightly from shot to shot and with the magnetization preparation sequence. In order to compare all our points in a single representation, we used normalized quantities. We chose a normalized temperature by the critical temperature of a single component Bose gas with the same atom number and trap frequencies:

$$\frac{T}{T_{c,id}} = \frac{k_B T}{\hbar \omega N^{1/3}} g_3(1)^{1/3}, \quad (4.12)$$

We use the temperature obtained from fitting with masks as described in the previous section, and the atom number from integration of bimodal fits. The trap frequencies are obtained from an interpolation of the results from Sec. 2.1.5 by the function shown in fig. 2.5. We binned each data set with respect to magnetization and reduced temperature and showed the average peak OD of each bin on fig. 4.13.

We first observe on figure 4.13 that the condensation behavior is different for each component, second that it is also different for each magnetic field. The first line shows the measurement taken with a magnetic field $B = 5.6$ G corresponding to $q = h \cdot 8.9$ kHz. In this regime, the quadratic

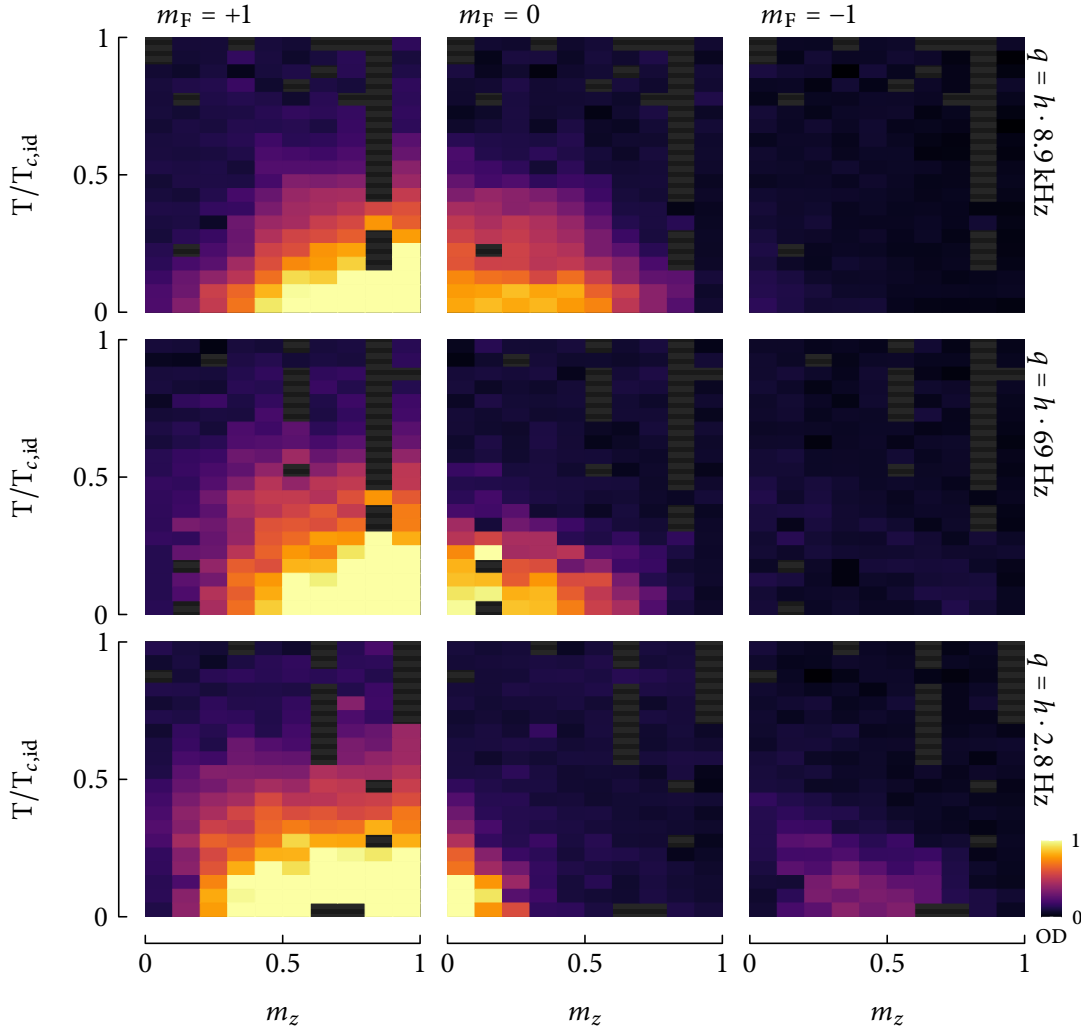


FIGURE 4.13: Graphical representation of the thermodynamics of a spin 1 Bose gas with antiferromagnetic interactions. We show the peak OD, binned in regard with reduced temperature $T/T_{c,id}$ and magnetization m_z . The three columns represent the peak OD of each Zeeman component. The first line represent the dataset taken at $B = 5.6$ G (corresponding to $q = h \cdot 8.9$ kHz, and $q \sim k_B T_{c1}$), and shows two condensation scenarii. For low magnetization, the $m_F = 0$ condenses first, followed by the $m_F = +1$ component. For magnetizations higher than 0.3, the $m_F = +1$ component condenses first followed by the $m_F = 0$ component. The $m_F = -1$ is not observed to condense. The second line shows the dataset taken at $B = 0.5$ G (corresponding to $q = h \cdot 70$ Hz, $q \ll k_B T_{c1}$ and $q > U_s$), and shows only one condensation scenario, where the $m_F = +1$ component condenses first, followed the $m_F = 0$ component. The third line shows the dataset at $B = 0.1$ G (corresponding to $q = h \cdot 2.7$ Hz, $q \ll k_B T_{c1}$ and $q < U_s$). This case differs from the second line because two magnetic phases are observed at low temperature. We observe several condensation scenarii, in which the $m_F = +1$ component always condenses first. Depending on the magnetization, we observe either one or two more critical temperatures. For $m_z \sim 0$ we observe the three components condense simultaneously although only the $m_F = 0$ component remains populated at low temperature. For $0.1 < m_z < 0.3$ we observe that the $m_F = -1$ condenses second, followed by $m_F = 0$ at a third critical temperature. When $m_z > 0.4$, we observe that only the $m_F = -1$ component condense.

Zeeman energy q is not negligible compared to the thermal energy at the critical point $k_B T_c$ such that for low magnetizations, the $m_F = 0$ component condenses before the $m_F = +1$ component. We do not observe the condensation of $m_F = -1$ in this case.

On the second line, taken for $B = 0.5$ G corresponding to $q = h \cdot 70$ Hz, the situation is different since the quadratic Zeeman energy is much smaller $q \ll k_B T_c$. The $m_F = +1$ component always condenses first unless the magnetization vanishes ($m_z = 0$ where it does not condense). We remark the $m_F = -1$ never condenses for $B = 0.5$ G. This is consistent with the expectation for low temperature clouds, where we should reconnect to the $T = 0$ phase diagram. Since $U_s \lesssim q$ in this case, we are in the large magnetic field limit in the broken-axisymmetry phase with negligible population in the $m_F = -1$ component due to the large quadratic Zeeman energy.

The third line shows the data taken for $B = 0.1$ G, which corresponds to $q \simeq 3$ Hz. This case is similar to the case $q = h \cdot 70$ Hz for the first critical temperature, as the $m_F = +1$ always condenses first. However, We observe either one or two additional critical temperatures depending on the magnetization. For $m_z \sim 0$ we observe the three components condense simultaneously. For $0.1 < m_z < 0.3$ we observe the $m_F = -1$ condenses at a second critical temperature, followed by $m_F = 0$ at a third critical temperature. When $m_z > 0.4$, we only observe the $m_F = -1$ component condense below the second critical temperature and the $m_F = 0$ component never condenses. We note that the condensation of the $m_F = -1$ component disagrees with ideal gas theory, as it would be inhibited by the slightest quadratic Zeeman energy (we recall at T_{c2} , $\mu_{-1} = -2q$ for an ideal spin 1 gas). However, it is consistent with the measurement from ref. [54], since for this magnetic field and at zero temperature, a critical magnetization of $m_z \sim 0.3$ separating the broken axisymmetry phase and the antiferromagnetic phase would correspond to $U_s = 60$ Hz (which is consistent with the value of 59 Hz computed in the Thomas Fermi limit with $N = 20000$ and $\omega = 2\pi \cdot 500$ Hz). This seems to indicate that this behavior constitutes an evidence that the spin changing interactions influence the thermodynamic of the system even near the second critical temperature.

4.2.3 Thermodynamic phase diagram

We plot the critical reduced temperatures for each component $T_{c,+1}$, $T_{c,0}$ and $T_{c,-1}$, defined as the reduced temperature at the critical point, as a function of the magnetization at the critical point (the critical magnetization $m_{z,c}$). We also represent the expectation from ideal gas theory. The slightly irregular behavior on these theoretical calculations for $B = 5.6$ G comes from the variation of the relevant parameters for the calculation of the phase diagram *i.e.* $\bar{\omega}$ and N within of the thermodynamic phase diagram.

This representation of the critical temperature allows direct comparison with ideal gas theory, and we notice in fig. 4.14 two major differences with the data. First, we consistently measure lower critical temperatures than what is expected from ideal gas theory. Second, we show the $m_F = -1$ component condenses even in presence of a magnetic field. Both effects originate from the interactions, and we will study them more in detail in the next section.

Before we turn to a more detailed theoretical description, we propose to discuss briefly the role of the spin-changing interactions. As the spin exchange are much weaker than the spin-independent interactions, we expect they have a much less dramatic effect than the latter on thermodynamic quantities such as the critical temperature. This effect is shown on fig. 4.15, in which we compare the transition temperature in the cases $q > U_s$ and $q < U_s$. We observe that the second transition happens at the same temperature (within experimental precision) for both dataset, regardless of the actual Zeeman component that condenses. This is a consequence of the very high temperature

as compared with magnetic energy scales $q, U_s \ll k_B T_{c2}$. As we will see in the next paragraph, the shift of this second critical temperature is mostly caused by the influence of the condensate, present during the second condensation, on the normal component. The effect of spin changing interaction is much more subtle, and consists in slightly favoring either $m_F = 0$ or $m_F = -1$ depending on the relative value of q, U_s , and of the magnetization (similar to what was discussed in chapter 3 and refs. [54, 192]). Given the complexity of the theoretical treatment of the spin changing interaction, we will mostly ignore them in further calculations.

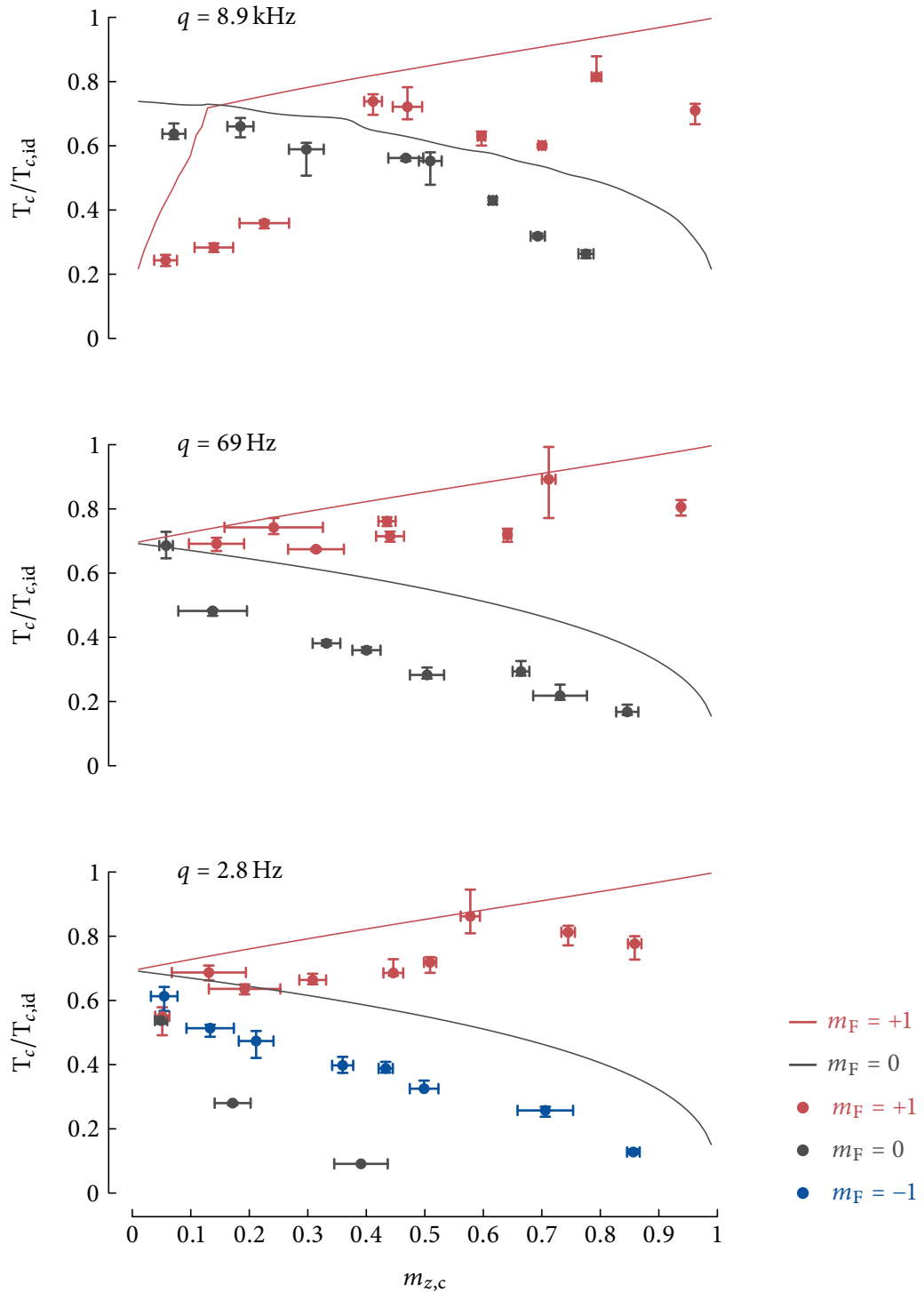


FIGURE 4.14: Coordinates of the critical points in the $\{m_z, T/T_{c,id}\}$ plane. This representation allows an accurate comparison with theory. We observe in the upper and middle panel, that the general shape of the phase diagram is well reproduced, but that there is a systematic downwards shift compared to the ideal gas prediction. The shift is much larger for the second critical temperature than for the first one. In the third panel, the ideal gas theory does not even reproduce the general shape of the phase diagram as it does not predict the condensation of the $m_F = -1$ component.

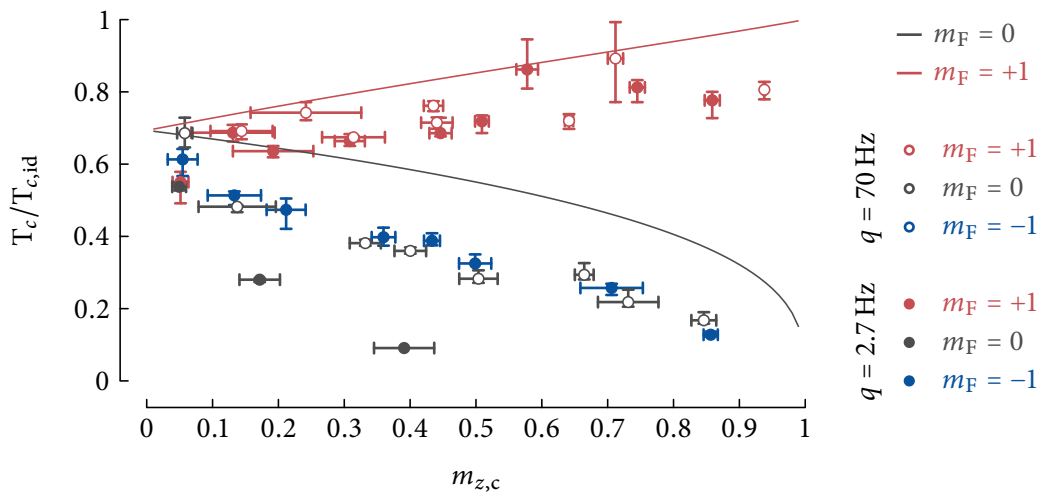


FIGURE 4.15: Direct comparison of the experimental phase diagram for $q = h \cdot 69$ Hz and $q = h \cdot 2.7$ Hz. We observe that the second critical temperature does not depend on the bias field irrespective of which Zeeman component condenses below it ($m_F = 0$ for $q = h \cdot 69$ Hz, $m_F = -1$ for $q = h \cdot 2.7$ Hz). This can be explained by the relatively low strength of the spin exchange interactions compared to the spin independent ones.

4.3 Hartree-Fock model

As we have seen in fig. 4.14, ideal gas theory is not able to describe quantitatively our datasets. As we discussed in chapter 1 section 1, the thermodynamics of single-component Bose gases is influenced by interactions. In this section, we will discuss the case of a spin 1 Bose gas.

The influence of interactions on the thermodynamics of Bose-Einstein condensates is studied nearly since Bose-Einstein condensates were realized in 1995 (see refs. [14, 100, 107, 201, 207–209]), and interactions were shown experimentally to affect the thermodynamics of scalar Bose gases (see refs [29, 108, 210–212]). These studies showed that near the critical point, the interactions within the thermal gas were slightly reducing the density near the trap center, hence reducing the critical temperature. This picture holds in the case of a spinor Bose gas for the first critical temperature T_{c1} , where only a thermal gas is present, because the spin-independent interactions are much stronger than the spin dependent ones. However, near the second critical temperature, the situation is different, and the presence of a dense condensate on top of the thermal gas needs to be considered specifically.

The thermodynamics of spin 1 gases was studied theoretically within a mean field approximation, in refs. [64, 87, 88] for an homogeneous gas and $q = 0$, in ref. [85, 89] for an harmonic trap and $q = 0$, and in refs [91, 92] for an homogeneous gas and $q \geq 0$. We noted that none of these article includes all elements that comes into play in our system, *e.g.* the spin changing interactions, quadratic Zeeman energy and an harmonic trap. We extend here the Hartree-Fock model of [91] (with added assumptions) to the case of harmonically trapped gases to describe our experiment.

In this section we will introduce the Hartree-Fock theory. We first study a simplified version that consists in a semi-ideal “four” gases model, in the spirit of ref. [201], consisting in three ideal thermal gases in interaction with a Thomas-Fermi BEC. In a second part, we compare the “simplified” and complete Hartree-Fock models that we use to obtain a description of our phase diagram and show a comparison of this model with our experimental data.

4.3.1 Hartree-Fock description

The Hartree-Fock (HF) theory is a mean-field approach, perhaps the simplest available to describe a many-body system. It consists in using an ansatz in which the complete system is modeled by a non interacting one with a effective potential describing the effect of interactions at equilibrium. This Hartree-Fock potential is determined self consistently in an iterative process.

We start by recalling the Hamiltonian of the interacting spinor system in second quantized picture (see chap. 1, Eq. (1.92)). It is expressed as a function of the spinor field operators $\hat{\Psi}_m$ with the equation:

$$\hat{\mathcal{H}} = \int d^3\mathbf{r} \left[\sum_m \hat{\Psi}_m^\dagger(\mathbf{r}) \overbrace{\left(\frac{\hbar\nabla}{2m} + V_{\text{ext}}(\mathbf{r}) + pm - q\delta_{m,0} \right)}^{\hat{\mathcal{H}}_{\text{sp}}} \hat{\Psi}_m(\mathbf{r}) + \underbrace{\sum_{m,n} \frac{\bar{g}}{2} \hat{\Psi}_m^\dagger(\mathbf{r}) \hat{\Psi}_n^\dagger(\mathbf{r}) \hat{\Psi}_n(\mathbf{r}) \hat{\Psi}_m(\mathbf{r})}_{=\bar{g}\hat{\rho}^2(\mathbf{r})/2} + \underbrace{\frac{g_s}{2} \sum_{\sigma,i,j,k,l} (\mathbf{F}_\sigma)_{ij} (\mathbf{F}_\sigma)_{kl} \hat{\Psi}_i^\dagger(\mathbf{r}) \hat{\Psi}_k^\dagger(\mathbf{r}) \hat{\Psi}_l(\mathbf{r}) \hat{\Psi}_j(\mathbf{r})}_{=g_s\mathcal{S}^2(\mathbf{r})/2} \right], \quad (4.13)$$

The first line contains single particle contributions, while the second line is the interaction Hamiltonian. Its first term describes spin-independent interaction, while the second describes spin

changing interactions. It is worth noting that the spin-dependent term is much weaker than the spin-independent one such that it will be neglected in order to simplify further computations. In the following, we seek an effective state, described by the density matrix $\hat{\rho}_{\text{HF}}$ that minimizes the Gibbs energy in a modified grand canonical ensemble in which the magnetization m_z is fixed. The expression of the Gibbs energy functional for the Hartree-Fock state is:

$$\begin{aligned} \mathcal{G}[\hat{\rho}_{\text{HF}}] &= TS_{\text{HF}} + \langle \hat{\mathcal{H}} \rangle_{\text{HF}} - \mu N_{\text{HF}} - \lambda m_{z,\text{HF}} \\ &= \text{Tr} \left(k_B T \hat{\rho}_{\text{HF}} \ln \hat{\rho}_{\text{HF}} + \hat{\rho}_{\text{HF}} \hat{\mathcal{H}} - \mu \hat{\rho}_{\text{HF}} \hat{N} - \lambda \hat{\rho}_{\text{HF}} \hat{S}_z \right), \end{aligned} \quad (4.14)$$

with \hat{N} the number operator, and λ a Lagrange multiplier introduced in addition to the chemical potential μ to enforce a particular average value of the magnetization. Under a mean field approximation, we consider an Hartree-Fock ansatz that can be written as the sum of a pure state that describes a condensate and a thermal density matrix ρ_{th} :

$$\hat{\rho}_{\text{HF}} = |\Phi\rangle \langle \Phi| + \hat{\rho}_{\text{th}}, \quad (4.15)$$

where $\Phi = \{\phi_{+1}, \phi_0, \phi_{-1}\}$ is the condensate wavefunction. In the Hartree-Fock approach, the thermal gas is described as an ideal gas in a Hartree-Fock potential V_{eff} (the full Hamiltonian will be written $\hat{\mathcal{H}}_{\text{HF}} = \hat{\mathcal{H}}_{\text{sp}} - V_{\text{ext}} + V_{\text{eff}}$). V_{eff} describes the effect of the interaction term of Eq. (4.13) and is in general determined self consistently. The density matrix used to describe the thermal component is then given by:

$$\hat{\rho}_{\text{th}} = \frac{1}{Z_0} e^{-\beta \hat{\mathcal{G}}_{\text{hf}}}, \quad (4.16)$$

where the free energy $\hat{\mathcal{G}}_{\text{HF}}$ is expressed as a function of the thermal population $\hat{n}_{\text{th}}(\mathbf{r}) = \text{Tr}(\rho_{\text{th}} \hat{N})$ and of the Hartree-Fock Hamiltonian $\hat{\mathcal{H}}_{\text{HF}}$:

$$\hat{\mathcal{G}}_{\text{hf}} = \hat{\mathcal{H}}_{\text{HF}} - \mu \int d^3\mathbf{r} \hat{n}_{\text{th}}(\mathbf{r}) - \lambda \int d^3\mathbf{r} \mathcal{S}_{z,\text{th}}(\mathbf{r}), \quad (4.17)$$

where μ is the chemical potential and λ is a Lagrange multiplier that ensures the conservation of the thermal magnetization $m_{z,\text{th}} = \int d^3\mathbf{r} \mathcal{S}_{z,\text{th}}(\mathbf{r})$, where:

$$\mathcal{S}_{z,\text{th}}(\mathbf{r}) = \text{Tr}(\hat{\rho}_{\text{th}} \hat{S}_z). \quad (4.18)$$

With this definition we can estimate the effective potential for each component, neglecting spin changing interactions (since they are much weaker than the spin-independent ones), such that :

$$V_{\text{eff},m}(\mathbf{r}) = \bar{g} (n_{\text{th}}(\mathbf{r}) + n_c(\mathbf{r}) + n_m(\mathbf{r})), \quad (4.19)$$

where we have defined the density of each component $n_m(\mathbf{r})$ and the condensed density $n_c(\mathbf{r}) = \sum_m \phi_m^*(\mathbf{r}) \phi_m(\mathbf{r})$. We note the last term accounts for bosonic enhancement.

In principle, the HF equations have to be solved by first solving for the ground state wavefunction (Gross-Pitaevskii equation) and for the excited state (eigenvalues of \mathcal{H}_{HF}) in a self-consistent procedure. The full diagonalization of the Hartree-Fock potential of Eq. (4.19) can be computationally intensive in our regime where $k_B T \gg \hbar\omega$. A large number of levels need to be considered and this must be repeated in each step used to determine self consistently the Hartree-Fock potential. An

alternative solution consists in using a semi classical approximation, as in chapter 1. In this case, the thermal density is given by the equation:

$$n_m(\mathbf{r}) = \text{Tr}(\hat{\rho}_{\text{th}} \hat{N}_m) \simeq \frac{1}{(2\pi\hbar)^3} \int \frac{d^3\mathbf{p}}{\exp(\beta \hat{\mathcal{H}}_{\text{sp}}(\mathbf{r}, \mathbf{p}) + V_{\text{eff},m}(\mathbf{r}) - \mu N - \lambda m_z) - 1} \quad (4.20)$$

We note that this equation needs to be solved self consistently for the three components as the thermal densities are “hidden” within the effective potential. A typical procedure to obtain the density for a given trap and a given set of parameter (N, m_z, q) consists in several steps. In each of them, one chooses *a priori* certain values of μ, λ and obtain the condensate wavefunction ϕ by solving 3 coupled Gross-Pitaevskii equations from (4.13) with an effective Hamiltonian given by the thermal density from a previous resolution step. Next, one obtains a new value for the thermal density given the new condensate wavefunction. In a final step, the actual atom number and magnetization are calculated, and compared with their target values. In case of disagreement, the values of λ, μ are modified and the procedure is repeated. We note the convergence of such procedure to the best approximation of actual ground state of the system is not trivial. Given the complexity of the above procedure, we will present in the following a simplified model, that is nevertheless sufficient to account for many of the thermodynamical properties of our system.

4.3.2 Semi-ideal “four gases” formalism

In this paragraph, we will develop a simplified modeling in the spirit of refs. [107, 201] in order to obtain a better understanding of the effect of interactions on the second critical temperature of spin 1 Bose gases. We ignore spin-dependent interactions in this model as these are much weaker than the spin-independent one. We discuss only the second critical temperature here, as a first approach to the shift of the first critical temperature would consist to apply the shift calculated for the scalar gas (see chap. 1 and ref. [100]).

Depending on the magnetic field, the condensate can be either in the $m_F = +1$ or in the $m_F = 0$ component. We distinguish between these cases by indexing quantities related to the condensed phase by $m = c$ with m the component that condenses (for example, for high magnetization, the condensed component density will be $n_{+1=c}$).

In this section, we will use the Thomas-Fermi approximation to calculate the condensed wave function, and a semi classical approximation to calculate the thermal densities. We will neglect the terms proportional to $\langle \hat{n}_{\text{th}}^2 \rangle$ in Eq. (4.17), due to the much lower density of the thermal component as compared to the condensed one ($\langle \hat{n}_{\text{th}}^2 \rangle \ll \langle \hat{n}_{\text{th}} \phi \rangle$). This corresponds to neglecting interactions among thermal atoms or deviations from the Thomas-Fermi wavefunction due to the thermal atoms. This semi-ideal approximation holds as long as the second critical temperature is “much” smaller than the first one. Near the point of simultaneous condensation, we however expect this treatment to fail.

The Hartree-Fock Hamiltonian is written:

$$\hat{\mathcal{H}}_{\text{HF}} = \int d^3\mathbf{r} \sum_m \hat{\Psi}_m^\dagger(\mathbf{r}) \left(\frac{\hbar \nabla}{2m} - q \delta_{m,0} + \underbrace{V_{\text{ext}}(\mathbf{r}) + (1 + \delta_{m,m=c}) g n_c^{(0)}(\mathbf{r})}_{V_{\text{eff}}(\mathbf{r})} \right) \hat{\Psi}_m(\mathbf{r}), \quad (4.21)$$

where $n_c = \max[0, (\mu_{m=c} - V_{\text{ext}}(\mathbf{r})) / \bar{g}]$ is the condensed density within the Thomas Fermi approximation, $\mu_{m=c}$ the chemical potential of the condensed component and where we note the

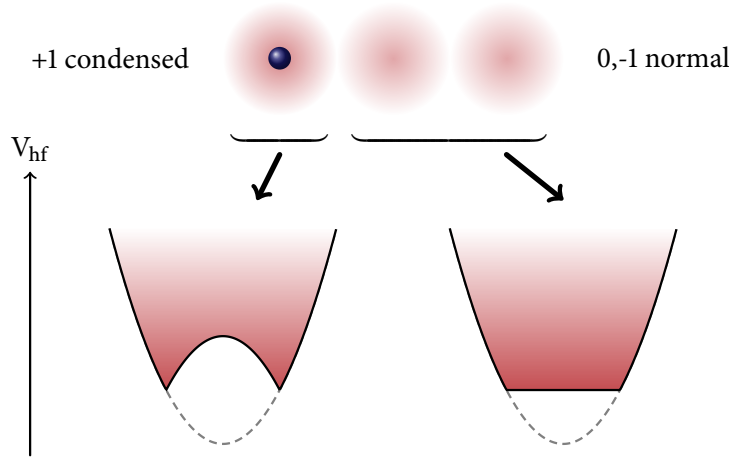


FIGURE 4.16: Effective potentials V_{eff} in presence of a condensate in the $m_F = +1$ component in an harmonic trap. The atoms in the $m_F = +1$ component experience a characteristic “W” potential, while the atoms in the $m_F = 0, -1$ component experience a flat bottom potential.

bosonic enhancement factor for the thermal component of the condensed specie. The effective Hartree-Fock potential V_{eff} is shown in fig. 4.16.

We now consider the case of an isotropic harmonic potential¹ of angular frequency ω in which the condensed density is an inverted parabola, and the Thomas Fermi radius is $R = \sqrt{2\mu_{m=c}/m\omega^2}$. The HF potential takes either the form of a “flat bottom” potential for the uncondensed Zeeman component (the mean field potential approximately compensates the trapping potential within the condensate volume, see fig. 4.16) or of a “W” trap (due to the indistinguishability between the normal and condensed atoms, the mean field potential bears an additional factor 2, see fig. 4.16) :

$$V_{\text{eff},m=\text{nc}} = \begin{cases} \frac{1}{2}m\omega^2 r^2, & \text{if } r > R_{\text{TF}}, \\ \mu_{m=c}, & \text{if } r < R_{\text{TF}}, \end{cases} \quad (4.22)$$

$$V_{\text{eff},m=c} = \begin{cases} \frac{1}{2}m\omega^2 r^2, & \text{if } r > R_{\text{TF}}, \\ 2\mu_{m=c} - \frac{1}{2}m\omega^2 r^2, & \text{if } r < R_{\text{TF}}. \end{cases} \quad (4.23)$$

We compute the thermal populations N'_m using the semi-classical approximation:

$$N_{\text{th},m} = \frac{1}{(2\pi\hbar)^3} \iint \frac{d^3\mathbf{p}d^3\mathbf{r}}{e^{\beta\left(\frac{\mathbf{p}^2}{2m} + V_{\text{eff},m}(\mathbf{r}) - \mu_m\right)} - 1} \quad (4.24)$$

¹Within this approach, the anisotropic case is actually equivalent. We define the characteristic lengths R_i in the three principal axis $i = x, y, z$, $R_i = \sqrt{\frac{2\mu}{m\omega_i^2}}$ and the Thomas-Fermi radius :

$$R_{\text{TF}} = \left(\prod_i R_i \right)^{1/3} = \sqrt{\frac{2\mu}{m\bar{\omega}^2}}.$$

It is possible to express the potentials by the only variable \tilde{r} with :

$$\tilde{r}^2 = \left(\sum_i \frac{x_i^2}{R_i^2} \right) R_{\text{TF}}^2.$$

such that we recover the case of an isotropic harmonic potential.

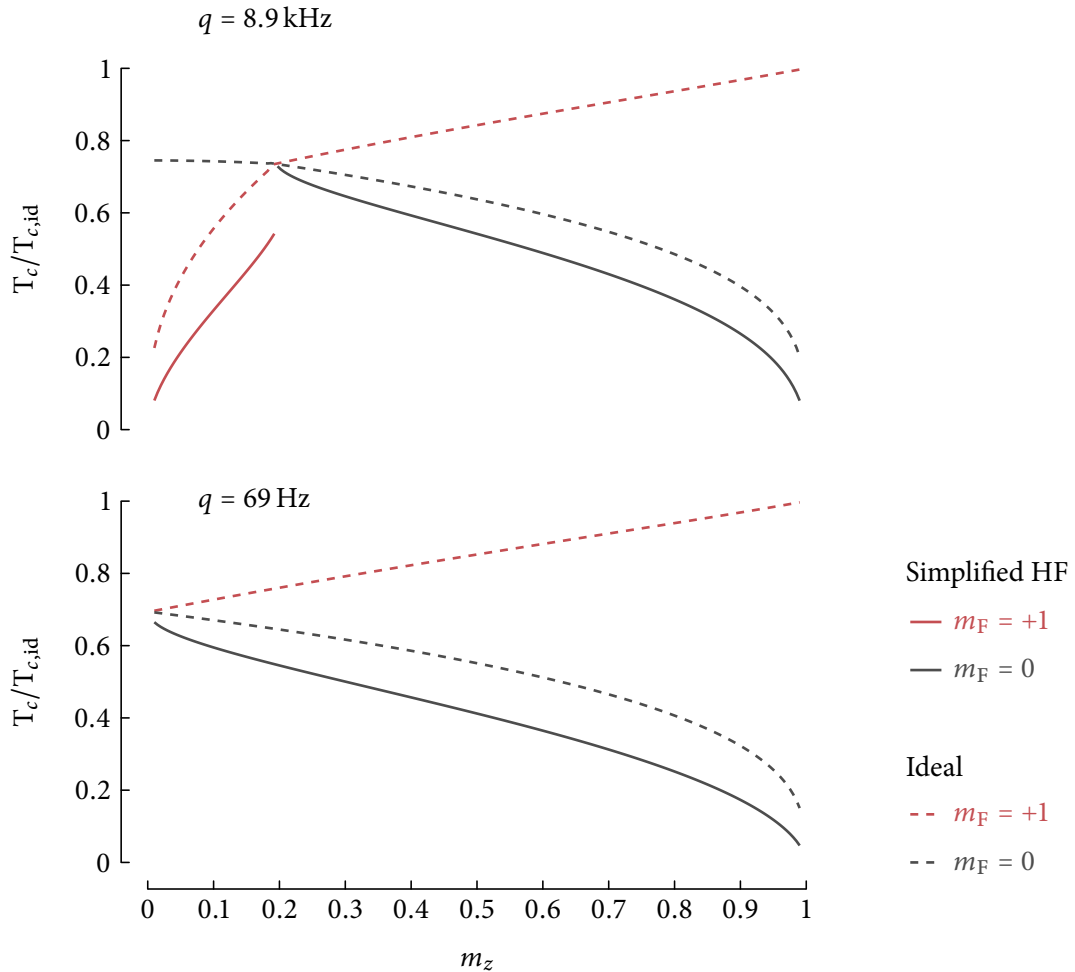


FIGURE 4.17: Effect of interactions on the thermodynamic phase diagram for $N = 50000$, $\omega = 2\pi \times 1200 \text{ s}^{-1}$ in a magnetic field $B = 0.5 \text{ G}$ and $B = 5.6 \text{ G}$. The dashed line shows the ideal gas phase diagram while the plain line display the effect of interactions on the second critical temperature. We observe that the reduction of the second critical temperature due to interaction is much larger than the one predicted for the first critical temperature by scalar gas theory (see chap. 1), as it is expected from the large density of the condensate as compared to the thermal gas at T_{c2} .

It may be useful at this point to recall the form of the effective chemical potential in the modified grand canonical ensemble (see chapter 1):

$$\mu_{+1} = \mu + \lambda, \quad (4.25)$$

$$\mu_0 = \mu - q, \quad (4.26)$$

$$\mu_{-1} = \mu - \lambda, \quad (4.27)$$

With these definitions, we determine $N'_{m=c}$ the thermal population of atoms in the first component that has condensed ($m_F = +1$ or 0 depending on q and m_z) and $N'_{m=nc}$ the thermal population in the two other components. The result can be expressed rather simply as:

$$N'_{m=nc} = \frac{4\pi}{3} \left(\frac{R_{TF}}{\lambda_{th}} \right)^3 g_{3/2} \left(e^{\beta(\mu_{m=nc} - \mu_{m=c})} \right) + \frac{t^3}{\Gamma(3/2)} \sum_{k=1}^{\infty} \frac{e^{\beta k \mu_{m=nc}}}{k^3} \Gamma \left(\frac{3}{2}, k\beta\mu_c \right), \quad (4.28)$$

$$N'_{m=c} = \frac{t^3}{\Gamma(3/2)} \sum_{k=1}^{\infty} \frac{e^{-\beta k \mu_{m=c}}}{k^3} h(k\beta\mu_{m=c}) + \frac{t^3}{\Gamma(3/2)} \sum_{k=1}^{\infty} \frac{e^{\beta k \mu_{m=c}}}{k^3} \Gamma \left(\frac{3}{2}, k\beta\mu_{m=c} \right), \quad (4.29)$$

where we recall the thermal de Broglie wavelength $\lambda_{th} = (2\pi\hbar^2/mk_B T)^{1/2}$ and the reduced temperature $t = k_B T/\hbar\omega$. We give the expression of the Γ and h functions¹:

$$\Gamma(n, x) = \int_x^{\infty} t^{n-1} e^{-t} dt, \quad (4.30)$$

$$h(x) = \int_0^x \sqrt{t} e^t dt. \quad (4.31)$$

We recall that $\Gamma(3/2) = \Gamma(3/2, 0) = \sqrt{\pi}/2$. In the limiting case where only one Zeeman state is populated, we recover the result of [201] for the thermal population $N'_{m=c}$. We compute the condensed atom number in the Thomas-Fermi approximation :

$$N_{m=c}^{BEC} = \begin{cases} \frac{1}{15} \left(\frac{2\mu_m}{\hbar\omega} \right)^{5/2} \frac{a_{ho}}{a}, & \text{if } \mu_m > 0 \\ 0, & \text{if } \mu_m \leq 0 \end{cases} \quad (4.32)$$

At the second critical point, regardless of the condensation scenario, in analogy to the ideal case (see table 1.1) we have :

$$\mu_{+1} = \mu_{m=c}, \quad (4.33)$$

$$\mu_0 = \mu_{m=c}, \quad (4.34)$$

$$\mu_{-1} = \mu_{m=c} - 2q. \quad (4.35)$$

The equation system to solve for the second critical temperature depends upon the first condensed specie. If $m_F = +1$ condense first, it is :

$$N = N_{+1}^{BEC} + N'_{+1=c} + N'_{0=nc} + N'_{-1=nc}, \quad (4.36)$$

$$M_z = N_{+1}^{BEC} + N'_{+1=c} - N'_{-1=nc} \quad (4.37)$$

¹the h function can be expressed as an incomplete gamma function $h(x) = -i\gamma(3/2, x)$ with $\gamma(n, x) = \int_0^x t^{n-1} e^{-t} dt$

If $m_F = 0$ condense first then the system to solve is :

$$N = N_0^{\text{BEC}} + N'_{+1=nc} + N'_{0=c} + N'_{-1=nc}, \quad (4.38)$$

$$M_z = N'_{+1=nc} - N'_{-1=nc} \quad (4.39)$$

We solve both systems numerically and obtain the results from figure 4.17. We note a discontinuity in the curve representing T_{c2} for $q = h \cdot 8.9 \text{ kHz}$. This is not a numerical artifact but rather a “feature” of this simplified HF model, and it can be retrieved by an analytical expansion around the point of simultaneous condensation (see annex E).

4.3.3 Numerical resolution of the HF model and comparison with data

As we have discussed in the above paragraph, the semi-ideal model in which we only consider the influence of the condensate on the thermal gas for the second critical temperature is no longer justified when two Zeeman components condense at similar temperatures. In this case, we use a more complete procedure. We calculate the density of the condensate according to the Thomas Fermi approximation, but in this case including the effect of the thermal component on the condensate density:

$$n_c(\mathbf{r}) = \frac{\mu_{m=c} - V(\mathbf{r}) - \bar{g}(n_{\text{th}}(\mathbf{r}) + n'_c(\mathbf{r}))}{\bar{g}}, \quad (4.40)$$

where n_{th} is the total density of the thermal component, n'_m the thermal density in the component m and n'_c the thermal density in the component that has condensed. Beside we compute the density of the thermal cloud within a semi-classical approximation :

$$n_m(\mathbf{r}) = g_{3/2} \left[\exp \left(\beta \left(\mu_m - V(\mathbf{r}) - \bar{g} \left[n_{\text{th}}(\mathbf{r}) + n'_m(\mathbf{r}) + (1 + \delta_{m,c})n_c(\mathbf{r}) \right] \right) \right) \right], \quad (4.41)$$

where n_c is the density of the condensed component in case there is a condensate. We note the additional term $n'_m(\mathbf{r})$ in the mean field potential accounts for bosonic enhancement. As mentioned in the first chapter, the condition for condensation is when the chemical potential reaches the value of the mean field potential at the region of highest density. In our case, this is always at the trap center.

First critical temperature

We follow two procedures to determine the critical temperature depending whether there is a condensate or not. In the case $T > T_{c1}$, the procedure consists in computing the chemical potential at the critical point. Similarly to the ideal case, either $m_F = +1$ condense first resulting in the following equation system:

$$\mu_{+1} = \bar{g}(n_{\text{th}}(\mathbf{0}) + n_{+1}(\mathbf{0})), \quad (4.42)$$

$$\mu_0 = \bar{g}(n_{\text{th}}(\mathbf{0}) + n_{+1}(\mathbf{0})) - q, \quad (4.43)$$

$$\mu_{-1} = \bar{g}(n_{\text{th}}(\mathbf{0}) + n_{+1}(\mathbf{0})) - 2\lambda. \quad (4.44)$$

Otherwise, if 0 condense first :

$$\mu_{+1} = \bar{g}(n_{\text{th}}(\mathbf{0}) + n_0(\mathbf{0})) - q + \lambda, \quad (4.45)$$

$$\mu_0 = \bar{g}(n_{\text{th}}(\mathbf{0}) + n_0(\mathbf{0})), \quad (4.46)$$

$$\mu_{-1} = \bar{g}(n_{\text{th}}(\mathbf{0}) + n_0(\mathbf{0})) - q - \lambda. \quad (4.47)$$

Using the above chemical potential, we obtain an equation system on the thermal population with Eq. (4.41) written as:

$$N = N'_{+1} + N'_0 + N'_{-1}, \quad (4.48)$$

$$M_z = N'_{+1} - N'_{-1}. \quad (4.49)$$

We obtain (T, λ) at the critical point by numerically solving the above system.

Second critical temperature

In the case of the second critical temperature, there is again two scenarii, depending on which Zeeman component condenses first. However, given we have neglected spin changing interactions, we cannot observe the $m_F = -1$ to condense. Regardless of condensation scenario, and using $\lambda = \mu_{+1} - \mu_0 - q$, we obtain:

$$\mu_{+1} = \bar{g} (n_c(\mathbf{0}) + n_{\text{th}}(\mathbf{0}) + n_{+1}(\mathbf{0})), \quad (4.50)$$

$$\mu_0 = \bar{g} (n_c(\mathbf{0}) + n_{\text{th}}(\mathbf{0}) + n_0(\mathbf{0})), \quad (4.51)$$

$$\mu_{-1} = \bar{g} (n_c(\mathbf{0}) + n_{\text{th}}(\mathbf{0}) + 3n_0(\mathbf{0})) - 2q. \quad (4.52)$$

Using these chemical potential we solve a set of equations similar to the one of the previous section *e.g.* (4.36),(4.37),(4.38),(4.39). In figure 4.18, we compare the results from this approach with the one of the simplified Hartree-Fock model presented above. We see that the critical temperatures obtained from the full HF model are consistently lower than the one obtained from the simplified one, which is consistent with taking into account additional interactions with the thermal component. We note the discontinuity for $q = h \cdot 8.9$ kHz seen on the simplified model remains present.

Comparison with data

Before we continue, we shall describe briefly how we handle comparison between the Hartree-Fock theory and the data. Our control parameters for exploring the thermodynamic phase diagram are the trap depth V_0 and the magnetization m_z . As the trap depth is decreased, the temperature T , the atom number N and the trap frequency $\bar{\omega}$ all change. Furthermore, we have observed that different preparation sequences give rise to different atom numbers. As such all data points showed in figs. 4.13, 4.14 and 4.15 have different parameters and a realistic theory should be calculated for the correct parameters corresponding to their respective position in the thermodynamic phase diagram $(m_z, T/T_{c,id})$.

We extend the normalization procedure applied to temperature to all energy scales and length scales (see ref. [100]). For example $\mu \rightarrow \mu/k_B T_{c,id}$. We also define two thermal length scales, one is the thermal size $R^* = (k_B T_{c,id}/m\omega^2)^{1/2}$ and the second is the de Broglie wavelength $\lambda^* = (2\pi\hbar/mk_B T_{c,id})^{1/2}$ at the critical point. Given this, it is natural to renormalize the length scales as $r \rightarrow r/R^*$. Using these units, the interaction strength can be reduced to a dimensionless parameter γ^* :

$$\gamma^* = \frac{2\bar{a}}{\lambda^*} \quad (4.53)$$

With this choice of normalization, the only parameter that varies within the phase diagram is the parameter γ^* . For our data, its value varies from 0.01 to 0.03 depending on the atom number

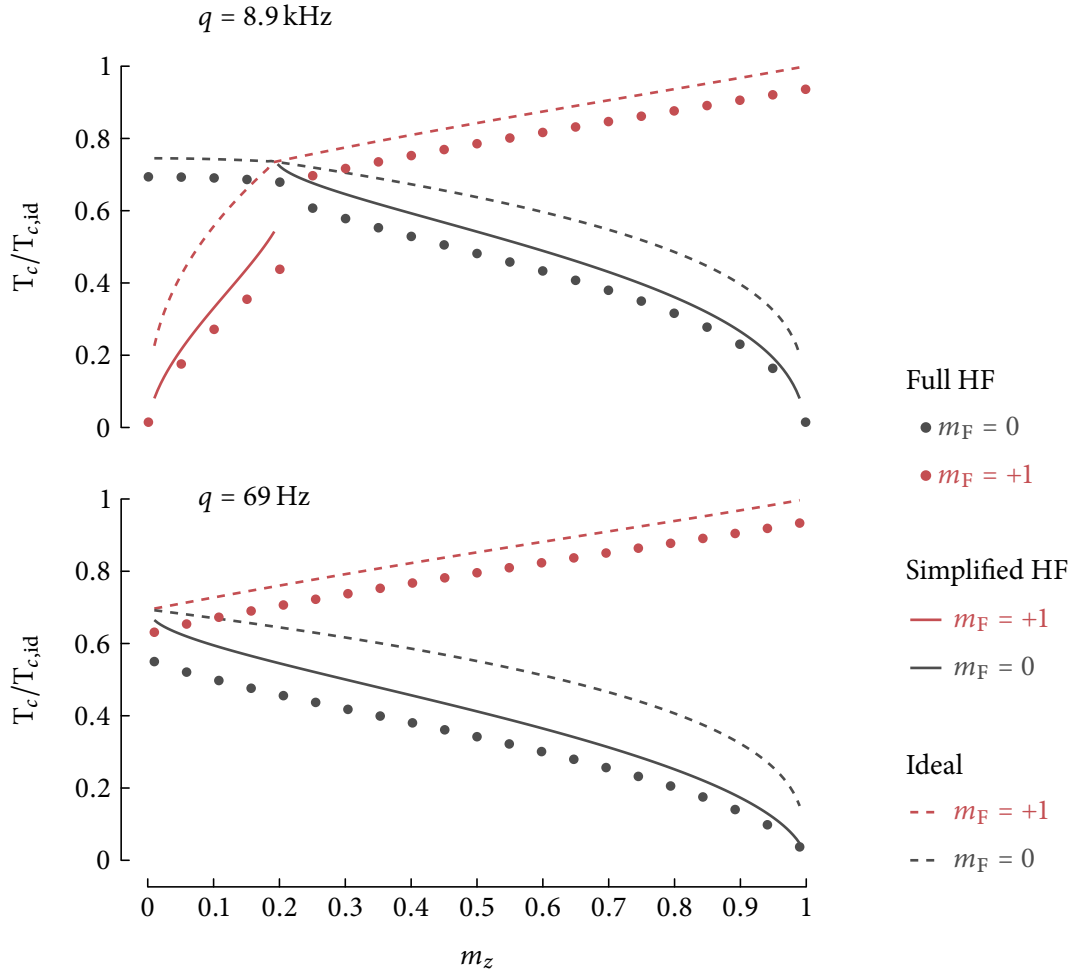


FIGURE 4.18: Comparison between the simplified HF model that neglects the mean field potential created by the thermal atoms with the full modeling for $N = 50000$, $\omega = 2\pi \times 1200 \text{ s}^{-1}$ in magnetic fields $B = 0.5\text{G}$ and $B = 5.6\text{G}$. We note that the full modeling always predicts a lower critical temperature than the simplified one, which is expected since it accounts for additional interactions from the thermal component. We also note that the disagreement between the simplified HF model and the full one is the largest when Zeeman components condense nearly simultaneously in the ideal case. The shift to the first critical temperature is similar to the one predicted by the scalar gas theory in chapter 1.

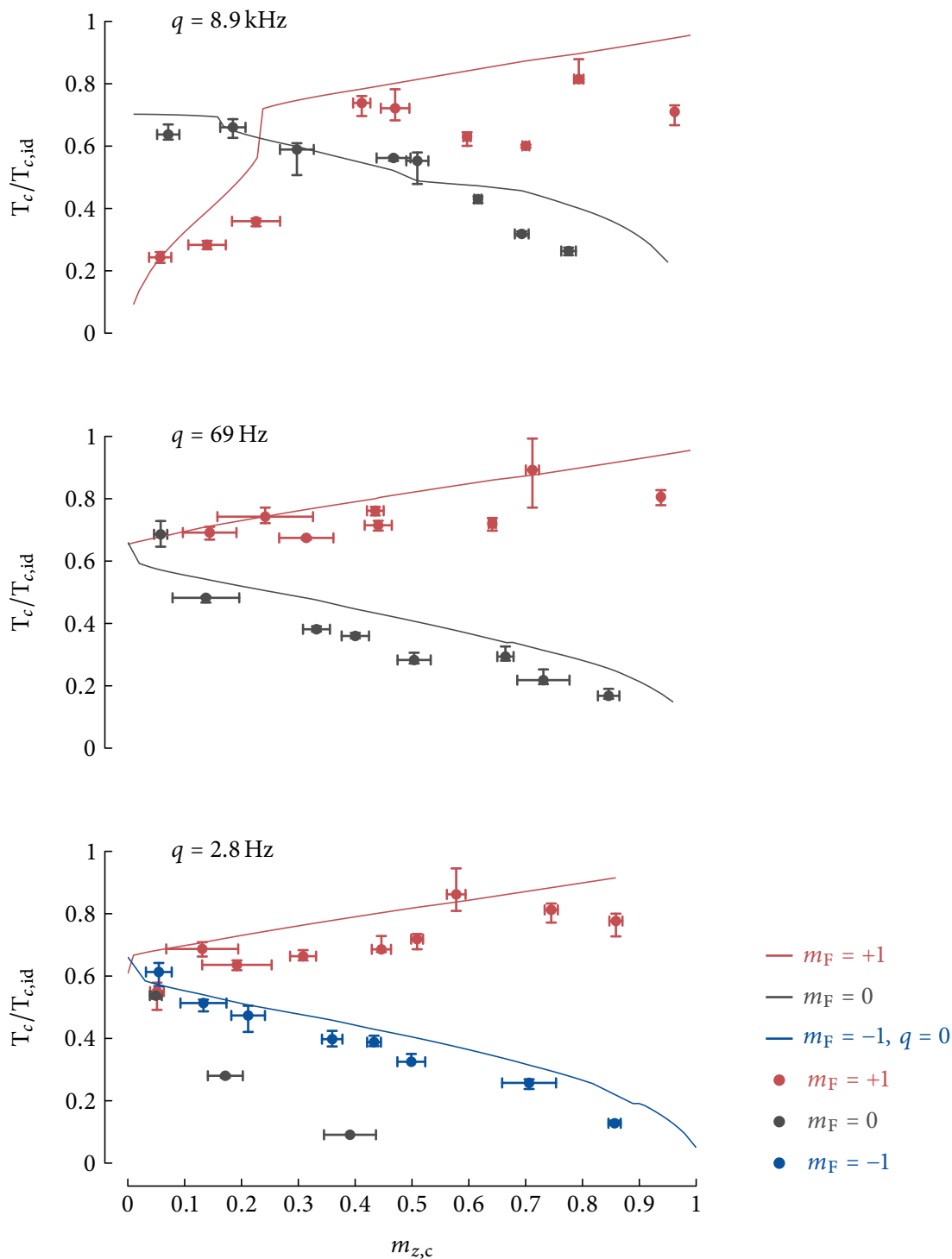


FIGURE 4.19: Comparison of data with the full Hartree-Fock model. We observe a systematic downward shift that we discuss in figures 4.20 and 4.21. The curve shown for the dataset $q = h \cdot 2.7 \text{ Hz}$ shows the expected second critical temperature for the $m_F = 0$ component in the Hartree-Fock model.

and trap frequencies considered. We use a linear interpolation of its value as a function of the magnetization to compute the theoretical curves shown in fig. 4.19, where we compare it to our measurement (that we already showed in fig. 4.14).

We observe the general shape of the phase diagram is well reproduced regardless of the value of q . It is worth noting that the case $q < U_s$, which would not predict the condensation of the $m_F = -1$ component, we have plotted the curve for $q \simeq 0$ where $m_F = -1$ and $m_F = 0$ condense simultaneously. Our calculations cannot account for the phases found below T_{c2} , however, the critical temperature of the $m_F = -1$ component is well reproduced. This is due to the fact that our model ignore spin exchange interaction, which must be taken into account in a more sophisticated theory. It is the object of an ongoing collaboration with Laurent de Forges de Parny, Adam Raçon and Tommaso Roscilde.

Effect of anharmonicities and finite atom number

We note that a downward shift of the data from the HF theory remains, by approximately 10%. This residual shift can be accounted for by two effects that were not considered so far in this chapter. First, using the semi classical approximation, we have ignored the effect of finite atom numbers that is estimated to shift the critical temperature by a value between -1% and -4% (according to chapter 1, Sec. 1.1.1, fig. 1.3) for critical atom numbers between 10^4 and 10^5 .

Additionally, the anharmonicity of the trapping potential should be taken into account. As discussed in Sec. 1.1.4, the precise estimation of this shift is limited by our understanding of the evaporation dynamics (and possibly by our precision in the determination of the potential shape). Nevertheless, we attempted to estimate this shift, by computing the critical atom number N_c in a realistic dimple trap potential V_{DT} composed of two crossing optical dipole traps, one of depth V_0 and size $w_h \sim 25 \mu\text{m}$ propagating horizontally and the second of depth αV_0 and size $w_v \sim 21 \mu\text{m}$ propagating vertically. We recall (see chapter 1) that it can be computed with the help of a semi classical approximation with the formula:

$$N_c = \int_0^{e_{\text{cutoff}}} \rho_{DT}(e) g_{BE}(e) de, \quad (4.54)$$

where $\rho_{DT}(e)$ is the density of state in the dimple trap calculated as in chapter 1 with Eq. (1.48). We recall that the Bose population is $g_{BE}(e) = (\exp(\eta e) - 1)^{-1}$, that $e = E/V_0$ is the normalized energy, and that $\eta = \beta V_0$ is the evaporation parameter. We considered three possible cases, in which the cutoff energy e_{cutoff} varies depending on the assumptions on the evaporation scenario:

1. The trap depth is set by gravity. Atoms with energy such that they are not trapped with purely vertical classical trajectory are not considered in the determination of the critical atom number. The energy cutoff e_{cutoff} is set at the energy of the last trapped trajectory ($e_{\text{cutoff}} \sim V_0 - mgw$ when the effect is small, and when the vertical arm does not hold atoms against gravity).
2. We consider the atoms trapped in the full dimple potential, including the horizontal arm. This is motivated by the specific influence of gravity, which is a one dimensional selection process and may not be relevant in the evaporation dynamics. We estimate the critical atom number in this case by setting the gravity to zero, and by setting the energy cutoff to $e_{\text{cutoff}} = 1 + \alpha$.

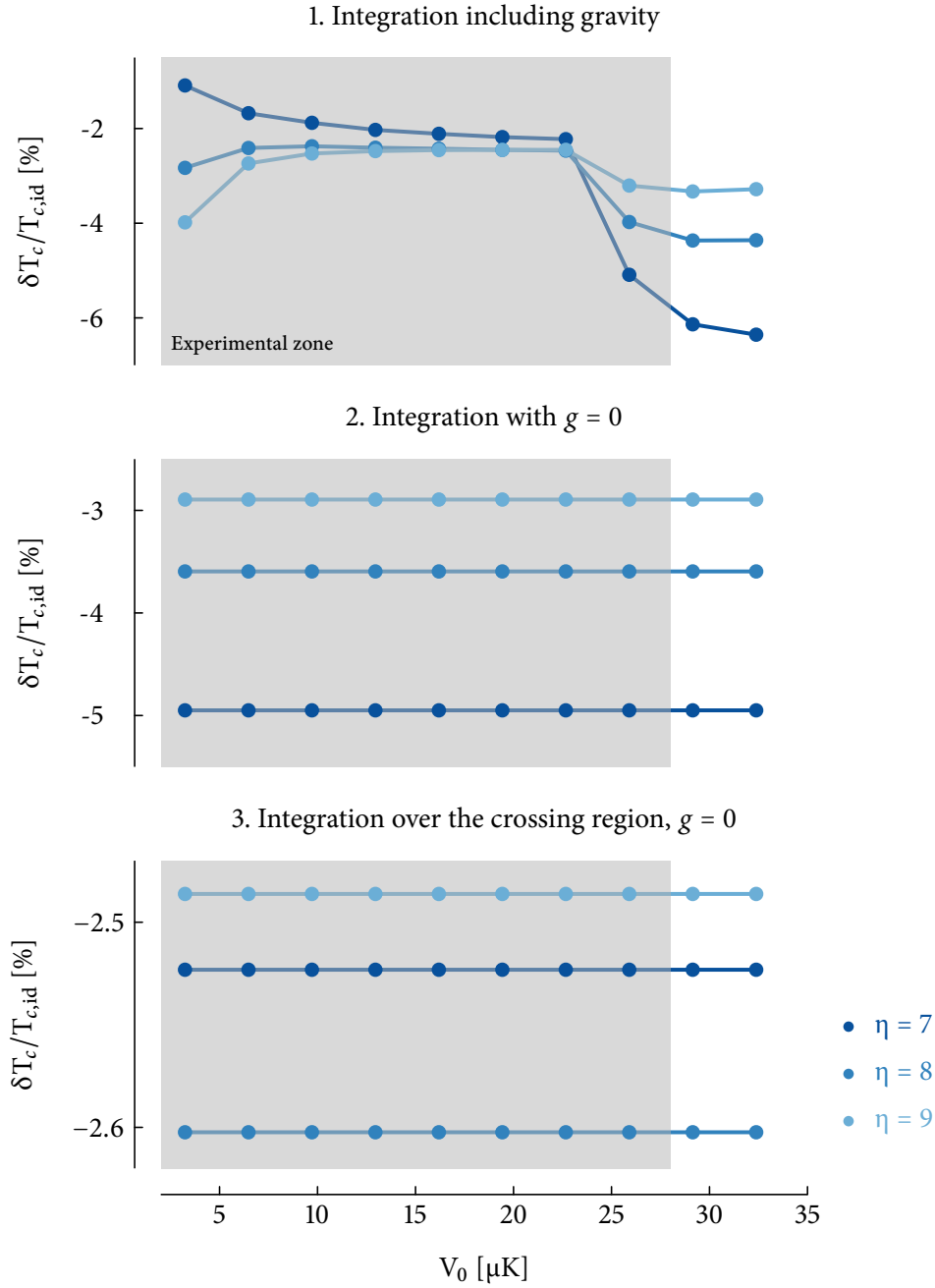


FIGURE 4.20: Expression of the anharmonic shift as a function of the trap depth, calculated for a given value of the evaporation parameters $\eta = V_0/k_B T$. The region in which critical temperature are measured is indicated by a shaded area. We note that calculating these quantities for a given η , make them independent on V_0 in absence of gravity. In the case the energy cutoff of the integration of the density is imposed by the gravity, we observe two regimes. For low trap depths, the vertical arms does not hold against gravity, and the anharmonic shift is comparable to the value where we consider only the crossing region. On the other hand, for the highest trap depth, the vertical arm may hold atoms against gravity, resulting in an increased critical atom number, thus reduced critical temperature. From these data, we estimate the shift due to anharmonicity is between -2% and -6%.

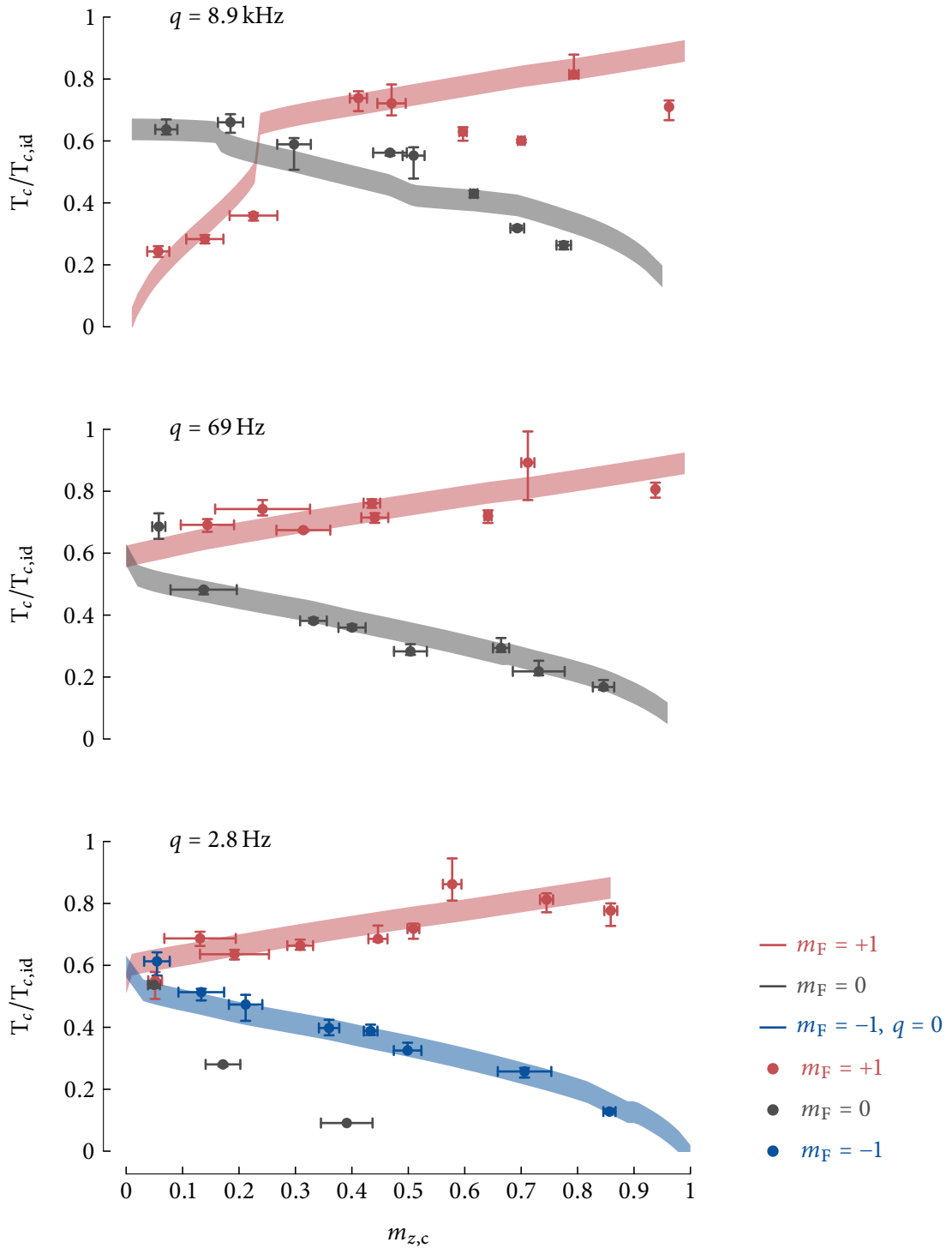


FIGURE 4.21: Comparison of data with the Full Hartree-Fock model including the possible finite size and anharmonic shift. This is represented as a shaded region of width 0.07. The maximum shift is expected to be 10% (6% for anharmonicities and 4% for finite atom number) and the minimum shift to be 3% (2% for anharmonicities and 1% for finite atom number).

3. We only consider atoms in the crossing region as it is the most densely populated region. As we discussed in chapter one, atoms that explore the arms are much less dense, and may not be in thermal equilibrium with the ones in the center. We estimate the critical atom number in this case by setting the gravity to zero, and by setting the energy cutoff to $e_{\text{cutoff}} = 1$ (we note that in our experimental case, $\alpha > 1$).

For the sake of clarity, we calculate the critical atom number at fixed evaporation parameter η , and varying the trap depth. This procedure allows to assess the role of gravity along the ramp, but eliminates the dependence on the trap depth in the case there is no gravity. The change in critical atom number δN_c as compared to the ideal case is converted in a critical temperature shift with $\delta N_c/N_{c,\text{id}} = -3\delta T_c/T_{c,\text{id}}$. We display the predicted critical temperature shift for each of these scenarii in fig. 4.20, and show that regardless of the precise scenario we consider, the shift due to anharmonicities is comprised between -2% and -6%. When the gravity is considered, in scenario 1, we note a change of behavior is observed on fig. 4.20 near $V_0 = 20 \mu\text{K}$. This change takes place when the trap depth begin to be large enough so the vertical arm is holding atoms against gravity. In this case, there is an increase in the critical atom number corresponding to atoms in this arm. We note that the predicted shift then comes closer to the case of scenario 2, while for lower trap depth, it is closer to scenario 3.

We represent the effect of this shift by plotting on a figure similar to fig. 4.19 a shaded region indicating the calculations from HF theory with the maximum (6% for anharmonicities and 4% for finite atom number) and minimum shift (2% for anharmonicities and 1% for finite atom number) we can expect. This is plotted in fig. 4.21, and we see, that taking into account these shifts would allows us to obtain a much better agreement between the Hartree Fock theory and our data, especially on the low magnetic fields cases. We note that if a more rigorous treatment of the finite size shift is likely to be possible (see ref. [85]), the lack of knowledge of the evaporation dynamic will probably not allow a more precise estimation of the shift due to anharmonicities.

4.4 Conclusion

In this chapter we studied the thermodynamics of a spin 1 Bose gas with antiferromagnetic interactions. In section 1, we have developed a new imaging procedure, using a boosted Stern-Gerlach sequence, that allowed us to measure the thermodynamic properties of high temperature clouds. We have developed a fitting procedure that allowed the determination of thermodynamic properties of the spinor gas such as atom numbers and temperatures. With these methods, we have explored the thermodynamic phase diagram of the gas by varying magnetization, temperature and quadratic Zeeman energy.

Depending on the magnetization and the quadratic Zeeman energy, we observed in section 2 four condensation scenarii. For magnetization $m_z \simeq 0$ the $m_F = 0$ component condenses alone. For high quadratic Zeeman energies $q \sim k_B T$, and low (but finite) magnetizations, $m_F = 0$ condenses first and the $m_F = +1$ component condenses at lower temperature. For finite magnetizations and $q > U_s$, the order is flipped and the $m_F = +1$ condenses first followed by the $m_F = 0$ component. For the former three scenarii, the $m_F = -1$ component does not condense, as expected by ideal gas theory in presence of a magnetic field.

The final scenario may be the most intriguing as it is not even predicted qualitatively by ideal theory. For low quadratic Zeeman energies $q < U_s$, the $m_F = +1$ condenses first, and is followed either by one or two more condensations. Depending on the magnetization, we observe that the

$m_F = -1$ condenses, even in presence of a finite magnetic field. Furthermore, at lower temperatures and low magnetizations, the $m_F = 0$ is also observed to condense. This latter scenario highlights the link between the second condensation and magnetic order. Indeed, this is not until the second component condenses that we observe the magnetic phases measured for a pure condensate in ref. [54]. We observe that these phases survive at finite temperatures, and we can guess the existence of a tricritical point, in which the magnetic phase transition crosses the second Bose-Einstein condensation temperature.

Further study of this regime requires an extensive theoretical description that is being investigated at the time this thesis is written by Laurent de Forges de Parny, Adam Rançon and Tommaso Roscilde. We expect this collaboration to bring a better understanding of the low magnetic field regimes and to raise new open questions about the finite temperature properties of spin 1 anti-ferromagnetic gases. In particular, we could investigate the existence of a tricritical point, either in a complete theory, or by a more precise experimental investigation in this regime of parameters. Another question that naturally arises, is what happens for higher interaction strength, in a lattice potential for example. This case, have been explored by the authors of refs. [77, 213], and predicts that each of the lobes of the Mott insulating phase in the ground state phase diagram of Bose-Hubbard model (see ref. [214]) bears a particular magnetic phase that depends on the parity of the filling of the insulator. The experimental study of the magnetic order as a function of the filling factor of the Mott insulator or the tunneling rate could provide insight on this behavior.

5

Conclusion

A LONG THIS MANUSCRIPT, we described an experimental study of spin 1 Bose gases with antiferromagnetic interactions. We have studied the magnetic properties of quasi pure spinor Bose-Einstein condensates and the thermodynamics of a spinor gas of sodium around the Bose-Einstein critical temperature.

5.1 Summary

In chapter 1, we have introduced the subject by recalling the most basic properties of spinor Bose-Einstein condensates. We started in section 1, by discussing the thermodynamics of a scalar Bose gas, and how it is affected by interactions, finite atom numbers and trap anharmonicities. In section 2, we have recalled the theoretical description of a scalar Bose-Einstein condensate with the help of the Gross-Pitaevskii equation. In section 3, we introduced spinor Bose-Einstein condensates, and described their scattering properties. Due to the rotational symmetry of the interaction hamiltonian, we have seen that the spin changing interactions conserve the magnetization m_z . We introduced the single mode approximation, which applies for tight trapping potentials and assumes that all Zeeman components condense with the same spatial wavefunction. We discussed a consequence of the conservation of the magnetization is that only the quadratic energy enters in the spin Hamiltonian. It effectively favors energetically the $m_F = 0$ component as compared to the $m_F = \pm 1$ components in presence of a magnetic field. In section 4, we have discussed the thermodynamics of the spin 1 gas with conserved magnetization. We showed that several sequential condensation scenarii are predicted depending on the magnetization and the quadratic Zeeman energy.

In chapter 2, we described the experimental apparatus and the measurement techniques that we used to produce and observe spinor Bose gases. In section 1, we described the experimental setup and the cooling steps, from laser cooling of sodium atoms to two-step evaporative cooling in optical dipole traps. We also showed how to characterize the trapping potential *in situ*. In section 2, we discussed the techniques that we have developed to detect spinor Bose-Einstein condensates, and extract atom numbers from absorption images. We then developed the origin and the influence of noise on extracted atom number, and then showed the calibration methods that we used to extract atomic densities. In section 3, we have described the fitting techniques

for scalar Bose gases. We showed how to obtain thermal sizes from fits to the wings of the time of flight distribution. In section 4, we developed the spin manipulation techniques that we have used through this work. We described how to perform spin rotation by applying a resonant radio frequency to the condensate, and how to achieve a good control of the magnetic environment necessary for spin manipulations. Then we discussed how to prepare the magnetization of the BEC with the help either of a depolarization sequence that consists in applying radiofrequency in presence of inhomogeneous broadening and spin diffusion, or from a polarization sequence that consists in spin distillation by evaporation in a magnetic gradient. We also discussed adiabatic rapid passage, that can be used to prepare reliably a BEC polarized in the $m_F = -1$ component. We discussed additional possibilities to manipulate the spins with Raman transitions in annex A, B, C.

In chapter 3, we turned to the study of the magnetic phases of quasi pure spinor condensates. In section 1, we recalled the mean field theory of spinor Bose-Einstein condensates with antiferromagnetic interactions, and the properties of the low temperature magnetic phases. The antiferromagnetic phase, observed for finite magnetization and low magnetic field, has a purely longitudinal spin and the $m_F = 0$ component is not populated. The broken axisymmetry phase is observed for higher magnetic fields. It has a transverse spin component that builds up with the population of the $m_F = 0$ component, that appears due to the quadratic Zeeman energy. In both phases, the antiferromagnetic nature of the spin exchange interaction results in a minimization of the transverse spin. The underlying mechanism consists in locking the relative phase of the Zeeman components $\Theta = \Phi_{+1} + \Phi_{-1} - 2\Phi_0 = \pi$. In section 2, we measured the transverse spin length using spin rotations. We showed that the signature of the transverse spin length lied in the fluctuations of the magnetization after a $\pi/2$ pulse, and demonstrated this way that the length of the transverse spin was indeed minimal given the properties of the state before the rotation. We discussed the effect of finite kinetic and spin temperature to obtain a quantitative description of our data.

Following the study of the phase locking mechanism, we turned in section 3 to low magnetizations and low magnetic field, where the degeneracy of the three Zeeman components give rise to large fluctuations of the spin populations. We observe that for low quadratic Zeeman energies and $m_z = 0$, that there are large fluctuations of the populations n_0 . We measured the fluctuations of the population of the $m_F = 0$ component and extracted spin temperatures from fits to the probability distributions. We show the dependence of the spin temperature with the evaporation trap depth, and compare it to the kinetic temperature. We demonstrate two regimes, one for low q where the spin temperature is consistently lower than the kinetic temperature and one for high quadratic Zeeman energies q where both temperatures are similar. We interpret the decoupling between the two degree of freedom in the first regime by the large difference in energy scales between typical kinetic excitation (*e.g.* spin waves) and the spin excitation. The coupling is restored when the quadratic Zeeman energy is increased as the condensate is polarized in $m_F = 0$, and the energy scale for spin excitation becomes on the order of q .

In the chapter 4, we explored the thermodynamics of a spin 1 Bose Einstein condensate near the Bose-Einstein critical temperature. In section 1, we discussed experimental methods, and the modifications to the procedures described in chapter 2 that were required to measure “high” temperature clouds. First, we developed a boosted Stern-Gerlach sequence in order to accommodate for the faster expansion of thermal clouds. As the highest temperature clouds were overlapping, we discussed how to obtain an absorption signal and how to relate this absorption signal to densities and atom numbers. Then we extended the fitting procedures developed in chapter 2 for three

components clouds. We use bimodal fits to obtain atom numbers, hence magnetizations. We measure the temperature by a procedure where we fit three Bose functions to masked images in order to exclude the influence of the condensate from the time of flight distributions.

In section 2 we discussed how to extract critical points from our data. As it is challenging to fit the signature of a small condensed fraction on top of a large thermal gas densities, we use the peak optical density as a proxy to the condensed fraction. We detected the critical point as a sharp increase of the optical density as the trap depth is decreased. The representation of this peak optical density as a function of the reduced variables magnetization m_z and temperature $T/T_{c,id}$ demonstrated several sequential condensation scenarios as predicted by ideal gas theory. We observe that for high quadratic Zeeman energy, either the $m_F = 0$ or the $m_F = +1$ condensates first depending on the magnetization. A lower second critical temperature is observed where $m_F = +1$ and $m_F = 0$ condense respectively. As predicted by ideal gas theory, the $m_F = -1$ do not condense in this case. When we decrease the magnetic field, hence q , the first condensation scenario, where the $m_F = 0$ condense first only happens for $m_z = 0$ (and it is the only component to condense). For even lower quadratic Zeeman energies, where $q < U_s$, we observe a completely different scenario. While the $m_F = +1$ component condenses first as for the intermediate magnetic field case, we observe either one or two more critical temperatures depending on the magnetization. We find that the $m_F = -1$ component condenses, which contradicts the predictions of ideal gas theory. Additionally, we find that the temperature at which it condenses is similar to the one at which $m_F = 0$ condenses in the intermediate magnetic field case. The comparison of critical temperatures with ideal gas theory reveals a large discrepancy, especially for the second critical temperature.

In a section 3, we discussed a simplified Hartree-Fock model to describe the effect of interactions on the critical temperature. We ignored spin exchange interactions, as they are much weaker than the spin independent ones. We considered condensates in the Thomas Fermi regime and applied a semiclassical approximation for the estimation of thermal populations. In a first model, we ignored the interaction between the thermal atoms, and focused on the description of the second critical temperature. In this picture, the thermal atoms of the condensed component experience a “W” shaped potential and the second component condenses in a flat bottom potential. In a more detailed model, we also consider the mean field potential of the thermal atoms. We find this refined description agrees well with the simplified model for the second critical temperature and additionally predicts of the shift of the first critical temperature similar to the one discussed in chapter 1. We compare the results of this model to our experimental data and find that despite good qualitative agreement, however with a remaining discrepancy of $\sim 10\%$ on all the data that we could explain by the combined effects of the finite atom number and trap anharmonicities.

5.2 Prospects

At this point, there are two natural directions that could be explored. First, we could extend the measurement of the phase locking mechanism to higher temperatures, and observe whether it survives below, near or above the second critical temperature. Another direction we could take would consist in study the dynamics of equilibration of the spin degree of freedom (see refs. [41, 203]). Two types of experiments could be performed, one where we would cool suddenly a cloud across T_{c2} at finite magnetization and low magnetic fields. For sufficiently low magnetic fields, we expect that a large spin temperature would result in condensation of the $m_F = 0$ component even if the mean field ground state predicts a vanishing population. Another experiment, would take place at low magnetizations $m_z \sim 0$ and low magnetic field, such that we can use the fluctuations

of the population to perform spin thermometry (see ref. [215]). In this case, we expect that a fast quench of the temperature would raise the quadratic Zeeman energy threshold for obtaining a non fluctuating state.

Perhaps as a longer term prospect, the recent installation of a 1D optical lattice along the axis of the horizontal arm of the dimple trap could allow the study of novel regimes of interaction strength. The references. [77, 213] suggests for example the study of peculiar magnetic order in Mott insulating phases, where the magnetic order in each site depends on the parity of the filling.

During the realization of this manuscript, our experimental team has developed an experimental procedure to create 1 dimensional Bose-Einstein condensates. The most striking difference between the systems presented in this thesis (that can be described within the single mode approximation) and 1D systems comes from the emergence of spin domains in the broken axisymmetry phase (see chapter 1, and ref.[55]). This is due to the non miscibility of the $m_F = 0$ and $m_F = \pm 1$ components. Our team is currently revisiting the study of the $T=0$ magnetic phase diagram in a gradient free 1D BEC. As the system undergo demixing as it crosses the $T=0$ magnetic transition, we believe the magnetic phase transition becomes a first order transition. We observed that this observation is very sensitive to gradients. Indeed, as the long direction of the trap has very low trapping frequencies, relevant spin dependent magnetic forces can be generated by very small magnetic gradients. Our team have developed a method to cancel these gradients by applying a bias in a specific direction, such that the magnetic forces are canceled along the weak direction. We believe these ongoing studies will allow a better understanding of the magnetic phases of spin 1 BECs out of the single mode approximation. A perhaps longer term goal would be to observe the dynamics of domain formation after a quench through the $T=0$ phase transition (see ref. [216]). We observe three domains at equilibrium if gradients are well compensated. The $m_F = 0$ sits in the center of the trap, and two domains $m_F = \pm 1$ components are on both ends of the weak axis of the 1D trapping potential. We could study whether in the case of a quench, we would observe the formation of several domains, and study the number of domain as a function of the magnetic field ramp speed.

Appendices

A

Alternative laser source for laser cooling and Raman transitions

The wavelength corresponding to the D1 and D2 lines of sodium (respectively 589.757 nm and 589.158 nm in vacuum) cannot be generated directly from laser diodes as in the case for Rubidium or Lithium D lines. Dye lasers used to be the most common source at these wavelengths but they suffer from a relatively high intrinsic noise levels and from frequent need of dangerous maintenance (as the dye used are very toxic and carcinogenic). For these reasons, Emmanuel Mimoun developed the laser source described in Chapter 2 and refs. [134, 143], based on intracavity sum frequency of 2 YAG lasers of wavelengths $\lambda = 1064$ nm and $\lambda = 1319$ nm. This solution works very well for laser cooling of sodium, however, the small tuning range of both YAG laser sources forbids applications that requires detuning of more than a few hundred MHz (such as Raman couplings see annexes B and C, or resonant addressing of the D1 line).

During my master's internship, we have developed an alternative source, based on a commercial laser source of wavelength $\lambda = 1178$ nm. This source is composed of a diode laser and a semiconductor optical amplifier – tapered amplifier (TA) – that provides us with 1.6 W of single mode laser light and of a frequency doubling apparatus in which we generate 589 nm light from intracavity second-harmonic generation (see refs. [134, 143, 148]). In this annex, we will describe shortly this laser source and its performances and demonstrate the tuning capability of the laser using iodine spectroscopy.

A.1 Second Harmonic Generation

Before we present the laser source itself, we will recall very shortly the laws of non linear optics leading to the generation of second harmonic in non linear crystals. More details on this matter can be found on ref. [134, 217].

Most materials develop an electric polarization \mathbf{P} proportional to an applied electric field \mathbf{E} : $\mathbf{P} = \epsilon_0 \chi^{(1)} \mathbf{E}$. However, a more detailed description (see ref.[217]) includes non linear terms that cannot be neglected when this field is strong. In potassium titanyl phosphate (KTP, see ref.[218]) crystals, such as the one used in this laser source, the absence of inversion symmetry leads to a second order term:

$$\mathbf{P}^{\text{NL}} = \mathbf{E} \overline{\chi}^{(2)} \mathbf{E}, \quad (\text{A.1})$$

where $\overline{\chi}^{(2)}$ is a third rank tensor named second order susceptibility. In the following, we will consider only linearly polarized light along axis “z”, which limit us to the term χ_{zzz} (also noted in crystallographic notations $d_{33} \sim 16 \text{ pm/V}$) of the susceptibility. In KTP, this axis is the one that displays the strongest non linearity.

We deduce from eq. A.1 that in presence of an electric field from a linearly polarized plane wave propagating along \mathbf{x} : $\mathbf{E} = E_0 \mathbf{e}_z \cos(\omega t - kx)$ such as the one produced by the 1178 nm laser, the material polarization will display a DC term and a term oscillating at $\omega_2 = 2\omega$, which corresponds to photons at a wavelength $\lambda_2 = \lambda/2 = 589 \text{ nm}$. In most cases, the non linearity is weak and the conversion efficiency small, such that the pump beam is considered to be unaffected by the SHG process. The second harmonic power P_2 at the output of a parallelepipedic crystal of length L illuminated uniformly on a surface S by the pump beam described above is:

$$P_2 = \alpha P_1^2 \text{sinc}^2 \left(\frac{\Delta k L}{2} \right), \quad (\text{A.2})$$

$$\alpha = \frac{2\omega^2 d_{33}^2 L^2}{\epsilon_0 c^3 S n_1^2 n_2}, \quad (\text{A.3})$$

where ϵ_0 is the vacuum permeability, c is the speed of light, α is the phase matched conversion efficiency (usually $\alpha \sim 10 \text{ mW/W}^2$) and n_1, n_2 are the material index of refraction for respectively the pump frequency and the second harmonic. The quantity Δk reflects a very important aspect of SHG that is called *phase matching* and corresponds to the necessity to cancel the difference in the wave vectors of the pump and second harmonic light: $\Delta k = k_2 - 2k_1 = (n_2 - n_1)2\omega/c = 0$. If phase matching is realized, the efficiency of the SHG is only limited by the system constraints such as available power, non-linearity coefficient or geometry. In reality, dispersion in the crystal prevents to obtain phase matching straightforwardly and the (large) phase dematching limits the conversion efficiency to a very low value (see $a = 0.1$ panel of fig. A.1, for phase matching dependence of the SHG efficiency).

One method to obtain phase matching in such configuration consist in using a periodically modified crystal structure with a period Λ (periodically poled KTP, PPKTP). With this method, the crystal properties are modified such that (see ref. [217]):

$$d_{33} \rightarrow d_{\text{eff}} = \frac{2d_{33}}{\pi}, \quad (\text{A.4})$$

$$\Delta k \rightarrow \Delta k - \frac{2\pi}{\Lambda}. \quad (\text{A.5})$$

Although the conversion efficiency is reduced to about 40 % of the ideal one, the phase matching parameter is not fixed anymore by the intrinsic properties of the crystal but can be tuned by the parameter Λ , the poling period. In practice, both the phase matching Δk and the poling period Λ can be tuned with temperature via respectively the index temperature dependence (given by Sellmeier relations, see ref. [219]) and the thermal expansion of the crystal (see ref. [218]). Proper initial design of the PPKTP crystal (which needs to be done for each particular frequency conversion process) ensures the phase matching temperature is a few (tens of) degrees above room temperature. We stabilize the crystal temperature at the phase matching value with a servo loop that controls a Peltier thermoelectric “cooler”.

Eq. (A.3) highlights that the conversion efficiency, for a given accessible power, is enhanced if the area S of the beam is small. This is due to the fact that for a given power, the field is stronger if the beam size is small. Laser light obey the laws of Gaussian optics, and in the case the laser is focused

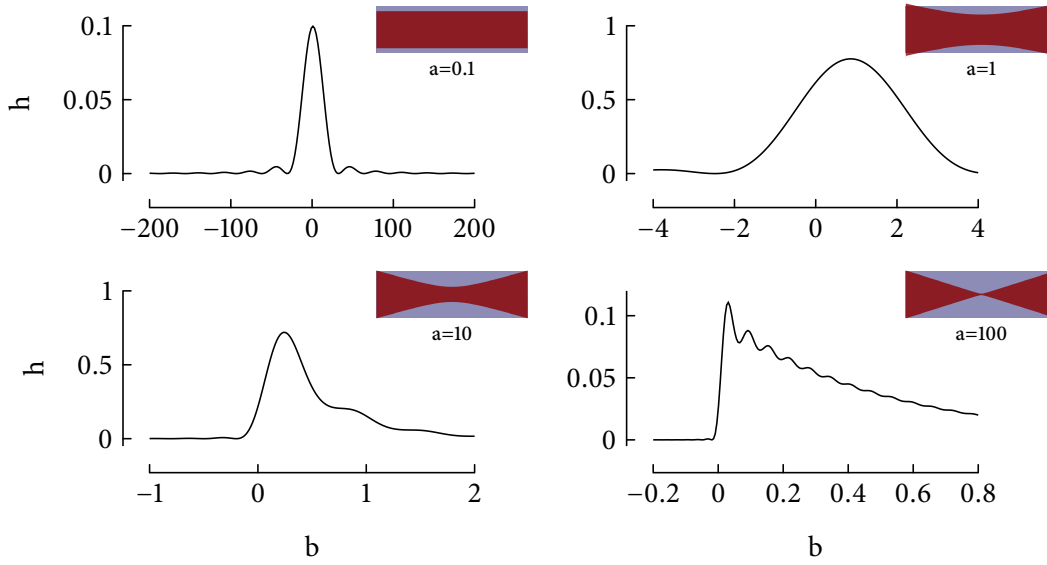


FIGURE A.1: Boyd-Kleinmann factor for different crystal sizes. We observe the peak value is higher for $a \sim 1$ (see fig. A.2). We recall $b = \left(\Delta k - \frac{2\pi}{\Lambda}\right)$ is the phase matching parameter, that is typically tuned by changing the temperature of the crystal.

inside the crystal, eq. (A.2) is not valid. SHG theory requires taking into account the Gaussian nature of the laser electric field (see refs. [217, 220]). In this case, the power on the output of the crystal can be expressed as a function of the quasi-phase matching parameter b from eq (A.5), and an additional parameter a that reflects the relative size of the crystal and the beam Rayleigh length z_R :

$$P_2 = \alpha_{\text{BK}} P_1^2, \quad (\text{A.6})$$

$$\alpha_{\text{BK}} = \frac{\omega^3 d_{\text{eff}}^2 L}{2\pi\epsilon_0 c^4 n_1 n_2} h \left(a = \frac{L}{2z_R}, b = \left(\Delta k - \frac{2\pi}{\Lambda}\right) z_R \right). \quad (\text{A.7})$$

The function h quantifies the effect of phase matching, and depends on the relative sizes of the crystal and the beam (see fig. A.1). We retrieve in particular a sinc function for very large waists. We see that the function changes strongly from a plane wave to a strongly focused beam. In particular, since the minimum size of a Gaussian beam is related to its divergence, the use of a very small waist may lead to poor SHG efficiency as the field is strong only in a very small volume of the crystal. The optimum for SHG is found when the Rayleigh range of the beam is comparable to the size of the crystal, $a \simeq 3$, $h \sim 1$ (see fig. A.2).

A.2 Intracavity frequency doubling

The second harmonic generation process is rather inefficient for pump powers accessible with our laser source (we measured $\alpha_{\text{eff}} \sim 16 \text{ mW/W}^2$). This can be circumvented by placing the doubling crystal within an optical cavity such that the power of interest is not the laser source power but rather the intracavity power. We designed a cavity which is resonant only for the pump frequency ω , but transparent for the doubled frequency 2ω . In this case, the efficiency of the doubling process is given by the cavity finesse, that determines the power build-up inside the cavity.

The intracavity power is ultimately limited by losses in the cavity (imperfect alignment, scattering off the optical surfaces, higher order non linear processes, thermal effects in the crystal, *etc.*). We chose a butterfly geometry similar to the one used in the sum frequency laser from ref. [134]. The cavity dimensions are chosen to maximize the conversion efficiency given the given dimensions of the PPKTP crystal, and according to Boyd-Kleinman theory.

Intracavity doubling requires the simultaneous realization of mode and impedance matching (see refs [134, 143, 148]) to achieve high SHG efficiencies. Mode matching refers to the adaptation of the spatial mode of the laser to the one of the cavity. We use a set of three lenses to set the input pump Gaussian beam size and position superimposed with the one of the cavity. As the mode of the tapered amplifier is not TEM₀₀ as opposed to the one of the cavity, perfect mode matching cannot be achieved, and is limited by the TEM₀₀ projection of the input beam. The mode matching is taken into account by a parameter η such that the power transmitted into the cavity mode of interest by the input coupler of the cavity is ηP_1 . We assume the remaining photons are reflected. We measured *a posteriori* from the intracavity power $\eta \sim 70\%$ (see eq. (A.8)) and from a fit to the output second harmonic power (see fig. A.3).

Impedance matching on the other hand refers to the proper choice of cavity coupler reflectivity R that maximizes the SHG efficiency. In order to understand this process better, we expressed the intracavity power as a function of the coupled input pump power ηP_1 (see [109]), SHG induced losses αP_{cav} per round trip and other losses p per round trip:

$$P_{\text{cav}} = \frac{(1 - R)\eta P_1}{(1 - \sqrt{(R(1 - p)(1 - \alpha P_{\text{cav}})})^2)} \quad (\text{A.8})$$

This allows us to calculate the reflectivity R of the input mirror that ensure impedance matching. Given low losses $p \sim 0.01$, we find $R \sim 90\%$.

The last ingredient for an efficient SHG process consists in a servo loop on the cavity length in order to keep the cavity resonant ($L_{\text{cav}} = N\lambda$). We installed piezo actuators on cavity mirrors, and

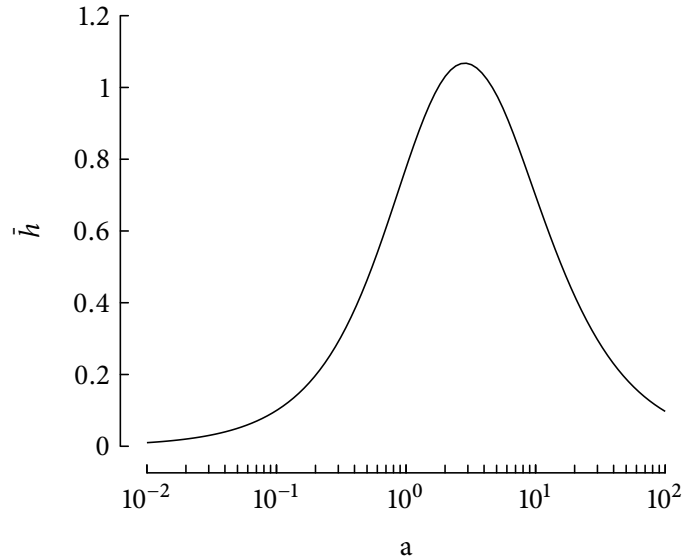


FIGURE A.2: Maximum value \bar{h} of the function h (see fig.A.1) as a function of the relative beam size.

stabilize the second harmonic output power.

We display on fig. A.3 the output power we obtain when we vary the temperature of the crystal. The plain line is a simulated curve (given eqs. (A.7) and (A.8)), with fitted losses, mode matching factor η and poling period. This theory does not take into account potential inhomogeneities of the crystal, or the effect of temperature gradients which may explain the imperfect agreement between experiment and theory. We demonstrate overall doubling efficiency of 38% (55% if we count only the mode matched light from the TA).

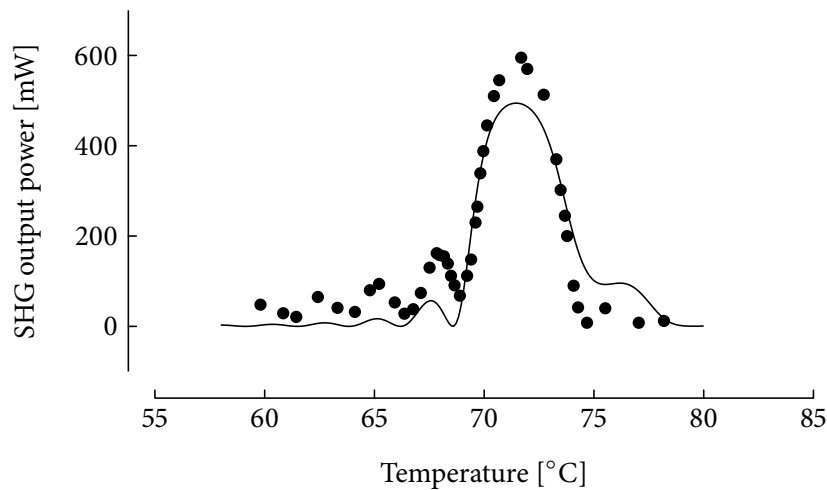


FIGURE A.3: Output power of the cavity as a function of temperature.

A.3 Iodine spectroscopy

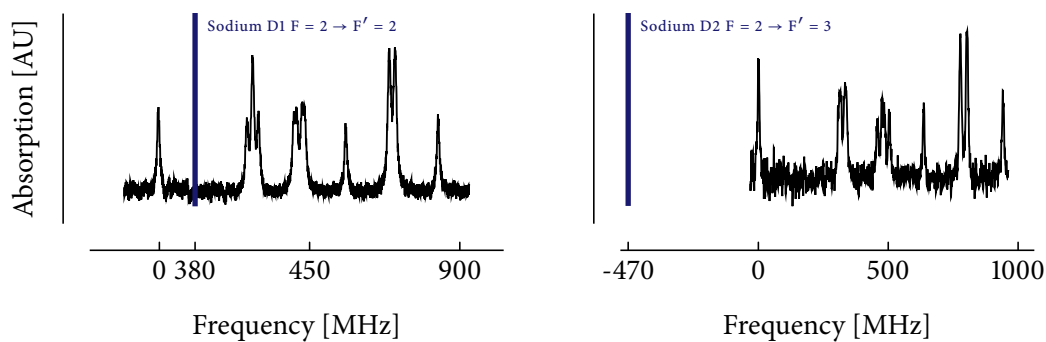


FIGURE A.4: Iodine Saturated absorption spectrum. P114(14-1) on the left and P38(15-2) on the right. We have represented the sodium D line frequency for scale.

We demonstrate on fig. A.4 the tuning possibilities of this laser by performing spectroscopy on iodine molecular lines by modulation transfer spectroscopy (see ref. [145, 221]). In particular, ref. [144] shows that the P114(14-1) line has similar frequency to the sodium D2 line, and that the P38(15-2) to the D1 line. In the future, a servo loop could be build to stabilize the frequency of

the laser on these spectroscopy signals, by acting on the laser diode current or cavity size. For applications such as Raman transitions, this is *a priori* not necessary.

B

Light-Atom Interaction in the ground state electronic manifold

In the main text, we have discussed optical dipole traps, and in particular, how we can trap atoms in the focus of red detuned laser beams. In this appendix, we will discuss a more refined treatment in which we will see that in the case of circularly polarized beams, the interaction with far detuned light can lead to more complex hamiltonian, analogous to magnetic fields (see ref [222] for a review).

B.1 Derivation of the lightshift hamiltonian

We calculate the light-shift operator for an alkali atom in the electronic ground state in presence of hyperfine coupling. The ground state is the $3^2S_{1/2}$ ($n = 0, l = 0, S = 1/2, J = 1/2$) which present two hyperfine multiplets which are $F = 1, 2$ for sodium (which nuclear spin is $3/2$). We consider the $3S \rightarrow 3P$ transition which split into two lines due to spin-orbit coupling: the D1 ($J = 1/2 \rightarrow J' = 1/2$) and the D2 ($J = 1/2 \rightarrow J' = 3/2$) lines. The excited state for the D1 line is the $3^2P_{1/2}$ ($n' = 1, l' = 1, s' = 1/2, J' = 1/2$) which splits into two hyperfine multiplets $F' = 1, 2$ for sodium. The excited state for the D2 line is the $3^2P_{3/2}$ state ($n = 1, l = 1, S = 1/2, J = 3/2$) which split into four hyperfine multiplets $F' = 0, 1, 2, 3$.

We consider a dipolar interaction with light:

$$\widehat{V}_{AL} = -\widehat{\mathbf{d}} \cdot \mathbf{E}_{\text{tot}}, \quad (\text{B.1})$$

and write the light field in the standard basis $\mathbf{e}_{\pm}, \mathbf{e}_0$ ¹:

$$\mathbf{E}_{\text{tot}} = \sum_q \mathbf{e}_q E_q \cos(\mathbf{k} \cdot \mathbf{r} - \omega t). \quad (\text{B.2})$$

We also define the complex field:

$$\tilde{\mathbf{E}} = \sum_q \frac{E_q}{2} \mathbf{e}_q e^{i(\mathbf{k} \cdot \mathbf{r} - \omega t)}. \quad (\text{B.3})$$

¹We remind the expression of the standard basis eigenvectors into the Cartesian basis: $\mathbf{e}_0 = \mathbf{e}_z$, $\mathbf{e}_+ = (\mathbf{e}_x + i\mathbf{e}_y)/\sqrt{2}$, $\mathbf{e}_- = (\mathbf{e}_x - i\mathbf{e}_y)/\sqrt{2}$.

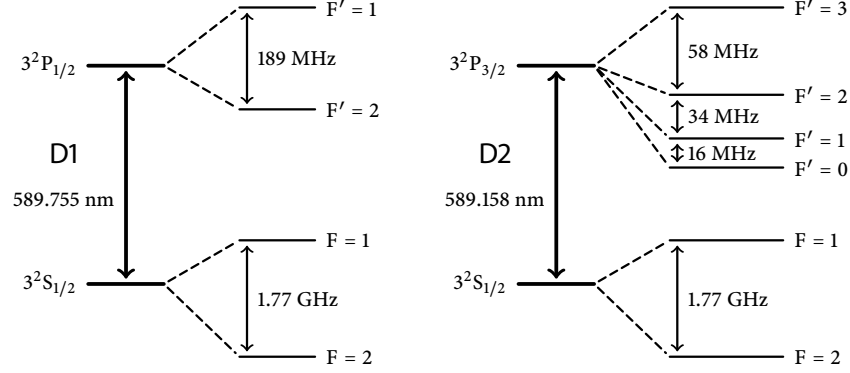


FIGURE B.1: Hyperfine structure of sodium

such that $\mathbf{E}_t = \tilde{\mathbf{E}} + \tilde{\mathbf{E}}^*$. In the limit of far detuned light, the population of the excited state as well as the ground-excited states coherences remain small and relax quickly compared with the ground state populations and coherences. Therefore, we apply the rotating wave approximation and perform an adiabatic elimination of the ground-excited states coherences in the interaction Hamiltonian. The result is an effective Hamiltonian acting in the electronic ground state manifold that is called the lightshift operator \hat{V}_{LS} [222]. Another point of view is to consider this as a result of second order perturbation theory:

$$\hat{V}_{LS} = \sum_{g_i, g_j, e_\nu} |g_i\rangle \langle g_j| \cdot \frac{\langle g_i | \hat{V}_{AL}^- | e_\nu \rangle \langle e_\nu | \hat{V}_{AL}^+ | g_j \rangle}{E_\nu - E_j - \hbar\omega_L}, \quad (\text{B.4})$$

where $\hat{V}_{AL}^+ = \hat{\mathbf{d}}\tilde{\mathbf{E}} = \sum_q \frac{1}{2} \mathbf{d} \cdot \mathbf{e}_q E_q$ and $\hat{V}_{AL}^- = (\hat{V}_{AL}^+)^\dagger$ are the two terms of \hat{V}_{AL} left after the RWA has been performed. We define a polarizability tensor α such that:

$$\hat{V}_{LS} = \frac{1}{4} \sum_{qq'} E_{q'}^* \alpha_{qq'} E_q, \quad (\text{B.5})$$

$$\alpha_{qq'} = \sum_{i,j,\nu} |g_i\rangle \langle g_j| \cdot \frac{\langle g_i | d_{q'}^\dagger | e_\nu \rangle \langle e_\nu | d_q | g_j \rangle}{E_\nu - E_j - \hbar\omega_L}. \quad (\text{B.6})$$

We also define the ground and excited state projectors:

$$P_J = \sum_{J, F, m_F} |J, F, m_F\rangle \langle J, F, m_F|, \quad (\text{B.7})$$

$$P_{J'} = \sum_{J', F', m_{F'}} |J', F', m_{F'}\rangle \langle J', F', m_{F'}|. \quad (\text{B.8})$$

Then we assume the detuning is large compared to the hyperfine splitting of the excited state (which is in the order of 100 MHz for sodium *cf* figure B.1). In that case, we write the lightshift operator can be simplified by letting $E_\nu - E_j - \hbar\omega_L \rightarrow E_{J'} - E_j - \hbar\omega_L = -\Delta_{1,2}$ depending whether $J' = 1/2$ or $J' = 3/2$. The polarizability tensor can then be rewritten:

$$\alpha_{qq'} \simeq - \sum_{i,j} |g_i\rangle \langle g_j| \cdot \left\langle g_i \left| \sum_{J'} \frac{1}{\Delta_{J'}} P_J d_{q'}^\dagger P_{J'} d'_q P_J \right| g_j \right\rangle. \quad (\text{B.9})$$

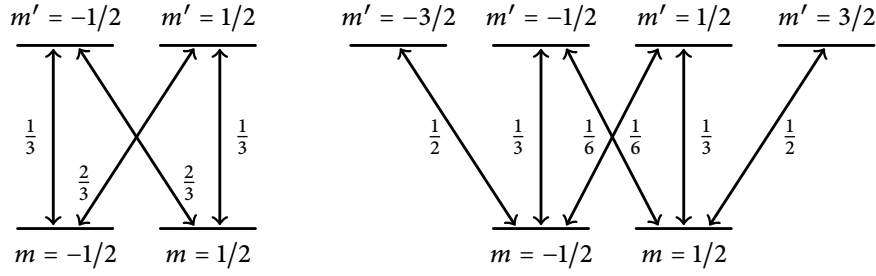


FIGURE B.2: relative transition strengths for the fine structure of the $S \rightarrow P$ line for alkali. All the figures on this schematics are to be understood within a square root.

Since d_q is an electronic dipole operator, it will not affect the nuclear spin. Therefore, we define a new tensor operator, acting only on the ground state fine basis subspace:

$$\alpha_{q,q'}^{(J)} = - \sum_{J'} \frac{1}{\Delta_{J'}} P_J d_{q'}^\dagger P_{J'} d_q P_J. \quad (\text{B.10})$$

We also define a reduced dipole operator \mathcal{D}_q , restricted to a single $J \rightarrow J'$ transition:

$$d_{\text{sp}}^2 \mathcal{D}_q^\dagger \mathcal{D}_q = (P_J d_{q'}^\dagger P_{J'}) (P_{J'} d_q P_J). \quad (\text{B.11})$$

Since it acts on a spin 1/2 multiplet, the tensor $\mathcal{D}_q^\dagger \mathcal{D}_q$ can be decomposed as a sum of Pauli matrices σ_k :

$$\mathcal{D}_i^\dagger \mathcal{D}_j = \frac{A}{3} \delta_{ij} I + \sum_k B \epsilon_{ijk} \sigma_k, \quad (\text{B.12})$$

where A and B are two constants that depend on the transition considered. The theorem of Wigner-Eckardt allows us to write [223]:

$$\langle nSLJm | d_q | nSL'J'm' \rangle = d_{JJ'} (-1)^{J'-1+m_J} \begin{pmatrix} J' & 1 & J \\ m_{J'} & -q & -m_J \end{pmatrix}, \quad (\text{B.13})$$

where $d_{JJ'} = \langle J || d || J' \rangle$ are the dipole matrix elements for the $J \rightarrow J'$ transition that can be found in reference [125]. We introduce Wigner's 3j symbols as a convenient way to express Clebsch-Gordan coefficients. The square of the 3j symbols represent the relative transition strength between sublevels m_J and $m_{J'}$, q being the angular momentum carried by the photon. The value of the relative transition strengths can be found on figure B.2. Then, it is convenient to further reduce the dipole operators with the help of 6j symbols, and introducing the $s \rightarrow p$ dipole matrix element $d_{\text{sp}} = \langle L = 0 || d || L' = 1 \rangle$:

$$d_{JJ'} = d_{\text{sp}} (-1)^{J'+3/2} \sqrt{(2J+1)(2J'+1)} \begin{Bmatrix} 0 & J & S \\ J' & 1 & 1 \end{Bmatrix}. \quad (\text{B.14})$$

As an illustration, we compute the reduced ground state operators for $J=3/2$, for example two π ($q = 0$) transitions can be expressed as:

$$\mathcal{D}_z^\dagger \mathcal{D}_z = \sum_{m_1, m_2, m'} 8 (-1)^{m_1+m_2} \begin{pmatrix} 3/2 & 1 & 1/2 \\ m' & 0 & -m_1 \end{pmatrix} \begin{pmatrix} 3/2 & 1 & 1/2 \\ m' & 0 & -m_2 \end{pmatrix} \begin{Bmatrix} 0 & 1/2 & 1/2 \\ 3/2 & 1 & 1 \end{Bmatrix}^2 |m_1\rangle \langle m_2|. \quad (\text{B.15})$$

Due to the properties of Wigner's 3j symbols, only the terms $m' = m_1 = m_2$ are non zero and:

$$\mathcal{D}_z^\dagger \mathcal{D}_z = -\frac{2}{9} \mathcal{I}d = \frac{A}{3} \mathcal{I}d. \quad (\text{B.16})$$

The procedure is similar for two σ_+ ($q = 1$) or σ_- ($q = -1$) transitions:

$$\mathcal{D}_+^\dagger \mathcal{D}_+ = \sum_{m,m'} 8(-1)^{2m} \begin{pmatrix} 3/2 & 1 & 1/2 \\ m' & -1 & -m \end{pmatrix}^2 \begin{Bmatrix} 0 & 1/2 & 1/2 \\ 3/2 & 1 & 1 \end{Bmatrix}^2 |m\rangle \langle m'|, \quad (\text{B.17})$$

$$\mathcal{D}_-^\dagger \mathcal{D}_- = \sum_{m,m'} 8(-1)^{2m} \begin{pmatrix} 3/2 & 1 & 1/2 \\ m' & 1 & -m \end{pmatrix}^2 \begin{Bmatrix} 0 & 1/2 & 1/2 \\ 3/2 & 1 & 1 \end{Bmatrix}^2 |m\rangle \langle m'|. \quad (\text{B.18})$$

Due to the symmetry properties of Wigner's 3j symbols, only the terms $m' = m_1 = m_2$ are non zero and:

$$\mathcal{D}_+^\dagger \mathcal{D}_+ = -\frac{1}{9} |-1/2\rangle \langle -1/2| - \frac{1}{3} |1/2\rangle \langle 1/2|, \quad (\text{B.19})$$

$$\mathcal{D}_-^\dagger \mathcal{D}_- = -\frac{1}{3} |-1/2\rangle \langle -1/2| - \frac{1}{9} |1/2\rangle \langle 1/2|. \quad (\text{B.20})$$

This allow us to express the parameter B as a function of these two operators:

$$\mathcal{D}_x^\dagger \mathcal{D}_y = B \epsilon_{xyz} \sigma_z = B \sigma_z, \quad (\text{B.21})$$

$$\mathcal{D}_x^\dagger \mathcal{D}_y = -\frac{i}{2} (\mathcal{D}_-^\dagger + \mathcal{D}_+^\dagger) (\mathcal{D}_+ - \mathcal{D}_-), \quad (\text{B.22})$$

$$= -\frac{i}{2} \underbrace{(\mathcal{D}_-^\dagger \mathcal{D}_+ - \mathcal{D}_+^\dagger \mathcal{D}_- + \mathcal{D}_+^\dagger \mathcal{D}_+ - \mathcal{D}_-^\dagger \mathcal{D}_-)}_{m_F = \pm 2}, \quad (\text{B.23})$$

$$= \frac{i}{6} \begin{bmatrix} 1-1/3 & 0 \\ 0 & 1/3-1 \end{bmatrix}, \quad (\text{B.24})$$

$$= \frac{i}{9} \sigma_z. \quad (\text{B.25})$$

We then consider the case of $J' = 1/2$:

$$\mathcal{D}_z^\dagger \mathcal{D}_z = \sum_{m,m'} 4(-1)^{2m} \begin{pmatrix} 1/2 & 1 & 1/2 \\ m' & 0 & -m \end{pmatrix}^2 \begin{Bmatrix} 0 & 1/2 & 1/2 \\ 3/2 & 1 & 1 \end{Bmatrix}^2 |m\rangle \langle m'|, \quad (\text{B.26})$$

$$\mathcal{D}_+^\dagger \mathcal{D}_+ = \sum_{m,m'} 4(-1)^{2m} \begin{pmatrix} 1/2 & 1 & 1/2 \\ m' & -1 & -m \end{pmatrix}^2 \begin{Bmatrix} 0 & 1/2 & 1/2 \\ 3/2 & 1 & 1 \end{Bmatrix}^2 |m\rangle \langle m'|, \quad (\text{B.27})$$

$$\mathcal{D}_-^\dagger \mathcal{D}_- = \sum_{m,m'} 4(-1)^{2m} \begin{pmatrix} 1/2 & 1 & 1/2 \\ m' & 1 & -m \end{pmatrix}^2 \begin{Bmatrix} 0 & 1/2 & 1/2 \\ 1/2 & 1 & 1 \end{Bmatrix}^2 |m\rangle \langle m'|, \quad (\text{B.28})$$

$$\mathcal{D}_z^\dagger \mathcal{D}_z = -\frac{1}{9} \mathcal{I}d, \quad (\text{B.29})$$

$$\mathcal{D}_+^\dagger \mathcal{D}_+ = -\frac{2}{9} |-1/2\rangle \langle -1/2|, \quad (\text{B.30})$$

$$\mathcal{D}_-^\dagger \mathcal{D}_- = -\frac{2}{9} |1/2\rangle \langle 1/2|, \quad (\text{B.31})$$

$$\mathcal{D}_x^\dagger \mathcal{D}_y = -\frac{i}{2} \begin{pmatrix} \frac{2}{9} & 0 \\ 0 & -\frac{2}{9} \end{pmatrix}, \quad (\text{B.32})$$

$$= -\frac{i}{9} \sigma_z. \quad (\text{B.33})$$

In summary, we express the fine structure polarizability tensor as:

$$\alpha_{qq'}^{(J)} = \frac{d_{\text{sp}}^2}{3} \left(\frac{2}{3\Delta_2} + \frac{1}{3\Delta_1} \right) \delta_{ij} + \frac{id_{\text{sp}}^2}{9} \left(\frac{1}{\Delta_1} - \frac{1}{\Delta_2} \right) \epsilon_{ijk} \sigma_k, \quad (\text{B.34})$$

and therefore, the lightshift operator as:

$$\widehat{V}_{\text{LS}}^{(J)} = \sum_{\alpha\beta} \frac{d_{\text{sp}}^2 E_\alpha^* E_\beta}{12} \left[\left(\frac{2}{3\Delta_2} + \frac{1}{3\Delta_1} \right) \delta_{\alpha\beta} + \frac{i}{3} \left(\frac{1}{\Delta_1} - \frac{1}{\Delta_2} \right) \epsilon_{\alpha\beta\gamma} \sigma_\gamma \right]. \quad (\text{B.35})$$

B.2 Lightshift operator in the hyperfine basis

In order to express the lightshift operator in the hyperfine basis, we could add hyperfine closure relations in the initial expression of the polarizability tensor in eq. (B.34). The matrix elements in the hyperfine state basis would then be written with Clebsch-Gordan coefficients and matrix elements from the tensor $\mathcal{D}_q^\dagger \mathcal{D}_{q'}$ in the fine basis. Another method consists in rewriting the polarizability tensor such that $\mathcal{D}_q^\dagger \mathcal{D}_{q'} = \mathcal{I}_F \otimes (\text{scalar} + \mathbf{vector})_J$. Then, the scalar part remains unchanged while changing basis, and the vector part can be simplified using Landé projection theorem:

$$\langle F, m_F | \mathbf{V} | F', m_{F'} \rangle = \frac{\langle F | \mathbf{F} \cdot \mathbf{V} | F \rangle}{F(F+1)} \times \langle F, m_F | F', m_{F'} \rangle. \quad (\text{B.36})$$

We use the relation $\langle \mathbf{F} \cdot \mathbf{J} \rangle = \langle \mathbf{I} \cdot \mathbf{J} \rangle + \langle \mathbf{J}^2 \rangle = \frac{\langle F^2 \rangle - \langle I^2 \rangle + \langle J^2 \rangle}{2}$ to get the prefactor which are 1/4 and -1/4 for, respectively, the HF ground state manifolds $F=2$ and $F=1$.

The lightshift operator then takes its final form:

$$\widehat{V}_{\text{LS}} = \frac{d_{\text{sp}}^2 |E|^2}{12} \left(\frac{2}{3\Delta_2} + \frac{1}{3\Delta_1} \right) \mathcal{I}d + \mathbf{W} \cdot \mathbf{F}, \quad (\text{B.37})$$

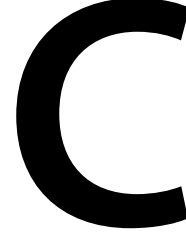
$$\mathbf{W} = \pm \frac{id_{\text{sp}}^2}{36} \left(\frac{1}{\Delta_1} - \frac{1}{\Delta_2} \right) \tilde{\mathbf{E}}^* \times \tilde{\mathbf{E}}, \quad (\text{B.38})$$

where the spin 1 matrices \mathbf{F}_i can be found in chapter 1, section 3. We notice that the vector \mathbf{W} acts on the atom the same way of a magnetic field does. Furthermore, this vector is not 0 only if the field contains σ_\pm polarization. Here, the sign of the vector \mathbf{W} correspond to the multiplets $F = I \pm \frac{1}{2}$.

We give the expression for the S \rightarrow P dipole matrix element for sodium (see ref. [37] for example):

$$d_{\text{sp}} = \sqrt{\frac{9}{8\pi^2} \epsilon_0 \lambda^3 \hbar \Gamma}, \quad (\text{B.39})$$

$$= 3.66 \times 10^{-29} \text{ C m} = 4.32 e a_0. \quad (\text{B.40})$$



Raman Schemes

Spin manipulation by RF coupling such as presented in chapter 2 is a well established technique, but however has limits. The large wavelength of RF fields prevents direct spatial addressing of the atoms and forbids large coupling in a metallic vacuum chamber. I will present here an alternative solution based on Raman transitions. This solution has been made accessible by the new laser diode based 589 nm laser that I have developed (and described in annex A), and offers the opportunity of position dependent couplings as well as large coupling strengths. It has one main drawback compared to magnetic coupling, which is the spontaneous emission from the finite detuning with the optical transition, that heats the atoms when the coupling is on. We recall the general expression of the lightshift that we derived in appendix B:

$$\hat{V}_{LS} = \frac{d_{sp}^2 |E|^2}{12} \left(\frac{2}{3\Delta_2} + \frac{1}{3\Delta_1} \right) + \mathbf{W} \cdot \mathbf{F}, \quad (C.1)$$

$$\mathbf{W} = \pm \frac{id_{sp}^2}{36} \left(\frac{1}{\Delta_1} - \frac{1}{\Delta_2} \right) \tilde{\mathbf{E}}^* \times \tilde{\mathbf{E}}, \quad (C.2)$$

The lightshift hamiltonian is the sum of a spin independent term, that we have considered for our dipole traps for example, and of a vector term, that acts as a magnetic field, and is non zero only in presence of circularly polarized light.

C.1 Rabi oscillations with copropagating beams

interaction Hamiltonian

We consider the manifold $F = 1$ ($F = I - 1/2$) of the ground state of an alkali atom in presence of two beams, propagating along axis \mathbf{x} , polarized along axis \mathbf{x} and \mathbf{z} respectively, in presence of a magnetic field along \mathbf{z} of frequencies ω_1 and ω_2 . The electric field is:

$$\mathbf{E} = \mathbf{e}_z E_0 \cos(\omega_1 t - k_L x) + \mathbf{e}_y E_0 \cos(\omega_2 t - k_L x), \quad (C.3)$$

and the vector \mathbf{W} is:

$$\mathbf{W} = -i \frac{d_{sp}^2 E_0^2}{144} \left(\frac{1}{\Delta_1} - \frac{1}{\Delta_2} \right) (e^{-i\Delta\omega t} - e^{i\Delta\omega t}) \mathbf{e}_x, \quad (C.4)$$

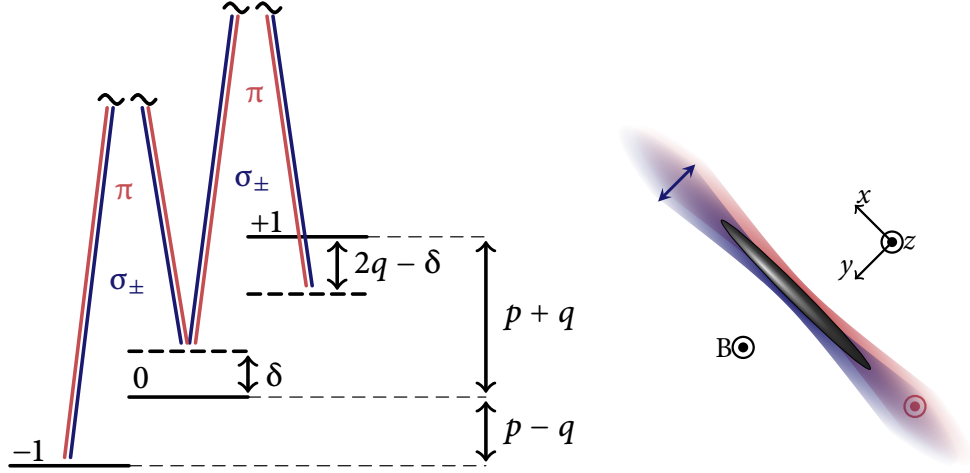


FIGURE C.1: Schematic of Raman coupling between Zeeman sub-levels in $F=1$. On the left, we show the three Zeeman levels of the $F=1$ manifold and the Raman transitions. On the right we show the laser geometry including a bias magnetic field B and the polarization of the lasers.

where we have defined according to figure C.1:

$$\Delta\omega = \omega_1 - \omega_2 = p - q + \delta, \quad (\text{C.5})$$

The interaction Hamiltonian is written:

$$\mathbf{W} \cdot \mathbf{F} = -i \frac{d_{\text{sp}}^2 E_0^2}{288} \left(\frac{1}{\Delta_1} - \frac{1}{\Delta_2} \right) (F_+ e^{-i\Delta\omega t} - F_+ e^{i\Delta\omega t} + F_- e^{-i\Delta\omega t} - F_- e^{i\Delta\omega t}). \quad (\text{C.6})$$

It is convenient to express the Hamiltonian in the referential precessing at $\Delta\omega$. It transforms F_+ into $F_+ e^{i\Delta\omega t}$ and F_- into $F_- e^{-i\Delta\omega t}$. We furthermore perform a rotating wave approximation, keeping only time-independent terms and obtain:

$$\mathbf{W} \cdot \mathbf{F}_{\text{rot}} = -i \frac{\Omega_R}{2} (F_+ - F_-) = \Omega_R \mathbf{F}_y, \quad (\text{C.7})$$

where we have defined the effective Rabi frequency Ω_R from the 2-level Rabi frequency $\Omega_0 = d_{\text{sp}} E_0$:

$$\Omega_R = \frac{\Omega_0^2}{144} \left(\frac{1}{\Delta_1} - \frac{1}{\Delta_2} \right). \quad (\text{C.8})$$

The Hamiltonian of the system is:

$$H_{\text{tot}} = \left(\frac{\mathbf{P}^2}{2M} + V_{\text{ext}} \right) \mathcal{I}d + (p - \Delta\omega) \mathbf{F}_z - q |0\rangle \langle 0| + \Omega_R \mathbf{F}_y, \quad (\text{C.9})$$

and can be decomposed as the sum of a diagonal part H_0 and a non-diagonal part H_{int} :

$$H_0 = \left(\frac{\mathbf{P}^2}{2M} + V_{\text{ext}} - q \right) \mathcal{I}d + \begin{pmatrix} 2q - \delta & 0 & 0 \\ 0 & 0 & 0 \\ 0 & 0 & \delta \end{pmatrix}, \quad (\text{C.10})$$

$$H_{\text{int}} = \Omega_R \mathbf{F}_y = \frac{\Omega_R}{\sqrt{2}i} \begin{pmatrix} 0 & -1 & 0 \\ 1 & 0 & -1 \\ 0 & 1 & 0 \end{pmatrix}. \quad (\text{C.11})$$

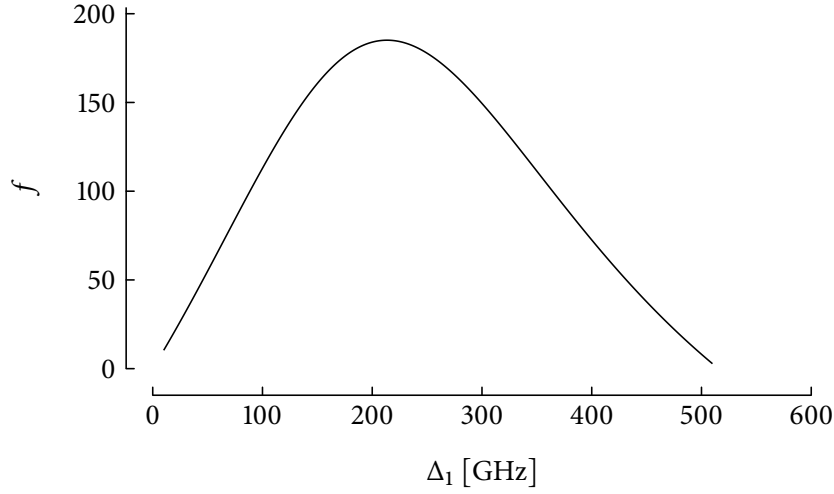


FIGURE C.2: Value of the figure of merit f as a function of the detuning of the Raman laser from the D1 transition. It corresponds to the number of Rabi cycles per spontaneous emission cycle and is calculated for the parameters of sodium.

Power per beam [mW]	Ω_0/h [GHz]	Ω_R/h [MHz]	$R_{\text{sp}}/2\pi$ [kHz]
100	17	2.6	1
10	5.4	0.26	0.1

TABLE C.1: Numerical estimation for Raman couplings with the geometry given in fig. C.1 beams and a waist of $100 \mu\text{m}$. Ω_0 is the one photon coupling, Ω_R is the two photons coupling and R_{sp} is the spontaneous emission rate. We observe that the coupling achieved with this parameters are at least one order of magnitude higher than what we can achieve with radiofrequencies (at most $\Omega \sim 20 \text{ kHz}$).

Rate of spontaneous emission and heating

In this paragraph, we calculate the spontaneous emission rate when a Raman coupling is applied in order to infer the heating rates. In the limit of far detuned fields, the saturation parameters of the D1 and D2 transition stay very small. In this limit, we can treat D1 and D2 lines as independent, and sum the contribution of both lines with their respective transition strengths. In this approximation, the spontaneous emission rate is:

$$R_{\text{sp}} = \Gamma \Omega_0^2 \left(\frac{1}{3\Delta_1^2} + \frac{2}{3\Delta_2^2} \right). \quad (\text{C.12})$$

In the limit where the effective Rabi frequency is very small compared to linear Zeeman Energy, such that the spin-dependent lightshift term can be neglected, we can define the figure of merit f :

$$f = \frac{\Omega_R^{\text{eff}}}{R_{\text{sp}}} = \frac{\frac{1}{\Delta_1} - \frac{1}{\Delta_2}}{48\Gamma \left(\frac{1}{\Delta_1^2} + \frac{2}{\Delta_2^2} \right)}. \quad (\text{C.13})$$

This quantity corresponds to the number of Rabi cycles one can perform before a spontaneous photon is emitted. It is showed in figure C.2. We find that the figure of merit reaches a maximum

$f = 185$ for a detuning of $\Delta_1/h = 214$ GHz. With this value for the detuning, and given beams of waist $w = 100 \mu\text{m}$, the values of relevant quantities are given on table C.I. For the following numerical estimations, we will always consider this detuning. We observe that the obtained couplings are high as compared with magnetic field (factor of 10 to 100 higher). We see that in 10 Rabi periods, there are 40 scattered photons in a 10000 atoms sample, corresponding to a 4 nK heating.

C.2 Spin Orbit coupling: *Spielman* scheme

We consider in this section the scheme used in [224], two beams: one polarized σ_+ propagating along z and one polarized along z propagating along x . The magnetic field is set along z . The electric field is:

$$\mathbf{E} = \mathbf{e}_+ E_0 \cos(\omega_1 t - k_L z) + \mathbf{e}_0 E_0 \cos(\omega_2 t - k_L x), \quad (\text{C.14})$$

and the vector field \mathbf{W} is written:

$$\mathbf{W} \cdot \mathbf{F} = \frac{d_{\text{sp}}^2 E_0^2}{144} \left(\frac{1}{\Delta_1} - \frac{1}{\Delta_2} \right) \left(\mathbf{F}_+ e^{-i(\Delta\omega t - k_L(z-x))} + \mathbf{F}_- e^{i(\Delta\omega t - k_L(z-x))} - \mathbf{F}_0 \right), \quad (\text{C.15})$$

If we now perform the same unitary transformation as in the previous section, and keep only the slow rotating terms, the interaction Hamiltonian is then:

$$\mathbf{W} \cdot \mathbf{F}_{\text{rot}} = \Omega_R \left(\mathbf{F}_+ e^{ik_L(z-x)} + \mathbf{F}_- e^{-ik_L(z-x)} - \mathbf{F}_0 \right), \quad (\text{C.16})$$

The full Hamiltonian is then written:

$$\begin{aligned} H_{\text{tot}} = & \left(\frac{\mathbf{p}^2}{2M} + V_{\text{ext}} \right) \mathcal{I}d + (p - \Delta\omega - \Omega_R) \mathbf{F}_z - q |0\rangle \langle 0| \\ & + 2\Omega_R \mathbf{F}_x \cos(k_L(z-x)) - 2\Omega_R \mathbf{F}_y \sin(k_L(z-x)). \end{aligned} \quad (\text{C.17})$$

We note that in presence of a large quadratic Zeeman energy such as in the case of ref. [224], only one of the Raman transition $m_F = 0 \rightarrow m_F = +1$ or $m_F = 0 \rightarrow m_F = -1$ can be resonant. These two components are not miscible which is an issue to observe the phase transition of ref. [224] for example. Direct coupling between the $m_F = +1$ and $m_F = -1$ states is not allowed in this geometry with two photons as we can only achieve $\Delta m_F = \pm 1$ with one σ and one π beam. As we will see in the next paragraph, this is can however be achieved by adding one additional σ beam with an appropriate frequency to realize a four photons transition.

C.3 Spin orbit coupling: 4 photons transitions

4 photon coupling

Direct coupling between the $m_F = +1$ and $m_F = -1$ states with Raman beams with the previous $\sigma\pi$ scheme is not possible due to momentum conservation. We examine a 4 photon scheme, where there are 2 σ_+ polarized beams, both propagating along z and of frequencies ω_1 and ω_3 and one π

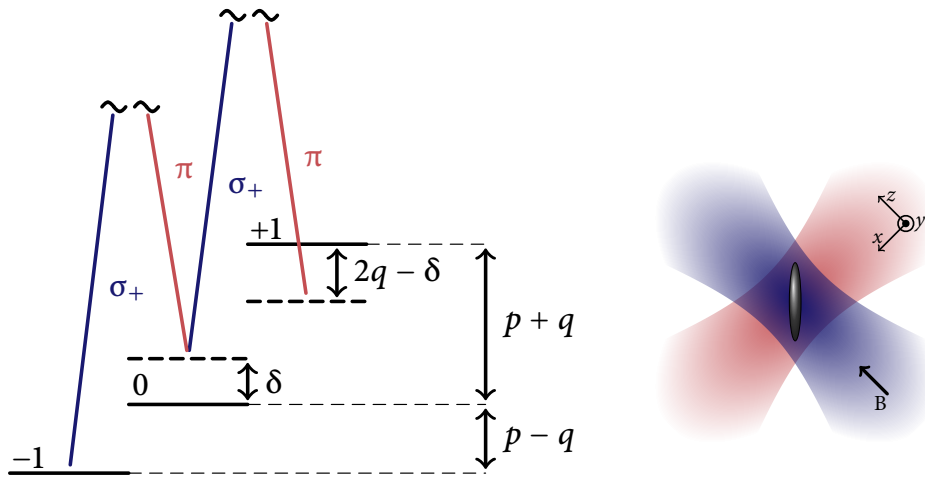


FIGURE C.3: Schematic of Raman coupling using one σ and one π beam crossing at an angle. We note that in presence of a large quadratic Zeeman energy, only two of the Zeeman states can be coupled resonantly.

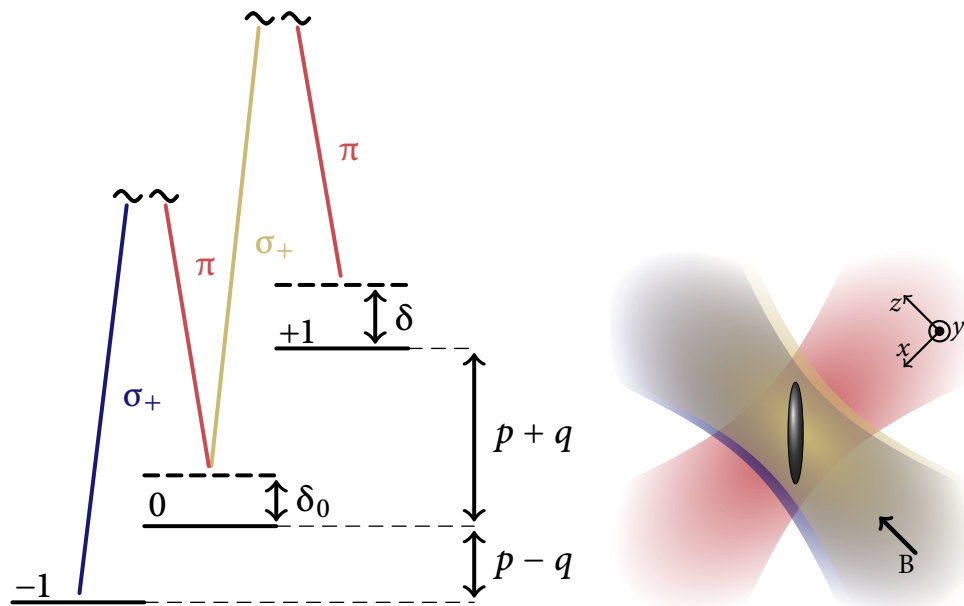


FIGURE C.4: Schematic of population transfer from $m_F = 1$ to $m_F = -1$ going through $m_F = 0$ with a four photon transition using two σ beams and one π beam. We note that an effective four photon coupling between the two states $m_F = \pm 1$ is realized only for a large enough detuning δ_0 .

polarized beam of frequency ω_2 propagating along x . According to the figure C.4 we have:

$$2\delta_m = \omega_1 - 2\omega_2 + \omega_3 = 2p + \delta, \quad (\text{C.18})$$

$$\delta_{12} = \omega_1 - \omega_2 = p - q + \delta_0, \quad (\text{C.19})$$

$$\delta_{32} = \omega_3 - \omega_2 = p + q - \delta_0 + \delta, \quad (\text{C.20})$$

$$\delta_{31} = \omega_3 - \omega_1 = 2q - 2\delta_0 + \delta, \quad (\text{C.21})$$

and the field is written:

$$\mathbf{E} = \mathbf{e}_+ E_0 \cos(\omega_1 t - k_L z) + \mathbf{e}_0 2E_0 \cos(\omega_2 t - k_L x) + \mathbf{e}_+ E_0 \cos(\omega_3 t - k_L z). \quad (\text{C.22})$$

The lightshift Hamiltonian containing only two photons transitions can be written as the sum of two operators describing the action of each pair of Raman beam:

$$\mathbf{W} \cdot \mathbf{F} = H^{(12)} + H^{(32)} - 2\Omega_R \cos(\delta_{13} t) \mathbf{F}_z \quad (\text{C.23})$$

$$H^{(12)} = \Omega_R \left(\mathbf{F}_+ e^{-i(\delta_{12} t - k_L(z-x))} + \mathbf{F}_- e^{i(\delta_{12} t - k_L(z-x))} - \mathbf{F}_z \right) \quad (\text{C.24})$$

$$H^{(32)} = \Omega_R \left(\mathbf{F}_+ e^{-i(\delta_{32} t - k_L(z-x))} + \mathbf{F}_- e^{i(\delta_{32} t - k_L(z-x))} - \mathbf{F}_z \right) \quad (\text{C.25})$$

We also consider the Hamiltonian for 4 photons processes:

$$H_{4\phi} = | +1 \rangle \langle -1 | \frac{\langle +1 | H^{(32)} | 0 \rangle \langle 0 | H^{(12)} | -1 \rangle}{\delta_0} + \text{h.c.}, \quad (\text{C.26})$$

$$= \frac{\Omega_R^2}{\delta_0} e^{-i(2\delta_m t - k_L(z-x))} | +1 \rangle \langle -1 | + \text{h.c.}. \quad (\text{C.27})$$

After a unitary transformation by operator $U_{\text{rot}} = \exp(-i\delta_m t \mathbf{F}_z)$, and keeping only stationary terms, the full hamiltonian is written:

$$\begin{aligned} H_{\text{tot}} = & \left(\frac{\mathbf{p}^2}{2M} + V_{\text{ext}} \right) \mathcal{I}d + (p - \delta_m - 2\Omega_R(1 + \cos(\delta_{13} t))) \mathbf{F}_z - q | 0 \rangle \langle 0 | \\ & + 2\Omega_R (\mathbf{F}_x \cos((\delta_{12} - \delta_m) t - ik_L(z-x)) - \mathbf{F}_y \cos((\delta_{12} - \delta_m) t - ik_L(z-x))) \\ & + 2\Omega_R (\mathbf{F}_x \cos((\delta_{32} - \delta_m) t - ik_L(z-x)) - \mathbf{F}_y \cos((\delta_{32} - \delta_m) t - ik_L(z-x))) \\ & + \frac{\Omega_{4\phi}}{2} (| +1 \rangle \langle -1 | e^{ik_L(z-x)} + | -1 \rangle \langle +1 | e^{-ik_L(z-x)}), \end{aligned} \quad (\text{C.28})$$

where we define the 4 photon Rabi frequency:

$$\Omega_{4\phi} = \frac{2\Omega_R^2}{\delta_0} = \frac{2\Omega_0^4}{\delta_0} \left(\frac{1}{\Delta_1} - \frac{1}{\Delta_2} \right)^2 \frac{1}{124}. \quad (\text{C.29})$$

We note that the factor 124 limits the coupling strength available with this scheme. The population of the intermediary state during this process is:

$$n_0 \propto \frac{\Omega_R^2}{\delta_0^2}. \quad (\text{C.30})$$

P_0 [mW]	δ_0/h [MHz]	Ω_R/h [MHz]	$\Omega_{4\phi}/h$ [Hz]	$R_{sp}/2\pi$ [kHz]	n_0 [%]
100	80	2.6	4.1k	1	0.01
100	10	2.6	33k	1	0.7
10	10	0.26	329	0.1	0.007
10	1	0.26	3.3k	0.1	0.7
10	0.1	0.26	33k	0.1	66
1	0.1	0.026	330	0.01	0.7
1	0.01	0.026	3.3k	0.01	66

TABLE C.2: Numerical estimations for 4 photons Raman couplings using beams of 100 μm . $P_0 = \epsilon_0 c |E_0|^2$ is the power per σ beam, Ω_R is the two photon Rabi frequency, $\Omega_{4\phi}$ is the 4 photons Rabi frequency, R_{sp} is the spontaneous emission rate and n_0 is the population in the state $m_F = 0$ during the process.

We calculated the rate of spontaneous emission by summing the contribution of the 3 beams:

$$R_{sp} = 4\Gamma\Omega_0^2 \left(\frac{1}{3\Delta_1^2} + \frac{2}{3\Delta_2^2} \right). \quad (C.31)$$

Hence, the way to favor the 4 photon process compared to the 2 photons one is to increase the intermediary detuning δ_0 up to a large value. If $p/h = 7$ MHz, $q/h = 28$ kHz, and we choose the following frequencies for the lasers:

$$\omega_1 = \omega_L + \omega_{AOM}, \quad (C.32)$$

$$\omega_3 = \omega_L - \omega_{AOM}, \quad (C.33)$$

$$\omega_2 = \omega_L - p. \quad (C.34)$$

In practice, ω_{AOM} could be either between 1 MHz and 10 MHz by using two AOMs with the same diffraction order, or ~ 100 MHz if we use two opposite diffraction order.

We compute some relevant quantities for this scheme on table C.2.

Spin orbit coupling Hamiltonian

With this parameter we can drop the rapidly oscillating terms from equation (C.28) to obtain:

$$H_{tot} = \left(\frac{\mathbf{p}^2}{2M} + V_{ext} \right) \mathcal{I}d + (-\delta/2 - 2\Omega_R) \mathbf{F}_z - q |0\rangle \langle 0| + \frac{\Omega_{4\phi}}{2} (|+1\rangle \langle -1| e^{ik_L(z-x)} + |-1\rangle \langle +1| e^{-ik_L(z-x)}), \quad (C.35)$$

The $m_f = 0$ state is decoupled, and we can rewrite the Hamiltonian in the pseudo spin 1/2 basis $\{m_f = -1, m_f = +1\}$:

$$H_2 = \left(\frac{\mathbf{p}^2}{2M} + V_{ext} \right) \mathcal{I}d - (\delta/2 + 2\Omega_R) \sigma_z + \Omega_{4\phi} \sigma_x \cos(k_L(z-x)) - \Omega_{4\phi} \sigma_y \sin(k_L(z-x)), \quad (C.36)$$

We define an alternate basis to ease the calculations:

$$\tilde{x} = (z + x)/\sqrt{2}, \quad (\text{C.37})$$

$$\tilde{y} = (z - x)/\sqrt{2}, \quad (\text{C.38})$$

$$\tilde{y} = y. \quad (\text{C.39})$$

Then we perform a rotation of angle $\hat{\Phi} = \sqrt{2}k\tilde{y}$ around the axis z . In particular, $\hat{\Phi}$ and $p_{\tilde{y}}^2$ do not commute and the application of the rotation operator to the kinetic energy create new terms describing spin-orbit coupling:

$$R_{\hat{\Phi}}^\dagger p_{\tilde{y}}^2 R_{\hat{\Phi}} = p_{\tilde{y}}^2 + 2\hbar\sqrt{2}k_L p_{\tilde{y}} \sigma_z + 2\hbar^2 k_L^2. \quad (\text{C.40})$$

The full Hamiltonian can be expressed:

$$R_{\hat{\Phi}}^\dagger H_2 R_{\hat{\Phi}} = \left(\frac{\mathbf{p}^2}{2M} + V_{\text{ext}} \right) \mathcal{I}d - (\delta/2 + 2\Omega_R) \sigma_z + \Omega_{4\phi} \sigma_x + 2 \frac{\hbar^2 \sqrt{2} k_L k_{\tilde{y}}}{2M} \sigma_z + 2E_{\text{rec}}, \quad (\text{C.41})$$

where E_{rec} is the recoil energy. We obtain an hamiltonian containing a spin-orbit coupling term.

conclusion

In table C.2 we show the coupling strength predicted for this scheme using realistic experimental parameters. As discussed in ref. [224] for example, relevant values for the Raman couplings are set by the recoil energy associated with the wavelength $\lambda = 589$ nm of the Raman laser which is $E_r \simeq 25$ kHz. We observe that even though table C.2 suggests that this regime can be reached with relatively high power in each beam ($P_0 = 100$ mW) and not too large intermediary detuning ($\delta_0 = h \cdot 10$ MHz), the calculated heating rate is likely to be too high to allow for a sufficient equilibration time to perform a spin orbit coupling experiment.

Even though the regime where we couple two components does not seem to be accessible, we could instead choose a relatively low value of the intermediary detuning δ_0 . The figure of merit would be similar to the case of two photon couplings, and would allow to couple the three Zeeman components resonantly in presence of a finite quadratic Zeeman energy.

D

Spin-mixing oscillations

In this appendix we will describe spin mixing oscillations, which are dynamical manifestations of the spin exchange interactions in spinor BEC (see refs. [43–45, 49, 51]). In our experiment, spin mixing oscillations manifest in two occasions. First, they are a very convenient way to measure spin-exchange interaction in spinor Bose-Einstein condensate. Second, spin mixing “oscillations” can affect the populations during a ramp of magnetic field. This can modify the measured populations after a Stern-Gerlach imaging sequence (see sec. 2.2.1), in which we ramp large fields to create the spin dependent force required for Stern-Gerlach imaging.

The theoretical description of spin-mixing oscillation follows from the time dependent Gross-Pitaevskii equation with the spin Hamiltonian (3.1) for a BEC in the single mode regime. Authors of ref. [44] derived a set of coupled equations for the evolution of the spinor wavefunction (3.2):

$$\dot{n}_0 = \frac{2U_s}{\hbar} n_0 \sqrt{(1 - n_0)^2 - m_z^2} \sin(\Theta) \quad (\text{D.1})$$

$$\dot{\Theta} = \frac{2q}{\hbar} + \frac{2U_s}{\hbar} (1 - 2n_0) + \left(\frac{2U_s}{\hbar} \right) \frac{(1 - n_0)(1 - 2n_0) - m_z^2}{\sqrt{(1 - n_0)^2 - m_z^2}} \cos(\Theta). \quad (\text{D.2})$$

These equations are solved numerically in the cases considered in this annex. In the following, I will present two examples of situations in which the description of spin-mixing oscillations allows either to measure the spin-exchange energy or to improve the accuracy of population counting.

D.1 Spin mixing oscillations after a Rabi Oscillation

We designed an experiment to trigger spin mixing oscillations on purpose to extract the spin exchange energy U_s from the measured oscillation period. We bring the cloud to a non equilibrium state by performing a spin rotation from a state polarized in $m_F = 0$ (see sec. 2.4.1) that has been “purified” by transverse distillation (see sec. 2.4.4) and observe the evolution of the population of the component $m_F = 0$ with a varying hold time. We set the initial population of the $m_F = 0$ state after a rotation to $n'_0 \sim 0.3$ and observe in figure fig. D.1 an oscillation of the population after a hold time as predicted in ref. [44]. It is worth noting that the magnetization of the sample does not vary during the oscillation because they originate from spin changing collisions that conserve m_z . We compute the evolution of n_0 from eqs.(D.1), (D.2), that we solve numerically. We extract

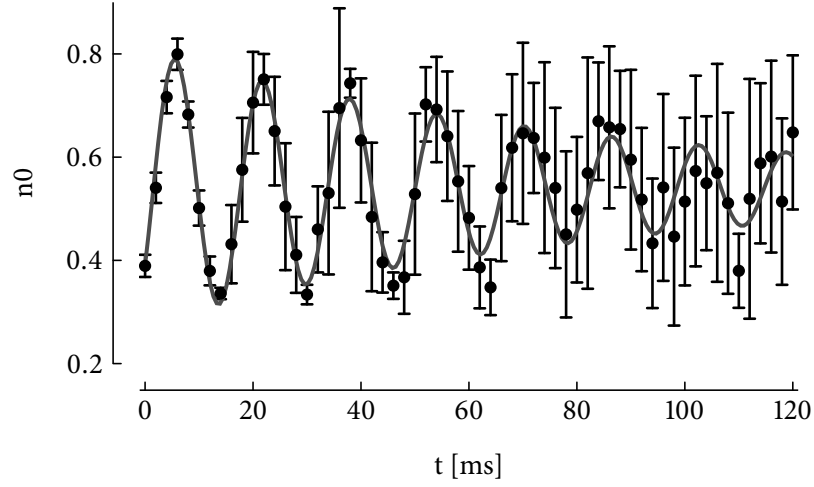


FIGURE D.1: Spin mixing oscillations obtained by free evolution of a spinor BEC during a time t after a rotation of a nematic state. We determine the period by a fit to a exponentially damped sine function (in red). We observe a rapid dephasing of the oscillation due to atom number fluctuations in this particular dataset.

the oscillation period by fitting numerical data and present them in fig. D.2. We can deduce from the oscillation period the actual interaction strength from our data $U_s = 38$ Hz.

We observe a rapid dephasing of spin mixing oscillation (only ~ 10 period are visible). This could be explained by atom number fluctuations during the data taking, that effectively varies the spin-exchange energy hence the spin mixing oscillatory period (see fig. D.2).

The oscillations presented in fig. D.1, are obtained from rotation of a nematic state such that $\Theta(t=0) = \pi$. We performed a similar experiment, this time by rotating an oriented state until $m_z \sim 0$. This produces quite different results, shown in fig. D.3 in which we compare the results of these two experiments. This is because in the case of the rotation of an oriented state, the phases of the three Zeeman component are equal $\phi_{+1} = \phi_0 = \phi_{-1}$ after rotation such that $\Theta(t=0) = 0$. In this case, the period of the oscillations, their amplitude and initial phase are different as observed in fig. D.3.

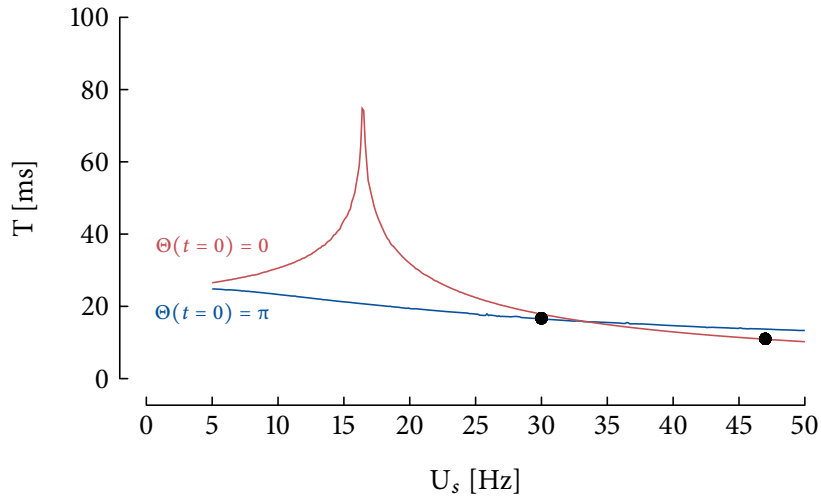


FIGURE D.2: Oscillation period of spin mixing oscillations obtained from a numerical solution of eqs (D.1),(D.2). We determine the period by performing a sinusoidal fit of the simulations for the first five oscillations. We plot with black points the periods, and corresponding spin exchange energy obtained from damped sinusoidal fits of the data shown in fig. D.3. We notice the data starting from an oriented state has higher spin exchange energy than the sample starting from a nematic state. This is due to the higher atom number in the latter case $N \simeq 11000$ compared to $N \simeq 7000$ in the former.

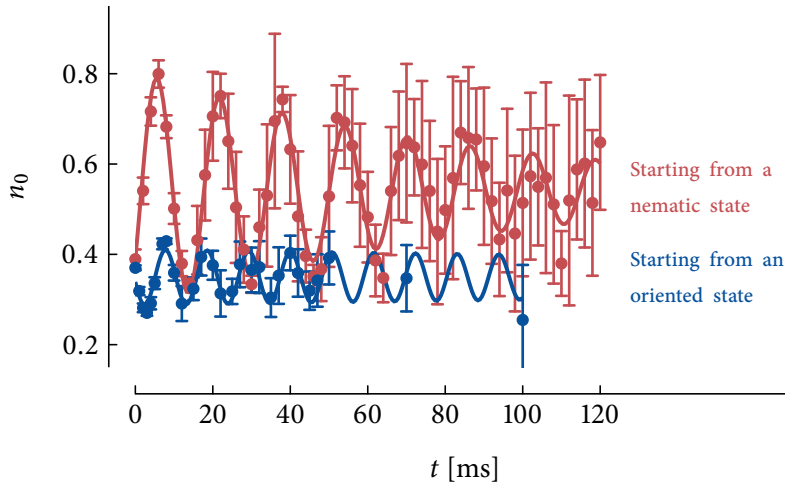


FIGURE D.3: Spin mixing oscillations obtained by free evolution of a spinor BEC during a time t after a Rotation of either a nematic or an oriented state. We observe that the initial derivative of the evolution is opposite in both case due to the different initial phase (populations in $m_F = 0$ are comparable and m_z is equal to 0 in both case).

D.2 Evolution of the populations during a magnetic field ramp

In the experiment, the measurement of populations after a Rabi oscillations requires a mechanism to “freeze” spin mixing dynamics. We do this by ramping a large homogeneous field immediately after the spin rotation. Indeed, in the case the quadratic Zeeman shift is large $q \gg U_s$, eq (D.2) reduces to $\Theta \simeq 2q/\hbar$, such that $\Theta \simeq 2qt/\hbar$. In this case, the right hand side of eq. (D.1) averages out, and the evolution of the populations is suppressed (see ref. [44]). We simulate this evolution by solving numerically eqs. (D.1), (D.2) including a time dependent quadratic Zeeman energy (see fig. D.4 for a representation of this ramp).

We start from a cloud with $m_z \simeq 0.33$, $n_0 \simeq 0.39$ (data from the measurement in chapter 3), and apply a linear ramp of magnetic field ramp along the y axis from 0 to 3 G in 3 ms. We show the effect of this ramp in fig. D.4. We notice that the main effect of the spin mixing oscillations in this case consist in a small systematic error on the order of 3% on the measured $m_F = 0$. This translates in an error of 1.5% in the populations of the $m_F = \pm 1$. The spin mixing dynamics does not affect the magnetization such that the measurement of phase locking described in chapter 3 is not affected. However, the measurement of the spin temperature, based on the actual mean of n_0 requires to be corrected for this effect. Concerning the measurement on chapter 4, we expect the datasets taken at $B = 0.5$ G and $B = 5.6$ G not to be affected due to the relatively high quadratic energy already before the magnetic field ramp of the Stern-Gerlach imaging sequence. The case of the dataset taken at $B = 0.1$ G is similar to the case described in sec. D.4. We do not expect that the small increase of population in the $m_F = 0$ to be mistaken for condensation, given the associated increase in density would be small.

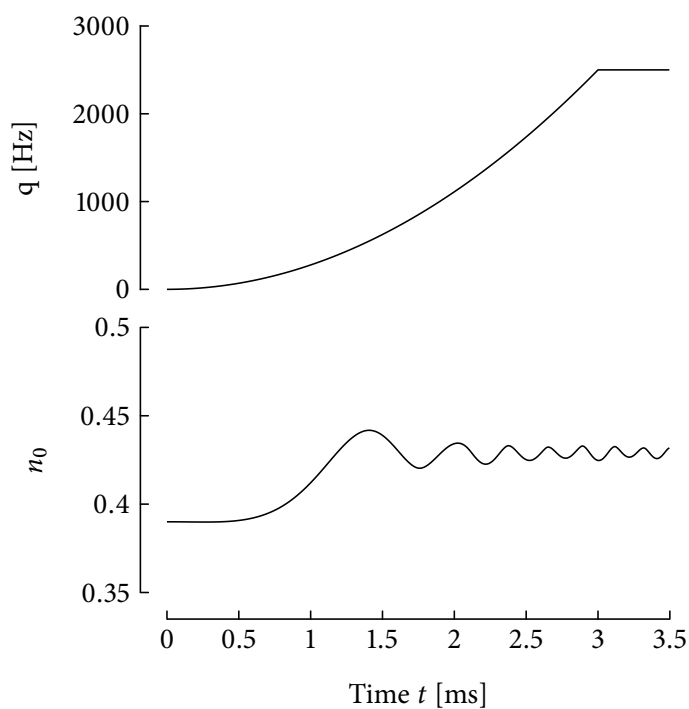


FIGURE D.4: Illustration of the effect of spin changing collisions during a ramp of the magnetic field. We use a linear ramp of the magnetic field, which corresponds to a quadratic ramp of the quadratic Zeeman energy. On the lower panel, we see an increase of n_0 of 3% between the beginning and the end of the magnetic field ramps (discarding the small amplitude oscillation after the ramp ends).

E

Perturbative development around the point of simultaneous condensation

We notice in fig. 4.17 a discontinuity of the second critical temperature T_{c2} , to the left of the point m_z^* (* stands for the point where both specie condense at the same time in the ideal case, the “crossing point”, as described in the first chapter) in the case where $B=5.6$ G (we recall it corresponds to $q = 8.9$ kHz, and that $\alpha = \exp(-\beta q)$).

Expansion near the point of simultaneous condensation

In this paragraph, we will show that the discontinuity can be deduced from a first order expansion around the point of coordinates $(M_z, t, \mu) = (M_z^*, t_*, 0)$ such that $(M_z, t, \mu) = (M_z^* + \delta M_z, t_* + \delta t, \delta \mu)$. Equations (4.36) and (4.37) on the one hand and (4.38) and (4.39) on the other hand, are computed using the chemical potentials at the second critical temperature in eqs. (4.33), (4.34), (4.35). The condensate population can be estimated within a Thomas Fermi approximation by $N_c = (2\delta\bar{\mu})^{5/2} a_{ho}/15a$. At first order in $\delta\bar{\mu}$, $\delta t/t_*$, we can neglect the condensate population and the expansion on both sides of the crossing point take the same form such that we have :

$$N = \overbrace{t_*^3 (2g_3(1) + g_3(\alpha^{*2}))}^N + t_*^3 (2g_2(1) + g_2(\alpha^{*2})) \delta\bar{\mu} + t_*^3 \left(\frac{3}{t_*} (2g_3(1) + g_3(\alpha^{*2})) + \frac{2\bar{q}}{t_*^2} g_2(\alpha^{*2}) \right) \delta t + O(\delta\bar{\mu}^{5/2}), \quad (E.1)$$

$$M_z^* + \delta M_z = \overbrace{t_*^3 (g_3(1) - g_3(\alpha^{*2}))}^{M_z^*} + t_*^3 (g_2(1) - g_2(\alpha^{*2})) \delta\bar{\mu} + t_*^3 \left(\frac{3}{t_*} (g_3(1) - g_3(\alpha^{*2})) - \frac{2\bar{q}}{t_*^2} g_2(\alpha^{*2}) \right) \delta t + O(\delta\bar{\mu}^{5/2}). \quad (E.2)$$

Here we introduce the reduced quadratic Zeeman energy and chemical potential $\bar{q} = q/\hbar\omega$ and $\delta\bar{\mu} = \delta\mu/\hbar\omega$, and the normalized magnetization $m_z = M_z/N$. We recall that $t = k_B T/\hbar\omega$ is the

reduced temperature. We simplify and renormalize eqs (E.1), (E.2) by N and M^* respectively and we obtain :

$$0 = \frac{2g_2(1) + g_2(\alpha^{*2})}{2g_3(1) + g_3(\alpha^{*2})} \delta\bar{\mu} + \left(\frac{3}{t_*} - \frac{2\bar{q}}{t_*^2} \frac{g_2(\alpha^{*2})}{2g_3(1) + g_3(\alpha^{*2})} \right) \delta t, \quad (\text{E.3})$$

$$\frac{\delta m_z}{m_z^*} = \frac{g_2(1) - g_2(\alpha^{*2})}{g_3(1) - g_3(\alpha^{*2})} \delta\bar{\mu} + \left(\frac{3}{t_*} - \frac{2\bar{q}}{t_*^2} \frac{g_2(\alpha^{*2})}{g_3(1) - g_3(\alpha^{*2})} \right) \delta t. \quad (\text{E.4})$$

We further develop:

$$0 = \left[\frac{2g_2(1) + g_2(\alpha^{*2})}{2g_3(1) + g_3(\alpha^{*2})} \right] \delta\bar{\mu} + \left[3 + \frac{2\bar{q}t_*^2}{N} g_2(\alpha^{*2}) \right] \frac{\delta t}{t_*}, \quad (\text{E.5})$$

$$\frac{\delta m_z}{m_z^*} = \left[\frac{g_2(1) - g_2(\alpha^{*2})}{g_3(1) - g_3(\alpha^{*2})} \right] \delta\bar{\mu} + \left[3 - \frac{2\bar{q}t_*^2}{m^*N} g_2(\alpha^{*2}) \right] \frac{\delta t}{t_*}. \quad (\text{E.6})$$

At this point, we propose to set:

$$0 = A\delta\bar{\mu} + B\delta t/t_*, \quad (\text{E.7})$$

$$\frac{\delta m_z}{m_z^*} = C\delta\bar{\mu} + D\delta t/t_*, \quad (\text{E.8})$$

such that :

$$\frac{\delta m_z}{m_z^*} = \left(D - \frac{BC}{A} \right) \frac{\delta t}{t_*}, \quad (\text{E.9})$$

If we consider the case of fig. 4.17, $N=50000$, $\omega = 2\pi \cdot 500$ Hz and $B = 5.6$ G, we have:

$$m_z^* = 0.18, \quad (\text{E.10})$$

$$t_* = 0.72N^{1/3}, \quad (\text{E.11})$$

$$A \simeq 1.33, B \simeq 4.42, C \simeq 1.46, D \simeq 3.1, \quad (\text{E.12})$$

$$\frac{\delta m_z}{m_z^*} \simeq -1.78\delta t/t_*. \quad (\text{E.13})$$

We see that with these coefficients, there are no couple of solutions $(\delta t, \delta\bar{\mu})$ that provide a physical solution when $\delta m_z < 0$ as $\delta t > 0$ contradicts the initial assumption used to write eqs. (4.39),(4.38). This is represented in fig. E.1, where we show the values of eq. (E.6) for several values of $\delta\bar{\mu}$. We see that when neglecting the condensate population near the crossing point, there are no solutions found to its left. This explains the discontinuity of the critical temperature in fig. 4.17. We note that this development does not describe well the case of an ideal gas (where the condensed population needs to be included even for very small $\delta t/t_*$). It does not explain either why the second condensation takes place at lower temperature. We will now consider what happens for lower temperatures where the approximation $\delta t/t_* \ll 1$ is not valid anymore. We note that for lower temperatures, there may be a large condensate such that $\delta\bar{\mu} \ll 1$ is not valid either.

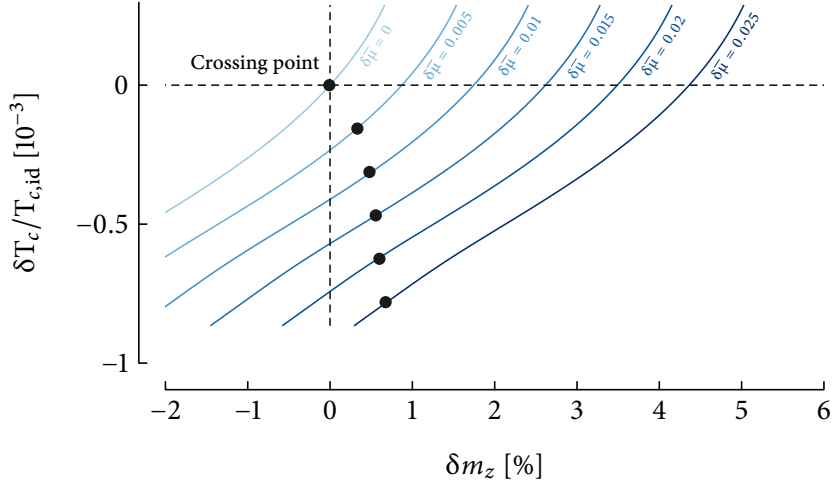


FIGURE E.1: Values of eq. (E.6) for several values of $\delta\bar{\mu}$. We plot the result of eq. (E.5) by a black dot on each line. We observe that there are no solutions found to the left of the crossing point.

Expansion at low temperatures

We try another approach in which we look at equations (4.38) and (4.39) at very low temperatures, such that $\bar{\mu}/t \gg 1$. In this case, we ignore the thermal population of the $m_F = \pm 1$ outside of the region of the condensate. This is done in eq. (4.28) by setting $\Gamma(3/2, k\beta\mu_c) \simeq 0$, such that at the second critical point we have:

$$N_{+1} = N'_{+1} \simeq \frac{4\pi}{3} (t\bar{\mu})^{3/2} g_{3/2}(1) \quad (\text{E.14})$$

$$N_0 = N_c + N'_0, \quad (\text{E.15})$$

$$N_{-1} = N'_{-1} \simeq \frac{4\pi}{3} (t\bar{\mu})^{3/2} g_{3/2}(\alpha^2) \quad (\text{E.16})$$

We have used the relation $(R_{TF}/\lambda_{th})^2 = t\bar{\mu}$ to express the thermal atom numbers in each component. We can obtain an equation on the second critical temperature by dividing (4.39) and (4.38) with definitions (E.14), (E.15), (E.16) for the population in each component. Within the assumption $\mu/t \gg 1$, the $m_F = 0$ is mostly condensed and we neglect its thermal population $N'_0 \ll N_c$ for the sake of simplicity. The condensed atom number is given in the Thomas Fermi approximation by:

$$N_c = \frac{(2\mu)^{5/2} a_{ho}}{15a} \quad (\text{E.17})$$

We finally obtain:

$$m_z \simeq \frac{g_{3/2}(1) - g_{3/2}(\alpha^2)}{(g_{3/2}(1) + g_{3/2}(\alpha^2)) + \frac{\sqrt{2}a_{ho}}{5\pi a} \frac{\bar{\mu}}{t}}. \quad (\text{E.18})$$

With this expression, we see that the issue highlighted by eqs. (E.5) and (E.6) no longer exists in the low temperature regime. We see that reducing the temperature reduces $\alpha = \exp(-\beta q)$ which in turn increases the magnetization. In other words, due to the conservation of magnetization the

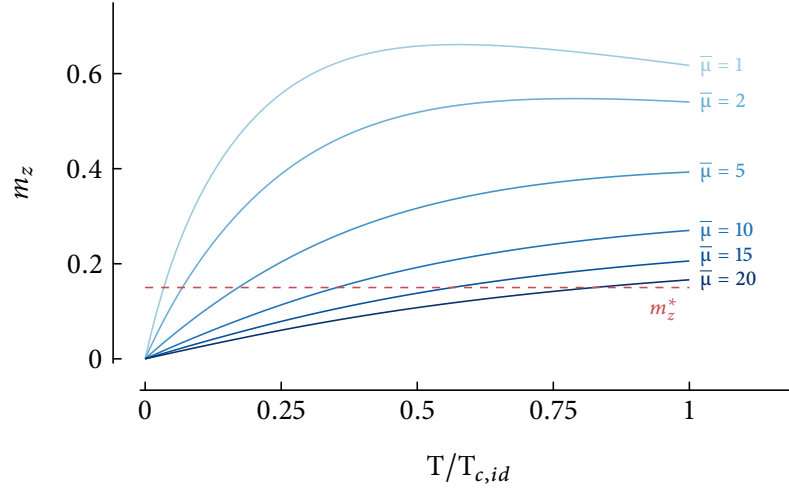
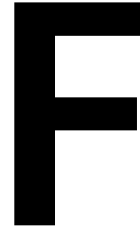


FIGURE E.2: Values of eq. (E.18) for several values of $\bar{\mu}$. We plot the value of the magnetization at the crossing point in red. Each intersection between the red dashed curve and eq. (E.18) is a solution. However, for higher values of $\bar{\mu}$ there are many solutions. The right solution will be determined by the dependence of the thermal population in the $m_F = 0$ state on temperature.

$m_F = -1$ components always have a slightly larger chemical potential than the $m_F = +1$ component. As such, as the temperature decreases, the $m_F = +1$ component will stay almost saturated while the $m_F = -1$ will be progressively depopulated. This explains that for $m_z < m_z^*$, no solution can be found if the condensate is ignored. The total magnetization of the gas can be reduced by the growth of the condensate. If we allow the chemical potential $\bar{\mu}$ to take a finite value, we see that it is possible to find a solution for the right hand side of eq. (E.18) just by increasing $\bar{\mu}$.

We plot in fig. E.2, eq. (E.18) for several values of $\bar{\mu}$. For $\mu > 0$ we observe that several couples of solution $(t, \bar{\mu})$ exist. The temperature dependence of the condensed fraction, which depends on the interaction strength, will fix which couple of solution to consider. In the case described by figure 4.17, the solution is around $(0.5, 15)$, such that the assumption $\bar{\mu}/t \gg 1$ is well verified and the model above is realistic. We note that in this case neglecting the thermal fraction of the $m_F = 0$ component is not completely justified (the formula derived in ref. [201] for low temperatures predicts $f_c \simeq 0.73$ for example), but this does not change the above behavior qualitatively.



Remerciements

A PREMIÈRE VUE, L'ÉCRITURE D'UNE THÈSE SE PERÇOIT COMME UN EXERCICE INDIVIDUEL. Pourtant, c'est le résultat de plusieurs années d'un travail qui n'aurait pu aboutir sans l'aide de nombreuses personnes, que je souhaite désormais remercier.

Tout d'abord, je remercie les membres du laboratoire Kastler Brossel et son directeur Antoine Heidmann, qui ont su m'offrir un cadre de travail stimulant et agréable pendant cette thèse. Ceci inclut bien évidemment tant les services techniques qu'administratifs non seulement du laboratoire (Thierry Tardieu et Audrey Gohlke) mais également des établissements d'accueil (Pascal Travers au Collège de France, Didier Courtiade notamment pour son aide lors du déménagement et les membres du service mécanique et électronique à l'ENS). Je remercie également Carmen Toderasc pour son aide au quotidien ainsi que pour l'organisation de la soutenance de thèse. Merci également aux membres du jury d'avoir accepté de lire et d'évaluer mon manuscrit.

Ensuite j'aimerais remercier plus particulièrement les membres du groupe *atomes froids* tant pour leur sympathie que pour m'avoir permis d'évoluer dans un environnement stimulant et agréable. Parmi eux, les résidents du deuxième étage du Collège de France sont particulièrement à remercier pour avoir su en plus supporter mes nombreuses facéties, dont l'usage ne se réservait pas aux moments opportuns. C'est pour cela que des remerciements plus importants encore vont aux membres de l'équipe, qui en plus de m'avoir aidé à obtenir les résultats présentés dans cette thèse, ont eu la patience de me supporter au quotidien au laboratoire (voir pour un été pour Davide Dreon). Ainsi, je remercie tout particulièrement (par ordre d'apparition) Vincent Corre, Tilman Zibold, Andrea Invernizzi, Karina Jiménez-García et Bertrand Évrard. Enfin, je voudrais remercier mes directeurs de thèse: Jean Dalibard, qui a su rester disponible tout au long de ma thèse malgré son agenda bien chargé et Fabrice Gerbier qui a très largement contribué à la réussite de cette thèse par son aide tant au quotidien que pendant la rédaction en répondant à mes nombreuses questions et en m'offrant toujours l'opportunité d'apprendre toutes les subtilités que peut présenter la pratique de la physique expérimentale.

Enfin, sur un plan plus personnel, j'aimerais remercier mes colocataires Mathieu Casado et Thomas Rigaldo, pour m'avoir supporté avant, pendant et après ma rédaction ainsi que l'ensemble de mes amis, que je ne citerai pas nommément pour éviter d'en oublier. Pour finir, je souhaite remercier les membres de ma famille pour leur soutien constant au fil des années ainsi que mes parents, mon frère et ma sœur dont le support m'a sans aucun doute mené jusqu'à l'achèvement de ce manuscrit.

Bibliography

- [1] Bernard Diu, Bernard Roulet, Claudine Guthmann, and Danielle Lederer. *Eléments de physique statistique*. Hermann, 1989.
- [2] L. D. Landau and E. M. Lifshitz. *Statistical Physics*. Pergamon Press, London, 1980.
- [3] Peter Mohn. *Magnetism in the Solid State*. Springer, 2005.
- [4] P. Kapitza. Viscosity of liquid helium below the λ -point. *Nature*, 141(3558):74–74, jan 1938.
- [5] J. G. Daunt and R. S. Smith. The problem of liquid helium—some recent aspects. *Reviews of Modern Physics*, 26(2):172–236, apr 1954.
- [6] Satyendra Nath Bose. Plancks gesetz und lichtquantenhypothese. *Z. phys*, 26(3):178, 1924.
- [7] Albert Einstein. *Quantentheorie des einatomigen idealen Gases*. Preussische Akademie der Wissenschaften, 1924.
- [8] Steven Chu. Nobel lecture: The manipulation of neutral particles. *Reviews of Modern Physics*, 70(3):685–706, jul 1998.
- [9] William D. Phillips. Nobel lecture: Laser cooling and trapping of neutral atoms. *Reviews of Modern Physics*, 70(3):721–741, jul 1998.
- [10] Claude N. Cohen-Tannoudji. Nobel lecture: Manipulating atoms with photons. *Reviews of Modern Physics*, 70(3):707–719, jul 1998.
- [11] Wolfgang Ketterle. Nobel lecture: When atoms behave as waves: Bose-Einstein condensation and the atom laser. *Reviews of Modern Physics*, 74(4):1131–1151, 2002.
- [12] E. A. Cornell and C. E. Wieman. Nobel lecture: Bose-einstein condensation in a dilute gas, the first 70 years and some recent experiments. *Reviews of Modern Physics*, 74(3):875–893, aug 2002.
- [13] Kendall B Davis, M-O Mewes, Michael R Andrews, NJ Van Druten, DS Durfee, DM Kurn, and Wolfgang Ketterle. Bose-einstein condensation in a gas of sodium atoms. *Physical review letters*, 75(22):3969, 1995.
- [14] Franco Dalfovo, Stefano Giorgini, Lev P. Pitaevskii, and Sandro Stringari. Theory of Bose-Einstein condensation in trapped gases. *Rev. Mod. Phys.*, 71:463, 1999.

- [15] Immanuel Bloch, Jean Dalibard, and Wilhelm Zwerger. Many-body physics with ultracold gases. *Rev. Mod. Phys.*, 80:885–964, July 2008.
- [16] S. Inouye, M. R. Andrews, J. Stenger, H.-J. Miesner, D. M. Stamper-Kurn, and W. Ketterle. Observation of feshbach resonances in a bose–einstein condensate. *Nature*, 392(6672):151–154, mar 1998.
- [17] Cheng Chin, Rudolf Grimm, Paul Julienne, and Eite Tiesinga. Feshbach resonances in ultracold gases. *Reviews of Modern Physics*, 82(2):1225–1286, apr 2010.
- [18] M. R. Andrews. Observation of interference between two bose condensates. *Science*, 275(5300):637–641, jan 1997.
- [19] T. Esslinger, I. Bloch, and T. W. Hänsch. Measurement of the spatial coherence of a trapped bose gas at the phase transition. *Nature*, 403(6766):166–170, jan 2000.
- [20] M. R. Matthews, B. P. Anderson, P. C. Haljan, D. S. Hall, C. E. Wieman, and E. A. Cornell. Vortices in a bose-einstein condensate. *Physical Review Letters*, 83(13):2498–2501, sep 1999.
- [21] K. W. Madison, F. Chevy, W. Wohlleben, and J. Dalibard. Vortex formation in a stirred bose-einstein condensate. *Physical Review Letters*, 84(5):806–809, jan 2000.
- [22] J. R. Abo-Shaeer, C. Raman, J. M. Vogels, and W. Ketterle. Observation of vortex lattices in bose-einstein condensates. *Science*, 292(5516):476–479, apr 2001.
- [23] C. Raman, M. Köhl, R. Onofrio, D. S. Durfee, C. E. Kuklewicz, Z. Hadzibabic, and W. Ketterle. Evidence for a critical velocity in a bose-einstein condensed gas. *Physical Review Letters*, 83(13):2502–2505, sep 1999.
- [24] Brian DeMarco and Deborah S Jin. Onset of fermi degeneracy in a trapped atomic gas. *Science*, 285(5434):1703–1706, 1999.
- [25] T. Kinoshita. Observation of a one-dimensional tonks-girardeau gas. *Science*, 305(5687):1125–1128, aug 2004.
- [26] Belén Paredes, Artur Widera, Valentin Murg, Olaf Mandel, Simon Fölling, Ignacio Cirac, Gora V. Shlyapnikov, Theodor W. Hänsch, and Immanuel Bloch. Tonks–girardeau gas of ultracold atoms in an optical lattice. *Nature*, 429(6989):277–281, may 2004.
- [27] Zoran Hadzibabic, Peter Krüger, Marc Cheneau, Baptiste Battelier, and Jean Dalibard. Berezinskii-kosterlitz-thouless crossover in a trapped atomic gas. *Nature*, 441(7097):1118–1121, jun 2006.
- [28] Rémi Desbuquois, Lauriane Chomaz, Tarik Yefsah, Julian Léonard, Jérôme Beugnon, Christof Weitenberg, and Jean Dalibard. Superfluid behaviour of a two-dimensional bose gas. *Nature Physics*, 8(9):645–648, jul 2012.
- [29] F. Gerbier, J. H. Thywissen, S. Richard, M. Hugbart, P. Bouyer, and A. Aspect. Critical temperature of a trapped, weakly interacting bose gas. *Phys. Rev. Lett.*, 92:030405, Jan 2004.

- [30] Markus Greiner, Olaf Mandel, Tilman Esslinger, Theodor W. Hänsch, and Immanuel Bloch. Quantum phase transition from a superfluid to a mott insulator in a gas of ultracold atoms. *Nature*, 415(6867):39–44, jan 2002.
- [31] I. Spielman, W. Phillips, and J. Porto. Mott-insulator transition in a two-dimensional atomic bose gas. *Physical Review Letters*, 98(8), feb 2007.
- [32] Thilo Stöferle, Henning Moritz, Christian Schori, Michael Köhl, and Tilman Esslinger. Transition from a strongly interacting 1d superfluid to a mott insulator. *Physical Review Letters*, 92(13), mar 2004.
- [33] Juliette Billy, Vincent Josse, Zhanchun Zuo, Alain Bernard, Ben Hambrecht, Pierre Luga, David Clément, Laurent Sanchez-Palencia, Philippe Bouyer, and Alain Aspect. Direct observation of anderson localization of matter waves in a controlled disorder. *Nature*, 453(7197):891–894, jun 2008.
- [34] M. Boll, T. A. Hilker, G. Salomon, A. Omran, J. Nespolo, L. Pollet, I. Bloch, and C. Gross. Spin- and density-resolved microscopy of antiferromagnetic correlations in fermi-hubbard chains. *Science*, 353(6305):1257–1260, sep 2016.
- [35] L. W. Cheuk, M. A. Nichols, K. R. Lawrence, M. Okan, H. Zhang, E. Khatami, N. Trivedi, T. Paiva, M. Rigol, and M. W. Zwierlein. Observation of spatial charge and spin correlations in the 2d fermi-hubbard model. *Science*, 353(6305):1260–1264, sep 2016.
- [36] D. M. Stamper-Kurn, M. R. Andrews, A. P. Chikkatur, S. Inouye, H.-J. Miesner, J. Stenger, and W. Ketterle. Optical confinement of a bose-einstein condensate. *Physical Review Letters*, 80(10):2027–2030, mar 1998.
- [37] Rudolf Grimm, Matthias Weidemüller, and Yurii B. Ovchinnikov. Optical dipole traps for neutral atoms. *Advances in Atomic, Molecular and Optical Physics Vol. 42, 95-170 (2000)*.
- [38] D. Vollhardt and P. W ölfle. *The Superfluid Phases of Helium 3*. Taylor and Francis, London, 1990.
- [39] D. D. Osheroff, R. C. Richardson, and D. M. Lee. Evidence for a new phase of SolidHe3. *Physical Review Letters*, 28(14):885–888, apr 1972.
- [40] H. Schmaljohann, M. Erhard, J. Kronjäger, M. Kottke, S. van Staa, L. Cacciapuoti, J. J. Arlt, K. Bongs, , and K. Sengstock. Dynamics of $f = 2$ Spinor Bose-Einstein condensates. *Phys. Rev. Lett.*, 92(4):040402, jan 2004.
- [41] H. Schmaljohann, M. Erhard, J. Kronjäger, K. Sengstock, and K. Bongs. Dynamics and thermodynamics in spinor quantum gases. *Applied Physics B*, 79(8):1001–1007, dec 2004.
- [42] H. Schmaljohann, M. Erhard, J. Kronjägert, M. Kottke, S. Van Staa, J. J. Arlt, K. Bongs, and K. Sengstock. Magnetism in ultracold quantum gases. *Journal of Modern Optics*, 51(12): 1829–1841, aug 2004.
- [43] J Kronjäger, C Becker, M Brinkmann, R Walser, Patrick Navez, K Bongs, and K Sengstock. Evolution of a spinor condensate: Coherent dynamics, dephasing, and revivals. *Physical Review A*, 72(6):063619, 2005.

- [44] Wenxian Zhang, D. L. Zhou, M.-S. Chang, M. S. Chapman, and L. You. Coherent spin mixing dynamics in a spin-1 atomic condensate. *Phys. Rev. A*, 72:013602, 2005.
- [45] H. Pu, C. K. Law, S. Raghavan, J. H. Eberly, and N. P. Bigelow. Spin-mixing dynamics of a spinor bose-einstein condensate. *Phys. Rev. A*, 60:1463–1470, Aug 1999.
- [46] C. K. Law, H. Pu, and N. P. Bigelow. Quantum spin mixing in spinor Bose-Einstein condensates. *Phys. Rev. Lett.*, 81:5257, 1998.
- [47] Y. Liu, S. Jung, S. E. Maxwell, L. D. Turner, E. Tiesinga, and P. D. Lett. Quantum phase transitions and continuous observation of spinor dynamics in an antiferromagnetic condensate. *Phys. Rev. Lett.*, 102:125301, Mar 2009.
- [48] F. Gerbier, Artur Widera, Simon Fölling, Olaf Mandel, and Immanuel Bloch. Resonant control of spin dynamics in ultracold quantum gases by microwave dressing. *Phys. Rev. A*, 73:041602(R), 2006.
- [49] Ming-Shien Chang, Qishu Qin, Wenxian Zhang, Li You, and Michael S. Chapman. Coherent spinor dynamics in a spin-1 Bose condensate. *Nature Physics*, 1:111, 2005.
- [50] M.-S. Chang, C. D. Hamley, M. D. Barrett, J. A. Sauer, K. M. Fortier, W. Zhang, L. You, and M. S. Chapman. Observation of spinor dynamics in optically trapped ^{87}Rb Bose-Einstein condensates. *Phys. Rev. Lett.*, 92:140403, 2004.
- [51] A. T. Black, E. Gomez, L. D. Turner, S. Jung, and P. D. Lett. Spinor dynamics in an antiferromagnetic spin-1 condensate. *Phys. Rev. Lett.*, 99:070403, Aug 2007.
- [52] LE Sadler, JM Higbie, SR Leslie, M Vengalattore, and DM Stamper-Kurn. Spontaneous symmetry breaking in a quenched ferromagnetic spinor bose-einstein condensate. *Nature*, 443(7109):312–315, 2006.
- [53] A. Vinit, E. M. Bookjans, C. A. R. Sá de Melo, and C. Raman. Antiferromagnetic spatial ordering in a quenched one-dimensional spinor gas. *Physical Review Letters*, 110(16), apr 2013.
- [54] David Jacob, Lingxuan Shao, Vincent Corre, Tilman Zibold, Luigi De Sarlo, Emmanuel Mimoun, Jean Dalibard, and Fabrice Gerbier. Phase diagram of spin-1 antiferromagnetic Bose-Einstein condensates. *Phys. Rev. A*, 86:061601, Dec 2012.
- [55] J Stenger, S Inouye, D Stamper-Kurn, H.-J Miesner, A Chikkatur, and W Ketterle. Spin domains in ground-state bose-einstein condensates. *Nature*, 396(6709):345–348, Nov 1998.
- [56] E. M. Bookjans, A. Vinit, and C. Raman. Quantum phase transition in an antiferromagnetic spinor Bose-Einstein condensate. *Phys. Rev. Lett.*, 107:195306, Nov 2011.
- [57] A. Vinit and C. Raman. Precise measurements on a quantum phase transition in antiferromagnetic spinor bose-einstein condensates. *Physical Review A*, 95(1), jan 2017.
- [58] M. Vengalattore, S. R. Leslie, J. Guzman, and D. M. Stamper-Kurn. Spontaneously modulated spin textures in a dipolar spinor bose-einstein condensate. *Physical Review Letters*, 100(17), may 2008.

- [59] M. Fattori, T. Koch, S. Goetz, A. Griesmaier, S. Hensler, J. Stuhler, and T. Pfau. Demagnetization cooling of a gas. *Nature Physics*, 2(11):765–768, oct 2006.
- [60] B. Pasquiou, E. Maréchal, G. Bismut, P. Pedri, L. Vernac, O. Gorceix, and B. Laburthe-Tolra. Spontaneous demagnetization of a dipolar spinor bose gas in an ultralow magnetic field. *Physical Review Letters*, 106(25), jun 2011.
- [61] B. Naylor, E. Maréchal, J. Huckans, O. Gorceix, P. Pedri, L. Vernac, and B. Laburthe-Tolra. Cooling of a bose-einstein condensate by spin distillation. *Phys. Rev. Lett.*, 115:243002, Dec 2015.
- [62] J. Stuhler, A. Griesmaier, T. Koch, M. Fattori, T. Pfau, S. Giovanazzi, P. Pedri, and L. Santos. Observation of dipole-dipole interaction in a degenerate quantum gas. *Physical Review Letters*, 95(15), oct 2005.
- [63] G. Bismut, B. Laburthe-Tolra, E. Maréchal, P. Pedri, O. Gorceix, and L. Vernac. Anisotropic excitation spectrum of a dipolar quantum bose gas. *Physical Review Letters*, 109(15), oct 2012.
- [64] Tomoya Isoshima, Tetsuo Ohmi, and Kazushige Machida. Double phase transitions in magnetized spinor Bose-Einstein condensation. *Journal of the Physical Society of Japan*, 69(12):3864–3869, 2000.
- [65] Tin-Lun Ho. Spinor Bose condensates in optical traps. *Phys. Rev. Lett.*, 81:742, 1998.
- [66] A.F.Andreev and I.A.Grishchuk. Spin nematics. *Zh.Eksp.Teor.Fiz.*, 87:467–475, 1984. (Sov.Phys.-JETP 1984, 60, pp. 267-271).
- [67] M. Blume and Y. Y. Hsieh. Biquadratic exchange and quadrupolar ordering. *Journal of Applied Physics*, 40(3):1249–1249, 1969.
- [68] P. G. de Gennes and J. Prost. *The Physics of Liquid Crystals*. Clarendon Press, Oxford, 1995.
- [69] P. Chandra, P. Coleman, and I. Ritchey. Magnets without moments: Spin nematics and beyond (invited). *Journal of Applied Physics*, 69(8):4974–4978, apr 1991.
- [70] P. Chandra and P. Coleman. Quantum spin nematics: Moment-free magnetism. *Physical Review Letters*, 66(1):100–103, jan 1991.
- [71] H. H. Chen and Peter M. Levy. Quadrupole phase transitions in magnetic solids. *Phys. Rev. Lett.*, 27:1383–1385, Nov 1971.
- [72] Satoru Nakatsuji, Yusuke Nambu, Hiroshi Tonomura, Osamu Sakai, Seth Jonas, Collin Broholm, Hirokazu Tsunetsugu, Yiming Qiu, and Yoshiteru Maeno. Spin disorder on a triangular lattice. *Science*, 309(5741):1697–1700, 2005.
- [73] Hirokazu Tsunetsugu and Mitsuhiro Arikawa. Spin nematic phase in s=1 triangular antiferromagnets. *J. Phys. Soc. Jpn*, 75(8):083701, 2006.
- [74] Subhro Bhattacharjee, Vijay B. Shenoy, and T. Senthil. Possible ferro-spin nematic order in NiGa_2S_4 . *Phys. Rev. B*, 74:092406, Sep 2006.

- [75] Andreas Läuchli, Frédéric Mila, and Karlo Penc. Quadrupolar phases of the $s = 1$ bilinear-biquadratic heisenberg model on the triangular lattice. *Phys. Rev. Lett.*, 97:087205, Aug 2006.
- [76] F. Michaud, F. Vernay, and F. Mila. Theory of inelastic light scattering in spin-1 systems: Resonant regimes and detection of quadrupolar order. *Phys. Rev. B*, 84:184424, Nov 2011.
- [77] Adilet Imambekov, M. D. Lukin, and E. Demler. Spin-exchange interactions of spin-one bosons in optical lattices: Singlet, nematic, and dimerized phases. *Phys. Rev. A*, 68:063602, 2003.
- [78] Michiel Snoek and Fei Zhou. Microscopic wave functions of spin-singlet and nematic mott states of spin-one bosons in high-dimensional bipartite lattices. *Phys. Rev. B*, 69:094410, Mar 2004.
- [79] F. Zhou, M. Snoek, J. Wiemer, and I. Affleck. Magnetically stabilized nematic order: three-dimensional bipartite optical lattices. *Phys. Rev. B*, 70:184434, Nov 2004.
- [80] Fei Zhou. Quantum spin nematic states in Bose–Einstein condensates. *International Journal of Modern Physics B*, 17(14):2643–2698, jun 2003.
- [81] Laurent de Forges de Parny, Hongyu Yang, and Frédéric Mila. Anderson tower of states and nematic order of spin-1 bosonic atoms on a 2d lattice. *Phys. Rev. Lett.*, 113:200402, Nov 2014.
- [82] Daniel Podolsky and Eugene Demler. Properties and detection of spin nematic order in strongly correlated electron systems. *New Journal of Physics*, 7(1):59, 2005.
- [83] Dan M. Stamper-Kurn and Masahito Ueda. Spinor Bose gases: Symmetries, magnetism, and quantum dynamics. *Reviews of Modern Physics*, 85(3):1191–1244, July 2013.
- [84] T. Ohmi and T. Machida. Bose-Einstein condensation with internal degrees of freedom in alkali atom gases. *J. Phys. Soc. Jpn*, 67:1822, 1998.
- [85] W.-J. Huang, S.-C. Gou, and Y.-C. Tsai. Transition temperature for the all-optical formation of $F=1$ spinor condensate. *Physical Review A*, 65(6), jun 2002.
- [86] Shun Uchino, Michikazu Kobayashi, and Masahito Ueda. Bogoliubov theory and Lee-Huang-Yang corrections in spin-1 and spin-2 Bose-Einstein condensates in the presence of the quadratic zeeman effect. *Phys. Rev. A*, 81:063632, Jun 2010.
- [87] Y.-M. Kao and T. F. Jiang. Transition temperatures of the trapped ideal spinor bose gas. *The European Physical Journal D*, 40(2):263–269, jun 2006.
- [88] Krisztián Kis-Szabó, Péter Szépfalusy, and Gergely Szirmai. Phases of a polar spin-1 bose gas in a magnetic field. *Physics Letters A*, 364(5):362–367, may 2007.
- [89] Wenxian Zhang, Su Yi, and L. You. Bose-einstein condensation of trapped interacting spin-1 atoms. *Phys. Rev. A*, 70:043611, Oct 2004.
- [90] Nguyen Thanh Phuc, Yuki Kawaguchi, and Masahito Ueda. Effects of thermal and quantum fluctuations on the phase diagram of a spin-1 ^{87}Rb Bose-Einstein condensate. *Phys. Rev. A*, 84:043645, Oct 2011.

- [91] Yuki Kawaguchi, Nguyen Thanh Phuc, and P. Blair Blakie. Finite-temperature phase diagram of a spin-1 Bose gas. *Phys. Rev. A*, 85:053611, May 2012.
- [92] Guillaume Lang and Emilia Witkowska. Thermodynamics of a spin-1 bose gas with fixed magnetization. *Phys. Rev. A*, 90:043609, Oct 2014.
- [93] Lev Pitaevskii and Sandro Stringari. *Bose-Einstein Condensation and Superfluidity*. Oxford University Press (OUP), January 2016.
- [94] Christopher J Pethick and Henrik Smith. *Bose-Einstein Condensation in Dilute Gases*. Cambridge University Press (CUP), 2008.
- [95] Siegfried Grossmann and Martin Holthaus. λ -transition to the Bose-Einstein condensate. *Zeitschrift für Naturforschung A*, 50(10), January 1995.
- [96] Siegfried Grossmann and Martin Holthaus. On Bose-Einstein condensation in harmonic traps. *Physics Letters A*, 208(3):188–192, November 1995.
- [97] H. Haugerud, T. Haugset, and F. Ravndal. A more accurate analysis of Bose-Einstein condensation in harmonic traps. *Physics Letters A*, 225(1-3):18–22, January 1997.
- [98] Wolfgang Ketterle and N. J. van Druten. Bose-Einstein condensation of a finite number of particles trapped in one or three dimensions. *Phys. Rev. A*, 54(1):656–660, July 1996.
- [99] T. Haugset, H. Haugerud, and J. O. Andersen. Bose-Einstein condensation in anisotropic harmonic traps. *Physical Review A*, 55(4):2922–2929, April 1997.
- [100] S Giorgini, LP Pitaevskii, and S Stringari. Thermodynamics of a trapped bose-condensed gas. *Journal of Low Temperature Physics*, 109(1):309–355, 1997.
- [101] J. Söding, D. Guéry-Odelin, P. Desbiolles, F. Chevy, H. Inamori, and J. Dalibard. Three-body decay of a rubidium bose-einstein condensate. *Applied Physics B*, 69(4):257–261, 1999.
- [102] Claude Cohen-Tannoudji, . Diu, Bernard, and Franck Laloe. *Quantum mechanics*. Wiley New York, 1977.
- [103] Jean Dalibard. Collisional dynamics of ultra-cold atomic gases. In *Proceedings of the International School of Physics-Enrico Fermi*, volume 321, page 14, 1999.
- [104] S. Knoop, T. Schuster, R. Scelle, A. Trautmann, J. Appmeier, M. K. Oberthaler, E. Tiesinga, and E. Tiemann. Feshbach spectroscopy and analysis of the interaction potentials of ultracold sodium. *Phys. Rev. A*, 83:042704, Apr 2011.
- [105] Victor V Goldman, Isaac F Silvera, and Anthony J Leggett. Atomic hydrogen in an inhomogeneous magnetic field: Density profile and bose-einstein condensation. *Physical Review B*, 24(5):2870, 1981.
- [106] David A Huse and Eric D Siggia. The density distribution of a weakly interacting bose gas in an external potential. *Journal of Low Temperature Physics*, 46(1-2):137–149, 1982.
- [107] S. Giorgini, L. P. Pitaevskii, and S. Stringari. Condensate fraction and critical temperature of a trapped interacting bose gas. *Phys. Rev. A*, 54:R4633–R4636, Dec 1996.

- [108] Fabrice Gerbier. *Condensats de Bose-Einstein dans un piège anisotrope*. Theses, Université Pierre et Marie Curie - Paris VI, September 2003.
- [109] Anthony E Siegman. *Lasers*. University Science Books, 1986.
- [110] Lena Simon and Walter T. Strunz. Bose gas in a single-beam optical dipole trap. *Physical Review A*, 81(6), jun 2010.
- [111] Wolfgang Ketterle and NJ Van Druten. Evaporative cooling of trapped atoms. *Advances in atomic, molecular, and optical physics*, 37:181–236, 1996.
- [112] D. W. Snoke and J. P. Wolfe. Population dynamics of a bose gas near saturation. *Physical Review B*, 39(7):4030–4037, mar 1989.
- [113] Kristian Helmerson, Alex Martin, and David E. Pritchard. Laser cooling of magnetically trapped neutral atoms. *Journal of the Optical Society of America B*, 9(11):1988, nov 1992.
- [114] C. R. Monroe, E. A. Cornell, C. A. Sackett, C. J. Myatt, and C. E. Wieman. Measurement of cs-cs elastic scattering at $T=30 \mu\text{k}$. *Physical Review Letters*, 70(4):414–417, jan 1993.
- [115] Daniel Suchet, Mihail Rabinovic, Thomas Reimann, Norman Kretschmar, Franz Sievers, Christophe Salomon, Johnathan Lau, Olga Goulko, Carlos Lobo, and Frédéric Chevy. Analog simulation of weyl particles with cold atoms. *EPL (Europhysics Letters)*, 114(2):26005, apr 2016.
- [116] Weizhu Bao and Yongyong Cai. Mathematical theory and numerical methods for bose-einstein condensation. *Kinetic and Related Models*, 6(1):1–135, 2013.
- [117] M. H. Anderson, J. R. Ensher, M. R. Matthews, C. E. Wieman, and E. A. Cornell. Observation of bose-einstein condensation in a dilute atomic vapor. *Science*, 269(5221):198–201, jul 1995.
- [118] Y Castin and R Dum. Bose-einstein condensates in time dependent traps. *Physical Review Letters*, 77(27):5315, 1996.
- [119] Vincent Corre. *Magnetism in spin-1 Bose-Einstein condensates with antiferromagnetic interactions*. PhD thesis, 2014.
- [120] Masahito Ueda and Yuki Kawaguchi. Spinor bose-einstein condensates. *arXiv:1001.2072v2*, 2000.
- [121] G. Bismut, B. Pasquiou, E. Maréchal, P. Pedri, L. Vernac, O. Gorceix, and B. Laburthe-Tolra. Collective excitations of a dipolar bose-einstein condensate. *Phys. Rev. Lett.*, 105(4), jul 2010.
- [122] T. Lahaye, J. Metz, B. Fröhlich, T. Koch, M. Meister, A. Griesmaier, T. Pfau, H. Saito, Y. Kawaguchi, and M. Ueda. d -wave collapse and explosion of a dipolar bose-einstein condensate. *Physical Review Letters*, 101(8), aug 2008.
- [123] K. Aikawa, A. Frisch, M. Mark, S. Baier, A. Rietzler, R. Grimm, and F. Ferlaino. Bose-einstein condensation of erbium. *Phys. Rev. Lett.*, 108(21), may 2012.
- [124] Christopher J Foot. *Atomic physics*, volume 7. Oxford University Press, 2005.

- [125] D. A. Steck. Sodium d line data. available at <http://steck.us/alkalidata>, 2003.
- [126] G. Breit and I. I. Rabi. Measurement of nuclear spin. *Physical Review*, 38(11):2082–2083, dec 1931.
- [127] S. Yi, Ö. E. Müstecaplıoğlu, C. P. Sun, and L. You. Single-mode approximation in a spinor-1 atomic condensate. *Phys. Rev. A*, 66:011601, Jul 2002.
- [128] Tomoya Isoshima, Kazushige Machida, and Tetsuo Ohmi. Spin-domain formation in spinor bose-einstein condensation. *Physical Review A*, 60(6):4857–4863, dec 1999.
- [129] D. S. Hall, M. R. Matthews, J. R. Ensher, C. E. Wieman, and E. A. Cornell. Dynamics of component separation in a binary mixture of bose-einstein condensates. *Physical Review Letters*, 81(8):1539–1542, aug 1998.
- [130] H. Pu, C.K. Law, and N.P. Bigelow. Complex quantum gases: spinor bose–einstein condensates of trapped atomic vapors. *Physica B: Condensed Matter*, 280(1-4):27–31, may 2000.
- [131] Wenxian Zhang, Su Yi, and Li You. Bose-Einstein condensation of trapped interacting spin-1 atoms. *Physical Review A*, 70(4):043611, 2004.
- [132] Guillaume Lang and Emilia Witkowska. Thermodynamics of a spin-1 Bose gas with fixed magnetization. *Physical Review A*, 90(4):043609, 2014.
- [133] W. Ketterle, D. S. Durfee, and D. M. Stamper-Kurn. Making, probing and understanding bose-einstein condensates. In M. Inguscio, S. Stringari, and C. E. Wieman, editors, *Proceedings of the International School on Physics Enrico Fermi 1998, Bose-Einstein Condensation in Atomic Gases*, pages 67–176. IOS Press, 1999. arXiv:cond-mat/9904034.
- [134] Emmanuel Mimoun. *Condensat de Bose-Einstein de sodium dans un piège mésoscopique*. PhD thesis, 2010.
- [135] David Jacob. *Condensats de Bose-Einstein de spin 1: étude expérimentale avec des atomes de sodium dans un piège optique*. PhD thesis, 2012.
- [136] Lingxuan Shao. *Theoretical and experimental study of spin-1 antiferromagnetic Bose-Einstein Condensates*. Theses, Ecole Normale Supérieure, July 2014.
- [137] Harold J Metcalf and Peter Straten. *Laser cooling and trapping of neutral atoms*. Wiley Online Library, 2007.
- [138] Jean Dalibard. Une brève histoire des atomes froids. *Cours du Collège de France*, 2015.
- [139] Jean Dalibard. *Atomes ultra-froids*. notes de cours.
- [140] Emmanuel Mimoun, Luigi De Sarlo, David Jacob, Jean Dalibard, and Fabrice Gerbier. Fast production of ultracold Sodium gases using light-induced desorption and optical trapping. *Phys. Rev. A*, 81:023631, Feb 2010.
- [141] Aviv Keshet and Wolfgang Ketterle. A distributed, graphical user interface based, computer control system for atomic physics experiments. *Review of Scientific Instruments*, 84(1):015105, 2013.

- [142] Vincent Dugrain, Peter Rosenbusch, and Jakob Reichel. Alkali vapor pressure modulation on the 100ms scale in a single-cell vacuum system for cold atom experiments. *Rev. Sci. Instrum.* 85, 083112 (2014).
- [143] E. Mimoun, L. Sarlo, J.-J. Zondy, J. Dalibard, and F. Gerbier. Solid-state laser system for laser cooling of sodium. *Applied Physics B*, 99(1-2):31–40, 2010.
- [144] P Juncar, J Pinard, J Hamon, and A Chartier. Absolute determination of the wavelengths of the sodium d1 and d2 lines by using a cw tunable dye laser stabilized on iodine. *Metrologia*, 17(3):77, 1981.
- [145] Jon H. Shirley. Modulation transfer processes in optical heterodyne saturation spectroscopy. *Optics Letters*, 7(11):537, nov 1982.
- [146] Jing Zhang, Dong Wei, Changde Xie, and Kunchi Peng. Characteristics of absorption and dispersion for rubidium d2 lines with the modulation transfer spectrum. *Optics express*, 11(11):1338–1344, 2003.
- [147] D J McCarron, S A King, and S L Cornish. Modulation transfer spectroscopy in atomic rubidium. *Measurement Science and Technology*, 19(10):105601, aug 2008.
- [148] Rodolphe Le Targat, J-J Zondy, and Pierre Lemonde. 75%-efficiency blue generation from an intracavity PPKTP frequency doubler. *Optics communications*, 247(4):471–481, 2005.
- [149] D Jacob, E Mimoun, L De Sarlo, M Weitz, J Dalibard, and F Gerbier. Production of sodium Bose Einstein condensates in an optical dimple trap. *New Journal of Physics*, 13(6):065022, 2011.
- [150] Matthias Scholl. *Probing an ytterbium Bose-Einstein condensate using an ultranarrow optical line : towards artificial gauge fields in optical lattices*. Theses, Université Pierre et Marie Curie - Paris VI, December 2014.
- [151] Toshiya Kinoshita, Trevor Wenger, and David S. Weiss. All-optical bose-einstein condensation using a compressible crossed dipole trap. *Phys. Rev. A*, 71(1), jan 2005.
- [152] Chen-Lung Hung, Xibo Zhang, Nathan Gemelke, and Cheng Chin. Accelerating evaporative cooling of atoms into bose-einstein condensation in optical traps. *Physical Review A*, 78(1), jul 2008.
- [153] J.-F. Clément, J.-P. Brantut, M. Robert de Saint-Vincent, R. A. Nyman, A. Aspect, T. Bourdel, and P. Bouyer. All-optical runaway evaporation to bose-einstein condensation. *Physical Review A*, 79(6), jun 2009.
- [154] D. M. Stamper-Kurn, H.-J. Miesner, A. P. Chikkatur, S. Inouye, J. Stenger, and W. Ketterle. Reversible formation of a bose-einstein condensate. *Physical Review Letters*, 81(11):2194–2197, sep 1998.
- [155] T. Weber. Bose-einstein condensation of cesium. *Science*, 299(5604):232–235, dec 2002.
- [156] Z-Y Ma, A M Thomas, C J Foot, and S L Cornish. The evaporative cooling of a gas of caesium atoms in the hydrodynamic regime. *Journal of Physics B: Atomic, Molecular and Optical Physics*, 36(16):3533–3540, aug 2003.

- [157] Zhao-Yuan Ma, Christopher J Foot, and Simon L Cornish. Optimized evaporative cooling using a dimple potential: an efficient route to bose–einstein condensation. *Journal of Physics B: Atomic, Molecular and Optical Physics*, 37(15):3187–3195, jul 2004.
- [158] D. Comparat, A. Fioretti, G. Stern, E. Dimova, B. Laburthe Tolra, and P. Pillet. Optimized production of large bose-einstein condensates. *Physical Review A*, 73(4), apr 2006.
- [159] D. B. Hume, I. Stroescu, M. Joos, W. Muessel, H. Strobel, and M. K. Oberthaler. Accurate atom counting in mesoscopic ensembles. *Physical Review Letters*, 111(25), dec 2013.
- [160] G Reinaudi, T Lahaye, Z Wang, and D Guéry-Odelin. Strong saturation absorption imaging of dense clouds of ultracold atoms. *Optics letters*, 32(21):3143–3145, 2007.
- [161] L Chomaz, L Corman, T Yefsah, R Desbuquois, and J Dalibard. Absorption imaging of a quasi-two-dimensional gas: a multiple scattering analysis. *New Journal of Physics*, 14(5):055001, 2012.
- [162] S. D. Jenkins, J. Ruostekoski, J. Javanainen, R. Bourgain, S. Jennewein, Y. R. P. Sortais, and A. Browaeys. Optical resonance shifts in the fluorescence of thermal and cold atomic gases. *Physical Review Letters*, 116(18), may 2016.
- [163] Tarik Yefsah, Rémi Desbuquois, Lauriane Chomaz, Kenneth J. Günter, and Jean Dalibard. Exploring the thermodynamics of a two-dimensional bose gas. *Physical Review Letters*, 107(13), sep 2011.
- [164] S. Stringari. Collective excitations of a trapped bose-condensed gas. *Physical Review Letters*, 77(12):2360–2363, sep 1996.
- [165] S. Friebe, C. D’Andrea, J. Walz, M. Weitz, and T. W. Hänsch. CO₂-laser optical lattice with cold rubidium atoms. *Physical Review A*, 57(1):R20–R23, jan 1998.
- [166] S. Balik, A. L. Win, and M. D. Havey. Imaging-based parametric resonance in an optical dipole-atom trap. *Physical Review A*, 80(2), aug 2009.
- [167] Vasilii Makhalov, Kirill Martiyanov, Tatiana Barmashova, and Andrey Turlapov. Precision measurement of a trapping potential for an ultracold gas. *Physics Letters A*, 379(4):327–332, feb 2015.
- [168] Walter Kohn. Cyclotron resonance and de haas-van alphen oscillations of an interacting electron gas. *Physical Review*, 123(4):1242–1244, aug 1961.
- [169] John F. Dobson. Harmonic-potential theorem: Implications for approximate many-body theories. *Physical Review Letters*, 73(16):2244–2247, oct 1994.
- [170] Walther Gerlach and Otto Stern. Der experimentelle nachweis der richtungsquantelung im magnetfeld. *Zeitschrift für Physik*, 9(1):349–352, 1922.
- [171] Walther Gerlach and Otto Stern. über die richtungsquantelung im magnetfeld. *Annalen der Physik*, 379(16):673–699, 1924.
- [172] T. E. Phipps and J. B. Taylor. The magnetic moment of the hydrogen atom. *Physical Review*, 29(2):309–320, feb 1927.

- [173] Joseph W Goodman. *Speckle phenomena in optics: theory and applications*. Roberts and Company Publishers, 2007.
- [174] Joseph W Goodman. Some fundamental properties of speckle. *JOSA*, 66(11):1145–1150, 1976.
- [175] Hector J Rabal and Roberto A Braga Jr. *Dynamic laser speckle and applications*. CRC Press, 2008.
- [176] S. E. Skipetrov, J. Peuser, R. Cerbino, P. Zakharov, B. Weber, and F. Scheffold. Noise in laser speckle correlation and imaging techniques. *Optics Express*, 18(14):14519, jun 2010.
- [177] JP Lewis. Fast normalized cross-correlation. In *Vision interface*, volume 10, pages 120–123, 1995.
- [178] Xiaolin Li, Min Ke, Bo Yan, and Yuzhu Wang. Reduction of interference fringes in absorption imaging of cold atom cloud using eigenface method. *Chin. Opt. Lett.*, 5(3):128–130, Mar 2007.
- [179] CF Ockeloen, AF Tauschinsky, RJC Spreeuw, and S Whitlock. Detection of small atom numbers through image processing. *Physical Review A*, 82(6):061606, 2010.
- [180] Caspar F. Ockeloen. Probing fluctuations in a lattice of mesoscopic atomic ensembles. Master's thesis, van der Waals-Zeeman Institute, University of Amsterdam, 2010.
- [181] Phillip L. Gould, George A. Ruff, and David E. Pritchard. Diffraction of atoms by light: The near-resonant kapitza-dirac effect. *Physical Review Letters*, 56(8):827–830, feb 1986.
- [182] P Jeffery Ungar, David S Weiss, Erling Riis, and Steven Chu. Optical molasses and multilevel atoms: theory. *JOSA B*, 6(11):2058–2071, 1989.
- [183] I. I. Rabi, J. R. Zacharias, S. Millman, and P. Kusch. A new method of measuring nuclear magnetic moment. *Physical Review*, 53(4):318–318, feb 1938.
- [184] Michael A Lombardi, Thomas P Heavner, and Steven R Jefferts. Nist primary frequency standards and the realization of the si second. *NCSLI Measure*, 2(4):74–89, 2007.
- [185] Charles P. Slichter. *Principles of Magnetic Resonance*. Springer Berlin Heidelberg, 1990.
- [186] Claude Cohen-Tannoudji, Jacques Dupont-Roc, and Gilbert Grynberg. *Processus d'interaction entre photons et atomes*. Edp Sciences, 2012.
- [187] Rodney Loudon. *The quantum theory of light*. OUP Oxford, 2000.
- [188] M. Lombardi. Création d'orientation par combinaison de deux alignements alignement et orientation des niveaux excités d'une décharge haute fréquence. *Journal de Physique*, 30(8-9):631–642, 1969.
- [189] C. Cohen-Tannoudji and J. Dupont-Roc. Orientation, par action d'un champ électrique "fictif", d'une vapeur initialement alignée. *Optics Communications*, 1(4):184–186, sep 1969.
- [190] F. Bloch. Nuclear induction. *Phys. Rev.*, 70:460–474, Oct 1946.

- [191] Karina Jiménez-García. *Artificial Gauge Fields for Ultracold Neutral Atoms*. PhD thesis, JQI, NIST, University of Maryland Gaithersburg, 2012.
- [192] T. Zibold, V. Corre, C. Frapolli, A. Invernizzi, J. Dalibard, and F. Gerbier. Spin-nematic order in antiferromagnetic spinor condensates. *Phys. Rev. A*, 93(2), February 2016.
- [193] V Corre, T Zibold, C Frapolli, L Shao, J Dalibard, and F Gerbier. Spin-1 condensates at thermal equilibrium: A SU(3) coherent state approach. *EPL (Europhysics Letters)*, 110(2): 26001, 2015.
- [194] Yuki Kawaguchi and Masahito Ueda. Spinor Bose–einstein condensates. *Physics Reports*, 520(5):253–381, 2012.
- [195] C. J Mullin, J. M. Keller, C. L. Hammer, and R. H. Good. Polarization and alignment of spin one states. *Annals of Physics*, 37(1):55–61, 1966.
- [196] B. A. Ivanov and A. K. Kolezhuk. Effective field theory for the $s = 1$ quantum nematic. *Phys. Rev. B*, 68:052401, Aug 2003.
- [197] Keiji Murata, Hiroki Saito, and Masahito Ueda. Broken-axisymmetry phase of a spin-1 ferromagnetic bose-einstein condensate. *Physical Review A*, 75(1), jan 2007.
- [198] Bernd Lücke, Manuel Scherer, Jens Kruse, Luca Pezzé, Frank Deuretzbacher, Phillip Hyllus, Jan Peise, Wolfgang Ertmer, Jan Arlt, Luis Santos, et al. Twin matter waves for interferometry beyond the classical limit. *Science*, 334(6057):773–776, 2011.
- [199] C Gross, H Strobel, E Nicklas, T Zibold, N Bar-Gill, G Kurizki, and MK Oberthaler. Atomic homodyne detection of continuous-variable entangled twin-atom states. *Nature*, 480(7376): 219–223, 2011.
- [200] Bernd Lücke, Jan Peise, Giuseppe Vitagliano, Jan Arlt, Luis Santos, Géza Tóth, and Carsten Klempt. Detecting multiparticle entanglement of dicke states. *Phys. Rev. Lett.*, 112(15): 155304, 2014.
- [201] M. Naraschewski and D. M. Stamper-Kurn. Analytical description of a trapped semi-ideal bose gas at finite temperature. *Physical Review A*, 58(3):2423–2426, sep 1998.
- [202] B. Pasquiou, E. Maréchal, L. Vernac, O. Gorceix, and B. Laburthe-Tolra. Thermodynamics of a Bose-Einstein condensate with free magnetization. *Phys. Rev. Lett.*, 108:045307, Jan 2012.
- [203] B. Naylor, M. Brewczyk, M. Gajda, O. Gorceix, E. Maréchal, L. Vernac, and B. Laburthe-Tolra. Competition between bose-einstein condensation and spin dynamics. *Physical Review Letters*, 117(18), oct 2016.
- [204] Ryan Olf, Fang Fang, G. Edward Marti, Andrew MacRae, and Dan M. Stamper-Kurn. Thermometry and cooling of a bose gas to 0.02 times the condensation temperature. *Nat Phys*, 11(9):720–723, September 2015.
- [205] Fang Fang, Ryan Olf, Shun Wu, Holger Kadau, and Dan M. Stamper-Kurn. Condensing magnons in a degenerate ferromagnetic spinor bose gas. *Phys. Rev. Lett.*, 116:095301, Mar 2016.

- [206] Gerhard Bohm and Günter Zech. *Introduction to statistics and data analysis for physicists*. DESY, 2010.
- [207] Markus Holzmann. *La transition de Bose-Einstein dans un gaz dilué*. Theses, Université Pierre et Marie Curie - Paris VI, June 2000.
- [208] Markus Holzmann, Werner Krauth, and Martin Naraschewski. Precision monte carlo test of the hartree-fock approximation for a trapped bose gas. *Physical Review A*, 59(4):2956–2961, apr 1999.
- [209] M. Holzmann, P. Grüter, and F. Laloë. Bose-einstein condensation in interacting gases. *The European Physical Journal B*, 10(4):739–760, aug 1999.
- [210] J. R. Ensher, D. S. Jin, M. R. Matthews, C. E. Wieman, and E. A. Cornell. Bose-einstein condensation in a dilute gas: Measurement of energy and ground-state occupation. *Physical Review Letters*, 77(25):4984–4987, dec 1996.
- [211] Robert P. Smith, Robert L. D. Campbell, Naaman Tammuz, and Zoran Hadzibabic. Effects of interactions on the critical temperature of a trapped bose gas. *Physical Review Letters*, 106(25), jun 2011.
- [212] Naaman Tammuz, Robert P. Smith, Robert L. D. Campbell, Scott Beattie, Stuart Moulder, Jean Dalibard, and Zoran Hadzibabic. Can a bose gas be saturated? *Physical Review Letters*, 106(23), jun 2011.
- [213] Adilet Imambekov, E. Demler, and M. D. Lukin. Magnetization plateaus for spin-one bosons in optical lattices: Stern-gerlach experiments with strongly correlated atoms. *Phys. Rev. Lett.*, 93:120405, 2004.
- [214] Matthew P. A. Fisher, Peter B. Weichman, G. Grinstein, and Daniel S. Fisher. Boson localization and the superfluid-insulator transition. *Physical Review B*, 40(1):546–570, jul 1989.
- [215] Arnau Sala, David López Núñez, Joan Martorell, Luigi De Sarlo, Tilman Zibold, Fabrice Gerbier, Artur Polls, and Bruno Juliá-Díaz. Shortcut to adiabaticity in spinor condensates. *Physical Review A*, 94(4), oct 2016.
- [216] Tomasz Świsłocki, Emilia Witkowska, and Michał Matuszewski. Nonadiabatic quantum phase transition in a trapped spinor condensate. *Physical Review A*, 94(4), oct 2016.
- [217] R.W. Boyd. *Nonlinear Optics*. Elsevier BV, 2003.
- [218] John D. Bierlein and Herman Vanherzeele. Potassium titanyl phosphate: properties and new applications. *J. Opt. Soc. Am. B*, 6(4):622–633, April 1989.
- [219] Kiyoshi Kato and Eiko Takaoka. Sellmeier and thermo-optic dispersion formulas for ktp. *Appl. Opt.*, 41(24):5040–5044, August 2002.
- [220] GD Boyd and DA Kleinman. Parametric interaction of focused gaussian light beams. *Journal of Applied Physics*, 39:3597, 1968.

-
- [221] J.L. Hall, L. Hollberg, T. Baer, and H.G. Robinson. Optical heterodyne saturation spectroscopy. *Applied Physics Letters*, 39(9):680–682, 1981.
- [222] N. Goldman, G. Juzeliūnas, P. Öhberg, and I. B. Spielman. Light-induced gauge fields for ultracold atoms. *Reports on Progress in Physics*, 77(12):126401, nov 2014.
- [223] A. R. Edmonds. *Angular Momentum in Quantum Mechanics*. Princeton University Press, 1996.
- [224] Y.-J. Lin, K. Jimenez-Garcia, and I. B. Spielman. Spin-orbit-coupled Bose-Einstein condensates. *Nature*, 471(7336):83–86, 2011.

Résumé

Dans ce manuscrit, nous présentons une étude expérimentale d'un gaz de Bose de spin 1 avec des interactions antiferromagnétiques avec des atomes de sodium ultra-froids dans l'état hyperfin $F=1$. Les trois composantes Zeeman sont piégées simultanément dans des pièges dipolaires optiques. Nous obtenons un condensat de Bose-Einstein spineur par refroidissement évaporatif et nous étudions ses propriétés magnétiques. Il y a deux types d'interactions dans le système : des interactions de contact qui ne changent pas les populations des composantes Zeeman et des interactions d'échange de spin qui les modifient. Une compétition entre l'énergie Zeeman et l'énergie d'échange impose l'ordre magnétique dans le système.

Nous étudions dans un premier temps les phases magnétiques de condensats de Bose-Einstein spineurs à température quasi nulle. L'état fondamental comporte deux phases qui sont observées en variant le champ magnétique (donc l'énergie Zeeman quadratique) et la magnétisation de l'échantillon. Dans la phase antiferromagnétique, le spin de l'échantillon est simplement selon l'axe du champ magnétique. Dans la phase polaire, une composante transverse apparaît pour minimiser l'énergie Zeeman. Pour une magnétisation nulle, le condensat spineur forme un nématique de spin. Cet état, nommé par analogie avec la phase nématique dans les cristaux liquides, est caractérisée par des fluctuations de spin orthogonales à un axe particulier, mais sans préférer une des deux directions sur cet axe. Dans chacune des deux phases, l'ordre nématique se manifeste par une minimisation de la longueur du spin transverse en imposant une valeur particulière (π) de la phase relative des composantes Zeeman $\theta = \phi_{+1} + \phi_{-1} - 2\phi_0$. Nous mesurons la longueur du spin transverse en analysant le bruit de spin après une rotation. Dans un second temps, nous étudions la thermodynamique d'un gaz de Bose de spin 1 près de la température critique pour la condensation de Bose-Einstein. Nous mesurons plusieurs scénarios de condensation séquentiels en fonction de la magnétisation et du champ magnétique. La température critique mesurée révèle que les interactions ont un effet important quand la condensation d'une composante se fait en présence d'un condensat dans une autre composante. Nous utilisons une théorie d'Hartree-Fock simplifiée, en négligeant les interactions d'échange de spin. Nous constatons que les résultats expérimentaux sont en bon accord. Cependant, pour de bas champs magnétiques, le diagramme de phase thermodynamique est largement modifié par les interactions d'échange de spin, ce qui pose de nouvelles questions sur leur rôle à température finie.

Mots Clés

Condensats de Bose-Einstein, magnétisme, spineur, gaz ultra-froids, ordre nématique de spin, thermodynamique.

Abstract

In this manuscript, we present an experimental study of a Spin 1 Bose gas with antiferromagnetic interactions with ultracold sodium atoms in the $F=1$ manifold. The three Zeeman components are trapped simultaneously in optical dipole traps. By performing evaporative cooling, we obtain quasi-pure spinor Bose-Einstein condensates of which we study the magnetic properties. There are two types of interactions between the constituents of the system: Contact interactions that do not change the Zeeman populations and spin-exchange contact interactions that do. A competition between Zeeman energy and the spin-exchange energy sets the magnetic ordering in the system.

We first study the magnetic phases of spinor Bose-Einstein condensates near zero temperature. The ground state presents two phases that are observed by varying the magnetic field (hence the quadratic Zeeman energy) and the magnetization of the sample. In the antiferromagnetic phase, the spin of the sample is purely along the direction of the magnetic field. In the broken-axisymmetry phase, a transverse component appears in order to minimize the Zeeman energy. For zero magnetization, the spinor condensate forms a spin nematic. This state, named in analogy with the liquid crystal nematic phase, is characterized by spin fluctuations orthogonal to a particular axis, with no preferred direction along that axis. In both phases, spin nematic order manifests as a minimization of the transverse spin length that is realized by enforcing a particular value (π) of the relative phase of the Zeeman components $\theta = \phi_{+1} + \phi_{-1} - 2\phi_0$. We measure the transverse spin length by analyzing spin noise after a spin rotation.

Second, we study the thermodynamics of an antiferromagnetic spin 1 Bose gas next to the critical temperature for Bose-Einstein condensation. We measure several sequential condensation scenarios depending on the magnetization and the magnetic field. The measured critical temperatures reveal a large effect of interactions when one of the Zeeman components condenses in presence of a condensate in another component. We use a simplified Hartree-Fock theory, neglecting the spin exchange interactions and note a good agreement with our data. However, for low magnetic fields, the thermodynamic phase diagram is strongly modified which raises new open questions about the role of spin exchange interactions at finite temperatures.

Keywords

Bose-Einstein condensates, magnetism, spinor, ultracold gases, spin nematic order, thermodynamics.